7-19-2021 12:00 PM

Impact of Local Fluidized Bed Hydrodynamics on the Distribution of Liquid Sprayed into the Bed

Yuan Li, *The University of Western Ontario*

Supervisor: Briens, Cedric, *The University of Western Ontario*
Joint Supervisor: Berruti, Franco, *The University of Western Ontario*
A thesis submitted in partial fulfillment of the requirements for the Doctor of Philosophy degree in Chemical and Biochemical Engineering

Abstract

In Fluid Coking, heavy oil is sprayed into a fluidized bed of hot coke particles that provide heat for the reaction and vaporization of the products, using nozzles located at different radial and axial locations of the reactor. In industrial units, imperfect initial liquid-solid contact results in the formation of wet agglomerates, which have been shown to cause fouling of the stripper sheds.

This thesis aims to reduce agglomerate formation by modifying the bed hydrodynamics in the spray region by adjusting the initial fluidization gas distribution or using a baffle.

Experimental methods were developed to study local gas flow, solids and liquid mixing, and initial liquid-solid contact. In each case, several measurement methods were applied to get reliable results.

Modifying the local bed hydrodynamics improves the initial liquid-solid contact. In industrial cokers, nozzles cannot be extended too far from the wall. The initial liquid-solid contact can be enhanced by directing gas bubbles near the nozzle tip, where they keep the bed fluidized to facilitate solids suction into the jet, and to the first half of the spray jet cavity, where they add solids to mix with the injected liquid.

Adjusting the initial fluidization gas distribution can reduce the proportion of the injected liquid initially trapped within wet agglomerates by 25 %, at a fluidization velocity of 1 m/s (typical of the upper rector sections). Adding a baffle reduces this proportion by 80 % and is even more effective at the lower fluidization velocities corresponding to the lower injection nozzles in cokers. Baffle performance is affected by the baffle geometry: vertical "flux tubes" located in some industrial baffles reduce the beneficial impact of the baffle on the initial liquid distribution. In cokers, baffles are applied to prevent wet solids from reaching the stripper at the bottom of the reactor. With the best baffle for initial liquid-solid contact, the wet solids took 5 to 10 % longer to travel from the spray region to the bed bottom. The baffle did not hinder the rapid mixing of wet solids from the spray region with the hot bed particles, which is required for rapid vaporization.

Keywords

Fluid coking, Bed hydrodynamics, Baffle, Agglomerates, Solids mixing, Vaporization rate

Summary for Lay Audience

The fluid bed is widely applied to provide a liquid-like behavior by fluidizing solid particles with gases because it provides excellent mass and heat transfer. The Fluid Coking™ technology uses this principle to upgrade bitumen by injecting bitumen with atomization gas into a bed filled with hot coke particles to be thermally cracked into more valuable lighter products. However, a portion of valuable liquid becomes trapped in agglomerates. The agglomerates could cause fouling in the bottom of the reactor (stripper section) and eventually plug it. Then the whole unit will have to be shut down for unplugging and cleaning. The main objective of this work is to develop strategies to reduce the formation of the agglomerates by modifying the local bed hydrodynamics and directing the gas bubbles to desired locations. We identified what kind of baffles or changes to the gas distributor can achieve this objective. Also, we ensured the modifications made are not detrimental to the wet solids mixing.

Co-Authorship Statement

The journal articles written from the thesis work are listed below. The individual contributions of all members are also indicated.

Article title: Impact of local fluidized bed hydrodynamics on the distribution of liquid sprayed into the bed. Powder Technology
Authors: Yuan Li, Francisco Sanchez Careaga, Cedric Briens, Franco Berruti, Jennifer McMillan
Status: Published in Powder Technology (2020)
Individual contribution: The manuscript was written by Yuan Li, who also conducted the experimental work and analyzed the data. Francisco wrote the code to collect the data. Cedric Briens, Franco Berruti, Jennifer McMillan reviewed various drafts of the article. Cedric Briens and Franco Berruti jointly supervised the work.

Article title: Applications of electrostatic probes in fluidized beds. Powder Technology
Authors: Yuan Li, Francisco Sanchez Careaga, Cedric Briens, Franco Berruti, Jennifer McMillan
Status:

Published in Powder Technology (2020)
Individual contribution: The manuscript was written by Yuan Li, who also conducted the experimental work and analyzed the data. Francisco wrote the code to collect the data. Cedric Briens, Franco Berruti, Jennifer McMillan reviewed various drafts of the article. Cedric Briens and Franco Berruti jointly supervised the work.

Article title: IMPACT OF FLUIDIZED BED HYDRODYNAMICS ON THE DISTRIBUTION OF LIQUID SPRAYED INTO THE BED
Authors: Yuan Li, Francisco Sanchez Careaga, Cedric Briens, Franco Berruti, Jennifer McMillan
Status: Published in CFB 13 conference proceedings (2021)
Individual contribution: The manuscript was written by Yuan Li, who also conducted the experimental work and analyzed the data. Francisco wrote the code to collect the data. Cedric Briens, Franco Berruti, Jennifer McMillan reviewed various drafts of the article. Cedric Briens and Franco Berruti jointly supervised the work.

Other than the published papers mainly included in chapters 4 and 5, chapter 6 is not yet a journal article.

Chapter 6:

Impact of gas bubble flow and baffle on wet solids mixing and vaporization rate with an ideal nozzle
Authors: Yuan Li, Francisco Sanchez Careaga, Cedric Briens, Franco Berruti, Jennifer McMillan
Individual contribution: The manuscript was written by Yuan Li, who also conducted the experimental work and analyzed the data. Francisco wrote the code to collect the data. Cedric Briens, Franco Berruti, Jennifer McMillan reviewed various drafts of the detailed outline. Cedric Briens and Franco Berruti jointly supervised the work.

Acknowledgments

During my Ph. D. program, I received help from a lot of people and institutions. I would like to send my sincere acknowledgment to them.

I am very grateful to both my supervisors Dr. Cedric Briens and Dr. Franco Berruti, for their support, guidance, and suggestions in this research.

I want to acknowledge Dr. Jennifer McMillan from Syncrude Canada Limited for their guidance and help transition and complete this research.

I want to thank the financial support to Syncrude Canada Limited; and the Natural Science and Engineering Research Council (NSERC) of Canada.

I want to acknowledge Western University, the Chemical and Biochemical Engineering Department, and Institute for Chemicals & Fuels from Alternative Resources (ICFAR) for giving me this opportunity work to work on this exciting project and work with these such friendly, helpful, intelligent people. I want to thank Francisco Sanchez Careaga, who wrote codes to collect data; Yohann Cochet, who helped with part of methods development; and Aaron Joness, who help me with some experiments.

Finally, I would like to express my deepest thanks to my parents: Lichun Wang and Xizhou Li. They brought me to this beloved world and supported me unconditionally. Also, I'd like to send thanks to all my family members. Without any of you, I would never be what I am now.

Table of Contents

List of Tables

List of Figures

Chapter 1

1 Introduction, literature review, and thesis objectives

This research aims to improve the interaction between feed droplets and solids in a fluidized bed by modifying local bed hydrodynamics. This study investigated the impact of superficial gas velocity, fluidization gas distribution, and baffles on bed hydrodynamics and liquid distribution.

This work can be applied to various fields that incorporate spraying liquid into a fluidized bed while agglomeration is undesired, such as oil and gas, pharmaceutical, food, fertilizer, and polymerization. There is a wide range where liquid injection in fluidized beds is applied in industrial production: Fluid Coking^{TM} technology [1]; Fluid Catalytic Cracking (FCC) [1]; linear low-density polyethylene production [2]; and coating, granulation, and agglomeration [3]. However, this work focused on Fluid CokingTM, which plays an essential role in Canada's economy. On average, about 15 % of raw bitumen used as feedstock for upgrading is lost in the conversion process [4]. This study is aimed at reducing the agglomerates in a Coker to improve liquid yield.

Section 1.1 describes the Fluid Coking process and several other industrial processes using liquid injection into a fluid bed. Section 1.2 reviews previous studies on the impact of superficial gas velocity, fluidizing gas distribution, and baffles on fluidized bed hydrodynamics. Section 1.3 reviews previous studies on the impact of superficial gas velocity, fluidizing gas distribution, and baffles on liquid distribution in fluidized beds. Moreover, section 1.4 provides an overview of the specific objectives of this thesis.

1.1 General introduction

1.1.1 Fluid Coking^{TM}

The oil reserves sources in the world and Canada are similar (Figure 1.1). In Canada, oil sands bitumen makes up 39% of the oil reserves (Figure 1.1). The heavy oil reserves, including heavy oil, extra-heavy oil, and oil sands bitumen, are now more extensive than the conventional reserves worldwide (Figure 1.1). Heavy oil requires upgrading

treatment, such as a hydrogen addition process or a carbon rejection process, before being used as transportation fuels and petrochemical feedstocks. Heavy oil has a high viscosity, high density, and high concentration of nitrogen, sulfur, and heavy metals [5].

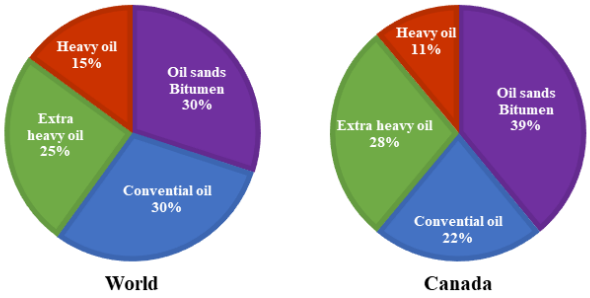

Figure 1.1 World and Canada [6] conventional and unconventional oil reserves

As a popular carbon rejection process, Fluid Coking^{TM} is used in Canada to upgrade around 15-20 % of heavy oil from the oilsands to produce about 400,000 barrels/day of light, synthetic crude oil. The Fluid Cokers of Syncrude in Northern Alberta produced around 314,600 barrels/s per day in 2019 [4].

In a Fluid Coker, preheated bitumen (350 ℃) is sprayed through steam atomization spray nozzles into a fluidized bed of hot coke particles (500-540 ℃) to be thermally cracked to condensable vapors (liquid products), non-condensable gases, and solid coke (Figure 1.2). These particles have a bulk density of 750–880 kg/m3, a particle density of 1440 kg/m3, and an average diameter of 150 - 200 μm [7, 8]. There are 6 rings of nozzles located at various heights. Each ring contains 10 to 18 spray nozzles [9]. The reactor pressure is between 0 to 3.5 bar. The superficial gas velocity is maintained between 0.3 and 1 m/s from the bottom to the reactor top [10]. The hot coke particles enter the bed at the top and move downward through the reactor section (Figure 1.2); they go through a stripper before being transferred to the burner, where partial combustion of the coke allows their reheating before being recirculated into the bed.

The fluidization gas carries the vapors to cyclones that separate solids from vapors and gas. The lighter vapors leave the coker for further condensation and upgrading. In the scrubber, new feed contacts the hydrocarbons and steam exiting from the reactor

cyclones: this preheats the feed and condenses heavy resids that are thus recycled to the reactor with the feed.

When spraying the bitumen into a bed of hot coke particles, the ideal case is that the bitumen droplets will be uniformly distributed on hot coke particles, which will then quickly disperse through the bed of dry, hot coke particles. However, a portion of the liquid is trapped in wet agglomerates formed with solid coke particles. A portion of coke particles flowing down from the spray region, carrying some agglomerates, go through a stripper section before being conveyed to a burner vessel, where they are reheated. The wet agglomerates and heavy hydrocarbons attached to coke particles will be stripped by steam in the stripper section (Figure 1.2). The coke particles are transported from the reactor to the burner (600 ℃) [10], where they are reheated by combustion with air. The hot coke particles are then circulated back to the reactor to maintain the temperature.

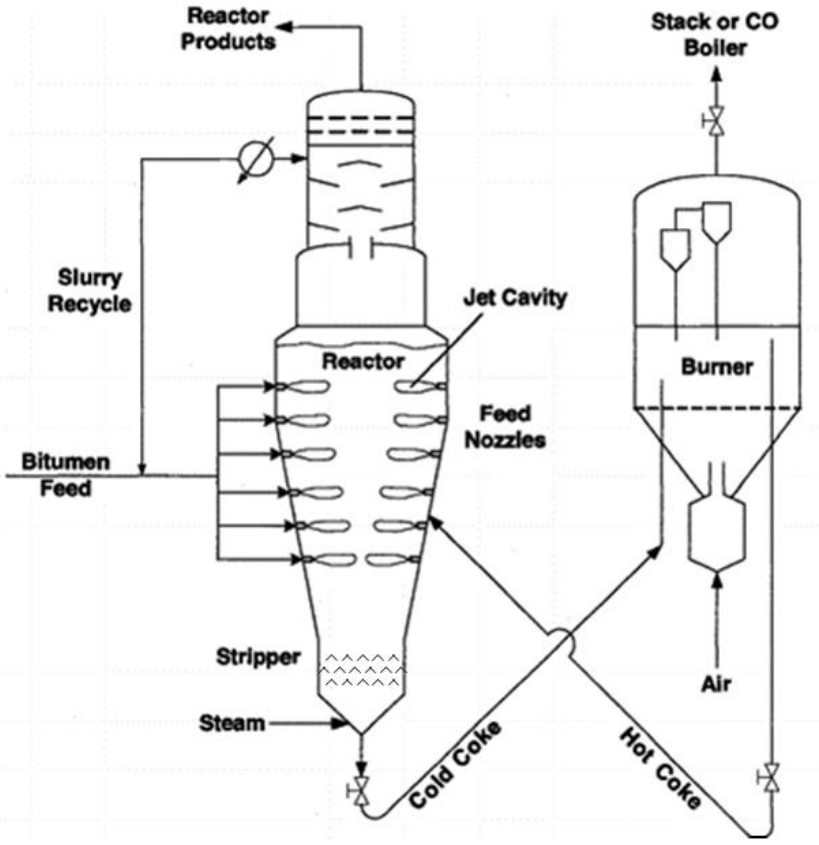

Figure 1.2 Simplified process flow diagram of Fluid Coking™ [11]

Wet agglomerates entrained with the particles flowing through the stripper are partially responsible for the fouling of the stripper sheds with coke deposits[12]. Stripper fouling is a common cause of premature shutdowns.

Wet agglomerates also reduce the yield of valuable vapor products due to insufficient mass and heat transfer. Some unreacted liquid trapped in agglomerates leaves the reactor with the cold coke and is combusted in the burner. Ali et al. [13] indicated that, at 502 °C, when liquid trapped in agglomerates was being thermally cracked, the undesirable coke yield increased by 12 % compared to thin films (20 μm). It is, therefore, essential to minimize the formation of wet agglomerates.

Inserting a ring-baffle above the stripper section has been proposed to increase the residence time of wet agglomerates above the baffle, providing more time for liquid conversion [14]. The patent also shows various other locations to install the baffle, for example, under the spray nozzles. However, they also indicated that better baffle locations, baffle geometries should be further studied. Figure 1.3 shows a commercial-scaled ring baffle with 22 “flux-tubes” applied in the industry [15]. The “flux-tubes” are O-shaped downcomers, which permit the downward flow of solids and upward flow of gas through the baffles [16].

Figure 1.3 Ring baffle with flux-tube in a Coker [15]

Another process called Flexicoking™ was developed based on Fluid Coking™. The main difference is that the Flexicoking™ process uses a gasifier (Figure 1.4). The coke is heated in the heater by the gasifier products and circulates back to the reactor as hot coke. The excess coke in the heater is transferred to the gasifier, where it reacts with air and steam to produce a gas. The gas and coke mixture flows back to the heater to heat the coke. After removing coke-fines and desulfurization, the gas that exits the overhead of the heater, which is called FLEXIGAS clean fuel gas (contains CO/H_2, N_2, and other compensations [15]), becomes a product fuel for refinery boilers and furnaces. Flexicoking converts 95% of coke generated in the reactor [17].

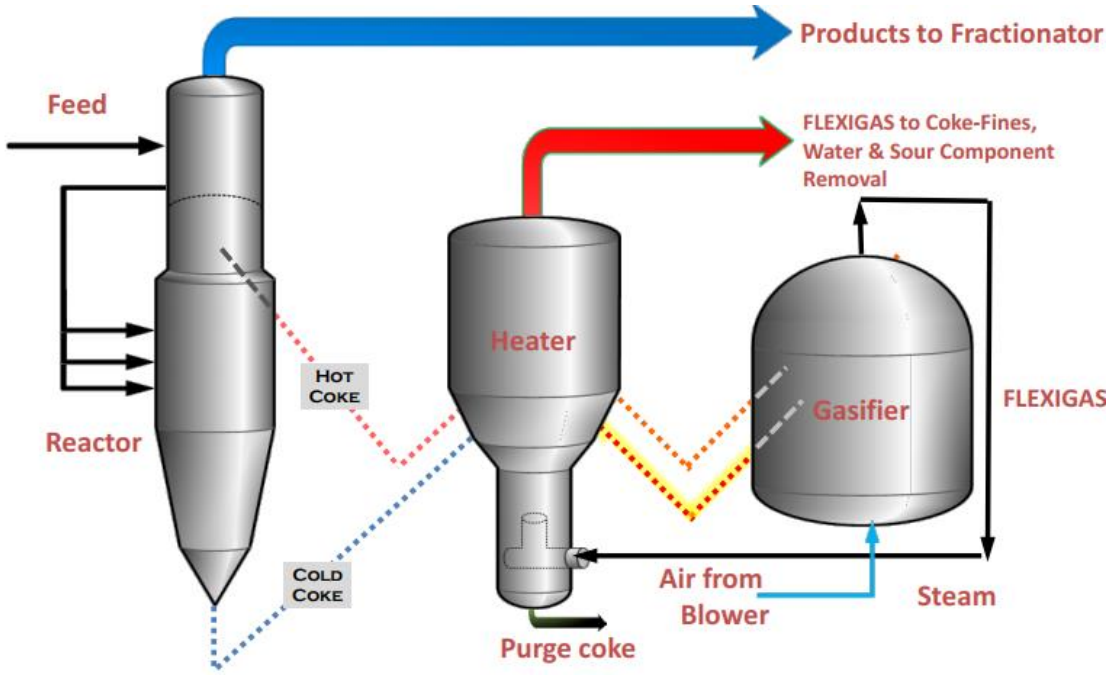

Figure 1.4 Simplified process flow diagram of Flexicoking™ [15]

1.1.2 Fluid beds with liquid injection application in other industrial processes

a. Fluid catalytic cracking (FCC)

Fluid catalyst cracking (FCC) is also an oil refining process that converts high-boiling point, high molecular weight hydrocarbon fractions of crude oil into more valuable products, such as gasoline and olefinic gases [18-20]. FCC is one of the most economically essential conversion processes in petroleum refineries. Worldwide, around 400 FCC units produce about 10 million barrels of gasoline per day [21].

Many oil companies have their own FCC reactor designs; Figure 1.5 shows the Universal Oil Product Company (UOP) FCC unit [1, 22]. The feed oil is preheated to 205 – 400 °C, then injected into the fast up-flowing lean-phase stream of regenerated catalyst. Practically, all reactions should be occurring in the up-flow riser. The plug flow of the vapors is closely approximated, which improves the selectivity of desired hydrocarbon fraction. The feed droplets evaporate on the hot catalyst surface and react at the surface of the catalyst particle pores. The light hydrocarbon product leaves the reactor as vapors,

while the coke generated during the cracking process covers the catalyst particles' surface and deactivates them. The deactivated catalyst particles are recovered by the cyclones and transferred to the regenerator. The regenerator temperature is kept between 580 and 700 °C to burn off the coke on the catalyst with air. After cleaning, the fuel gas from the regenerator flows into the heat and power recovery section [23]. The coke content in the catalyst leaving the reactor is about 0.5 to 1.5 wt %, and it is reduced to around 0.15 to 0.35 wt % when leaving the regenerator [1].

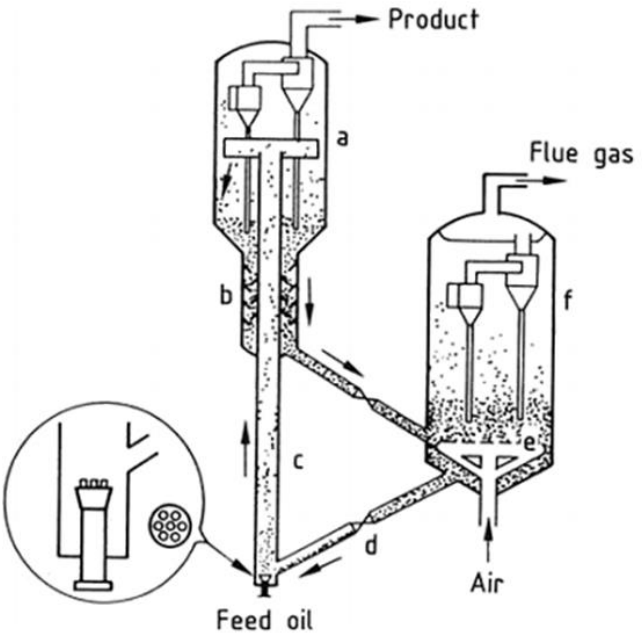

Figure 1.5 Riser cracking process (UOP system [1]), a) Reactor; b) stripper; c) riser; d) slide valve; e) air grid; f) regenerator. [1]

The advantages of FCC reactors are as follows: high conversion happens rapidly in an FCC reactor; in the riser, there is nearly a plug flow of vapors, limiting over-cracking and increasing the gasoline yield. The system drawbacks are as follows: the catalyst is quickly poisoned by vanadium and nickel; for heavier feedstocks, the excess heat generated while removing coke from the catalyst in the regenerator must be removed [1].

The interaction between the heavy feed oil and catalyst is the critical factor of the oil production efficiency. The oil droplet evaporation rate may become a limiting factor in FCC reactions because of the short contact time [24].

b. Linear low-density polyethylene production

Polyethylene is made by the reaction of multiple ethylene molecules in catalyst particles to break the double bond and connect the carbon atoms into a chain, which is the most common plastic used nowadays. The monomer, ethylene, is generally produced via steam cracking of crude oil derivatives. It is common to have the refinery, cracker, and polymer plant at a single site [2]. The linear low-density polyethylene (LLDPE) is a linear polyethylene with significant numbers of short branches commonly made by copolymerization of ethylene with longer-chain olefins. The LLDPE can make lower thickness plastic products, such as plastic wraps, stretch wraps, buckets, and containers.

Figure 1.6 shows the LLDPE process licensed by British Petroleum (BP). The prepolymers are generated in the pre-polymerization reactor before being fed into the fluidized bed reactor. The pre-polymerization aims to dilute the very active catalyst, thus minimizing the risk of hot spots in the fluidized bed reactor. The reactor is fluidized by the recycled gas stream containing the monomer from the bottom of the unit. The polymerization is complete at 75 to 110 °C and about 2 MPa, using a Ziegler-Natta catalyst [2].

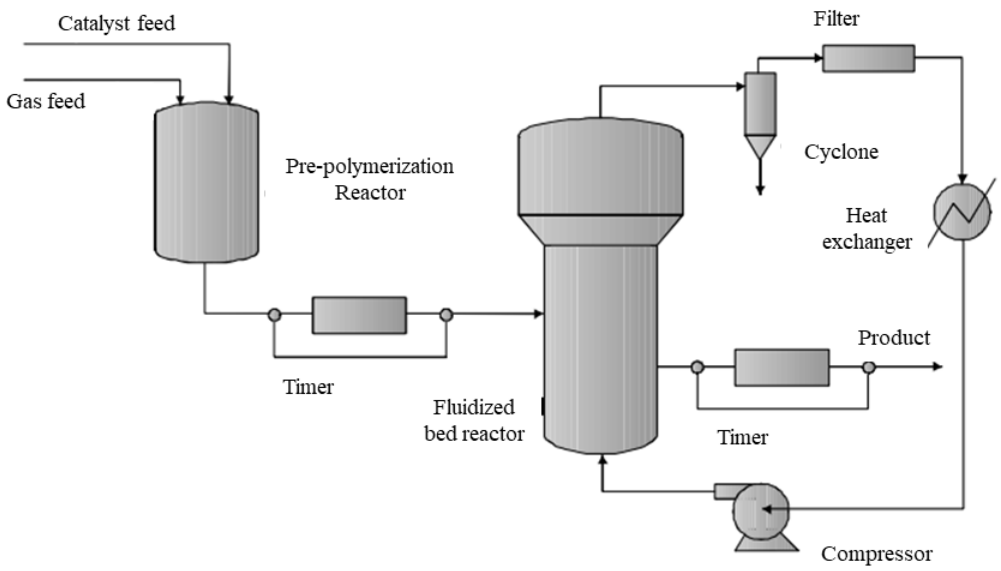

Figure 1.6 Industrial LLDPE (BP Chemical Technology) [25]

The greatest challenge of LLDPE is heat removal control. Polymerization is highly exothermic, which can result in local overheating. Overheating can lead to poor product quality, deactivation of the catalyst, or undesired agglomeration. If a local "hot spot" is generated, the location becomes a nucleus for polymerization at a much faster rate. The granules could fuse into a sheet or a big agglomerate. When the agglomerate is too heavy to fluidize, it will fall to the gas distributor. The worst case is eventually to entirely block the gas distributor, ceasing heat removal and bed fluidization. This has occurred in the past, and the reactor bed was converted into a single polymer chunk. The unit had to be shut down, and the polymer chunk had to be cut into small pieces and removed gradually [2]. An additional issue is that the heat of polymerization cannot be removed with in-bed heat exchangers.

The issue stated above is usually resolved by adding a liquid hydrocarbon, such as pentane or hexene, to the recycled gas stream. The condensable hydrocarbon is condensed at the heat exchanger. The condensed droplets are evaporated at hot spots in the bed to remove the heat [2, 26]. The process is called the "condensed mode" operation [2]. Also, additional cooling can be applied by directly injecting condensed liquid with

spray nozzles [24, 27]. The solids mixing redistributing the catalyst in hotter and colder regions also helps to reduce the hot spots.

c. Coating, granulation, and agglomeration

The coating, granulation, and agglomeration processes using fluid beds are essential applications in the food and pharmaceutical industries. Mainly, the same apparatus is applied for the processes (coating, granulation, and drying) [28, 29], which reduces the cost and simplifies the process.

The coating process design is highly dependent on the demands. The first is to decide the coating objectives, for example, to protect the core, mask a flavor, or change the color. [30]. The second is to define how the core will be released, determining the shape, size, and coating thickness. The last step is to define the appropriate compromise between the composition of the coating solutions. [28]

During recent decades, many aspects have been tested to optimize the design. Figure 1.7 shows typical spray nozzle locations that are used to inject the coating liquid. Spraying from the top (Figure 1.7a) has a low efficiency between particles and liquid contact; however, it is easy to handle (top position, no interaction with the plate or air flow). It is the most popular choice with continuous fluid beds. Spraying from the bottom (Figure 1.7b) results in a high concentration of wet particles, which may cause undesired agglomeration. By inserting the spray nozzle inside the column, the Wurster fluid bed (Figure 1.7c) enhances particle circulation to increase the drying rate and reduce agglomeration. The rotator system (Figure 1.7d) gives a similar coating quality to the Wurster fluid bed; however, the high agitation prevents its application to crumbly or brittle materials. [28]

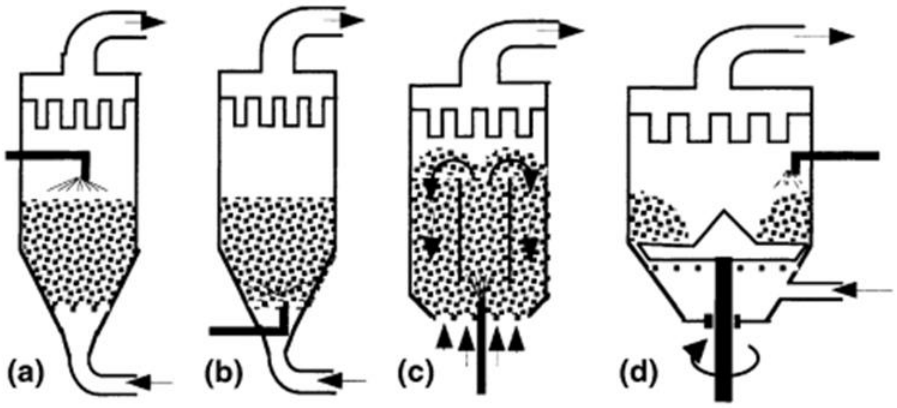

Figure 1.7 Different types of batch fluid beds: (a) top spray; (b) bottom spray; (c) Wurster; (d) rotor with side spray [28]

A similar apparatus can be applied for granulation and agglomeration. The mechanism is slightly different from the coating. In the coating process, the purpose is to achieve a uniform liquid layer over the core and dry this layer quickly before particles can agglomerate. Several layers can be applied based on the demand. In the granulation and agglomeration processes, the purpose is to achieve a good distribution of a liquid binder solution over the surface of the particles. The wet agglomerates are then formed as the binder connects particles. When the solvent is evaporated due to the heat convection from agglomerates to particles, strong granules are formed [31]. The granule size depends on the demands, which can be controlled by changing the binder solvent strength, binder solution droplet size, fluidization gas velocity, injection flowrate, spray nozzle design, temperature, or pressure. [32-35].

1.2 Literature review: fluid bed hydrodynamics

The bed hydrodynamics influences the liquid distribution and, hence, the agglomerate formation. This section reviews the literature on two factors that affect fluidized bed hydrodynamics: the fluidization regime and the gas distribution.

1.2.1 Fluid bed hydrodynamics: bubbling to turbulent regime transition

With increasing superficial gas velocity, a fluid bed can experience the following regimes (Figure 1.8): fixed bed, bubbling regime, slugging, turbulent regime, fast fluidization, and

pneumatic transport [36]. In the bubbling regime, gas bubbles are created at the gas distributor. They coalesce to form larger bubbles, while some large bubbles split into smaller ones. They carry the solids in the bubble wakes. Slugging occurs when gas bubbles grow until they fill almost the whole cross-section of the fluid bed. However, the maximum stable bubble size or the turbulent regime may be reached before slugging can establish itself. In the turbulent regime, the gas flows as small, elongated voids that constantly appear and disappear. When the gas velocity further increases, substantial solids entrainment can be seen, which is the fast fluidization regime. Cyclones can be applied to recycle the solids. If no solids are recycled, it is called pneumatic conveying (transport). [36, 37]

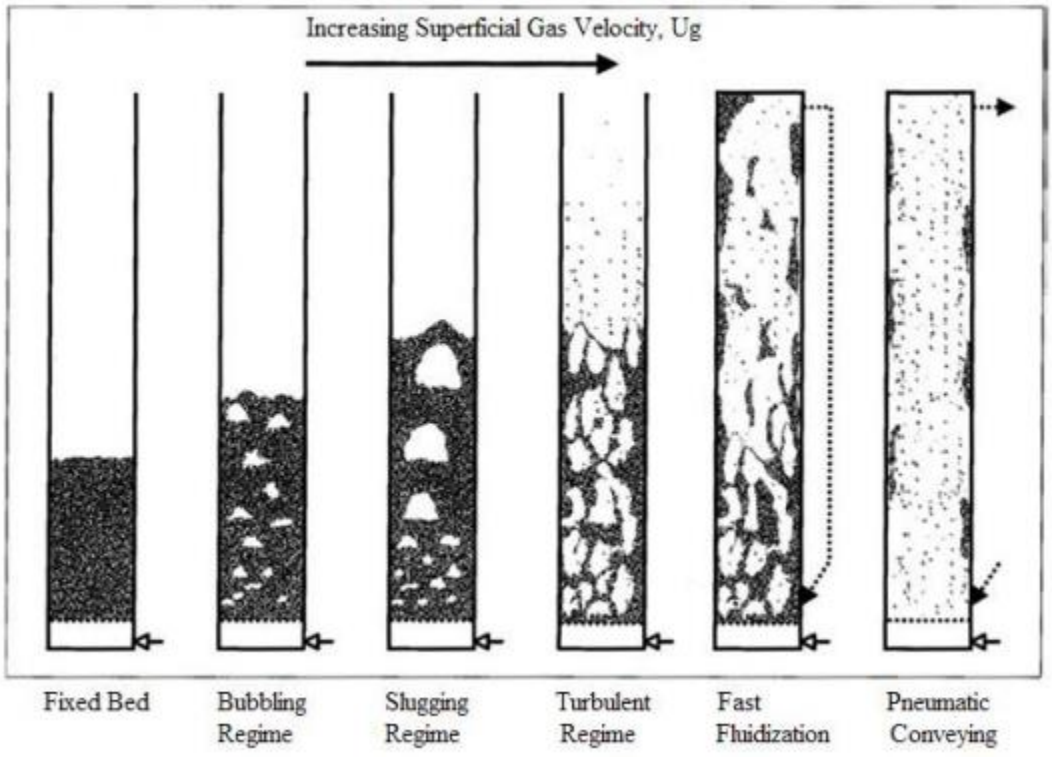

Figure 1.8 Fluidization regime-changing with the increase of gas velocity [38]

The turbulent flow regime is preferred in many commercial fluid bed reactors because of superior gas-solid contact [37] and favorable bed-to-surface heat transfer [39]. However, based on various models, the calculated transition velocity from bubbling to turbulent can

vary significantly. For example, using a typical industrial Fluid Coker operating conditions, using pure steam properties, Figure 1.9 shows that the calculated minimum turbulent velocity (U_{mt}) varies from 0.4 to 2 m/s. The superficial gas velocity varies from 0.4 to 0.9 m/s from the bottom to the top. The correlations cannot predict whether the coker is in a turbulent or bubbling regime or whether the lower levels closer to the Coker bottom are in the bubbling regime. The higher levels closer to the top are in the turbulent regime.

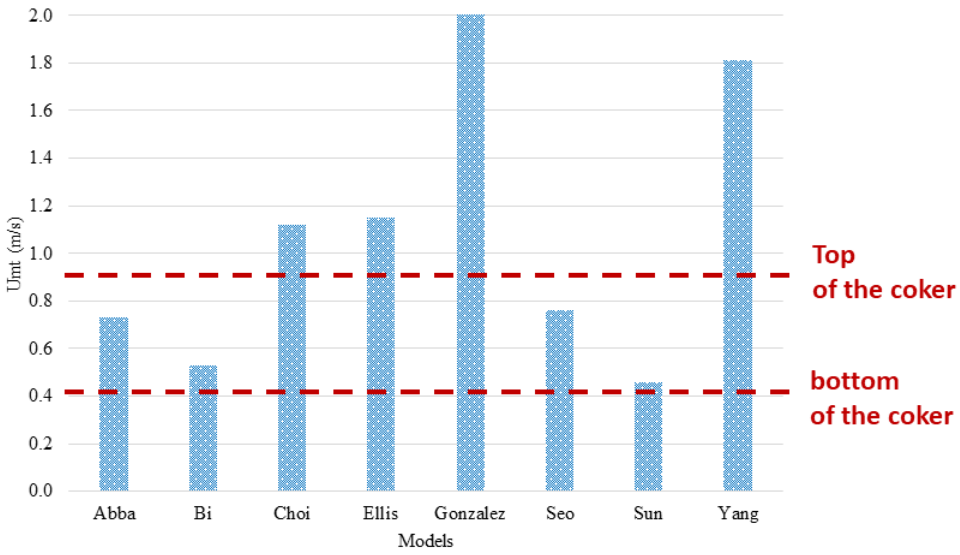

Figure 1.9 Calculated minimum bubbling to turbulent regime transition velocity (Industrial Fluid Coker, using pure steam properties) (provided by a fellow student, Yohann Cochet [40])

To study the bubbling and turbulent regime impact on liquid distribution, we need first to address four essential questions:

a. How to detect the transition from bubbling to turbulent?
b. How do operating conditions affect the transition from bubbling to turbulent?
c. Can different regions of the bed be in bubbling and turbulent regimes?
d. What are the prediction methods to get U_{mt} and how reliable are they?

And finally,

e. What are the impacts of the turbulent regime on gas and solids mixing?
f. What are the impacts of the turbulent regime on heat and mass transfer?

a. Methods to detect the transition from bubbling to turbulent

This section reviews the methods to measure the minimum turbulent fluidization velocity. We first introduce the intrusive methods: pressure measurements, optical probes, and capacitance probes. Then we introduce the non-intrusive methods: visual observation, vibration, acoustic emission technique, Radioactive particle tracking (RPT), Electrical capacitance tomography (ETC), Magnetic Resonances (MR), Computed Tomography (CT), and X-ray. The first four non-intrusive methods are relatively cheaper, while the last four give the transition of regimes and information about bubble characteristics, with a higher cost on equipment.

i. Pressure fluctuations

The pressure fluctuations method is the most used method to detect the bubbling to turbulent regime transition. A capacitance probe shows that the minimum turbulent fluidization velocity is when bubbles and slugs reach their maximum size [41]. At superficial gas velocities higher than U_{mt}, the bubbles breakup rate increases faster than their formation rate [41]. Both absolute [42-45] and differential [46-51] pressure measurements can be used to detect the U_{mt}. They are taken as a standard method for turbulent regime detection in almost all the published studies and the U_{mt} obtained from pressure fluctuations may be compared with other methods.

Usually, the standard deviation (σ), the normalized standard deviation or coefficient of variation (cv) of the pressure is plotted against superficial gas velocity (V_g). The σ, normalized σ or cv first increases with the increase of V_g, when minimum turbulent velocity (U_{mt}) (also called U_c in some references) is reached, the σ or cv reaches its maximum value. This is when the large bubbles start to break into small bubbles and interstitial gas.

Figure 1.10 shows two typical curves of the standard deviation of the pressure fluctuations against the increasing superficial gas velocity. It can be seen that after reaching the peak, the standard deviation does not always drop, as shown in Figure 1.10A [1, 51-54]; in some publications, it plateaus after the peak (Figure 1.10B) [46, 55-57]. The reason is unknown; however, it does not affect the value of minimum turbulent velocity.

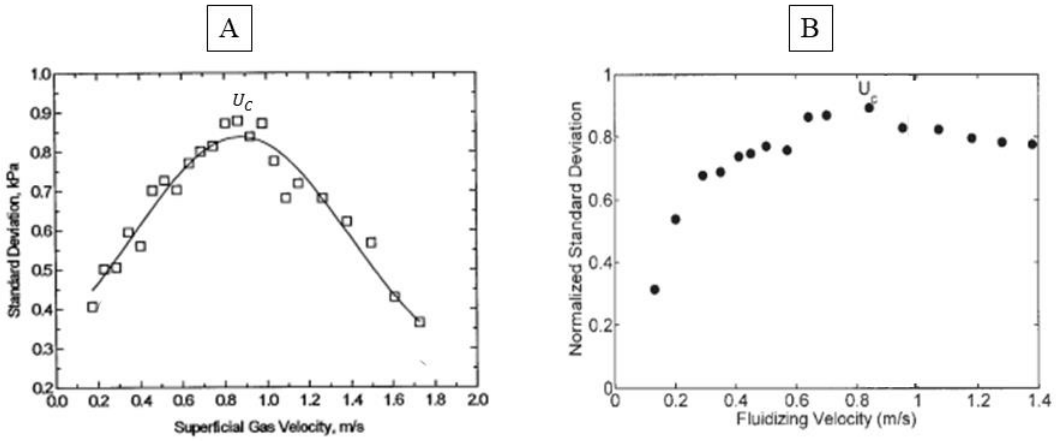

Figure 1.10 A. Typical curve of differential pressure fluctuations with increasing V_g from Bi, 1994 [52], B. Curve of differential pressure fluctuations with increasing V_g from Andreux, 2005 [46]

Other than the parameters mentioned above, other parameters have been shown to give similar U_{mt}, such as skewness [42], flatness [42], average cycle frequency [42, 50], Chaos analysis [49], Fourier transform [50], Wavelet transforms and fluidized bed structures [50], and entropy [58].

ii. Optical probes

An optical probe measures local, instantaneous bed voidage. Preliminary calibration is required. The probe contains a bundle of fibers projecting light onto a swarm of particles interspersed with light-receiving fibers, which measure the intensity of the light reflected from the particles [59]. After placing a quartz glass window of 0.5 mm thickness on the

probe tip, the optical fiber signal exhibits a nearly linear response against the local voidage [55].

Andreux et al. [46] found that the value of U_{mt} can be determined by the maximum of the local voidage dominating frequency from the optical probe, which gives lower transition velocity (0.45 m/s) from the breaking point in the pressure fluctuation curve (0.81 m/s). Ellis et al. [59] found a sudden drop of Hurst exponents from the optical probe signal, suggesting a change in the high-frequency fluctuations. However, the value of U_{mt} found by the optical probe (0.65 m/s) is lower than that from the pressure fluctuations (0.75 m/s). They claimed that the bed operating in a turbulent flow regime has a broad spectrum of voidage and behavior, with no clear delineation criteria between the two phases [59].

The U_{mt} obtained from optical probes was compared with non-intrusive methods other than the conventional pressure fluctuations. Du et al. [60] found that an optical probe gives very similar U_{mt} compared to Electrical capacitance tomography (ETC) using the cross-sectional time-average voidage. They also found that the optical probe gives the same voidage as ETC in the core region, while it overestimates the voidage close to the bed wall. Tebianian et al. [61] showed an agreement of U_{mt} from the cross-sectional time-average voidage from both an optical probe and X-ray.

iii. Capacitance probes

Chehbouni et al. [41, 62] used a capacitance probe to provide the local gas holdup, as the electric capacity of the medium surrounding the probe tip is approximately proportional to its voidage [63]. The value of the voidage (ϵ) was calculated with a linear interpolation between an empty ($\varepsilon = 1$) and fixed bed ($\varepsilon = 0.4$). Gonzalez et al. [44] used the same method as Chehbouni et al. [41, 62]: a capacitance sensor to detect the local bed density. They found that the mean voidage fraction and standard deviation of local density/ mean gave similar U_{mt}, which also agreed with pressure fluctuation results.

iv. Visual observation

Visual observation can be used as a very crude method to detect U_{mt}. Shabanian et al. [64] found the results by observing the bed height that agreed with the results obtained from bed pressure fluctuations.

Visual observation sometimes finds the transition when the pressure measurement does not level off to give a U_{mt}. Brink et al. [65] found that when testing the impact of a multi-vertex gas distributor on U_{mt}, the pressure fluctuations do not give a transition, as their standard deviation does not level off. When testing the standard perforated gas distributor (baseline), the pressure standard deviation leveled off like other publications. In their case, most bubbles spanned the cross-sectional section of the 2D bed, making the visual observation of the bubble size possible. They filmed the column for 30 s for each run. Then they obtained the bubble size analysis frame-by-frame. By doing so, they successfully obtained the U_{mt} for both gas distributors tested.

v. Vibrations

Azizpour et al. [66] mounted two accelerometers 10 cm above the distributor plate. They found that applying several data analysis methods, such as autocorrelation function and Hurst exponent analysis to the vibration signal can give U_{mt}. The time delay between two accelerometers becomes maximum when it reaches U_{mt}, using the autocorrelation function. The Hurst exponent of the macrostructure reaches the maximum at U_{mt}. However, the U_{mt} obtained in this research with vibration signal was not compared with other methods or correlation calculated value.

vi. Acoustic emission technique

Zhou et al. [67] mounted several acoustic emission sensors on the outer riser surface with vacuum greases. They found that the U_{mt} obtained from the standard deviation of acoustic signals agreed well with the pressure fluctuations. They also found that the U_{mt} = 8.8 U_{mf} similar to previous results from Dang et al. [68]. Dang et al. [68], using the infrared technique, found that the bed was in a turbulent regime when Vg > 7 U_{mf}.

vii. Radioactive particle tracking (RPT)

Tamadondar et al. [69] used radioactive particle tracking (RPT) to track particle trajectories. Sixteen scintillation detectors were placed on sliding rails, which recorded 820,000 positions in 5 hrs. They found that the standard deviation and skewness of the time-position data can be used to obtain U_{mt}. This result agreed with U_{mt} from the standard deviation of pressure fluctuations and the Bi and Grace correlation [70].

viii. Electrical capacitance tomography (ECT)

The ECT system is non-intrusive, which is one of a handful of real-time tomography techniques. It consists of a capacitance sensor, data acquisition system, and computer system for image reconstruction, interpretation, and display. The capacitance sensor array consists of a twin-plane sensor using 12 electrodes for each plane attached to the outside of the column wall. For U_{mt} detection, the transition from cross-sectional time-averaged bed voidage agreed with optical probe results.

ix. Magnetic Resonance (MR) Imaging

Holland et al. [71] found the ultrafast measurements of the voidage with magnetic resonance imaging (MR) were used to examine the void structures, which can distinguish different flow regimes. The ultrafast (25 ms acquisition) 2D images of the voidage were acquired in the transverse (x-y) plane using a FLASH imaging sequence. The results of U_{mt} agreed with that of pressure fluctuations.

x. Computed Tomography (CT)

Nedeltchev et al. [72] measured the photon count time series at 0.365 m above the gas distributor through computed tomography. They found that the entropy (bit/s) and information entropy (bit) could distinguish between the bubbly and churn-turbulent flow. However, the results of U_{mt} obtained in this research were not compared with other methods or correlation predictions.

xi. X-ray

Saayman et al. [73] used X-ray to get the void size. They found that the standard deviation from void size can give U_{mt}, which agreed with the pressure fluctuations. They also saw the gas bubble shape changed from cylindrical shapes in the bubbling regime to elongated cylinders with diameters slightly less than the bubbling regime's slugs or fast fluidization regime's core annulus.

Tebianian et al. [61] also used X-ray to study fluid bed behavior. They found parameters, such as entropy, skewness, and kurtosis, from the grayscale intensity probability distribution functions (PDF) (voidage data) of X-ray images, can give U_{mt}. This has been confirmed with other methods that measure voidage, such as an optical probe.

b. Impact of operating conditions on the transition from bubbling to turbulent

This section reviews the impact of operating conditions on the minimum turbulent fluidization velocity (U_{mt}), such as particle properties, temperature, operating pressure, column diameter, bed height, 2D or 3D fluid bed geometry, gas distributor design, and interparticle forces.

i. Particle properties

The impact on U_{mt} of several particle properties have been studied, such as Sauter mean diameter, particle density, particle size distribution, and impact of fines.

Cai et al. [54] found that higher Sauter-mean diameter particles give larger transition velocity, U_{mt}. Similar results were also found by Shiea et al. [74], who tested three different sizes of sand, and Xiang et al. [75], who tested three types of glass beads. He et al. [45] investigated two non-spherical particles in groups B and D. The only difference was the particle size range (group B: 0.1-0.6 mm; Group D: 0.71-0.8 mm). They found that for non-spherical particles, the coarser particles also have a larger U_{mt}.

Cai et al. [54] found that larger particle density gives a larger U_{mt} at all temperatures from 50 to 450 °C. Chehbouni et al. [62] found that the product of particle size and density ($\rho_P d_P$) has a significant effect on U_{mt}, while comparing to three other hydrodynamic factors, column diameter, static bed height, and size distribution (wide and

narrow). The most commonly tested particles are FCC and sand. Sand usually has larger Sauter mean diameter, and particle density, which both result in a larger U_{mt} [41, 54, 55, 61].

To study the particle size distribution effect on U_{mt}, Rim et al. [76] tested five types of monosize glass beads and their binary and ternary mixtures. Particles with a broader size distribution have a lower U_{mt} for the same Sauter mean diameter. Sun and Grace [51] found that bed voidage tended to be smaller with a broader PSD, which reduces the dense phase effective viscosity. One would therefore expect an earlier transition from bubbling or turbulent fluidization for beds with lower viscosity.

Rim et al. [76] also studied the impact of fines content on U_{mt}. By combining various monosize glass beads, they found that by increasing the fines fraction from 0 to 0.5, the U_{mt} decreased by about a third. This early transition to turbulent fluidization results from the fine particles acting as lubricants [77]. Saayman et al. [78] replaced 27 wt % of the bed particles with fines, which resulted in a decrease in Sauter-mean diameter from 59 to 41 μm, and found a slight decrease of U_{mt}.

ii. Operating pressure

Many industrial processes operate under pressures higher than atmospheric pressure, such as FCC, LLDPE, Fluid Coking introduced previously, and coal combustion and gasification [1]. Increasing pressure increases the emulsion phase voidage and results in smaller and less stable bubbles [55]; the pressure fluctuation amplitude decreases [54]. Increasing pressure reduces U_{mt} [54, 55].

iii. Temperature

Cai et al. [54] found that by increasing temperature, the value of U_{mt} increases. The temperature range was from 50 to 450 °C. They tested eight kinds of particles, including group A and B powders, under two operating pressures: 1×10^5 and 8×10^5 Pa. Ellis et al. [55] found the same impact of temperature on U_{mt}. They tested three temperatures at 20, 160, 240 °C at two pressures at 0.2 and 0.4 MPa. The conclusion that increasing

temperature decreases U_{mt} was confirmed by Gonzalez [56]et al., who tested a more comprehensive range of temperatures from 20 to 790 °C with three different particles, and Seo et al. [47], who also tested a wide range of temperatures from 20 to 600 °C.

Increasing the bed temperature increases the gas viscosity, and the gas density decreases. To investigate whether the increase of U_{mt} was due to the gas viscosity increase or gas density decrease, Ellis et al. [55] first tested the impact of gas density by changing the operating pressure only, as gas density increases with pressure, but gas viscosity is nearly unaffected. According to the correlation from Eq.1-1, the U_{mt} drops with increasing gas density.

$$Re_c = \frac{\rho_g U_{mt} d_P}{\mu_g} = aAr^b \qquad 1\text{-}1$$

Where the value of a and b are given in the table built by Horio [79]. As the gas density decreases with increasing bed temperature, this could explain the corresponding increase of U_{mt}.

Furthermore, to study the impact of gas viscosity on U_{mt}, Ellis et al. [55] replotted their data in the form of the standard deviation of pressure fluctuation against volumetric flux (Q_c) to compensate for the gas density change (using Eq.1-2) with temperature, using Eq.1-1:

$$Q_c \propto \mu_g^{1-2b} \qquad 1\text{-}2$$

They found that with the increase of temperature, the transition of pressure fluctuation on Q_c decreases (Figure 1.11). A similar trend was found by Cai et al.[54] that by increasing temperature, the transition of pressure fluctuation on the gas flow rate (in kg/s) decreases. To conclude, the increase of gas viscosity increases the bed temperature, resulting in an earlier transition. Therefore, the delay of U_{mt} at higher temperature results mainly from the decrease of gas density.

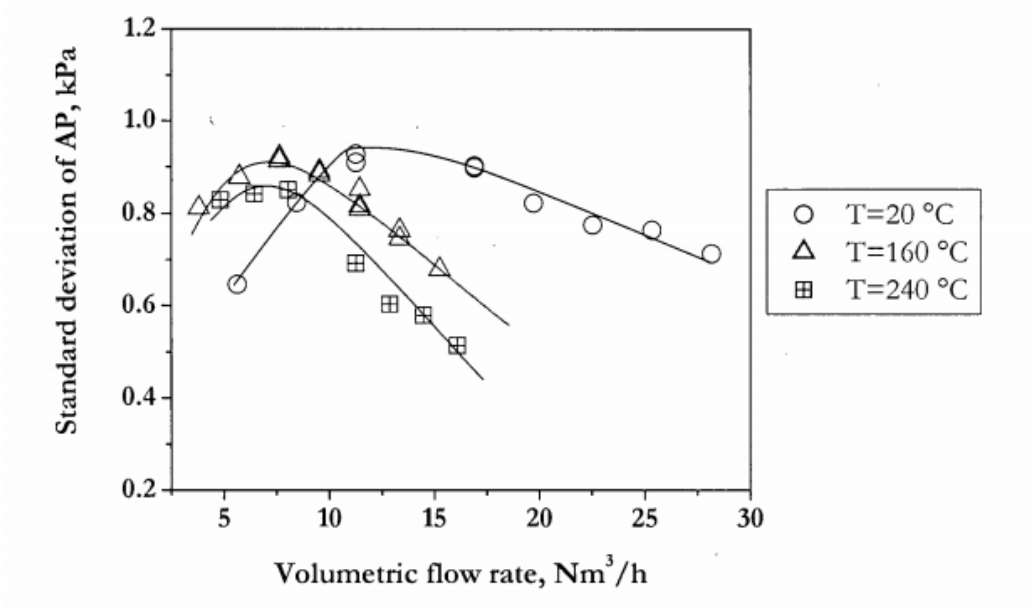

Figure 1.11 Standard deviation of gauge pressure signals against volumetric gas flow rate with various operating temperatures [55]

iv. Column diameter (D) and static bed height (H)

Chehbouni et al. [60] found the column diameter has an essential impact on U_{mt} while comparing to particle properties, static bed height, and size distribution (wide and narrow) with a cylindrical bed.

Chehbouni et al. [62] found that the static bed height has a slight impact on U_{mt}. Figure 1.12 shows that Zhu et al. [57] found a slight increase of U_{mt} when increasing the static bed height. By increasing the static bed height from 0.9 to 1.2 m, the U_{mt} increased from 0.8 to 1 m/s. This most significant variation of U_{mt} was obtained at the lowest measuring location above the gas distributor. As Figure 1.12 shows, by moving the measuring location upwards, they found that the difference became smaller with increasing axial level, which indicates the effect of increasing static bed height has larger impact on the lower section of the bed.

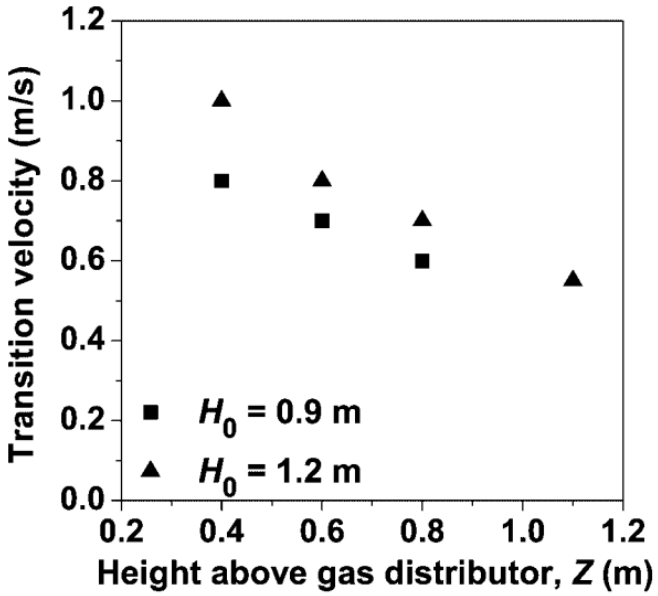

Figure 1.12 Effects of static bed height on regime transition velocity [57]

Some studies showed the impact of both bed height (H) and column diameter (D) as the H/D ratio (Figure 1.13) on the U_{mt}. Ellis et al. [55] plotted U_{mt} against the H/D (including their data and some results from Bi et al. [52]) and found that U_{mt} kept increasing with increasing H/D below a H/D of 3. When H/D became larger than 3, the U_{mt} leveled off.

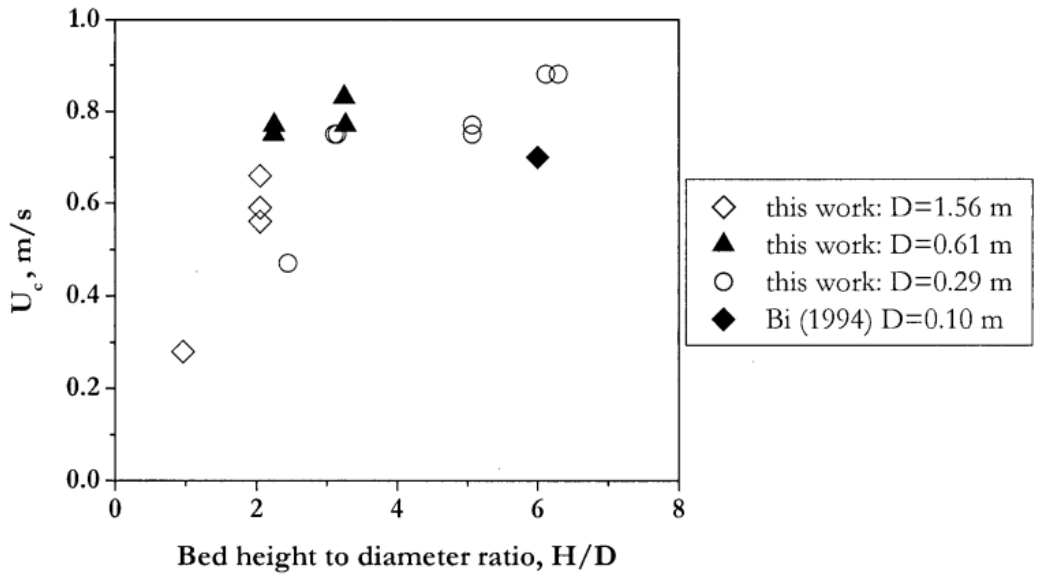

Figure 1.13 Impact of H/D ratio on Uc (U_{mt}) (Data from Ellis et al. [55] and Bi [52])

v. Column geometry: 2D and 3D

Information regarding the impact of 2D or 3D geometry on U_{mt} is scarce. By now, most of the experiments to detect U_{mt} were performed in cylindrical 3D columns [41, 46, 47, 52, 54-56, 58, 63, 66, 72, 80, 81]. Several experiments were done in rectangular 2D columns [45, 65]. Table 1-1 shows U_{mt} measured with similar conditions except the column geometry found in two different studies. Brink et al. [65] used FCC particles, tested with two gas distributors. The conventional gas distributor gave a U_{mt} of 0.3 m/s, and the multi-vertex distributor gave a slightly smaller U_{mt} of 0.25 m/s. Similar results (0.26 m/s) were found with a 3D column with similar conditions from Chehbouni et al. [41].

Reference	Brink, 2011		Chehbouni, 1994
Column type	2D		3D
Rectangular column length, m	0.4		
Rectangular column width, m	0.025		
Column diameter, m			0.082
Operating Pressure	Ambient pressure		Ambient pressure
Fluidization gas	Air		Air
Gas distributor	Conventional perforated plate distributor	Multi-vortex distributor	Bubble cap distributor
temperature, $°C$	15		25
Fix bed height, m	0.4		0.45
Solids	FCC		FCC
Sauter mean diameter, μm	86		78
Apparent particle density, kg/m^3	1580		1450
Experimental methods	Absolute pressure fluctuations	Visual observation	pressure
Location of measurement above distributor, m	0.3	0.3	0.45
$U_{mt}, m/s$	0.3	0.25	0.26

Table 1-1 Impact of 2D and 3D column on U_{mt} from different literature (Brink et al. [65] and Chehbouni et al. [41]) used similar conditions.

vi. Gas distributor

Not many studies have discussed the impact of the gas distributor. Figure 1.14 shows gas distributors from three studies that provided information about their impact on U_{mt}. They all find that the gas distributor design does not affect U_{mt} significantly. Brink et al. [65] (Figure 1.14A) found very similar U_{mt} between conventional perforated plate distributor (0.3 m/s) and their specially designed multi-vertex gas distributor (0.25 m/s). Rahimpour et al. [82] (Figure 1.14B) found that for a specific size of sand (three sizes of sand particles were measured), the velocity of the onset of turbulent fluidization is almost the same for the three types of distributors. Wormsbecker et al. [83] (Figure 1.14C) used two data analysis parameters of the pressure fluctuation: standard deviation and average cycle frequency. Both give almost the same U_{mt} for three gas distributor designs.

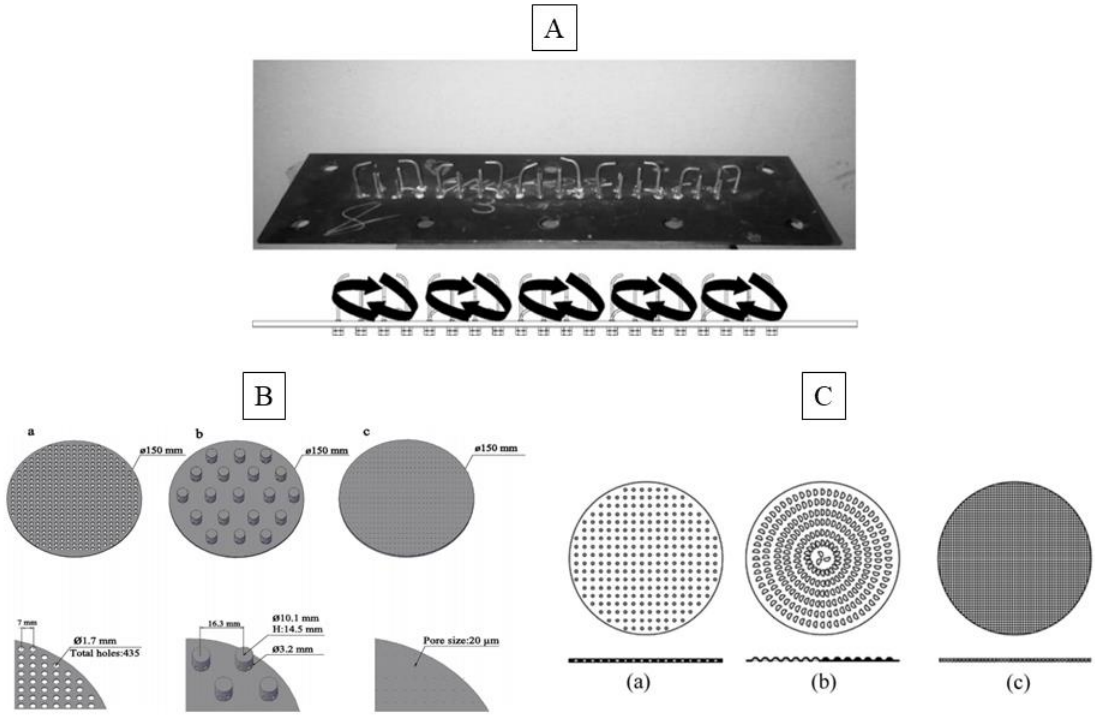

Figure 1.14 A. Multi-vertex distributor photograph (Top), and front view of the gas flow pattern (bottom) (Brink et al. [65]), B. Distributor designs: a. perforated plate, b. bubble cap, c. porous plate (Rahimpour et al. [82]), C. Distributor designs: a. perforated plate, b. punched plate, c. Dutch weave mesh (Wormsbecker et al. [83])

vii. Interparticle forces

In industry, the processes with liquid injection could have cohesivity increasing inter-particle forces (IPFs). Shabanian et al. [64] used a polymer coating approach to increase and adjust the level of IPFs. They found that enhancing the level of IPFs can alter the bed fluidization behavior from Group B behavior to Group A and even Group C. The particle behavior change results in a loser structure in a fixed bed, which can hold more gas inside, increasing U_{mt}.

c. Minimum turbulent transition velocity at different regions

The difference between local measurements from optical probes and pressure measurements may suggest the turbulent regime could occur locally. Andreux et al. [46] found that the time-averaged voidage measured by an optical probe first increases then levels off with increasing V_g. However, this critical velocity (0.45 m/s) is well below the transition velocity found by pressure measurements (0.81 m/s). This is not due to a sudden global change of bed structure, such as the appearance of core-annulus, as they found that the radial gas distribution profile has a flat shape at all velocities. They found this new transition velocity (0.45 m/s) agreed well with the breaking point found from local solid volume concentration in the bubble and emulsion phases.

Ellis et al. [55] also found there is a slightly earlier transition obtained from the optical probe (0.65 m/s under their conditions) compared to pressure measurements (0.75 m/s). The sensitivity from voidage signals (from the optical probe) to the change in local fluctuations may suggest a viable means of deducing the transition velocity.

However, the pressure fluctuation information is too general to give a local measurement. Bi et al. [84] summarized that the fluid bed's pressure fluctuation could have several origins. The first source is the pressure fluctuation directly generated from bubbles flowing past the pressure measurement locations. The second source is from the bed level fluctuations or bed surface waves due to the sloshing motion caused by bubble eruption. The third source is the vibration of the fluid bed. A fluid bed can sustain an oscillation when subject to a disturbance. The disturbance comes from sources stated in this paragraph. Other sources of pressure fluctuations can be generated from the wind box beneath the gas distributor, bubble/jet formation in the distributor region, and bubble coalescence and breakup in the bed.

i. Axial locations

With the increasing height of the measuring location above the gas distributor, the U_{mt} was slightly decreased using pressure measurements [41, 45, 55, 57, 75, 85]. For example, Ellis et al. [55] found that the U_{mt} decreased from 0.6 to 0.5 m/s with the static bed height of 0.6 m measured from locations from 0.3 to 0.8 m above the gas distributor. The decrease of U_{mt} is consistent, while a more significant drop with higher static bed

height is seen. The drop of U_{mt} was more significant with a higher static bed height of 1.1 m, from 0.9 to 0.7 m/s, measured from 0.4 to 1.1 m.

Compared to pressure fluctuations, the measurement from optical probes and capacitance probes may be considered more "local." The methods are introduced previously in Chapter 1.2.1. Ellis et al. [55] plotted the average cross-sectional voidage against superficial gas velocity to obtain the U_{mt} at various axial measuring positions. However, the transition is not clear. Unfortunately, not much research studied the impact of axial positions on U_{mt} using local measurements.

Saayman et al. [73] applied X-ray to get average void-movement velocity at various axial positions. Figure 1.15A shows two arrays from one side, while Figure 1.15B shows three arrays and detectors to measure from various angles. They can be moved to measure various axial locations. They found only at 0.2 m above the gas distributor, the average void-movement velocity increases and then plateaus at the same U_{mt} found by pressure fluctuations. At higher axial locations (up to 0.5 m), the average void-movement velocity keeps increasing with the increase of superficial gas velocity.

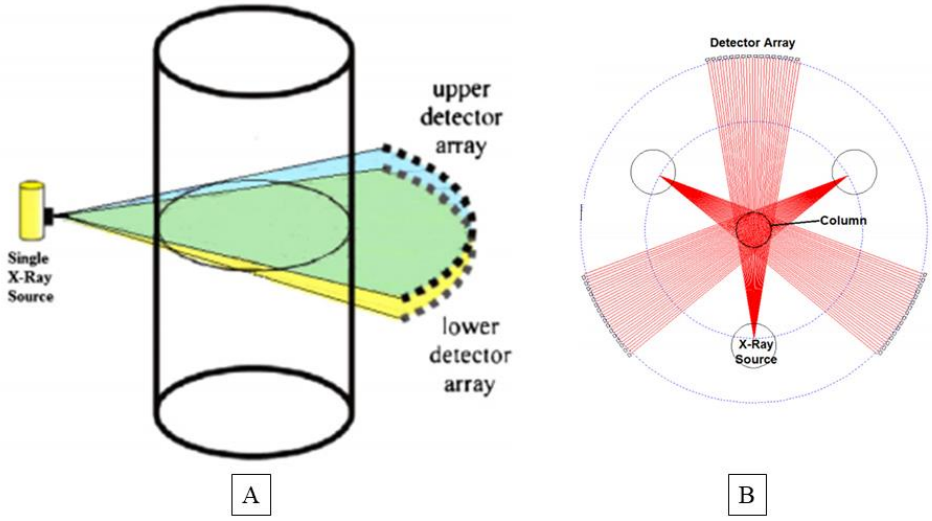

Figure 1.15 Detector array(s) of A. a single upper and lower detector array (side view), B. three detectors arrays and sources (Top view) [73]

ii. Radial locations

Very little attention has been given to investigating the flow regime transition for local flow structures [57].

Zhu et al. [57] found the time-averaged solids concentration at various radial locations (r/R=0, 0.74, 0.98) showed significant difference. By increasing the gas velocity, the local solids concentration first decreases; when the U_{mt} is reached, the solid concentration levels off for all locations. The r/R=0 is the bed center, r/R=0.74 is the middle point between the bed center and the bed wall, while r/R=0.98 is at the wall region. They found that the center and middle region gave a similar U_{mt} while smaller than that of the wall region. This could occur in a Fluid Coker as well.

d. Predictions to get U_{mt} and their reliability

Table 1-2 shows the correlations that were used to calculate U_{mt} in a Fluid Coker; the results have been shown earlier in Figure 1.9. The large variability of U_{mt} calculated with different correlations might be due to how the correlation was developed, such as how many factors a correlation includes. Therefore, the factors involved in each correlation were shown in the last column.

Reference	Model/ Correlation	Factors
Abba et al. [86]	$Re_c = 0.74\ Ar^{0.426}$	Same as Bi et al. [87], with additional data from Bi et al. [52], they did not specify which ones.
Bi et al. [87]	$U_{mt} = U_{mf} + 1.21Ar^{0.04}(0.00037Ar^{0.0764}g)^{\frac{1}{3}} /(2.27Ar^{-0.21} - 0.3Ar^{0.04}$	Particle property, column size, and static bed height, axial location, operating pressure

Choi et al. [88]	$U_{mt} = (gd_P)^{0.5}\left(\frac{0.211}{D} + \frac{2.42\times10^{-3}}{D^{1.27}}\right)\left(\frac{\mu_{g\,20}}{\mu_g}\right)^{0.2}\left(\frac{\rho_{g\,20}}{\rho_g}\frac{(\rho_P-\rho_g)}{\rho_g}\frac{D}{d_P}\right)^{0.27}$	Temperature, particle properties, operating pressure, bed diameter
Ellis et al. [55]	$Re_c = 0.459\,Ar^{0.454}\left(\frac{H}{D}\right)^{0.183\ln(d_P\rho_P)+0.83}$, for $H/D < 3$ $Re_c = 0.371\,Ar^{0.742}$, for $H/D \geq 3$	Group A powder properties, H/D radio
Gonzalez et al. [56]	$Fr_c = \frac{U_{mt}}{(gD)^{0.5}} = 0.261Ar^{0.1}((\rho_{g\,20}/\rho_g)(\mu_g/\mu_{g\,20}))^{0.27}$	Temperature, particle properties, static bed height
Seo et al. [47]	$Re_c = 0.973\,Ar^{0.36}$	Column diameter, temperature
Sun et al. [89]	$U_c = U_{mf} + d_{b\,max}^2\frac{g^{0.5}}{z_c^{1.5}}$ $d_{b\,max} = 1.32\,d_P\left(\frac{\rho_P-\rho_g}{\rho_g}\right)\left(\frac{\frac{\rho_P-\rho_g}{\rho_g}-\varepsilon_{mf}}{1-\varepsilon_{mf}}\right)$ $z_c = 2.25\left(\frac{0.6\,D}{d_{b\,max}+0.6\,D}\right)^{0.5} d_{b\,max}$	Maximum bubble diameter, column diameter
Yang et al. [90]	$K = 0.883Re_c^{-0.485}$ $\frac{U_i}{U_t} = 25.49\,Re_c^{-0.582}$	Bed material, transition voidage, cluster size, number of particles in a cluster, the density of the cluster

Note: $Re_c = \frac{\rho_g d_P U_{mt}}{\mu_g}$; $Ar = \frac{\rho_g(\rho_P - \rho_g) d_P^3 g}{{\mu_g}^2}$

Table 1-2 Model and correlations to predict U_{mt} and the factors applied to build them.

e. Impacts of the turbulent regime on gas and solids mixing

i. Gas mixing

The impact of turbulent regime on gas flow patterns becomes hard to analyze, as the gas flow turns into intermittent continuous and discontinuous phase: it is an intermediate regime between the bubbling fluidization regime, where the emulsion is the continuous phase, and the fast fluidization regime, where gas is the continuous phase [85]. The gas mixing in a fluid bed can be characterized by three coefficients: axial dispersion coefficient, backmixing coefficient, and radial mixing coefficient. The downward stick-slip motion of particles along the inner wall of a fluid bed tends to drag gas upstream, resulting in backmixing [91]. Axial mixing includes the contributions from backmixing and the up-flowing gas [85].

In a thorough review from Bi et al. [85], most publications focus on axial mixing. Using tracers, such as H_2 [92], CO_2 [93], Ar [53], He [94], steady or unsteady, the researchers found that the axial dispersion coefficient decreases when the superficial gas velocity increases beyond U_{mt}.

Most studies about gas mixing in turbulent regimes focus on axial mixing, while Lee et al. [93] and Du et al. [95] studied radial gas mixing. Lee et al. [93] used group B powders (glass beads), and CO_2 as a gas tracer. They found that the radial dispersion coefficient increased significantly with the gas velocity after U_{mt} is reached. Their data suggested that the radial dispersion coefficient is approximately an order of magnitude less than the axial dispersion coefficient. Du et al. [95] used group A powders and He as a gas tracer. They found that both axial and radial gas dispersion coefficients first increased with superficial gas velocity, then peaked at U_{mt}, then decreased with the further increase of superficial gas velocity.

The backmixing dispersion can be evaluated by detecting the gas tracer from below the tracer injection location. Lee et al. [93] found by injecting at the center of the bed, when increasing the superficial gas velocity, the backmixing dispersion coefficient first increased, then decreased slightly beyond U_{mt}.

ii. Solids mixing

With group A powder (FCC), Du et al. [95] found that before U_{mt}, the increasing superficial gas velocity did not help both the axial and radial solids dispersion; the value of solids dispersion coefficient was a plateau. However, both the axial and radial solids dispersion coefficient increased primarily when the turbulent regime was reached. In the bubbling regime, the solids were carried in the bubble wakes, sent to the bed surface, then dispersed by bursting bubbles, and descended to the bed bottom (gross solid circulation). Meanwhile, when bubbles rise, the solids in bubble wakes exchange with their surroundings, which pushes the solids near the bubbles to move side-to-side in the bed (local solids circulation). In the turbulent regime, Du et al. [95] applied the electrical capacitance tomography (ETC) technique to see that there are more solids around the bubble/void phase compared to the bubbling regime. The intermittent movement of the cluster and voids enhanced both the gross and local solids' circulations. The increase of gas-particle interaction in the turbulent regime also contributes to significant improvement of the solids dispersion beyond U_{mt}.

f. Impact of the turbulent regime on heat and mass transfer

i. Heat transfer

There are mainly three heat transfer types in a fluid bed, gas-particle, particle-particle, and suspension-surface heat transfer. The thermal gradient between voids and the dense surface is minimal due to the particles' large surface area. The particle-particle heat transfer due to particle collision is good so that it is rarely considered a limiting factor in overall heat transfer analysis. Thus, the limiting factor of the overall heat transfer in a fluid bed is the suspension-surface heat transfer [85]. The suspension-surface heat transfer includes the convective flow of solids from bulk to heat transfer surface, gas convection from bed to heat transfer surface, and radiation [85].

The bed to surface heat transfer coefficient was found to reach its maximum value ahead of the U_{mt} [96-98]. Molerus et al. [98] showed this finding was valid for all the particle diameters in Figure 1.16. Similar results were obtained by Stefanova et al. [97] with two different column diameters ($D = 0.29\ and\ 1.56\ m$).

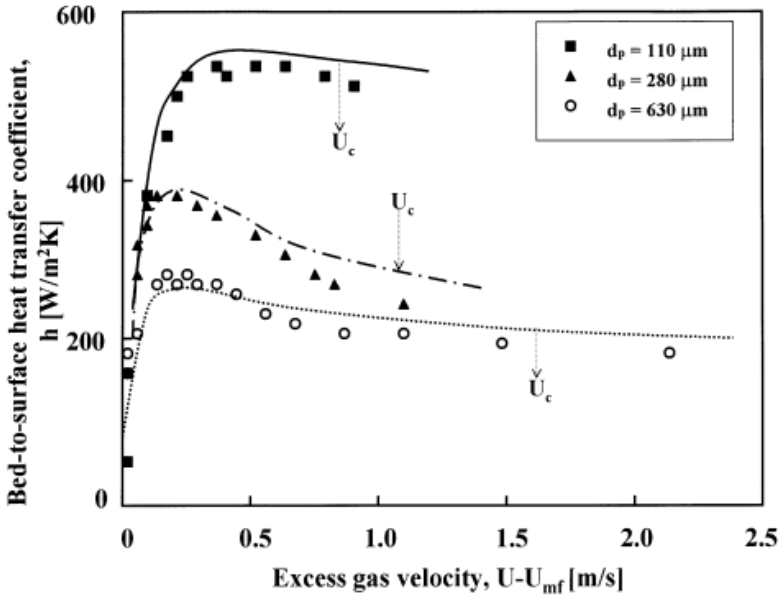

Figure 1.16 Bed-surface heat transfer vs. excess gas velocities with various particle diameters tested. [98]

ii. Mass transfer

One of the most attractive features of operating in the turbulent regime is the enhanced interphase mass transfer. Theoretically, the short lifetime of voids promotes gas-solid contact throughout the turbulent fluidized bed. It can be seen in most published studies, when the superficial gas velocity increases, the mass transfer rate increases as well [85]. The mass transfer rate does not peak like other features discussed above, making it hard to find a relationship with the U_{mt}. However, it indicates that operating at a higher superficial gas velocity is beneficial to mass transfer.

Even though the turbulent fluidized bed reactors are applied widely in fields, such as FCC reactors, Mobil methanol to gasoline process, or acrylonitrile. [91], the impact of

U_{mt} on product yield or operating issues, such as erosion of internals, and particle grinding, is rarely reported. This research will present the impact of U_{mt} on gas distribution, initial liquid distribution, and evaporation.

1.2.2 Impact of gas distribution on bed hydrodynamics

Studies have shown that the initial liquid distribution can be significantly changed by modifying the gas distribution near the spray jet [27, 99]. An excellent initial liquid distribution is essential to increase the yield and decrease the agglomerate formation [99-101]. The gas distribution in a Fluid Coker can be changed by steam injection in the lower section of the Reactor, the vapor from feed injection [9, 102], and through the use of internals, such as baffles [14, 27]. Various gas distributor configurations allowed for variations in gas distribution in lab-scale studies.

a. Feed injection

In a Fluid Coker, both CFD and cold model studies show that the gas bubbles concentrate to the central region, which creates a core-annulus structure [9, 102]. There is no distinct interface between the dilute core and the dense annular region but a gradual transition [102]. Near the column wall, the voidage is around 0.4 to 0.5 in the dense annulus, while in the core region near the bed center, the voidage is around 0.7 to 0.8 [9, 102]. Solids flow upwards in the dilute core region (around 1.5 m/s) and flow downward in the dense wall region (around 0.5 m/s) [9, 102]. However, the feed injection can modify the gas distribution [9, 102].

The feed injection and its vapors produced affect bed hydrodynamics in a Fluid Coker. Gas jets to simulate spray jets have been applied in other experiments and numerical studies of Fluid Cokers [9, 40, 102], which assumes nearly instantaneous vaporization when the feed is injected into the Coker. Experimentally, Song et al. [102] used air to simulate vaporized hydrocarbons and steam in a Fluid Coker in a cold model. They found that at the bottom of the Coker, the gas distribution was relatively uniform. As the gas rises, voids coalesce with feed jets, and their size increases dramatically in the core region.

Li et al. [9] used CFD modeling to study the impact of spray nozzle penetrations on bed hydrodynamics. They found good agreement between their numerical results and the UBC cold model from Song et al.[102]. The spray nozzles do not extend much beyond the Coker wall, because they need to prevent jet interaction with opposing nozzles, and they need to ensure that a rodding tool can be inserted into the nozzles to clear them when they are plugged. In UBC cold model, the feed nozzle location is about r/R=0.9, where the bed wall is r/R =1. They found that when the spray nozzles were retracted to the wall, the voidage is higher at the wall region, and the dense annular region becomes thinner [9]. The low upward movements of solid particles when the nozzle is retracted to the wall implies less axial solid mixing. Moreover, they found that using nozzle penetrations greater than usual for the third and fourth nozzle rings (1^{st} to 6^{th} rings from top to bottom) gave no significant difference in both voidage and gas velocity profiles [9].

b. Gas distributor configurations

Many studies change the gas distributor configurations to investigate gas distribution's impact on bed hydrodynamics [8, 99, 103-105]. Even though changing the gas distributor in a commercial Fluid Coker can be difficult, the benefit from redirecting the gas bubbles to a specific region can be discovered and investigated with lab-scaled beds by changing the gas distributor configurations. In a commercial Fluid Coker, modifying the feed injection locations, changing the column taper, or adding internals could achieve similar beneficial gas distribution.

Xing et al. [105] used CFD modeling to study the impact of gas distribution. They found that with a tall rectangular bed (static bed height of 1.65 m), the inlet of gas coming in from the western half, the eastern half, or evenly from a flat distributor, at 1.17 m above, the gas distribution will become the same: a symmetrical gas distribution. However, with an inclined distributor applying the same gas distributor configurations, it is possible, even high in the bed, to concentrate the gas to the western, eastern, or center of the bed.

Li et al. [99] were able to change the gas distributor configurations of an inclined distributor. There are 20 valves distributed evenly in two rows at the bottom of the

distributor. The gas bubble distribution was measured with tribo-probes (so-called E-probes). The method is introduced in Chapter 3 in detail. By opening ten valves each time at different locations, gas bubbles just below the spray level can be directed to the western side, middle, or eastern side of the rectangular column, consistent with what Xing et al. [105] have found with CFD modeling. Li et al. [99] also found that the mass of solids entrained to the cyclones on the western and eastern sides of the bed agree well with where the gas bubbles concentrate. For example, when more gas bubbles concentrate on the western side, the mass of solids entrained in the western side cyclone is more significant than that of the eastern side cyclone.

Xing et al. [105] also studied the impact of gas distributor configurations on solids dispersion with CFD modeling. They release particles at a given location in the bed and track the time it takes for the first 10 % of solids to reach the distributor section (τ_{10}). The distributor section is considered the stripper section. Therefore, if the first 10 % of solids reach the gas distributor was too quickly, it means that wet particles would reach the stripper section too quickly, resulting in the loss of valuable hydrocarbons to the burner fouling in the stripper section. They found that there was no significant difference found on τ_{10} using various gas distributor configurations with the inclined distributor (with a superficial gas velocity ranging from 0.4 to 1 m/s).

Silitonga et al. [8] studied the impact of gas distribution on vapor saturation. They could also have either an even gas distribution or concentrate bubbles to the western or eastern side of the bed by adjusting the flowrate of inlet fluidization gas from two sides of a rectangular bed. They found that the proportion of accumulated liquid was reduced when the gas bubbles were directed near the spray region.

A lot of other studies focus on the types of gas distributor design, such as bubble cap, perforated plate, porous plate, various modified perforated plates (Figure 1.14) [65, 82, 83], or spargers [106]. However, these designs might affect characteristics, such as initial gas bubble diameter, pressure drop across the gas distributor, or pressure fluctuation signals [65, 82, 83] [106], but most of the studies do not show that they have a significant impact on the gas distribution. It is consistent with the primary purpose of having the gas

distributor in most reactors, which is to uniformly distribute the fluidization gas into the bed [107].

c. Baffles

The Fluid Coker hydrodynamics can be modified by internals. Baffles are the most often reported internals in publications and applied in the industry [108].

i. Baffles in dense and low-velocity fluid beds

The baffle designs used in fluidized beds are based on the purposes. In dense and low-velocity fluid beds, baffles are often used to decrease gas bubble size to enhance gas-solid contact, improve uniform lateral gas distribution, suppress axial gas-solid backing, and reduce solids entrainment[108]. There are three major types of baffles, horizontal baffles [109], vertical baffles (like heat exchanger tubes), and fixed packings [110]. The example in Figure 1.17 shows a horizontal baffle from Zhang et al. [109], which was to use the baffles to classify particles. Figure 1.18 shows a pagoda baffle, which was the earliest developed fixed packing baffle [110]. Jin et al. [110] found that the pagoda baffles break up bubbles and enhance gas-solid contact by analyzing still and movie photographs.

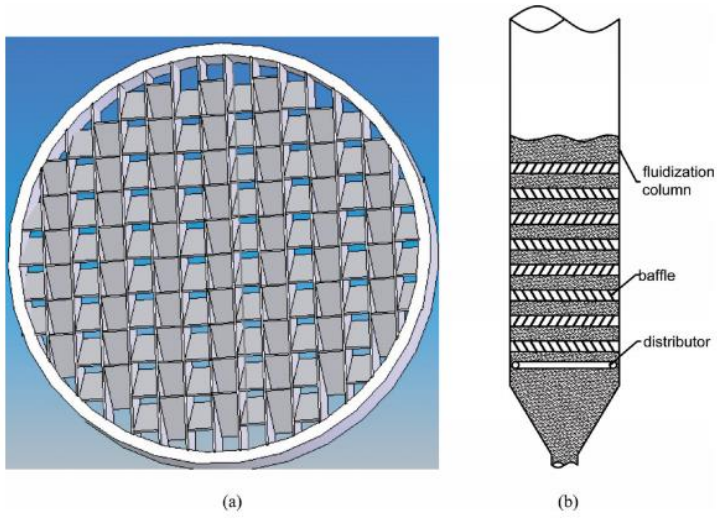

Figure 1.17 Schematic structure of baffle and fluid bed for fine and coarse FCC Particle segregation [109]

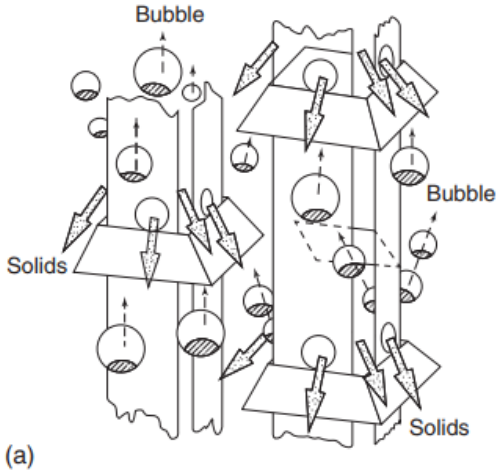

Figure 1.18 Pagoda-shape internals [110]

ii. Baffles in high-velocity fast fluidized beds

In high velocity fast fluidized beds, the baffles are often used to change the core-annular flow structure to redirect the gas bubbles or solids to the desired locations. This section introduces baffles investigated in circulating fluidized bed risers, FCC strippers, and Fluid Cokers.

The circulating fluidized bed (CFB) riser [111-113] can be modified with ring baffles, and Figure 1.19A shows a CFB riser diagram [112], where the arrows indicate ring baffle locations. The baffle geometry, for example, airfoil-shaped, rectangular, circular, and trapezoidal ring baffles (Figure 1.19B- E), impact bed hydrodynamics [111, 112, 114].

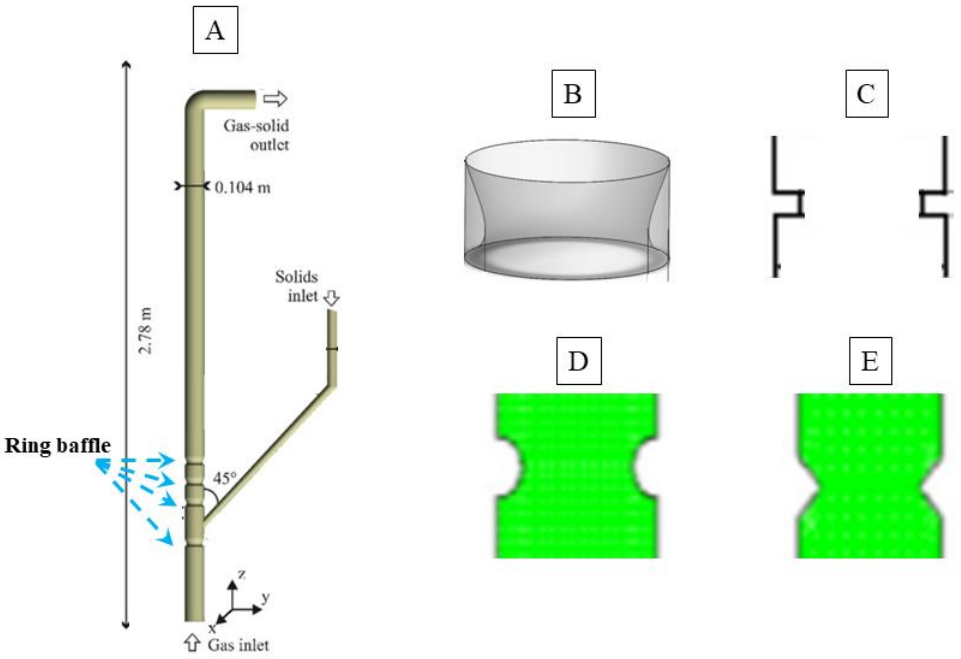

Figure 1.19 A. Example of a CFB riser [112], B. Airfoil-shaped ring-type baffle [112], C. Rectangular ring baffle [111], D. Circular ring baffle [114], E. Trapezoidal ring baffle [114]

Compared to the no baffle case, the ring baffles increase solids mixing, the solids velocity near the wall, and redirect the particles to the riser center [111, 112]. Ring baffles decrease the overall axial solid dispersion intensity [111]. The more homogeneous distribution of the particles in the radial direction would enhance gas-solids contact, and consequently increases the yield of desired products of the chemical reactions [111, 115]. Ring baffles reduced the backflow near the wall [114]. These studies also indicated that the ring baffles only have a slight pressure drop reduction in the riser flow [111, 112].

Wang et al. [111] investigated the impact of the number and axial distance between the ring baffles using CFD modeling. Wang et al. [111] found that increasing the number of ring baffles and the axial distance between ring baffles increases the solid circulation rate and solid inventory height, decreases solid cycle time in the system and solids residence time in the riser.

Shah et al. [113] investigated the impact of baffle size and axial distance on FCC yields. First, they calibrated their simulation results with the plant yield from an FCC riser. When they apply the model to various baffle sizes and spacing, they found that longer baffles (more locking cross-sectional area) and smaller spacings further increases the dispersion, yielding more homogeneous radial profiles. They found that larger spacing does not increase the yield because the impact on the regional flow close to baffles was much higher than that in regions away from baffles.

The baffles in FCC strippers are much larger than that of the risers because they are applied to minimize valuable liquid product flow entrained with the regenerator catalyst. Figure 1.20A shows the UOP FCC unit (introduced in section 1.1.2); in the blue circle, the baffles in the stripper section are located.

Mckeen et al. [116] used CFD modeling in a 2D simulation to see the impact of baffle and baffle geometry. The present model can only resolve maldistribution in the radial direction. However, the general case of maldistribution occurring over the complete cross-section cannot be simulated. Comparing to the no baffle case, they found both baffle geometries improved breakup and redistribution of bubbles. Near constant bubble size was maintained over the height of the baffled stripper, where bubbles coalesced to large slugs in the non-baffled stripper. They also found that the baffle with a downcomer (Figure 1.20B) mitigated flooding. Flooding is a result of local catalyst velocities being more significant than the steam bubble rise velocities. This is caused by high catalyst fluxes and steam rates or restrictive baffle designs.

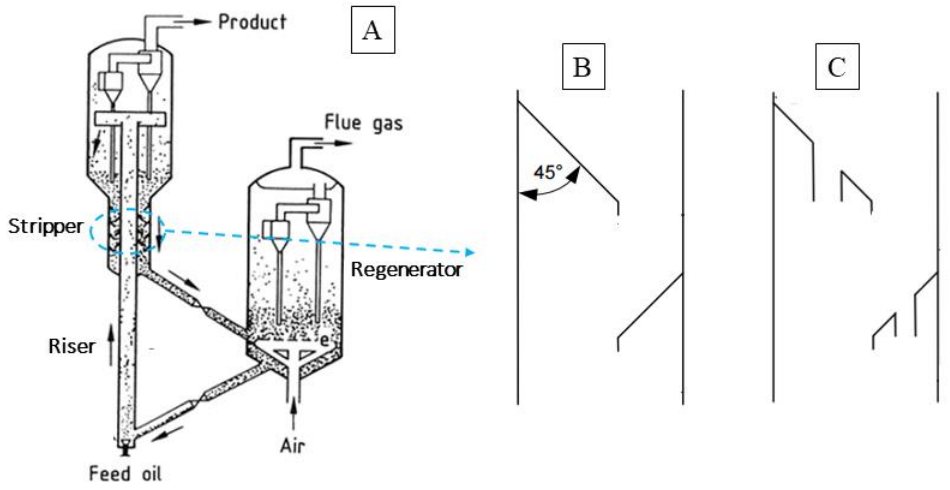

Figure 1.20 A. UOP FCC unit [1] B. Baffle type A [116], C. Baffle type B [116]

Veluswamy et al. [117] studied a similar baffle geometry shown in Figure 1.20B but in a 3D system (Figure 1.21). They found that the particle phase accumulates over the donut baffle at a low air flowrate, leading to local defluidization zones. Near the stripper column walls, the disk baffle resulted in a lower solid holdup, while the donut baffle resulted in a higher solid holdup.

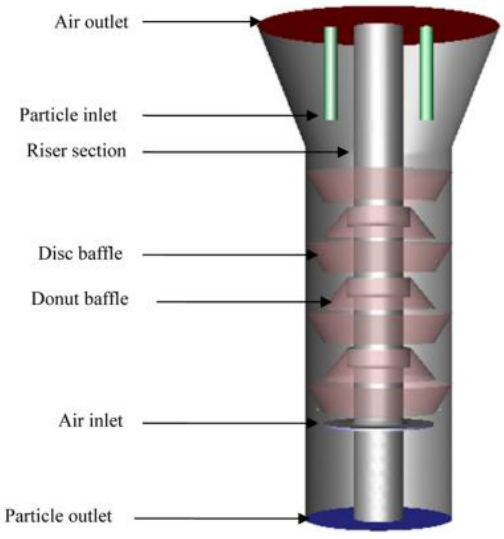

Figure 1.21 Baffle in an FCC stripper with CFD simulation in 3D [117]

In Fluid Cokers, ring baffles can be used to hinder solids mixing between the reaction zone and the stripper section [118-120]. Sanchez Careaga et al. [118] and Cochet et al.

[119] used radioactive particle tracking and found that a baffle above the stripper section resulted in an increased residence time of wet agglomerates above the baffle, thus providing more time for liquid conversion.

The patent from Wyatt et al. [14] proposes ring baffles below the injection nozzle rings to increase the time available for drying of the solids by reducing solids by-passing. Table 1-3 shows that a model was built to evaluate ring baffles' impact on unit yield (liquid and coke) compared to the no baffle case. For both cases, the yield of liquid increases while the yield of coke decreases. They indicated that the best location and best geometry, with or without downcomers (so-called flux-tube), should be further studied.

Reactor Configuration	Change in C5+ liquid yield from base, wt %	Change in coke yield from base, wt %
Single Baffle with downcomers	1.0	−1.5
Two Baffles with downcomers	0.2	−1.0

Table 1-3 Predicted impact of baffles on liquid and coke yield [16]

Jahanmiri et al. [27] used a small rectangular bed to study the baffle impact with and without flux-tubes on gas distribution and initial liquid distribution. They found that the asymmetrical baffle would redirect the gas bubbles to the baffle tip. With a flux-tube, the gas bubbles would be redirected to the center of the flux-tube. This study's limitations include low liquid flux from the spray jet, room temperature only, and low superficial gas velocity.

Xing et al. [103] used CFD modeling to test the impact of baffle geometry with a rectangular column. The results from their simulation will be compared in this thesis with experimental results. They found that all baffle geometries have a gas pocket created under the baffle. The baffle can redirect the gas bubbles, while the baffle geometry has a significant impact. The baffle video with a flux-tube shows a small portion of the bubbles

goes down through the tube. Changing the length and diameter of the flux-tube did not have a significant impact on gas distribution. As for solids dispersion, they found that a symmetrical baffle with and without flux-tubes does not increase the time required for the solids to reach the stripper section. They found that the baffle with flux-tubes reduced the time it takes for the solids to reach the stripper. Note that the simulation was done in a lab-scaled rectangular unit. The solids dispersion numerical results, however, lack experimental verification. They also used solid particles instead of agglomerates, which should be stickier and larger. However, they convey an important message: not all baffles can positively impact the Fluid Coking process.

1.3 Literature review: liquid injection in fluid beds

When liquid is sprayed into a fluid bed, a portion can be trapped in wet agglomerates. The agglomeration formation process is introduced in section 1.1. The agglomerates are unwanted in a Fluid Coker, as stated above. With a high gas to liquid ratio spray jet, the formation of agglomerates can be avoided [121], as very fine droplets were created. However, it would not be suitable for a commercial unit, as oil feedrates would need to be reduced to maintain the superficial velocity at the top of the bed within an acceptable range. There would also be additional costs associated with increasing the steam flowrate and treating the resulting wastewater.

1.3.1 Methods to evaluate the liquid distribution

This section reviews three methods highly related to this research to evaluate liquid distribution quality. In the end, references to other methods that have been used to evaluate liquid distribution are given.

Many studies have applied a conductance method to evaluate liquid distribution [122-125]. Figure 1.22 shows the circuit diagram of the conductance technique. An electrical AC sinusoidal signal with a frequency of 100 Hz and an RMS (root-mean-square) voltage of 6.7 V is applied to electrodes immersed in the fluidized bed. The resistance of the resistor is known. Using Ohm’s law, the bed resistance can be calculated, and so can the bed conductance. Calibration can be performed to relate the conductance with free moisture wt % in the bed calculated from mass balance. The value of the calculated free

liquid mass can be verified with titration (using Karl-Fisher). They found that the bed conductivity increases linearly with the increase of free moisture wt % in the bed. They found that by increasing GLR in the spray nozzle, there was an increase of the free moisture, which agrees with the results from Portoghese et al. [126] and Mohagheghi et al. [125].

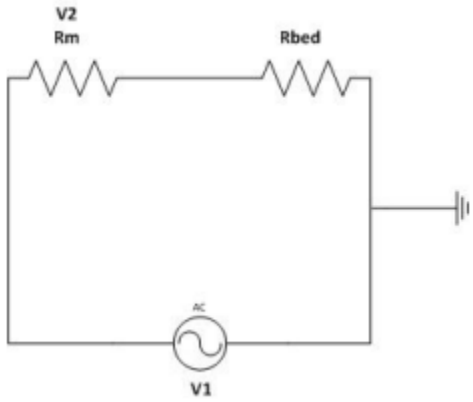

Figure 1.22 Circuit diagram of conductance technique [122]

Portoghese et al. [126] used triboelectric probes to evaluate the liquid distribution. In this method, no extra power is supplied. The bed is first fluidized. The attrition between particle and particle, particle to gas bubbles, and particle to steel triboelectric probe create an electrical charge. When the electrons' charge and discharge reach a steady-state, the cycle of the measured signal can give information about gas bubble flow distribution [27]. However, when there is a liquid spray, the phenomenon is more complicated. The current first increases to the maximum value, then it decreases sharply. The increase of electric current was due to the bed's conductivity increase because there was more liquid [122, 127]. The decrease may be from two or more impacts; one is from the bed's discharge, as there is no external power supply, the other one is the mixing and evaporation in the bed.

For this thesis, the conductivity method will be used. We found that the conductivity probes (called E-probes in this thesis) give a more reliable measurement of the local free moisture than triboelectric probes.

A Gum Arabic method developed by Reyes et al. [101] can evaluate the initial liquid distribution quality by estimating how much liquid is trapped in agglomerates and the size distribution and liquid content of the agglomerates. This method, which uses safe materials at moderate temperature, can provide similar agglomerate properties in a Fluid Coker by changing conditions, such as binder solution component, solids material, operating temperature, or pH[101, 128]. The binder solution contains 92 wt% water, 6 wt% of Gum Arabic, and 2 wt% of blue dye. After retrieving the agglomerates, they can be dissolved in water, and the blue dye concentration can be measured with a UV spectrometer. This provides the amount of water initially trapped in agglomerates by mass balance. This method has been widely used to give the initial liquid distribution quality because, for most experiments, the researchers slump the bed just after injection [27, 99, 101, 103, 104, 129].

Methods to evaluate liquid distribution quality are not limited to the ones introduced above. The above methods are the ones applied in this thesis. Other methods can be found elsewhere, for example, X-ray [130], acoustic emission method [131], and other binder solutions that create strong agglomerates [132].

1.3.2 Impact of superficial gas velocity on liquid distribution

Mohagheghi et al. [133] found increasing superficial gas velocity during injection increases free moisture in the bed with the conductance method. However, they did study superficial gas velocities higher than 0.4 m/s.

Li et al. [99] studied the impact of superficial gas velocity with the Gum Arabic method. They found that increasing the superficial gas velocity from 0.18 to 2.2 m/s during injection decreases the fraction of the injected liquid initially trapped in agglomerates dropped from 0.92 to 0.48. However, the trend is non-linear. After the superficial gas velocity reached 1.2 m/s, the decrease of initial liquid trapped in agglomerates leveled off. They believed that it is related to the transition from bubbling to turbulent. Jahanmiri et al. [27] also found by increasing superficial gas velocity from 0.3 to 0.45 m/s, the fraction of initial liquid trapped decreased from 0.3 to 0.15.

Li et al. [99] also studied the impact of drying gas velocity. They found that by increasing the superficial gas velocity during drying, less liquid is trapped in agglomerates. However, they did not show the impact of drying time.

1.3.3 Impact of fluidizing gas distribution on liquid distribution

Song et al. [102] did experiments with optical probes to measure bed voidage distribution, using a pressurized fully cylindrical cold model of a commercial coker. They found that the voidage of the radial profile increased gradually from the wall to the center of the column, which created a core-annular flow structure. Particles in the descending outer region were entrained by the feed jets into the core region. The results were confirmed by Li et al. [9] with CFD modeling (Figure 1.23).

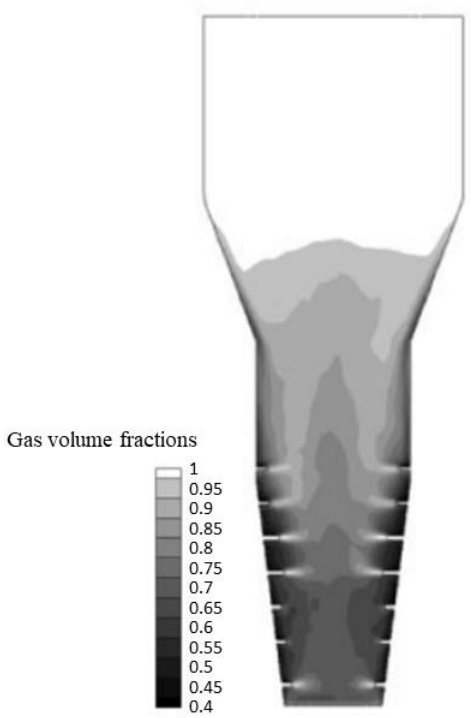

Figure 1.23 Typical gas volume fraction distribution in a coker from CFD modeling (Li et al. [9])

Joness et al. [103] found by changing the nozzle size, with the same injection location and liquid flux, the spray jets penetrate deeper into the bed, gives a lower fraction of the

injected liquid that is initially trapped in agglomerates, using the Gum Arabic method. It could be due to at deeper injection locations; there are more gas bubbles,

Li et al. [99] used the Gum Arabic method. They found that by concentrating the gas bubbles to the western side, the middle and eastern side of the rectangular bed, with a fixed nozzle location, the fraction of the injected liquid initially trapped in agglomerates could be varied from 0.4 to 0.7.

Bhatti et al. [104] studied the impact of gas distribution on agglomerates size distribution with the Gum Arabic method. The unit they used is the same as Silitonga et al.[8]. They found that with the same average superficial gas velocity among the cross-sectional area, by concentrating the fluidization gas to the jet tip, the initial liquid trapped in agglomerates fraction is lower than when having gas distributed evenly over the jet length.

However, both [99, 104] studies only have one nozzle location, and only a few gas distributions were tested. There is not enough data to determine where to redirect the gas bubbles to promote the initial liquid distribution.

1.3.4 Impact of baffles on the initial liquid distribution

The initial liquid distribution quality was defined as the jet-bed interaction quality when the liquid was just spread into the bed. In a batch reactor, it is the time at the end of injection. Jahanmiri et al. [27] showed that solids deposit on the baffle's upper surface when injecting near the bed wall using water. At the same time, the problem is resolved by further penetrating the spray nozzle. This indicated that with the baffle, the nozzle tip should be adjusted to have good liquid-bed contact. With the Gum Arabic method, they found that injecting just above the baffle tip, the fraction of the injected liquid initially trapped in agglomerates decreased from 0.14 (no baffle case) to 0.06. The baffle with a flux-tube gave very similar results compared to the baffle without a flux-tube. As the baffle redirects the gas bubbles to the baffle tip and injecting just above the baffle tip enhances the liquid-bed contact, injecting where gas bubbles concentrate becomes interesting for our study.

1.4 Thesis objectives and thesis structure

Past studies have shown that Fluid Cokers perform better and more reliably with a good initial distribution of liquid feedstock on hot coke particles. Recent studies suggest that this initial liquid distribution can be improved by modifying the local bed hydrodynamics, near the spray jet cavity. However, there is not enough published information on how to enhance the initial liquid distribution by optimizing the local bed hydrodynamics. The main objective of the thesis is to provide this information.

This thesis focuses on obtaining reliable, detailed experimental data in a scaled-down model to reach a fundamental understanding of how local hydrodynamics affects the initial liquid distribution. This will provide engineers designing or modifying commercial cokers with the tools required to improve liquid distribution.

The first objective is to develop or adapt measurement methods to study local gas flow, initial liquid-solid contact, and solids mixing. In each case, several measurement methods will be applied to get reliable results.

The second objective is to study the effect of inlet fluidization gas distribution and the impact of baffles on the local gas distribution. Baffles have been introduced in some commercial cokers to modify solids mixing, and recent studies have suggested that they could be used to modify the local gas distribution.

The third objective is to understand the impact of the local gas distribution, just below the spray jet cavity, on the initial liquid distribution of the fluidized bed particles. This requires measuring the initial liquid distribution over a wide range of local gas distributions, correlating liquid distribution to local gas flows, and developing a simple, scalable model based on the fundamental insights that will be obtained from this study.

The fourth objective is to ensure that a design modification, such as the addition of a baffle that improves the initial liquid distribution, does not have a detrimental impact on other important aspects of fluid coker operation. For example, rapid dispersion of wet particles from the spray region to other regions of the fluidized bed is essential to achieve efficient heat transfer from the hot, dry bed particles to the wet particles. It is also

important to prevent the rapid transfer of wet particles from the spray region to the lower bed regions, where they would foul the stripper sheds or result in undesirable liquid losses to the burner.

1.5 Nomenclature

a		The coefficient in Eq.1-1
Ar		Archimedes number
b		The coefficient in Eq.1-1
C_{PS}	$kJ/(kg \cdot K)$	Specific heat capacity of solid particles
cv		Coefficient of variation
D	m	Column diameter
$d_{b\,max}$	m	Maximum gas bubble diameter
d_P	m	Density of solids
E_z	cm^2/s	Axial mixing dispersion coefficient of the solid particles
g	m/s^2	The gravity of earth, 9.81 m/s^2
h	$W/(m^2 \cdot K)$	Heat transfer coefficient
H	m	Static bed height
K		The volume of aggregates (clusters) per unit volume of solid
k_{te}	$kJ/(m \cdot K \cdot s)$	Axial thermal conductivity of bed

Q_c	m^3/s	Volumetric flow rate at which standard deviation of pressure fluctuation reaches a maximum
r/R		Radial position in a cylindrical column
Re_c		Reynolds number at the minimum turbulent velocity
U_C	m/s	Minimum turbulent velocity in other literature
U_i	m/s	Terminal velocity of a cluster
U_{mf}	m/s	Minimum fluidization gas velocity
U_{mt}	m/s	Minimum turbulent velocity
U_t	m/s	Terminal velocity of a single particle
V_g	m/s	Superficial gas velocity
z_C		Coefficient defined in correlation from [89]
Greek		
ε		Bed voidage
ε_{mf}		Voidage at minimum fluidization
μ_g	$kg/(m.s)$	The viscosity of the fluidization gas
$\mu_{g\,20}$	$kg/(m.s)$	The viscosity of the fluidization gas at 20 °C
$\mu_{g\,T}$	$kg/(m.s)$	The viscosity of the fluidization gas at temperature T

ρ_g	kg/m^3	The density of the fluidization gas
$\rho_{g\ 20}$	kg/m^3	The density of the fluidization gas at 20 °C
ρ_P	kg/m^3	The density of the solids
σ	Pa	The standard deviation of pressure fluctuation

1.6 References

1. Kunii, D. and O. Levenspiel, *Fluidization engineering*. 1991: Butterworth-Heinemann.

2. Mun, T.C., *Production of Polyethylene Using Gas Fluidized Bed Reactor*. Hydrocarbon Processing, 2003.

3. Shelukar, S., et al., *Identification and characterization of factors controlling tablet coating uniformity in a Wurster coating process.* Powder Technology, 2000. **110**(1): p. 29-36.

4. Regulator, A.E. *Upgraded Bitumen Production.* [cited 2021 02.13]; Available from: https://www.aer.ca/providing-information/data-and-reports/statistical-reports/st98/crude-bitumen/production/upgraded-bitumen.

5. Gray, M.R., *Upgrading oilsands bitumen and heavy oil*. 2015: University of Alberta.

6. Board, N.E., *Canadian Refinery Overview.* Energy Market Assessment, 2018.

7. Matsen, J.M., *Scale-up of fluidized bed processes: Principle and practice.* Powder Technology, 1996. **88**(3): p. 237-244.

8. Silitonga, H., *EVOLUTION AND FLOW OF VAPORS IN A FLUIDIZED BED*. 2021, Western University.

9. Li, T., et al., *Numerical investigation of FLUID COKING™ units, Part I: Hydrodynamics of a scaled cold flow model.* The Canadian Journal of Chemical Engineering, 2012. **90**(2): p. 442-456.

10. Pfeiffer, R.W., D.S. Borey, and C.E. Jahnig, *Fluid coking of heavy hydrocarbons*. 1959, Google Patents.

11. House, P., *Interaction of gas-liquid jets with gas-solid fluidized beds: Effect on liquid-solid contact and impact on fluid coker operation*. 2007, Faculty of Graduate Studies, University of Western Ontario.

12. Careaga, F.J.S., *Hydrodynamics in Recirculating Fluidized Bed Mimicking the Stripper Section of the Fluid Coker* in *Chemical and Biochemical Engineering* 2013, Western University.

13. Ali, M., et al., *Coke Yield and Heat Transfer in Reaction of Liquid-Solid Agglomerates of Athabasca Vacuum Residue.* Canadian Journal of Chemical Engineering, 2010. **88**(1): p. 48-54.

14. WYATT, J.e.a., *CIRCULATING FLUID BED REACTOR WITH IMPROVED CIRCULATION*, U.S.P.A. Publication, Editor. 2011: United States. p. 9.

15. Kamienski, P., et al. *FLEXICOKING™ Resid Upgrading Technology*. in *11th International BBTC Conference*. 2013. Dubrovnik.

16. WYATT, J.T., et al., *Circulating fluid bed reactor with improved circulation*. 2013, Google Patents.

17. ExxonMobil. *Flexible resid upgrading technology*. 2017.

18. Gary, J.H., G.E. Handwerk, and M.J. Kaiser, *Petroleum refining: technology and economics*. 2007: CRC press.

19. Sadeghbeigi, R., *Fluid catalytic cracking handbook*. 1995: Elsevier.

20. Speight, J.G., *The chemistry and technology of petroleum*. 2014: CRC press.

21. Speight, J., *The Chemistry and Technology of Petroleum.* 2006.

22. Werther, J., E.U. Hartge, and S. Heinrich, *Fluidized‐Bed Reactors–Status and Some Development Perspectives.* Chemie Ingenieur Technik, 2014. **86**(12): p. 2022-2038.

23. Yang, W.-c., *Handbook of fluidization and fluid-particle systems*. 2003: CRC press.

24. Silitonga, H.M., et al., *EVOLUTION AND FLOW OF VAPORS IN A FLUIDIZED BED*, in *CFB13*. 2020.

25. Fernandes, F.A. and L.M. Lona, *Fluidized bed reactor for polyethylene production. The influence of polyethylene prepolymerization.* Brazilian Journal of Chemical Engineering, 2000. **17**(2): p. 163-170.

26. Alizadeh, M., et al., *Modeling of fluidized bed reactor of ethylene polymerization.* Chemical Engineering Journal, 2004. **97**(1): p. 27-35.

27. Jahanmiri, M., *Use of a Baffle to Enhance Distribution of a Liquid Sprayed into a Gas-Solid Fluidized Bed*. 2017, MESc thesis, Western University.

28. Teunou, E. and D. Poncelet, *Batch and continuous fluid bed coating - Review and state of the art.* Journal of Food Engineering, 2002. **53**(4): p. 325-340.

29. Burggraeve, A., et al., *Process analytical tools for monitoring, understanding, and control of pharmaceutical fluidized bed granulation: A review.* Eur J Pharm Biopharm, 2013. **83**(1): p. 2-15.

30. Seyedin, S.H., et al., *Experimental Investigation and CFD Simulation of Top Spray Fluidized Bed Coating System.* Periodica Polytechnica Chemical Engineering, 2016.

31. Jacob, M., *Granulation equipment*, in *Handbook of powder Technology*. 2007, Elsevier. p. 417-476.

32. Ennis, B.J., G. Tardos, and R. Pfeffer, *A microlevel-based characterization of granulation phenomena.* Powder Technology, 1991. **65**(1-3): p. 257-272.

33. Bilgili, E., et al., *Experimental study of fluidized bed co-granulation of two active pharmaceutical ingredients: an industrial scale-up perspective.* Particulate Science and Technology, 2011. **29**(3): p. 285-309.

34. Fries, L., et al., *DEM–CFD modeling of a fluidized bed spray granulator.* Chemical Engineering Science, 2011. **66**(11): p. 2340-2355.

35. Amini, H., et al., *A semi-theoretical model for simulating the temporal evolution of moisture-temperature during industrial fluidized bed granulation.* European Journal of Pharmaceutics and Biopharmaceutics, 2020. **151**: p. 137-152.

36. Crowe, C.T., *Multiphase flow handbook*. Vol. 59. 2005: CRC press.

37. Grace, J.R., X. Bi, and N. Ellis, *Essentials of Fluidization Technology*. 2020, Wiley-VCH.

38. Grace, J.R., *Contacting modes and behaviour classification of gas—solid and other two‐phase suspensions.* The Canadian Journal of Chemical Engineering, 1986. **64**(3): p. 353-363.

39. Bi, H.T., et al., *A state-of-the-art review of gas}solid turbulent #uidization.* Chemical Engineering Science, 2000.

40. Cochet, Y., *Impact of column geometry and internals on gas and particle flows in a fluidized bed with downward solids circulation*, in *Chemical and Biochemical Engineering*. 2021, Western University: unpublished.

41. Chehbouni, A., et al., *Characterization of the flow transition between bubbling and turbulent fluidization.* Industrial & engineering chemistry research, 1994. **33**(8): p. 1889-1896.

42. Arjmandi-Tash, O., A. Zarghami, and R. Zarghami, *Dominant Flow Structures in Gas–Solid Fluidized Beds Using Time and Frequency Domains Analyses.* Particulate Science and Technology, 2014. **32**(5): p. 498-505.

43. Brink, H.G., J. Saayman, and W. Nicol, *Two dimensional fluidised bed reactor: Performance of a novel multi-vortex distributor.* Chemical engineering journal, 2011. **175**: p. 484-493.

44. Gonzalez, A., et al., *Effect of temperature on the onset of turbulent fluidization.* 1995.

45. He, H., et al., *Statistical and frequency analysis of the pressure fluctuation in a fluidized bed of non-spherical particles.* Particuology, 2014. **16**: p. 178-186.

46. Andreux, R., et al., *New description of fluidization regimes.* AIChE Journal, 2005. **51**(4): p. 1125-1130.

47. Seo, M.W., et al., *The transition velocities in a dual circulating fluidized bed reactor with variation of temperatures.* Powder Technology, 2014. **264**: p. 583-591.

48. Bi, X., *Flow Regime Transitions in Gas-solid Fluidization and Transport*, in *Chemical Engineering*. 1994, The University of British Columbia.

49. Ellis, N., et al., *Characterization of dynamic behaviour in gas–solid turbulent fluidized bed using chaos and wavelet analyses.* Chemical Engineering Journal, 2003. **96**(1-3): p. 105-116.

50. Manafi, M., R. Zarghami, and N. Mostoufi, *Effect of electrostatic charge of particles on hydrodynamics of gas-solid fluidized beds.* Advanced Powder Technology, 2019. **30**(4): p. 815-828.

51. Sun, G. and J.R. Grace, *Effect of particle size distribution in different fluidization regimes.* AIChE Journal, 1992. **38**(5): p. 716-722.

52. Bi, X., *Flow regime transitions in gas-solid fluidization and transport*. 1994, University of British Columbia.

53. Foka, M., et al., *Gas phase hydrodynamics of a gas-solid turbulent fluidized bed reactor.* Chemical Engineering Science, 1996. **51**(5): p. 713-723.

54. Cai, P., et al., *Effect of operating temperature and pressure on the transition from bubbling to turbulent fluidization.* FLUIDIZATION AND FLUID PARTICLE SYSTEMS: FUNDAMENTALS AND APPLICATIONS. PAPERS

PRESENTED AT AICHE ANNUAL MEETING, WASHINGTON, 1989(270) }edited by L. S. Fan], New York, U.S.A., American Institute Chemical Engineers, 1989, p.37-43. (IS).

55. Ellis, N., *Hydrodynamics of gas-solid turbulent fluidized beds*. 2003, University of British Columbia: UBC.

56. Gonzalez, A., J. Chaouki, and A. Chehbouni. *Effect of temperature on the onset of turbulent fluidization*. in *Proc, of 8th International Symposium of the Engineering Foundation, Fluidization VIII, Tours, France*. 1995.

57. Zhu, H. and J. Zhu, *New investigation in regime transition from bubbling to turbulent fluidization.* The Canadian Journal of Chemical Engineering, 2008. **86**(3): p. 553-562.

58. Nedeltchev, S. and A. Shaikh, *A new method for identification of the main transition velocities in multiphase reactors based on information entropy theory.* Chemical Engineering Science, 2013. **100**: p. 2-14.

59. Ellis, N., et al., *Characterization of dynamic behaviour in gas-solid turbulent fluidized bed using chaos and wavelet analyses.* Chemical Engineering Journal, 2003. **96**(1-3): p. 105-116.

60. Du, B., W. Warsito, and L.S. Fan, *Bed nonhomogeneity in turbulent gas‐solid fluidization.* AIChE Journal, 2003. **49**(5): p. 1109-1126.

61. Tebianian, S., et al., *X-ray imaging for flow characterization and investigation of invasive probe interference in travelling fluidized bed.* Chemical Engineering Research and Design, 2015. **104**: p. 191-202.

62. --Chehbouni, A., et al., *Effects of different parameters on the onset of fluidization in a turbulent regime.* Canadian Journal of Chemical Engineering, 1995. **73**(1): p. 41-50.

63. Brereton, C., *Fluid mechanics of high velocity fluidised beds*. 1987, University of British Columbia.

64. Shabanian, J. and J. Chaouki, *Hydrodynamics of a gas–solid fluidized bed with thermally induced interparticle forces.* Chemical Engineering Journal, 2015. **259**: p. 135-152.

65. Brink, H.G., J. Saayman, and W. Nicol, *Two dimensional fluidised bed reactor: Performance of a novel multi-vortex distributor.* Chemical Engineering Journal, 2011. **175**(1): p. 484-493.

66. Azizpour, H., et al., *Vibration time series analysis of bubbling and turbulent fluidization.* Particuology, 2012. **10**(3): p. 292-297.

67. Zhou, Y., et al., *Flow regime identification in gas-solid two-phase fluidization via acoustic emission technique.* Chemical Engineering Journal, 2018. **334**: p. 1484-1492.

68. Dang, T., F. Gallucci, and M. van Sint Annaland, *Gas mixing study in freely bubbling and turbulent gas–solid fluidized beds with a novel infrared technique coupled with digital image analysis.* Chemical Engineering Science, 2014. **116**: p. 38-48.

69. Tamadondar, M.R., et al., *Using particle trajectory for determining the fluidization regime in gas–solid fluidized beds.* Advanced Powder Technology, 2012. **23**(3): p. 349-351.

70. Bi, H.T. and J.R. Grace, *Effect of measurement method on the velocities used to demarcate the onset of turbulent fluidization.* The Chemical Engineering Journal and the Biochemical Engineering Journal, 1995. **57**(3): p. 261-271.

71. Holland, D.J., et al., *Magnetic resonance studies of fluidization regimes.* Industrial and Engineering Chemistry Research, 2010. **49**(12): p. 5891-5899.

72. Nedeltchev, S., *New methods for flow regime identification in bubble columns and fluidized beds.* Chemical Engineering Science, 2015. **137**: p. 436-446.

73. Saayman, J., et al., *Fast X-ray tomography for the quantification of the bubbling-, turbulent- and fast fluidization-flow regimes and void structures.* Chemical Engineering Journal, 2013. **234**: p. 437-447.

74. Shiea, M., et al., *Predicting transition velocities from bubbling to turbulent fluidization by S-statistics on vibration signals.* Particulate Science and Technology, 2013. **31**(1): p. 10-15.

75. Xiang, J., et al., *Mathematical analysis of characteristic pressure fluctuations in a bubbling fluidized bed.* Powder Technology, 2018. **333**: p. 167-179.

76. Rim, G. and D. Lee, *Bubbling to turbulent bed regime transition of ternary particles in a gas–solid fluidized bed.* Powder Technology, 2016. **290**: p. 45-52.

77. Zenz, F.A., *Fluidization and fluid-particle systems*. 1960: Reinhold Publishing Corporation.

78. Saayman, J., N. Ellis, and W. Nicol, *Fluidization of high-density particles: The influence of fines on reactor performance.* Powder Technology, 2013. **245**: p. 48-55.

79. Grace, J.R., T.M. Knowlton, and A.A. Avidan, *Circulating Fluidized Beds*. 1996: Springer Netherlands.

80. Arjmandi-Tash, O., A. Zarghami, and R. Zarghami, *Dominant flow structures in gas-solid fluidized beds using time and frequency domains analyses.* Particulate Science and Technology, 2014. **32**(5): p. 498-505.

81. Manafi, M., R. Zarghami, and N. Mostoufi, *Effect of electrostatic charge of particles on hydrodynamics of gas-solid fluidized beds.* Advanced Powder Technology, 2019.

82. Rahimpour, F., R. Zarghami, and N. Mostoufi, *Effect of distributor on fluidized bed hydrodynamics.* The Canadian Journal of Chemical Engineering, 2017. **95**(11): p. 2221-2234.

83. Wormsbecker, M. and T. Pugsley, *Distributor Induced Hydrodynamics in a Conical Fluidized Bed Dryer.* Drying Technology, 2009. **27**(6): p. 797-804.

84. Bi, H.T., *A critical review of the complex pressure fluctuation phenomenon in gas-solids fluidized beds.* Chemical Engineering Science, 2007. **62**(13): p. 3473-3493.

85. Bi, H.T., et al., *A state-of-the-art review of gas–solid turbulent fluidization.* Chemical Engineering Science, 2000. **55**(21): p. 4789-4825.

86. Abba, I.A., et al., *Spanning the flow regimes: generic fluidized‐bed reactor model.* AIChE Journal, 2003. **49**(7): p. 1838-1848.

87. Bi, H., J. Grace, and K. Lim, *Transition from bubbling to turbulent fluidization.* Industrial & engineering chemistry research, 1995. **34**(11): p. 4003-4008.

88. Choi, J.-H., H.-J. Ryu, and C.-K. Yi, *A model for the temperature effect on onset velocity of turbulent fluidization of Geldart type A particles.* Korean Journal of Chemical Engineering, 2010. **28**(1): p. 304-307.

89. Sun, G. *Transition to turbulent fluidization and its prediction*. in *Fluidization VI*. 1989. Banff, Canada: Engineering Foundation.

90. Yang, W.-C., *Mechanistic models for transitions between regimes of fluidization.* AIChE Journal, 1984. **30**(6): p. 1025-1027.

91. Grace, J.R., *Hydrodynamics of Bubbling Fluidization.* Essentials of Fluidization Technology, 2020: p. 131-152.

92. Li, Y. and P. Wu, *A study on axial gas mixing in a fast fluidized bed.* Circulating fluidized bed technology III, 1991: p. 581-586.

93. LEE, G.S. and S.D. KIM, *Gas mixing in slugging and turbulent fluidized beds.* Chemical Engineering Communications, 1989. **86**(1): p. 91-111.

94. Li, J. and H. Weinstein, *An experimental comparison of gas backmixing in fluidized beds across the regime spectrum.* Chemical Engineering Science, 1989. **44**(8): p. 1697-1705.

95. Du, B., et al., *Gas and solids mixing in a turbulent fluidized bed.* AIChE Journal, 2002. **48**(9): p. 1896-1909.

96. Molerus, O., *Heat transfer in gas fluidized beds part 2. Dependence of heat transfer on gas velocity.* Powder technology, 1992. **70**(1): p. 15-20.

97. Stefanova, A., et al., *Local hydrodynamics and heat transfer in fluidized beds of different diameter.* Powder Technology, 2011. **212**(1): p. 57-63.

98. Molerus, O., A. Burschka, and S. Dietz, *Particle migration at solid surfaces and heat transfer in bubbling fluidized beds—II. Prediction of heat transfer in bubbling fluidized beds.* Chemical Engineering Science, 1995. **50**(5): p. 879-885.

99. Li, L., *Effect of Local Bed Hydrodynamics on the Distribution of Liquid in a Fluidized Bed*. 2016, MESc thesis, Western University.

100. Knapper, B.A., et al., *Measurement of efficiency of distribution of liquid feed in a gas-solid fluidized bed reactor.* International Journal of Chemical Reactor Engineering, 2002. **1**(1).

101. Reyes, L.A.P., *Effect of temperature and successive sprays on liquid distribution in fluidized beds*. 2015, School of Graduate and Postdoctoral Studies, University of Western Ontario.

102. Song, X., et al., *Hydrodynamics of the reactor section in fluid cokers.* Powder Technology, 2004. **147**(1-3): p. 126-136.

103. Joness, A.M., *The Effect of Scale on Spray Nozzle Performance.* 2019.

104. Bhatti, M.O.I., *Study of Motion of Agglomerates Through a Fluidized Bed*. 2017, MESc thesis, Western University.

105. Xing, X., *Numerical study of the effect of gas distributors and baffles on the bubble distribution, gas and solid mixing in a fluidized bed,* in *Chemical and biochemical engineering*. 2020, Western University. p. 292.

106. Akbari, V., et al., *Model-based analysis of the impact of the distributor on the hydrodynamic performance of industrial polydisperse gas phase fluidized bed polymerization reactors.* Powder technology, 2014. **267**: p. 398-411.

107. Briens, C. and J. McMillan, *Jets in Fluidized Beds,* in *Essentials of Fluidization Technology*. 2020. p. 457-498.

108. Zhang, Y., *Baffles and Aids to Fluidization*, in *Essentials of Fluidization Technology*. 2020. p. 431-455.

109. Zhang, Y., et al., *Systematic Investigation of Particle Segregation in Binary Fluidized Beds with and without Multilayer Horizontal Baffles.* Industrial & Engineering Chemistry Research, 2012. **51**(13): p. 5022-5036.

110. Jin, Y., et al., *Pagoda-shaped internal baffles for fluidized bed reactors.* Int. Chem. Eng, 1982. **22**(2): p. 269-279.

111. Wang, S., et al., *CFD-DEM study of the effect of ring baffles on system performance of a full-loop circulating fluidized bed.* Chemical Engineering Science, 2019. **196**: p. 130-144.

112. Rossbach, V., et al., *Gas-solid flow in a ring-baffled CFB riser: Numerical and experimental analysis.* Powder Technology, 2019. **345**: p. 521-531.

113. Shah, M.T., et al., *Effect of baffles on performance of fluid catalytic cracking riser.* Particuology, 2018. **38**: p. 18-30.

114. Benzarti, S., H. Mhiri, and H. Bournot, *Numerical simulation of baffled circulating fluidized bed with Geldart B particles.* Powder Technology, 2021. **380**: p. 629-637.

115. Chalermsinsuwan, B., T. Samruamphianskun, and P. Piumsomboon, *Effect of operating parameters inside circulating fluidized bed reactor riser with ring baffles using CFD simulation and experimental design analysis.* Chemical Engineering Research and Design, 2014. **92**(11): p. 2479-2492.

116. McKeen, T. and T.S. Pugsley, *Simulation of cold flow FCC stripper hydrodynamics at small scale using computational fluid dynamics.* International Journal of Chemical Reactor Engineering, 2003. **1**(1).

117. Veluswamy, G.K., et al., *Hydrodynamic Study of Fluid Catalytic Cracker Unit Stripper.* Industrial & Engineering Chemistry Research, 2013. **52**(12): p. 4660-4671.

118. Sanchez Careaga, F.J., et al., *Agglomerate behavior in a recirculating fluidized bed with sheds: Effect of sheds.* Advanced Powder Technology, 2018. **29**(7): p. 1758-1770.

119. Cochet, Y., et al., *Impact of column geometry and internals on gas and particle flows in a fluidized bed with downward solids circulation: Effect of lateral injection profile and baffles.* Powder Technology, 2020.

120. Du, B., et al., *Fluid bed coking process with decoupled coking zone and stripping zone*. 2017, Google Patents.

121. Mohagheghi, M., et al., *The effects of liquid properties and bed hydrodynamics on the distribution of liquid on solid fluidized particles in a cold-model fluidized bed.* Powder Technology, 2014. **256**: p. 5-12.

122. Zirgachianzadeh, M. and T.U.o.W. Ontario, *Liquid Distribution from Industrial Scale Spray Jets in Fluidized Beds*. 2012, Western University.

123. Portoghese, F., et al., *Effect of the injection-nozzle geometry on the interaction between a gas–liquid jet and a gas–solid fluidized bed.* Chemical Engineering and Processing: Process Intensification, 2010. **49**(6): p. 605-615.

124. Leach, A., et al., *Use of pulsations to enhance the distribution of liquid injected into fluidized particles with commercial-scale nozzles.* AIChE Journal, 2013. **59**(3): p. 719-728.

125. Mohagheghi Dar Ranji, M., *Impact of Local Bed Hydrodynamics on Jet-Bed Interaction*. 2014, PhD thesis, Western University.

126. Portoghese, F., et al., *Electric conductance method to study the contact of injected liquid with fluidized particles.* AIChE Journal, 2008. **54**(7): p. 1770-1781.

127. Leach, A., et al., *A new and rapid method for the evaluation of the liquid–solid contact resulting from liquid injection into a fluidized bed.* Powder Technology, 2008. **184**(1): p. 44-51.

128. Morales, C.B., *Development and Application of an Experimental Model for the Fluid Coking Process*. 2013, The University of Western Ontario.

129. Idowu, J., C. Briens, and D. Pjontek, *Spraying Slurries: Impact of Slurry Properties on Spray Characteristics and Agglomerate Formation in Fluidized Beds.* Mater. Sci., 2018.

130. Ariyapadi, S., et al., *Digital X-ray imaging technique to study the horizontal injection of gas-liquid jets into fluidized beds.* International Journal of Chemical Reactor Engineering, 2003. **1**(1): p. A 56.

131. Tsujimoto, H., et al., *Monitoring particle fluidization in a fluidized bed granulator with an acoustic emission sensor.* Powder technology, 2000. **113**(1-2): p. 88-96.

132. Morales, C.B., et al., *Low-temperature experimental model of liquid injection and reaction in a fluidized bed.* The Canadian Journal of Chemical Engineering, 2016. **94**(5): p. 886-895.

133. Mohagheghi, M., et al., *Study of the effect of local hydrodynamics on liquid distribution in a gas–solid fluidized bed using a capacitance method.* Fuel, 2013. **107**: p. 236-245.

Chapter 2

2 Experimental equipment, materials, and procedures

The main objective of the thesis is to investigate how to enhance the initial liquid distribution by optimizing the local bed hydrodynamics. To achieve the main objective, we applied a fluid bed that could provide a wide range of fluidization gas velocities (0.18-1.56 m/s). And it could be easily modified to provide a large range of gas bubble flows profiles in the spray region. The gas bubble flow pattern was modified by changing the gas distributor configuration or adding baffle(s). The fluid bed applied in this research was designed as a scaled-down version of the radius of the commercial coker with a scaling factor of around 0.11. The rectangular 2D fluid bed was applied to simplify the baffle installation and reduce the complexity of the research, while the results are still applicable when scaled to a 3D column [1].

This section introduces the general equipment and material used in this research. The detailed modification and changes based on the general equipment and material to facilitate each method will be introduced in chapter 3.

2.1 General equipment and material

Figure 2.1 shows a schematic diagram of the fluidized bed apparatus. The main body had a rectangular cross-section of 0.5 m × 0.1 m and a height of 1.15 m. Any location in the bed could be described based on its coordinate (x, z), where x was the lateral location and z was the vertical location. The bottom of the rectangular section (special designed gas distributor) was set as the reference elevation (z = 0 m). The lateral direction varied from x = 0 m at the western wall (“W” in Figure 2.1) to 0.5 m at the eastern wall (“E” in Figure 2.1). The special rectangular gas distributor was designed for two purposes: to ease the drainage of solids, and to be able to modify the gas bubble flow pattern of the whole bed (details in section 2.1.2).

Five cyclones arranged in 3 stages recovered entrained solids and allowed for operation at high fluidization velocities (up to 1.6 m/s). Two parallel sets of primary and secondary

cyclones were installed inside the unit, while the standard tertiary cyclone was located outside the unit and exhausted outside the building. The downcomers of the secondary cyclones extended outside of the unit to collect the fine entrained solids that had escaped the primary cyclones.

A heater made of six U-shaped heating elements was immersed into the fluidized bed upper region (Figure 2.2). When fluidizing with a low gas velocity (0.15 m/s), the solids circulation could convey the heat to the whole unit efficiently while minimizing heat losses to the fluidization gas.

The measuring locations consisted of an array of ¼" (6.35 mm) ports. There were 12 rows, with 9 ports for each row, except for the second row, which had 10 ports. These ports were usually occupied by electrostatic probes (E-probes) for gas bubble profile measurements. However, they could be replaced as needed by other probes, such as thermocouples or snubbers for pressure measurements. The details of which locations were employed with specific methods can be found in each chapter.

The other measuring location indicated with the symbol "P" in Figure 2.1 was for the freeboard pressure measurement. It was used to monitor liquid evaporation for experiments with liquid injection, as described in section 3.7.

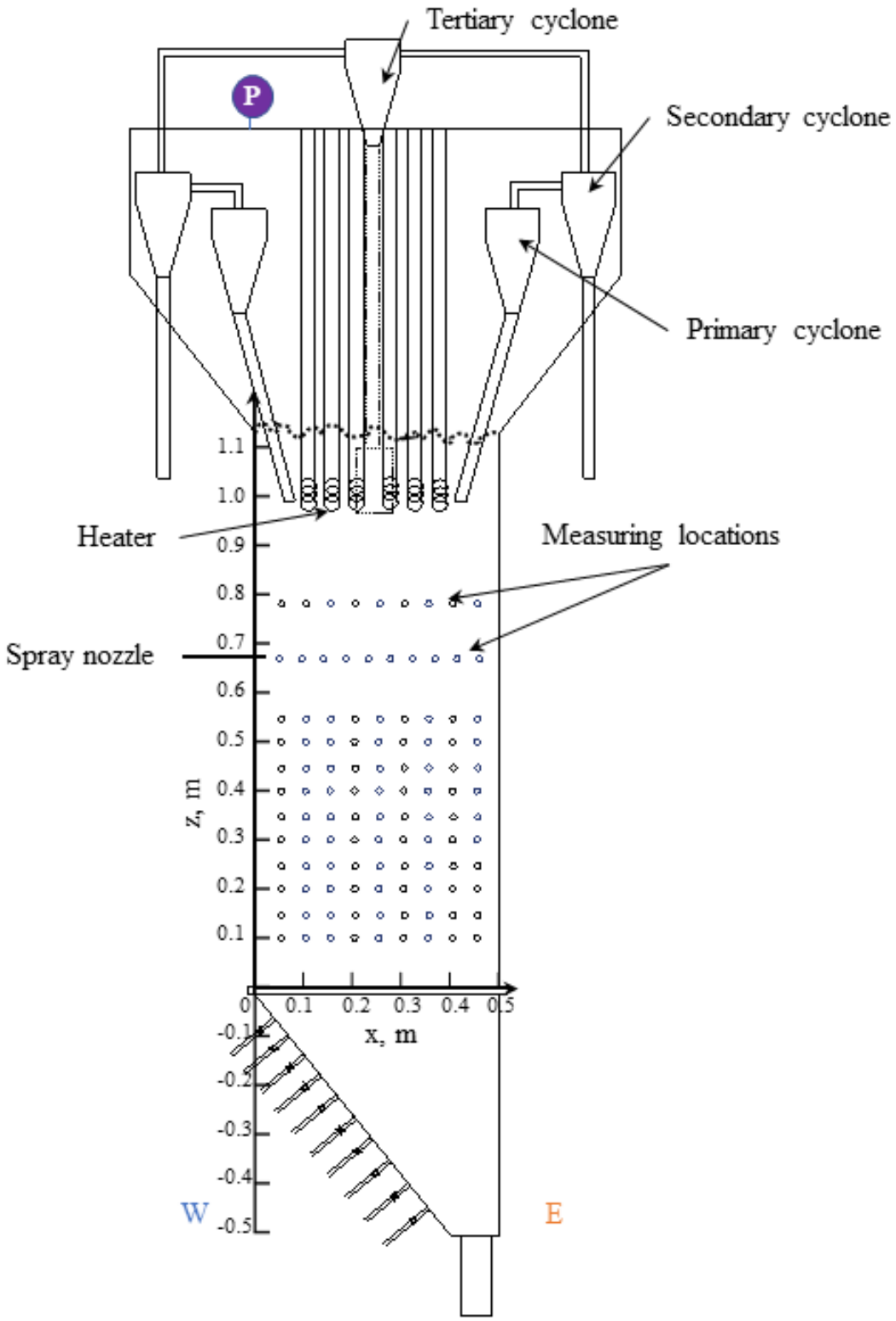

Figure 2.1 Schematic diagram of the lab-scaled fluid bed

Most of the experiments used silica sand, a group B powder with a Sauter mean diameter of 190 μm and an apparent particle density of 2650 kg/m^3. This allowed for the simulation of the formation of the agglomerate in a coker with coke and bitumen with an experimental model that uses silica sand and a water-based binder solution (Gum Arabic solution, introduced in section 3.4), which Reyes et al. [2] successfully developed. The sand mass was 108 kg for all runs, except for runs with the flat perforated plate distributor, for which it was 91 kg. Figure 2.2 shows the cumulative size distribution of the sand. The defluidized bed height was approximately 1.65 m. Compressed air was used to fluidize the bed (the relative humidity was lower than 5% at room temperature) (details see section 2.1.2). The minimum fluidization gas velocity was 0.033 m/s and 0.027 m/s at 30 °C and 130 °C, respectively. There were two different liquids that have been most frequently used as an injection: DI water and Gum Arabic solution (details see section 3.4).

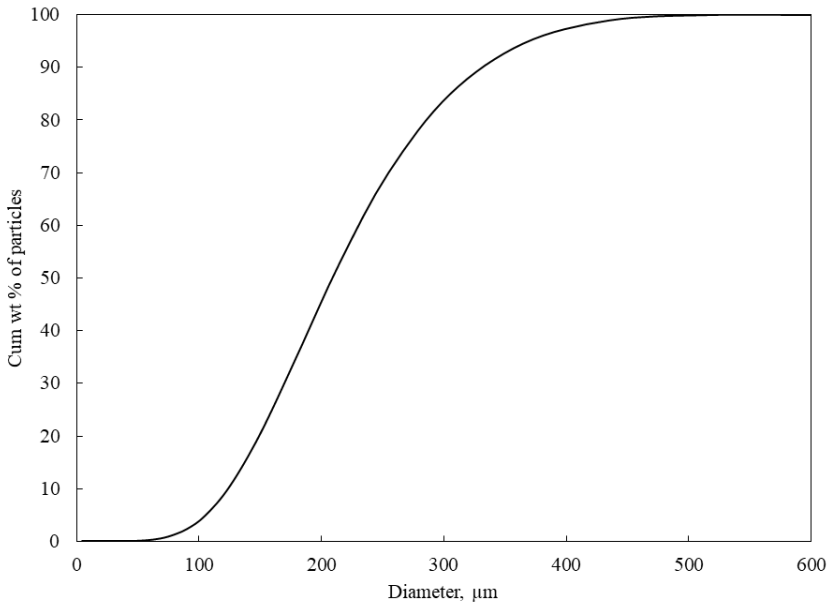

Figure 2.2 Size distribution of silica sand used in the experiments

2.1.1 Injection system

The spray nozzle is shown in Figure 2.1 at the most frequently used liquid injection level. The spray nozzle could be moved to reach various lateral locations, to expose the spray jet to different local bed hydrodynamics. Other ports could be used to insert the spray nozzle at different vertical locations or from the other side of the unit; they will be introduced in section 2.1.4 to show the relative location to a baffle.

Figure 2.3 A shows the schematic diagram of the injection system. The blue arrow shows the flow direction. The top compressed nitrogen line was set at 241 psig to pressurize the liquid blow tank. In most experiments, 200 g of liquid (water or a binder solution (introduced in chapter 3)) was loaded in the blow tank. The blow tank was pressurized, the atomization gas flow was initiated, and the computer opened the solenoid valve to start the liquid flow. A sonic orifice of 0.254 mm combined with an upstream pressure regulator set at 467 psig (3.32 MPa) provided a stable atomization nitrogen flow.

A restriction of 1.6 mm diameter was used to stabilize the liquid flow in the line connecting the blow tank to the pre-mixer, where liquid and gas flows merged. The gas-liquid mixture flowed through a conduit with an inner diameter of 1.93 mm. This conduit was reinforced with a 13.26 mm outer diameter stainless steel tube to prevent bending at a high superficial gas velocity in the fluidized bed. The liquid then reached a scaled-down TEB nozzle.

Figure 2.3 B shows the schematic diagram of the scaled-down version of an industrial spray nozzle (TEB nozzle [3]) with a convergent-divergent-convergent geometry. This geometry has been shown to promote the breakup of large liquid ligaments and droplets into fine droplets [4].

The outlet diameter of the spray nozzle was 1 mm, the gas to liquid mass ratio (GLR) was 2 %, and the liquid flowrate was 17.5 g/s to achieve a commercially representative liquid flux of 22.3 g/(s.mm2) through the nozzle tip [4]. Joness et al. used the same equipment in both open-air and the fluidized bed to confirm that the spray jet is stable under these conditions [4]. Similar injection systems have been used in previous studies [2, 4-10].

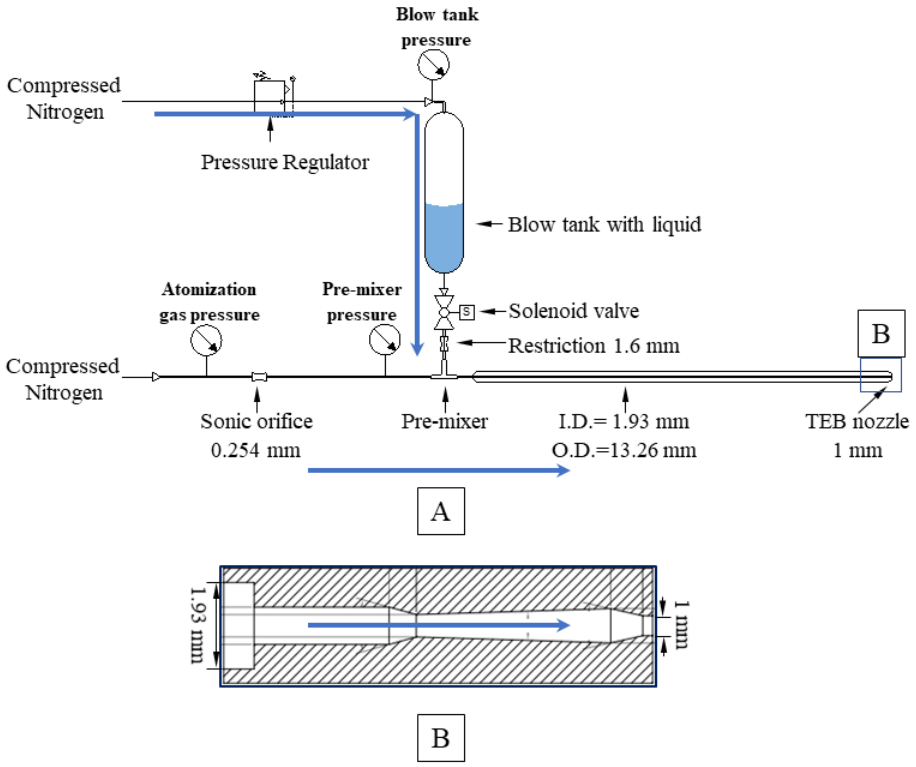

Figure 2.3 Schematic diagram of A. Injection system, B. Scaled-down TEB nozzle

A special HGLR spray nozzle was employed in some experiments to prevent the wet agglomerate formation in the fluid bed using a high gas to liquid mass ratio of 107 % (or 30 % when applicable). It consisted of a 4.94 mm diameter straight pipe. It was typically operated with a much lower flowrate (1.6 g/s or 4.5 g/s when applicable). Only 100 g of deionized water was injected in each run (instead of 200 g) to enable faster drying and reheating of the bed solids. Details can be found in sections 3.5 to 3.7 and Chapter 6.

2.1.2 Gas distributor configuration

The triangular gas distributor section was installed just below the main body for negative elevations ($z < 0$). An inclined distributor was used to facilitate agglomerates recovery. Second, using CFD modeling, Xing et al. [11] showed that an inclined distributor could change the gas bubble flow pattern of the whole bed, while a flat distributor could not (details in section 4.4).

Figure 2.4 shows the gas distributor configurations used in this research. There were two main distributors: an inclined distributor (Figure 2.4 A, B, C) and a flat distributor (Figure 2.4 D, E). The inclined distributor consisted of 20 tuyeres, and each tuyere was provided with a shut-off valve to modify the gas distribution. Each tuyere was supplied with a sonic orifice to ensure that the gas flowrate was the same through each opened tuyere. Each tuyere had three 3 mm holes (Figure 2.4 F), where the gas flow direction is shown with a green arrow. The detailed information on tuyere design can be found in [5]. The last tuyere was 0.1 m away from the eastern side bed wall to provide space for the solids drainage pipe. Opening 10 tuyeres on the western side of the bed provided the western case gas distributor configuration (Figure 2.4 A). Similarly, opening 10 tuyeres evenly along the whole length of the inclined distributor provided the even case configuration (Figure 2.4 B). Opening 10 tuyeres on the eastern side of the bed provided the eastern case configuration (Figure 2.4 C).

To obtain data with a more conventional gas distributor (Figure 2.4 D), we inserted a perforated plate (Figure 2.4 E) above the triangular section, which then acted as a wind-box. The gas perforated plate consisted of 36 small holes distributed in 2 rows. Each hole was 3 mm in diameter, and the center-to-center distance between adjacent holes was 27 mm. The western, even, and eastern cases were opened to verify that the gas inlet configuration into the wind-box had no impact on the fluidized bed.

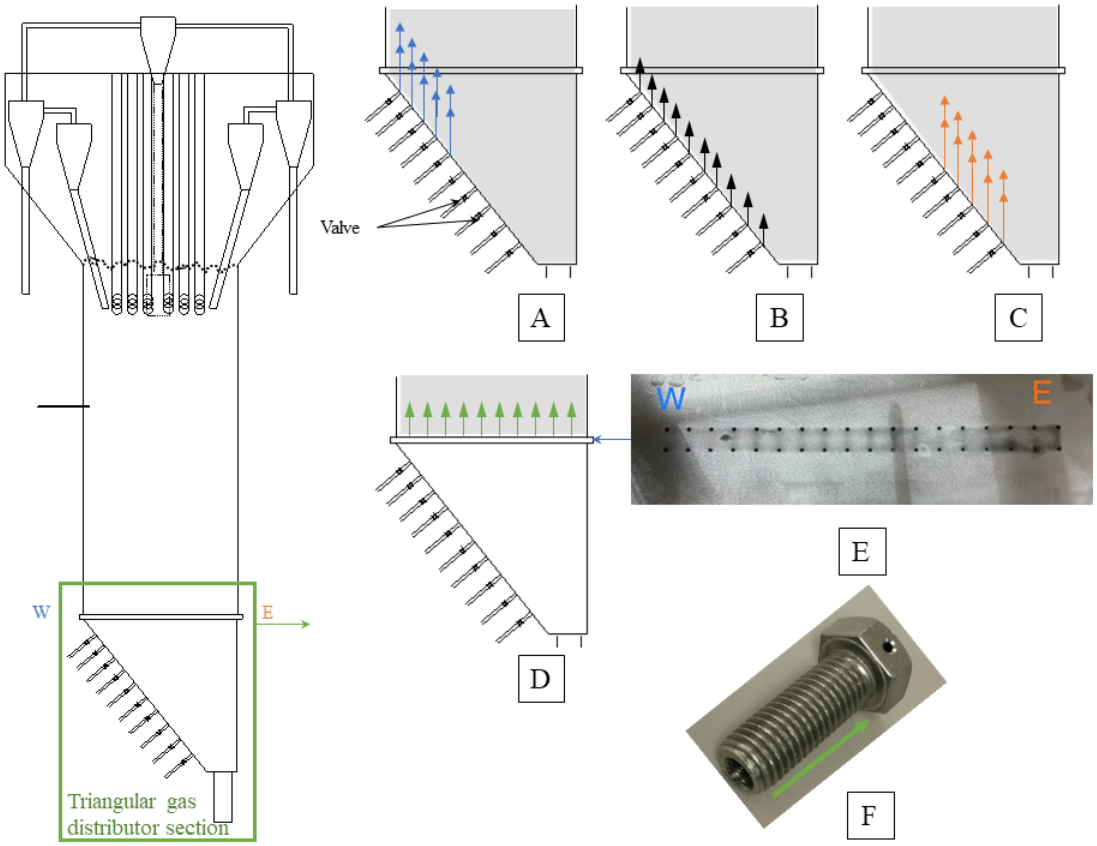

Figure 2.4 Schematic diagrams of the configurations of different gas distributors A. Inclined distributor, western case, B. Inclined distributor, even case, C. Inclined distributor, eastern case, D. Flat distributor, E. Photo of perforated plate, F. Photo of a tuyere (adapted from Li [5])

2.1.3 Baffle designs

Figure 2.5A is a photo of a ring baffle utilized in a commercial Fluid Coker [12]. Sanchez Careaga et al. found that the ring baffle installed just above the stripper section increased agglomerates' residence time [13]. In this research, various baffle locations have been tested to show their impact on gas and liquid distribution.

The ring baffle (Figure 2.5A) is open from the bottom (there is an empty pocket under the baffle). It occupies approximately 50 % of the cross-sectional area of the vessel [14].

There is a flux-tube in each small section of the ring baffle. As stated in a patent [14], "To promote drying of the coke particles, it may be desirable to provide a lip at the inner periphery of the baffle." Figure 2.5B shows a scaled-down baffle of a small section of the industrial baffle, which was an adaption to the 2D geometry of the industrial design (Figure 2.5A). The details of dimensions and the modification to the flux-tube are shown in Figure 2.6 B and Figure 2.6 C. Not many modifications to the flux-tube geometry have been tested because the CFD modeling [11] suggests an insignificant impact from changing flux-tube diameter and length.

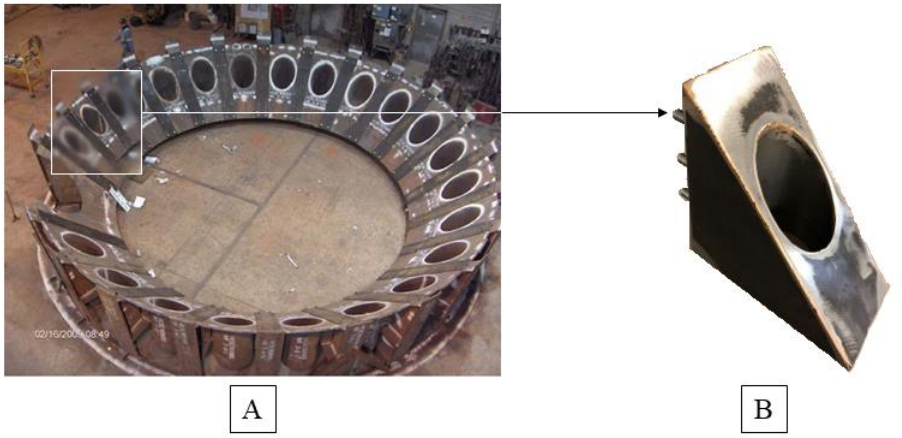

Figure 2.5 Photo of A. commercial-scale ring-baffle, B. Lab-scaled baffle

a. Asymmetrical baffle

Figure 2.6 shows the schematic diagrams of various asymmetrical baffle geometries. The displayed baffle location is a typical set-up used in this research, where the top of the baffle was 0.1 m below the spray level. Baffle Type A1 (Figure 2.6 A) was a basic geometry of the baffle design. Other baffle geometries are designed based on baffle Type A1.

Baffle Type A1 (Figure 2.6 A) consisted of a single open-ended right triangle shape with an internal angle of 45°, having the same width as the bed and extending 0.18 m horizontally from the wall (0.18 m × 0.1 m × 0.18 m). Baffle Type A2 (Figure 2.6 B) had

the exact dimensions of A1 but included a flux-tube, a hollow pipe. The diameter of the flux-tube was 0.08 m. The flux-tube length was extended to the same level as the bottom edge of the baffle. Baffle Type A3 (Figure 2.6 C) was baffle Type A2 modified by shortening the flux-tube: the bottom of baffle Type A3 flux-tube ended 0.034 m above the bottom edge of the baffle. Baffle Type A4 (Figure 2.6 D) has a larger blocking cross-sectional area (50 %) than the baffle Type A1 (36 %), and the dimensions of Baffle Type A4 were 0.25 m × 0.1 m × 0.18 m.

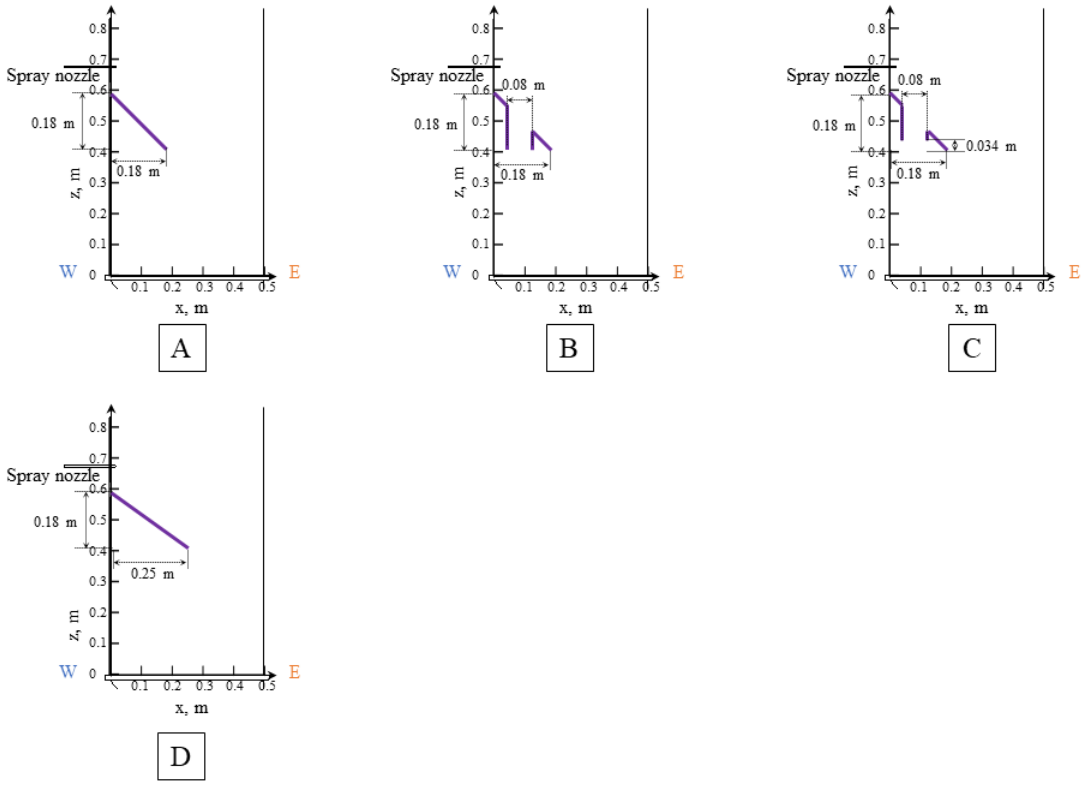

Figure 2.6 Schematic diagram of asymmetrical baffle: A. Type A1, B. Type A2, C. Type A3, D. Type A4

b. Symmetrical baffle

Baffle Type S1 (Figure 2.7A) consisted of two smaller half baffles (0.125 m × 0.1 m × 0.125 m), with a 50 % total blocking cross-sectional area. This simulates the effect of the ring baffle in the cylindrical fluid coker in a 2D bed. The solids are shown in grey, and

the baffle pockets (triangular area below the baffle) are shown in white (Figure 2.7A and B). Additionally, Figure 2.7B shows a connector tube installed to connect the two baffle pockets of baffle Type S1. This equilibrates the pressures in pockets under each half baffle because, in the industrial coker, there is a single pocket under the whole baffle, where the pressure is the same. Figure 2.7C and D showed photos of the top and front view of the brass tube connector (0.0127 m diameter). This test was to determine whether the symmetrical baffle can simulate the baffle of a commercial fluid coker.

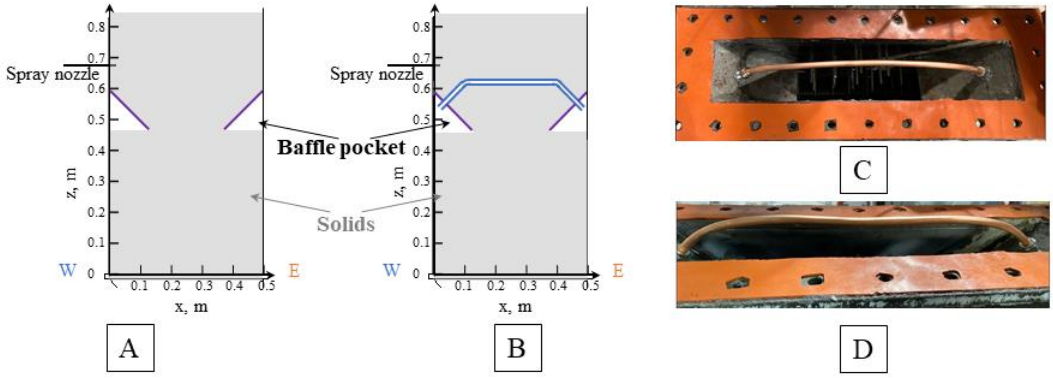

Figure 2.7 Schematic diagram of A. Type S1, B. Baffle Type S1 with connector, C. Photo of a top view of Baffle Type S1 with connector, D. Photo of a front view of Baffle Type S1 with connector

2.1.4 Combinations of conditions

The various injection locations, gas distributors, baffle geometries, and baffle locations relative to the spray nozzle can be combined to give a much more complete picture of their impact on gas and liquid distribution.

a. Baffle locations

Figure 2.8 shows an example of possible relative locations between the spray nozzle and baffle Type A1, which could be moved to different vertical locations. Figure 2.8 A to C shows examples of moving the baffle away from the injection level. The unit was

designed to maximize the flexibility of various possibilities of baffle and nozzle positions.

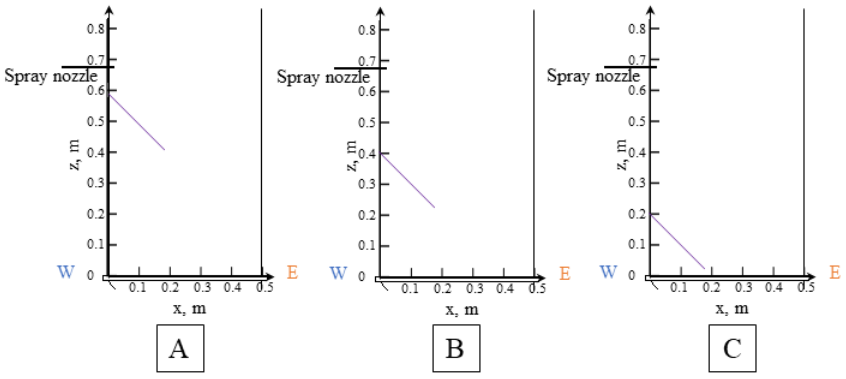

Figure 2.8 Schematic diagram of location of injection nozzle and asymmetrical baffle (baffle type A1): A. Nozzle locations (0,0.67) to (0.25,0.67), baffle top (0,0.57), baffle tip (0.18, 0.39), B. Nozzle locations (0,0.67) to (0.25,0.67), baffle top (0,0.4), baffle tip (0.18, 0.22), C. Nozzle locations (0,0.67) to (0.25,0.67), baffle top (0,0.2), baffle tip (0.18, 0.02)

b. Spray nozzle locations

Figure 2.9 shows an example of possible relative locations between the spray nozzle and baffle Type A1 obtained by moving the spray nozzle. The baffle Type A1 was fixed at the displayed location; in Figure 2.9A, the nozzle location was set to inject from the same side above the baffle. In Figure 2.9B, the nozzle location was set to inject from the same side, below the baffle. In Figure 2.9C, the nozzle location was inside the baffle by half of the baffle length. In Figure 2.9D, the nozzle location was inside the baffle and at the same level as the baffle tip.

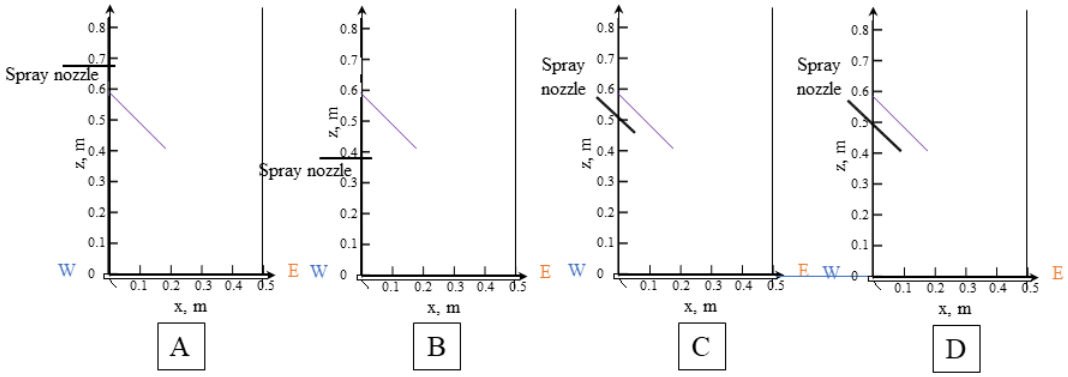

Figure 2.9 Schematic diagram of location of injection nozzle and asymmetrical baffle (baffle type A1): A. Nozzle locations (0,0.67) to (0.25,0.67), baffle top (0,0.57), baffle tip (0.18, 0.39), B. Nozzle locations (0,0.37) to (0.25,0.67), baffle top (0,0.57), baffle tip (0.18, 0.39), C. Nozzle locations (0.05,0.55) to (0.5,0.67), baffle top (0,0.57), baffle tip (0.18, 0.39) D. Nozzle locations (0.09,0.4) to (0.5,0.67), baffle top (0,0.57), baffle tip (0.18, 0.39)

The spray nozzle was installed on the western side bed wall and moved along the horizontal direction. The maximum jet penetration applied in this research was 0.23 m (details in section 3.2). Therefore, the typical moving range of the spray nozzle tip was 0 to 0.25 m to prevent the jet from hitting the wall.

c. Gas distributor configurations

The gas distributor configurations shown in Figure 2.4 have been tested with some selected baffles and spray nozzle locations (details see chapter 4).

2.2 Nomenclature

E		Eastern side bed wall
$I.D.$	m	Inner diameter

$O.D.$	m	Outer diameter
TEB		Base, Terence E
W		Western side bed wall
x	m	Horizontal location in the bed
z	m	Vertical location in the bed

2.3 References

1. Börner, M., et al., *Experimental spray zone characterization in top-spray fluidized bed granulation.* Chemical Engineering Science, 2014. **116**: p. 317-330.

2. Reyes, L.A.P., *Effect of temperature and successive sprays on liquid distribution in fluidized beds*. 2015, School of Graduate and Postdoctoral Studies, University of Western Ontario.

3. Base, T.E., et al., *Nozzle for atomizing liquid in two phase flow*. 1999, Google Patents.

4. Joness, A.M., *The Effect of Scale on Spray Nozzle Performance.* 2019.

5. Li, L., *Effect of Local Bed Hydrodynamics on the Distribution of Liquid in a Fluidized Bed*. 2016, MESc thesis, Western University.

6. Jahanmiri, M., *Use of a Baffle to Enhance Distribution of a Liquid Sprayed into a Gas-Solid Fluidized Bed*. 2017, MESc thesis, Western University.

7. Idowu, J., C. Briens, and D. Pjontek, *Spraying Slurries: Impact of Slurry Properties on Spray Characteristics and Agglomerate Formation in Fluidized Beds.* Mater. Sci., 2018.

8. Morales, C.B., *Development and Application of an Experimental Model for the Fluid Coking Process*. 2013, The University of Western Ontario.

9. Bhatti, M.O.I., *Study of Motion of Agglomerates Through a Fluidized Bed*. 2017, MESc thesis, Western University.

10. Silitonga, H.M., et al., *EVOLUTION AND FLOW OF VAPORS IN A FLUIDIZED BED*, in *CFB13*. 2020.

11. Xing, X., *Numerical study of the effect of gas distributors and baffles on the bubble distribution, gas and solid mixing in a fluidized bed*, in *Chemical and biochemical engineering*. 2020, Western University. p. 292.

12. Kamienski, P., et al. *FLEXICOKING™ Resid Upgrading Technology*. in *11th International BBTC Conference*. 2013. Dubrovnik.

13. Careaga, F.J.S., et al., *Agglomerate behavior in a recirculating fluidized bed with sheds: Effect of ring baffles.* Particuology, 2018. **38**: p. 143-151.

14. WYATT, J.T., et al., *Circulating fluid bed reactor with improved circulation*. 2013, Google Patents.

Chapter 3

3 Experimental methods

The general objective of the research is to enhance the initial liquid distribution by optimizing the local bed hydrodynamics. This thesis requires reliable, detailed experimental data in a scaled-down model. Methods were developed to provide the following information:

- The gas bubble distribution over the column cross-section. Of particular importance is the local volumetric flux of bubble gas, as it is expected to affect the contact between the injected liquid and the bed particles, i.e. the initial liquid distribution.

- The jet penetration depth. Since the initial liquid distribution depends on the interactions between the jet cavity and the bed hydrodynamics, it is important to locate exactly the jet cavity.

- Slugging. With the high fluidization velocities and two-dimensional column geometry used in this study, it is important to check that gas bubbles do not span the short distance between the column walls.

- Quality of the initial distribution of the injected liquid. The main purpose of this thesis is to improve this initial liquid distribution.

- Mixing of wet solids. Rapid dispersion of wet particles from the spray region to other regions of the fluidized bed is essential to achieve rapid heat transfer from the hot, dry bed particles to the wet particles. It is also important to prevent the rapid transfer of wet particles from the spray region to the lower bed regions, where they would foul the stripper sheds. Methods were developed to measure the local liquid concentration, track the wet solids and quantify the mixing of wet solids.

- Vaporization rate of the injected liquid. This measurement provided a way to evaluate how quickly wet solids from the spray region are dispersed and mixed with the bed solids.

- Minimum turbulent fluidization velocity. The hydrodynamics of a fluidized bed is affected by the fluidization regime.

This chapter describes all the experimental methods used in this research and their validation. For each method, modifications and improvements developed for this thesis are first outlined, and the method is then described in detail.

3.1 Gas distribution measurement

3.1.1 Introduction

Using E-probes (electrostatic-probes) for gas distribution measurements was first developed by Jahanmiri [1]. This method has been applied widely in fluidized beds [2-5]. In earlier publications, these probes were called triboprobes because it was thought that most of their current resulted from the triboelectric current due to the friction of the bed particles on the grounded probe surface. The motion of charged bed particles near the probe surface also induced current fluctuations through the probe. Both phenomena were greatly intensified when gas bubbles flow past the probe surface.

Although there were many other methods to obtain gas distribution, such as optical probes [6], X-ray [7], and CFD modeling [8], E-probes were employed in this research because they were cheap, suitable for high gas velocity, high temperature (depends on the E-probe material), high bed density (1500 kg/m^3 in our research), and large scale units.

This thesis improved the original E-probe method from both the calibration procedure and data analysis aspects. From the aspect of the calibration procedure, three extreme inlet gas distributor configurations were included, western, even, and eastern cases, to ensure the calibration applies to a wide range of gas distributions. In his thesis, Jahanmiri's [1] correlation correlated the local flux with the standard deviation and cycle

time of the E-probe signal; this thesis developed a simpler and better correlation with the cycle amplitude of the E-probe signal.

The results from E-probes were also validated with a radiation transmission method [9] and CFD modeling [8]. The radiation transmission method measured the absorption of γ rays through the bed thickness, which was affected by the local bed density and, hence, the bubble gas concentration.

3.1.2 The experimental set-up, material, and standard procedure

Figure 3.1 shows the experimental set-up for the E-probe measurement (Figure 3.1 A) and the radiation transmission method (Figure 3.1 B) for validations. In this method, we did not perform liquid injections. However, a frequently used injection location level was shown with a spray nozzle (Figure 3.1). This injection level provided most of the results to study the correlation between gas distribution and the initial liquid distribution.

Figure 3.1 A shows the principle of the electrostatic current measurement. When no gas bubbles were present in the bed, a flat signal was recorded. When sand particles carried in bubble wakes hit a probe, they stripped electrons from their surface, inducing an electrical current that could be monitored (there was also the possible contribution of current induced by the fast, local motion of the electrostatically charged bed particles caused by the gas bubbles). The 7 rows of probes (64 probes) recorded the raw signal simultaneously for 10 min in a dry bed at 30 °C. The impact of a higher bed temperature of 130 °C on the gas distribution can be found in chapter 4.

Each electrostatic probe was made of a 6.35 mm diameter stainless steel rod connected to a 1 MΩ resistor to obtain a significant voltage drop with a small current. The voltage was then recorded by the data acquisition systems (DAQ) at an acquisition frequency of 100 Hz. Two National Instrument DAQs were used, and they were synchronized with a signal generator. The typical amplitude of the raw signal ranges from −0.15 to 0.15 VDC everywhere in the bed. The penetration of the probes was half of the bed width of 5 cm (Figure 3.1 A). Teflon fittings were used to provide electrical insulation between the bed wall and the E-probes.

Figure 3.1 B shows the principle of the validation method, a radiation transmission method [9]. A scandium-46 thin radioactive particle (1 cm diameter) was placed outside of a bed wall. The sodium iodide (NaI) scintillation detector (Advanced Measurement Technology Inc., Oak Ridge, TN, USA) was outside the opposite bed wall to receive the radiation signal expressed in counts per second. When the bed was fluidized, and gas bubbles flowed between the radioactive source and the detector, the local bed voidage increased, reducing the density of the material through which radiation was transmitted and increasing the measured counts per second.

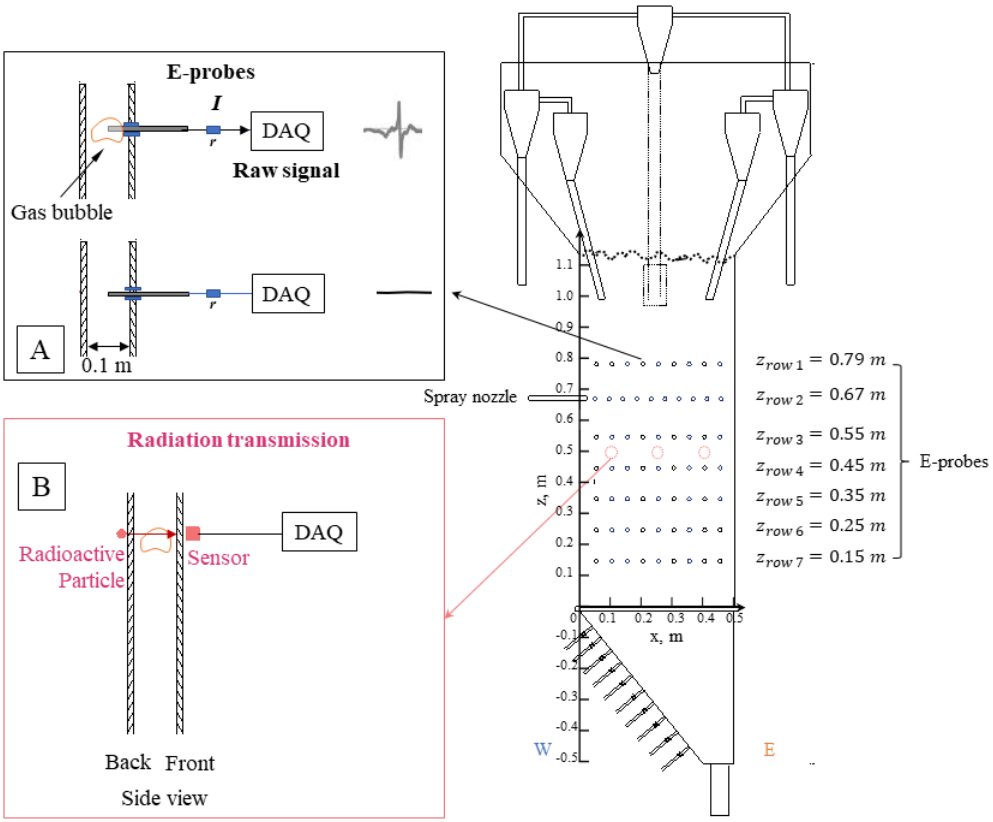

Figure 3.1 Schematic diagram of principle and location of A. Electrostatic-probe method, B. Radioactive transmission method

The standard procedures were:

1) The bed was fluidized for 3 min while the electrostatic data was recorded.
2) Between each run, the bed was left fluidized at new conditions for 1 min.

3.1.3 Data processing

a. E-probe method

Figure 3.2 shows 10 s of the raw signal obtained from the same electrostatic probes at different fluidization velocities. The even case gas distributor configuration (Figure 2.4) was used with three probe locations: bed center (x = 0.25 m), 0.05 m from the western wall (x = 0.05 m), and 0.05 m from the eastern wall (x = 0.45 m). The inlet gas was evenly distributed at the gas distributor. As gas bubbles rose through the bed, they coalesced and broke-up, and tended to migrate to the bed center [10]. Therefore, a stronger signal was expected at the bed center. The raw signal exhibited in Figure 3.2 showed much stronger fluctuations at 1 m/s than at 0.33 m/s for all 3 probe locations. At both velocities, the signals were stronger at the center than near the bed walls because gas bubbles concentrated near the center with this gas distributor configuration.

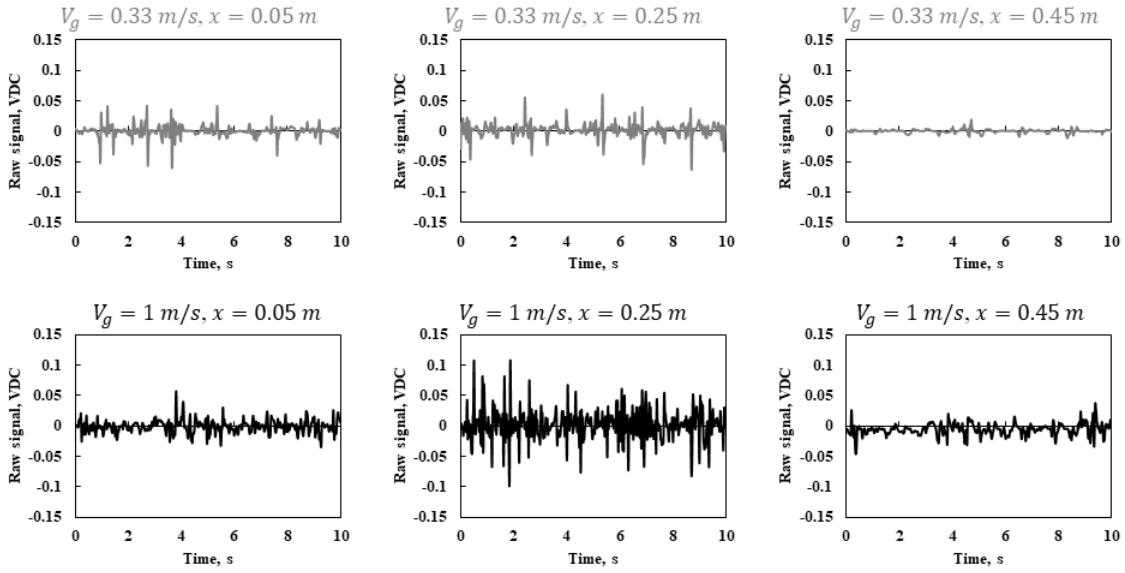

Figure 3.2 Raw signal from tribo-probes (No baffle, inclined distributor, even case $V_g = 0.33\ m/s$ and $V_g = 0.1\ m/s, x = 0.05, 0.25, and\ 0.45\ m, z = 0.55\ m$)

The local bubble volumetric flux (q_{bi}) around each probe was divided by the cross-sectional average volumetric flux ($\overline{q_b}$) to obtain the dimensionless gas flux profile:

$$q_i = \frac{q_{bi}}{\overline{q_b}} \tag{3-1}$$

For a group B powder such as the sand particles used in this study, the cross-sectional average volumetric flux could be obtained from:

$$\overline{q_b} = V_g - U_{mf} \tag{3-2}$$

where V_g was the superficial gas velocity, and U_{mf} was the minimum fluidization gas velocity.

For each row that contained 9 E-probes:

$$\overline{q_{b,cal}} = \left[\sum_{i=1}^{9} q_{bi} \cdot \lambda_i\right] \Big/ (w \cdot d) \tag{3-3}$$

where λ_i was the local cross-sectional area corresponding to 1 probe (i.e., 1/9 of the total column cross-section area), $w \cdot d$ is the total column cross-sectional area.

Experiments were conducted at various superficial gas velocities. The Excel "Solver" was applied to match the cross-sectional average bubble flowrate obtained from Eq.3-2 with the average local values obtained from electrostatic signals Eq.3-3.

Jahanmiri et al.[1] developed a general correlation to characterize the difference in signal strength (raw signal shown in Figure 3.2):

$$q_{bi} = \alpha \cdot B_i^{\beta} \cdot C_i^{\gamma} \tag{3-4}$$

where B_i and C_i were the parameters from signal analysis of the electrostatic signal, $\alpha, \beta, \text{and } \gamma$ were the coefficients found with "Solver" in Excel.

The parameters found by Jahanmiri et al.. [1] were tested with our data. We found that the combination of standard deviation and cycle time provided a good correlation. However, a new single parameter, cycle amplitude, provided an even better and simpler correlation, as shown in Eq. 3-5:

$$q_{bi} = \alpha \cdot A_i^{\beta} \quad 3\text{-}5$$

where A was the cycle amplitude, α and β were the coefficients found with “Solver” in Excel.

An example of applying the cycle analysis method to identify the cycle time was shown in Figure 3.3. The signal analysis program divided raw data gathered from each probe into time segments of various lengths to performed a rescaled range analysis of the persistence of a time series originally proposed by Hurst [11]. This analysis was adapted to detect and characterize cycles [12]. The V statistic was developed to detect cyclic behavior in stock markets [13] and has been applied to detect flow regimes in multiphase systems [12]. If a signal exhibited cyclic behavior, the V-statistic vs. time interval plot would not be a straight line. The peak in the plot corresponds to the cycle time. More details of this method can be found in the paper from Briens et al. [12]. The calculated V statistic detected the cycle time from a well-defined peak, as in the example shown in Figure 3.3. The cycle amplitude was then obtained by dividing the raw signal into segments of a length equal to the cycle time [12]. The difference between standard deviation and average was calculated for each segment, and the process was repeated with more segments until the required confidence interval was reached [12].

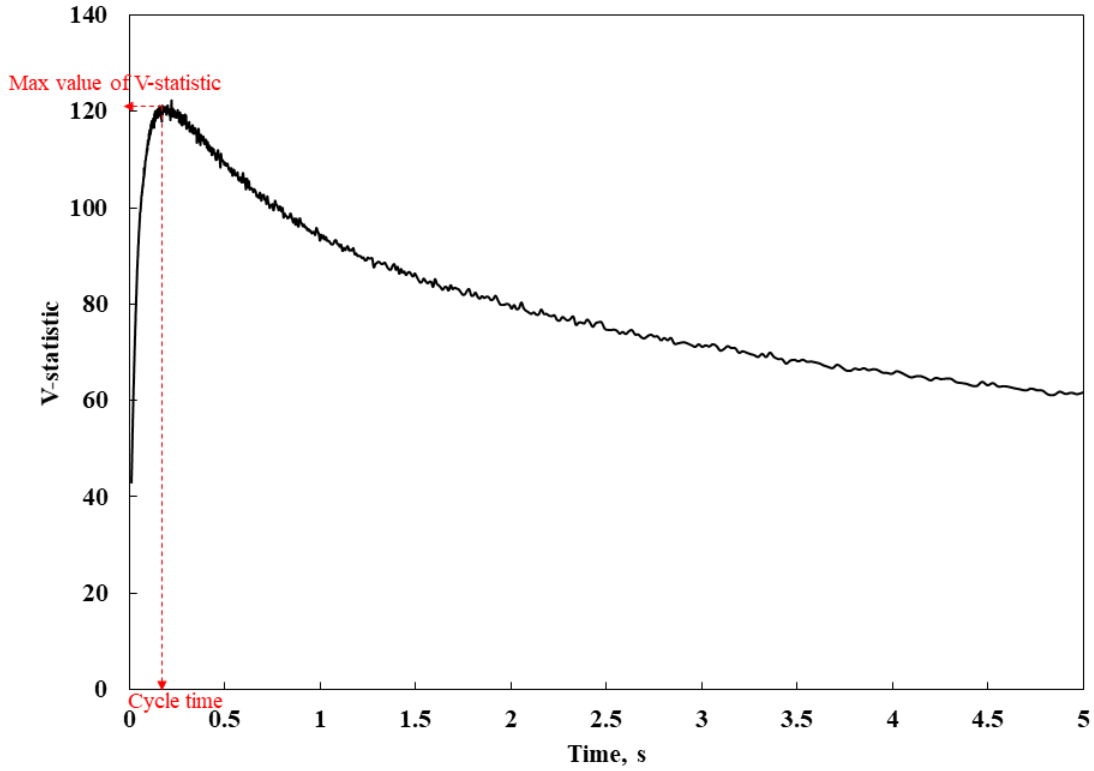

Figure 3.3 Example of V-statistic changing with time interval (No baffle, inclined distributor, even case, $V_g = 1\ m/s, x = 0.25\ m, z = 0.55\ m$)

Once the cycle time had been determined, the cycle amplitude or cycle strength was calculated, using the method described in [12]. The average difference from all segments and repeats was defined as the cycle amplitude (A). The cycle amplitude was affected by the size and frequency of the bubbles. The impact of the superficial gas velocity on the cycle amplitude along a row ($z = 0.55\ m$) is shown in Figure 3.4. At the same superficial gas velocity, the cycle amplitude at the center was higher than near the sides. At the gas distributor section, there was no inlet fluidization gas from $x = 0.4 - 0.5\ m$, because of the solids extraction pipe (see Figure 3.1); therefore, there were less gas bubbles there. Thus, the smaller cycle amplitude was expected near the eastern side bed wall. Figure 3.4 shows that the cycle amplitude increased when increasing the superficial gas velocity from 0.23 to 1 m/s.

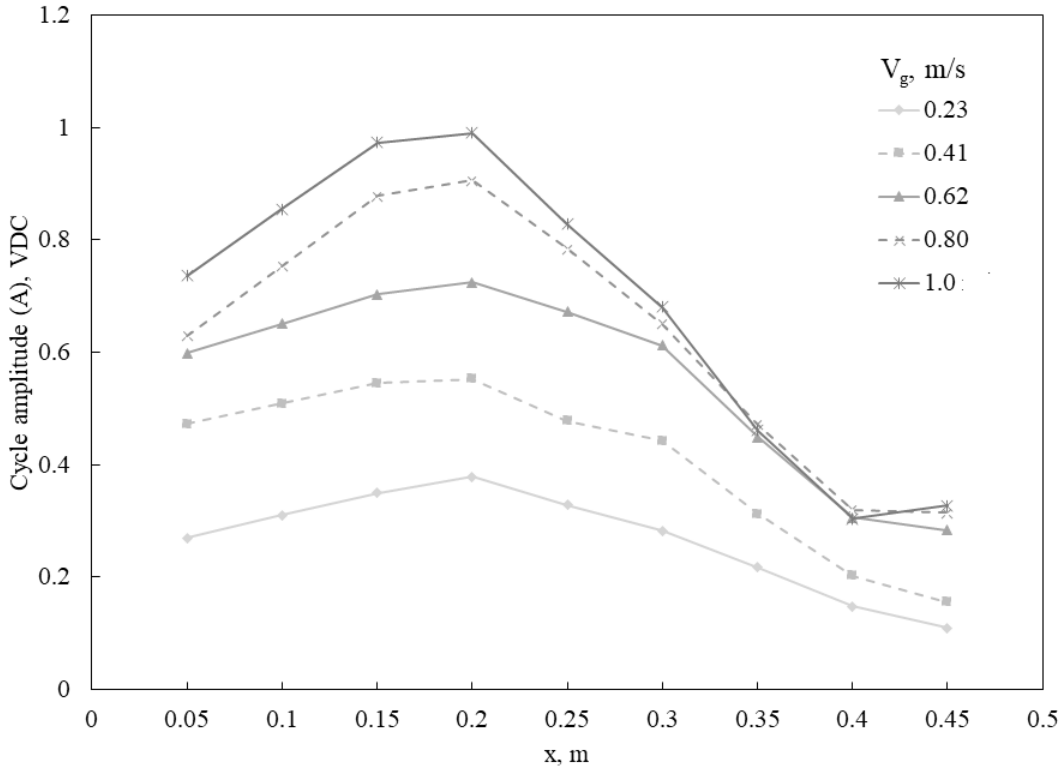

Figure 3.4 Impact of superficial gas velocity (V_g) on cycle amplitude (No baffle, inclined distributor, even case, $x = 0–0.5\ m$, z = 0.55 m)

The calibration was performed with 15 fluidization velocities (ranging from 0.18 to 1 m/s) and 3 gas distributor configurations (Figure 2.4), giving 45 conditions and a total of 2070 points when using the top 5 E-probes rows. In Figure 3.5A, the dimensionless gas flux (q_i) was calculated from cycle time and standard deviation with Eq.3-4, while in Figure 3.5B, it was calculated from only the cycle amplitude. It shows that using cycle amplitude gave a much better match of the cross-sectional average bubble gas flux (Eq. 3-2). In Figure 3.5B, $q_{bi} = \alpha \cdot A_i^{1.54}$. The coefficient α would be eliminated when

calculating the dimensionless gas flux defined with Eq. 3-1: $q_i = q_{bi}/\overline{q_b}$.

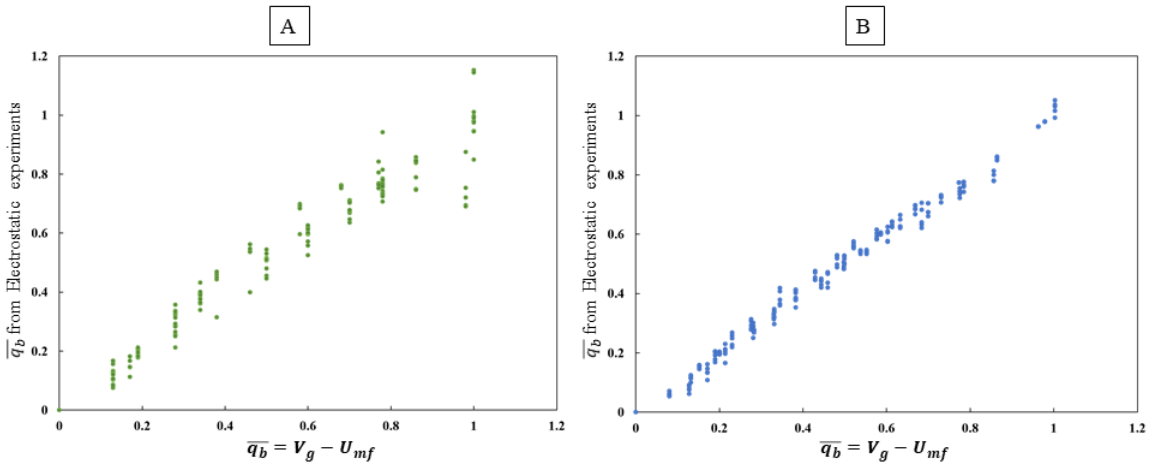

Figure 3.5 Calibration between the calculated average volumetric flux of gas bubbles ($\overline{q_b}$) with electrostatic probe signal and the empirical calculated average volumetric flux of the cross-sectional bed area ($\overline{q_b} = V_g - U_{mf}$): A. $\overline{q_b}$ calculated with cycle time and standard deviation; B. $\overline{q_b}$ calculated with cycle amplitude. (From first five rows, no baffle, inclined distributor with western, even, eastern cases, $V_g = 0 - 1\ m$, 11 velocities for each case)

Figure 3.6 shows a significant impact of the gas distributor configuration (Figure 2.4) on the lateral gas profile (for $z = 0.55\ m$). The reason why with the even case, the q_i was higher on the western side than that of the eastern side was explained earlier in this section. The next section used the radiation transmission method to confirm the results obtained with the E-probes.

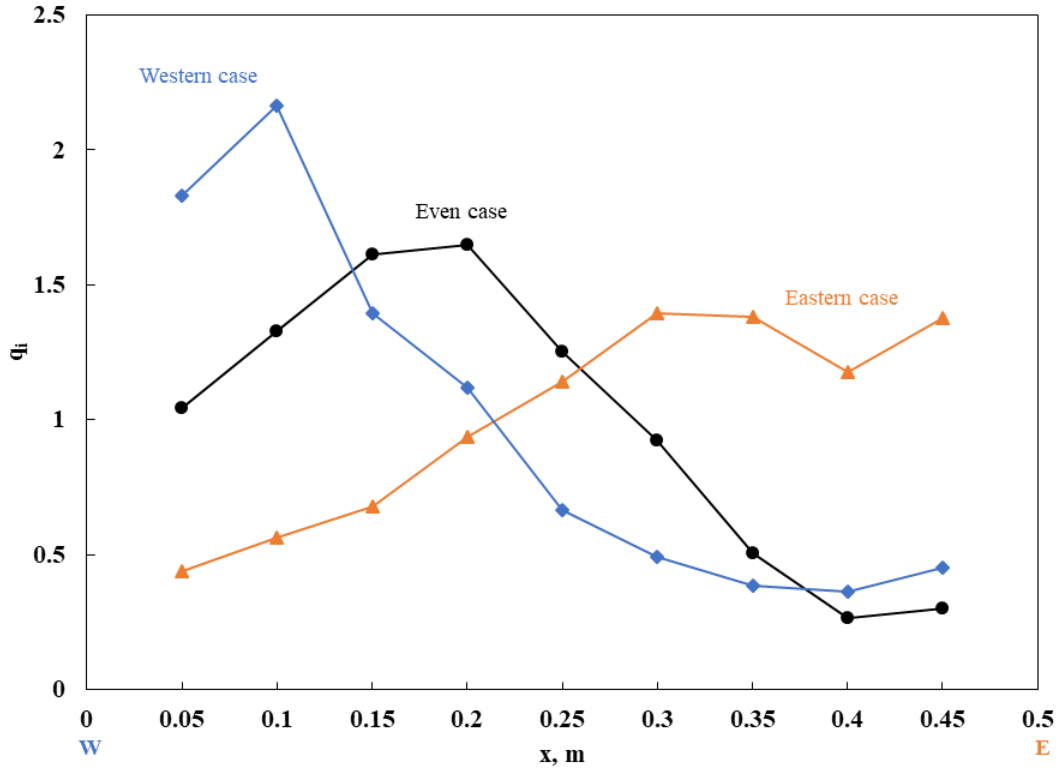

Figure 3.6 Impact of gas distributor configuration on lateral gas profile (No baffle, inclined distributor, $V_g = 1\ m/s, z = 0.55\ m$)

b. Radiation transmission method (validation method)

As shown in Figure 3.1 B, a thin scandium-46 radioactive particle (1 cm diameter) was placed outside the back wall of the bed. In contrast, a detector was set to receive the radiation signals on the outside of the opposite bed wall. Two preliminary measurements of the radioactive counts per second were performed: first with no solids in the bed (C_{empty}), and then with a bed filled with defluidized solids (C_{mf}).

When the bed was fluidized, and gas bubbles flowed between the radioactive source and the detector, the local bed voidage changed, changing the density of the material through which radiation was transmitted and changing the measured counts per second. Because the fluidized solids belong to Geldart's group B, the density of the emulsion phase did not

change with fluidization velocity. The local fraction of the bed volume that was occupied by bubbles (x_{bi}) could be obtained from:

$$x_{bi} = 1 - \frac{\ln(C) - \ln(C_{empty})}{\ln(C_{mf}) - \ln(C_{empty})} \quad 3\text{-}6$$

Three measuring locations were shown in Figure 3.1 B. The dimensionless gas bubble concentration x_i:

$$x_i = \frac{x_{bi}}{\overline{x_b}} \quad 3\text{-}7$$

Figure 3.7 compares the lateral gas bubble profile from the E-probe method and dimensionless gas bubble concentration from the radiation transmission method for 3 gas distributor configurations: western, even, and eastern cases(Figure 2.4). Both methods showed the same trends: the E-probe method showed the dimensionless bubble gas flux; the radiation transmission method gave the dimensionless gas bubble concentration. It meant that the bubble velocity did not change much with the lateral location.

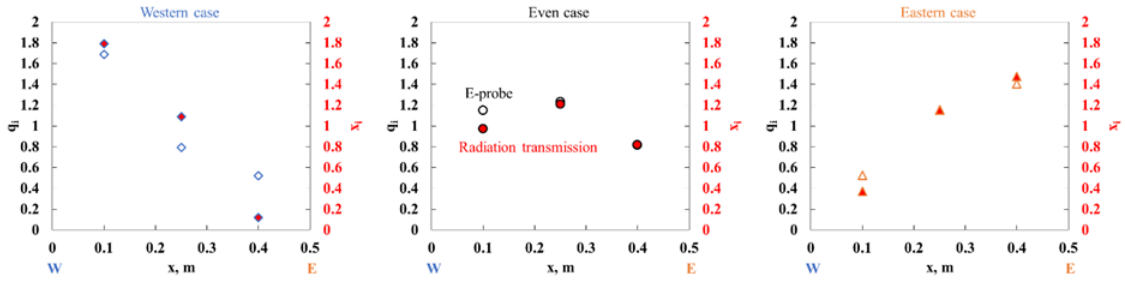

Figure 3.7 Comparison of dimensionless gas bubble flow profile from E-probe method ($z = 0.55\ m$) and normalized gas bubble concentration from radiation transmission method ($z = 0.5\ m$) (Western, even, eastern cases, no baffle, inclined distributor, $V_g = 1\ m/s, x = 0.1, 0.25, 0.4\ m$)

3.1.4 Example of results and reproducibility check

As shown in Figure 3.1, seven rows of E-probes were distributed evenly in the bed. One objective of this research is to study the impact of gas distribution on initial liquid

distribution quality. To map the gas flux information everywhere inside the bed, we applied an interpolation technique. Then we compared the initial results from the E-probes with interpolated results to ensure no over-interpolation was performed.

Figure 3.8 shows an example of a gas distribution map with (right) and without (left) interpolation with the western case, 0.2 m/s, without a baffle. To interpolate, first, the E-probe q_i results were obtained at each probe location, which gave a coordinate of (x, z, q_i) (Figure 3.8 (left)). Then a linear interpolation was applied to give an interpolated result with an interval of 1 cm for each vertical location. The new coordinate of (x, z, q_i) was then input into TableCurve 3D to create an interpolating equation of the form:

$$q_i = f(x, z) \qquad 3\text{-}8$$

Excel was then used to plot the new interpolated q_i results from this equation, with pre-set color scales with an interval of (0.0025,0.0025) (Figure 3.8 (right)). The R^2 of q_i between with (Figure 3.8 (right)) and without interpolation (Figure 3.8 (left)) cases was 0.982.

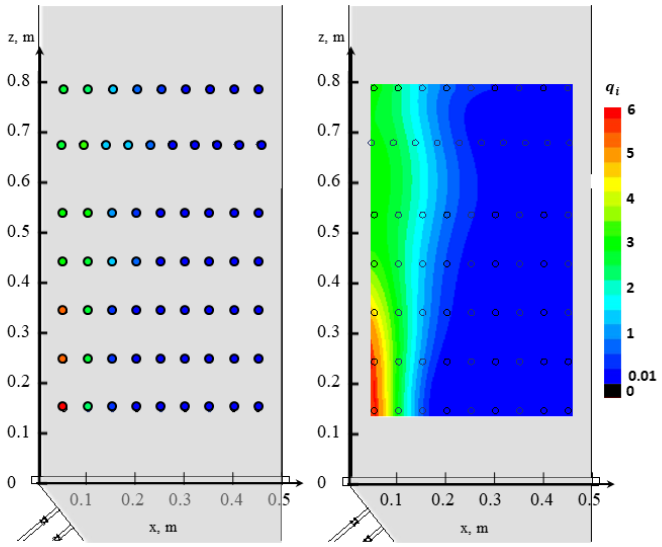

Figure 3.8 Raw E-probe q_i results without interpolation (left) vs. interpolated results from TableCurve 3D (right) (No baffle, inclined distributor, western case, $V_g = 0.2\ m/s$)

Figure 3.9 shows three replicates of three cases with and without a baffle at the spray level. It shows that the reproducibility was good with the E-probe method. Table 3-1 shows the good reproducibility also applied to other locations and other cases with and without a baffle.

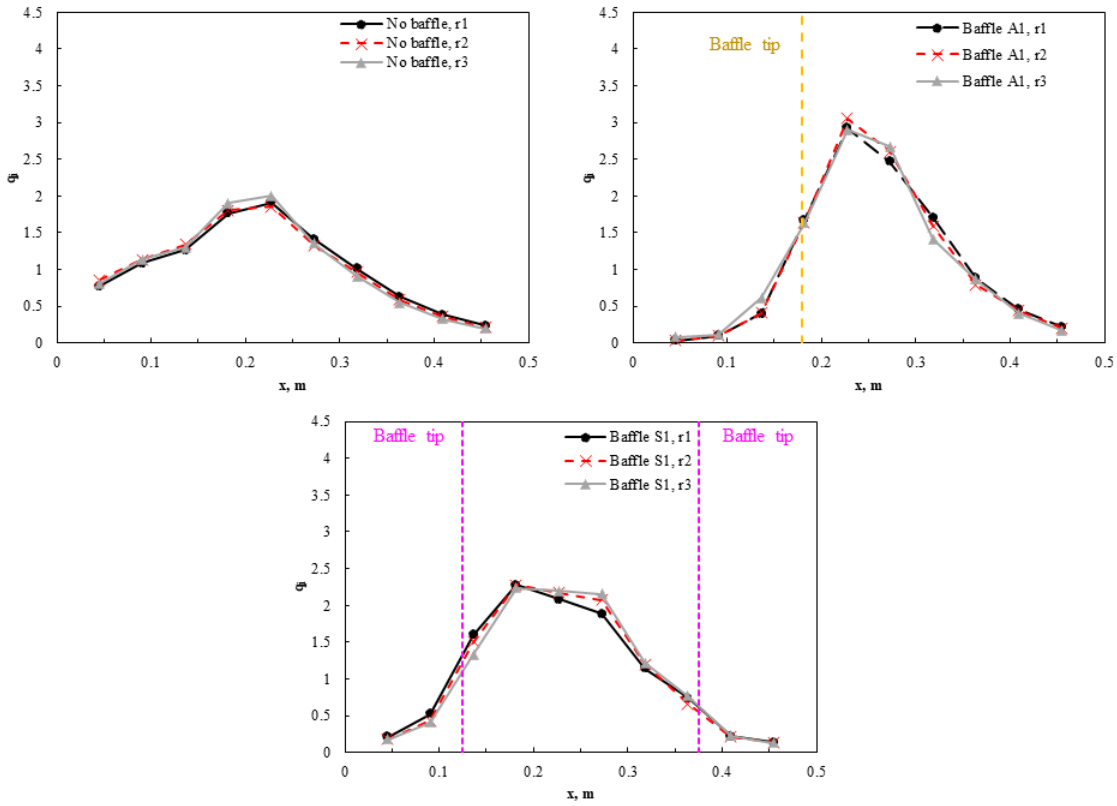

Figure 3.9 Gas distribution replicates with and without baffle at spray level (No baffle, inclined distributor, even case, $x = 0\text{–}0.5\ m$, $z = 0.67\ m$)

Conditions	$\frac{\sum_{i=1}^{64} \sigma_{Replicates,i}}{64}$ *
No baffle, inclined distributor, western case, 1 m/s	0.028
No baffle, inclined distributor, even case, 1 m/s	0.043
No baffle, inclined distributor, eastern case, 1 m/s	0.048
Baffle A1, inclined distributor, even case, 1 m/s	0.045
Baffle S1, inclined distributor, even case, 1 m/s	0.043

* The standard deviation of the dimensionless q_i of 3 replicates for probe i: $\sigma_{Replicates,i}$
Average of $\sigma_{Replicates}$ of all probes in the bed: $\frac{\sum_{i=1}^{64} \sigma_{Replicates,i}}{64}$

Table 3-1 Reproducibility of the gas distribution

3.2 Jet penetration measurements

3.2.1 Introduction

The spray jet penetration in a fluidized bed was essential information for this thesis research. From the point of view of a commercial coker, spray nozzles are horizontal to maximize the horizontal penetration of the spray jets, which is about 2 m [14]. Interactions between the jets issuing from different nozzles should generally be avoided [15]. It is important to minimize the risk of wet agglomerates interact with another feed jet and being rewetted. Experiments showed that the rewetted agglomerates were stronger and more difficult to broke-up [16].

Past studies have used various methods to measure the jet penetration in a fluid bed. Bruhns et al. [17] installed thermocouples near the spray region to obtain the jet penetration. They kept the bed temperature at 150 °C, then injected water slowly for 5 to 10 min. The temperature near the spray jet was about 20 °C and increased quickly as the distance from the thermocouple location to the spray jet increased. The jet penetration was from the nozzle tip to where the bed temperature was at the boiling point of water. The jet penetration from temperature measurement was validated by Ariyapadi et al.[18] with X-ray experiments. Furthermore, they developed a model to estimate the jet penetration, which was validated by thermocouple and X-ray experimental methods. In large-scale units, the jets were more powerful. Sanchez Careaga et al. [14] introduced bendable tubes into the bed along the penetration direction of the spray jet. They found

that the jet penetration was from the nozzle tip to the last bent rod. The results were validated with the model from Ariyapadi et al.[18].

The drawback of the thermocouple method for jet penetration measurement was that it could over-estimate jet penetration. It could detect the very cold solids propelled by the jet past its tip during the expansion part of its expansion-contraction cycle. Therefore, E-probes were used to detect jet penetration, and the thermocouple method was used as a validation method. Compared to thermocouples, another advantage of the E-probe measurement was that it did not require pre-heating of the bed. Compared to bendable tubes, they could be used unlimited times. Moreover, E-probes were cheap and could be applied for other measurements, such as gas bubble distribution (section 3.1) and bubble spanning check (section 3.3).

3.2.2 The experimental set-up, material, and standard procedure

Figure 3.10A shows how the electrostatic probes at the spray level were utilized to detect the penetration of the gas-liquid spray jet at 30 °C. If the liquid hit an electrostatic probe during injection, the average frequency of its electrostatic current decreased sharply, as the water eliminated the electric charge.

Another method (Figure 3.10B) used a thermocouple located at the wall opposite the spray nozzle [26, 27]; its penetration into the bed was only 1 cm, so the rising gas bubbles did not bend it. The bed temperature was raised above 100 °C. The movable spray nozzle was gradually moved towards the thermocouple in different runs until the cold injected liquid hit the thermocouple.

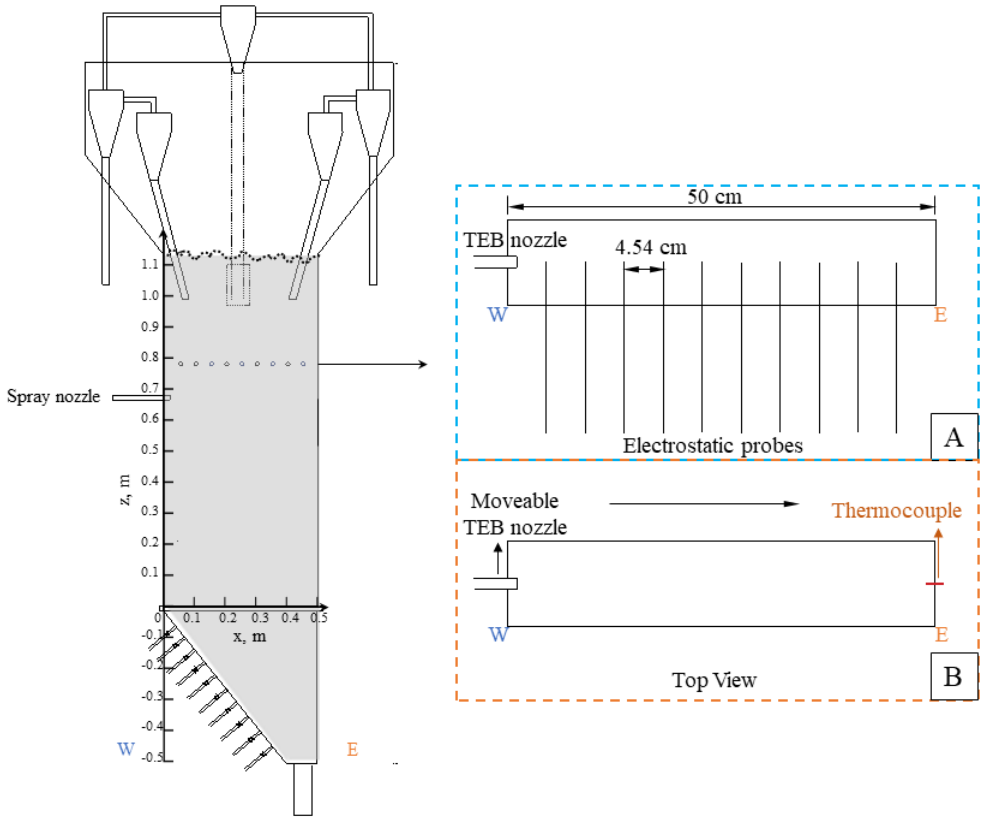

Figure 3.10 Schematic diagram A. Location of electrostatic probe method for gas-liquid spray jet penetration measurement, B. Location of thermocouple method for gas-liquid spray jet penetration measurement. ($z = 0.67\ m$)

The standard procedures were:

1) The bed was fluidized for 1 min before injection.

2) The liquid was injected into the bed.

3) The bed was continuously fluidized for 10 min to dry the bed. (The drying time required was validated with conductance probes: section 3.5)

3.2.3 Example of results

Figure 3.11A shows that the raw signal from the electrostatic probe that was 13.7 cm away from the western side bed wall changed before and after the liquid injection: the

liquid injection started at 0 s and ended at 11.4 s. The raw current from the probe increased slightly and then dropped sharply as the spray liquid and high-velocity wet particles hit it, as the water eliminated the electric charge.

The fluctuations of the electrostatic current were characterized by their average frequency, obtained from a power spectrum analysis. Figure 3.11B shows the average frequency from 10 probes at the spray level before and after the injection began. When the liquid from the spray jet hit a probe, the average frequency dropped sharply. There was a negligible difference between average frequencies before and after injection for the probes far from the nozzle tip, where the jet did not reach. There was a large difference between the frequencies before and after injection for probes within the jet cavity. The impact of the spray jet disappeared at 23 cm from the nozzle tip, which corresponds to the jet length. The thermocouple method provided a similar jet length. Figure 3.11C shows how the temperature was affected by the distance from the spray nozzle tip when cold liquid was injected into the hot bed. When the thermocouple was far from the jet, there was a slight temperature drop due to the cooling effect of the liquid on the bed particles. When the jet reached the thermocouple, there was a sharp, much larger temperature drop. Figure 3.11D shows the temperature drop as a function of the distance between spray nozzle tip and thermocouple: it indicated a jet length of about 26 cm. The thermocouple method provided a slightly larger jet length than the electrostatic-probe method. The thermocouple could detect the very cold solids propelled by the jet past its tip during the expansion part of its expansion-contraction cycle.

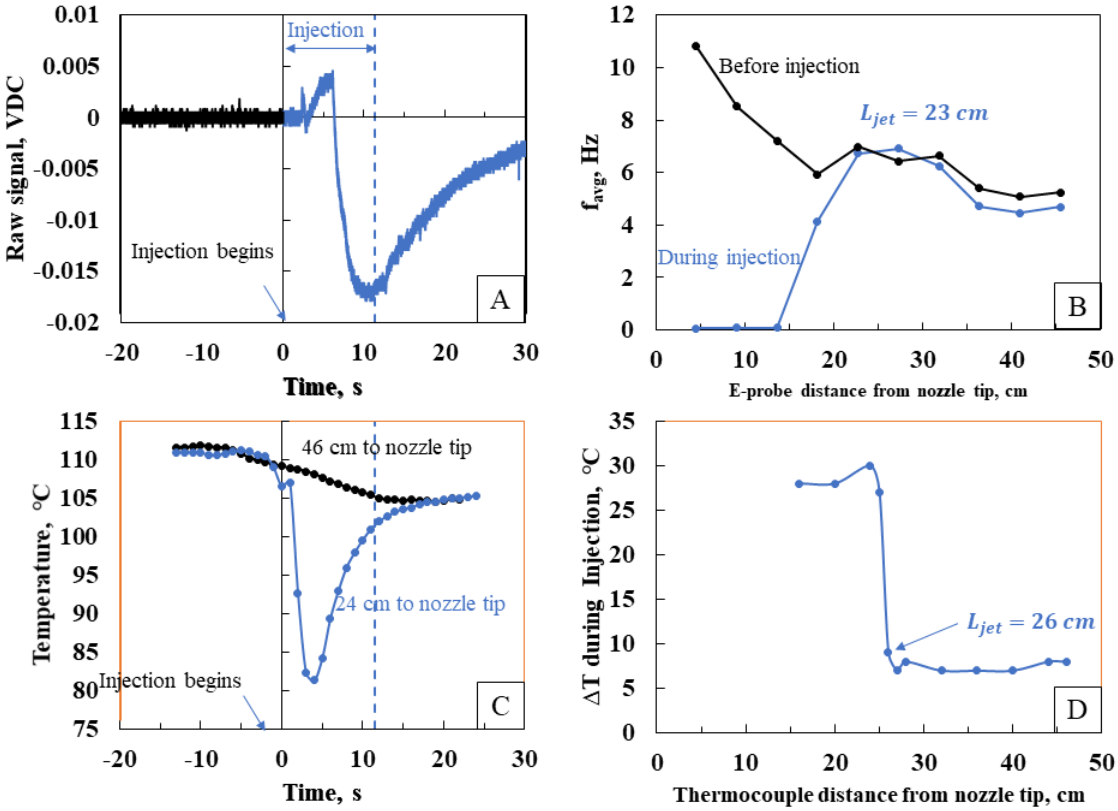

Figure 3.11 A. Raw signal from the electrostatic signal before and after injection at 13.7 cm from nozzle tip (30 °C), B. Comparison of average frequency from the electrostatic signal before and after injection (30 °C), C. Raw signals from thermocouple when nozzle tip at 24 cm and 46 cm, D. Temperature drop while moving the spray nozzle towards the thermocouple. (Inclined distributor, No baffle, even case, $V_g = 1\ m/s$, $x_{inj} = 0.01$, $z_{inj} = 0.67\ m$)

3.3 Check for bubble spanning between front and back bed wall

3.3.1 Introduction

Smaller gas bubbles are usually desired in a fluid bed, as the surface area enhances mass transfer in the bed. One of the most attractive features of operating in the turbulent regime is the enhanced interphase mass transfer [19]. In the turbulent regime, the gas flows as small, elongated voids that constantly appear and disappear. From experiments shown in section 3.8, the turbulent transition velocities in this study were usually between

0.3 to 0.5 m/s. Theoretically, there should not be gas bubbles spanning between the bed walls. This section is to validate this hypothesis with experiments.

There were some other methods to detect gas bubbles spanning or slugging in a fluidized bed, such as visualization [27, 28] or the impact of slugging on axial solids mixing [20, 21]. The visualization method required a clear fluid bed. The use of slugging on axial solids mixing required heating [21] or tracers [20]. Compared to these methods, theoretically, the E-probes could be applied to most fluid beds, and they do not need heating or tracers. Moreover, they could measure other features in the bed, such as gas distribution and gas-liquid spray penetration.

The improvements to the E-probe measurement were that the cross-correlation coefficient was applied to show if two probes with different insertion distances measured the same bubbles. From the point of view of the procedure, a specially designed arrangement of E-probes was created for this objective (Figure 3.12).

3.3.2 The experimental set-up, material, and standard procedure

As shown in Figure 3.12, two sets of E-probes were inserted from the front and back bed wall with different distances: the near configuration and the far configuration. The insertion distance of the E-probes for the near configuration was 0.63 cm, while it was 9 cm for the far configuration. The cross-correlation coefficient was calculated for each couple of E-probes from the front and back bed wall. If gas bubbles spanned the gap between the walls (10 cm), the two signals with probes in the far configuration would be as well correlated as the probes in the near configuration.

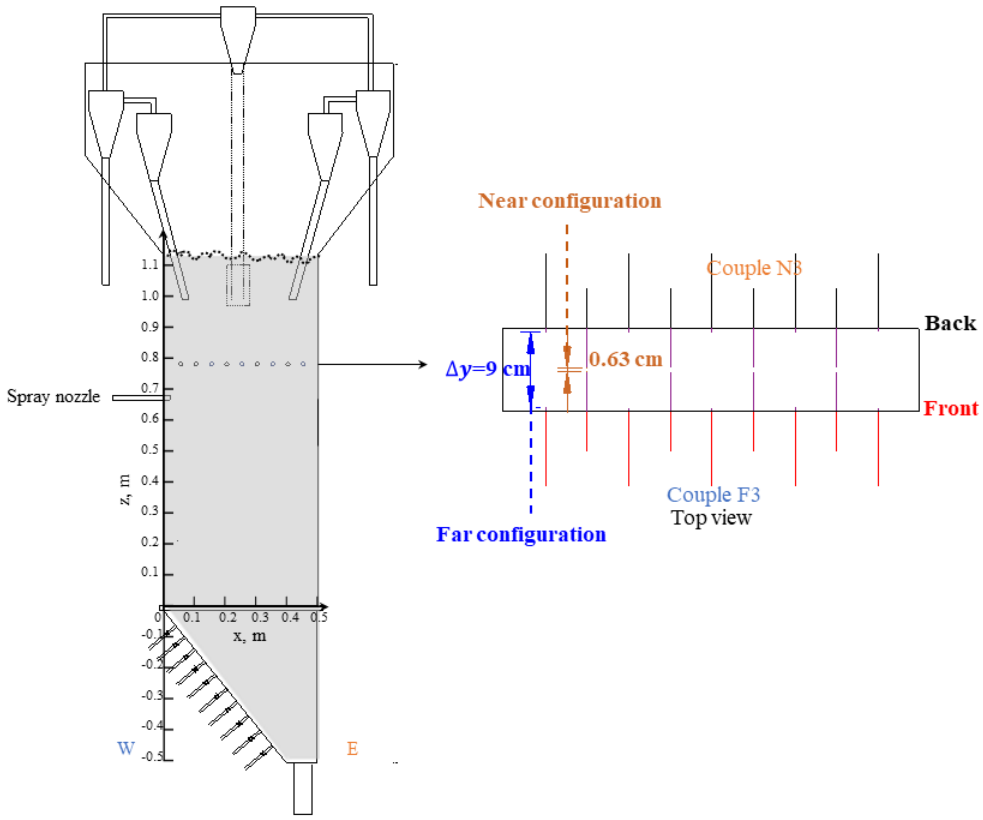

Figure 3.12 Schematic diagram of location of E-probes for detection of bubble spanning between front and back bed wall

The standard procedures were the same as stated in section 3.1.

3.3.3 Data processing

Figure 3.13 shows the cross-correlation coefficient of the two examples shown in Figure 3.12. It indicated that there was no time delay between front and back bed wall E-probes. The near configuration (couple N3) showed a higher maximum cross-correlation coefficient than the far configuration (couple F3). It was expected because the two probes in the near configuration detected the same gas bubbles. If the far configurations were detecting the same bubbles, this would mean that the gas bubbles span the distance between the front and back bed walls. Because the maximum cross-correlation of the far configuration was much lower than that of the near configuration, the far configuration was not detecting the same gas bubbles.

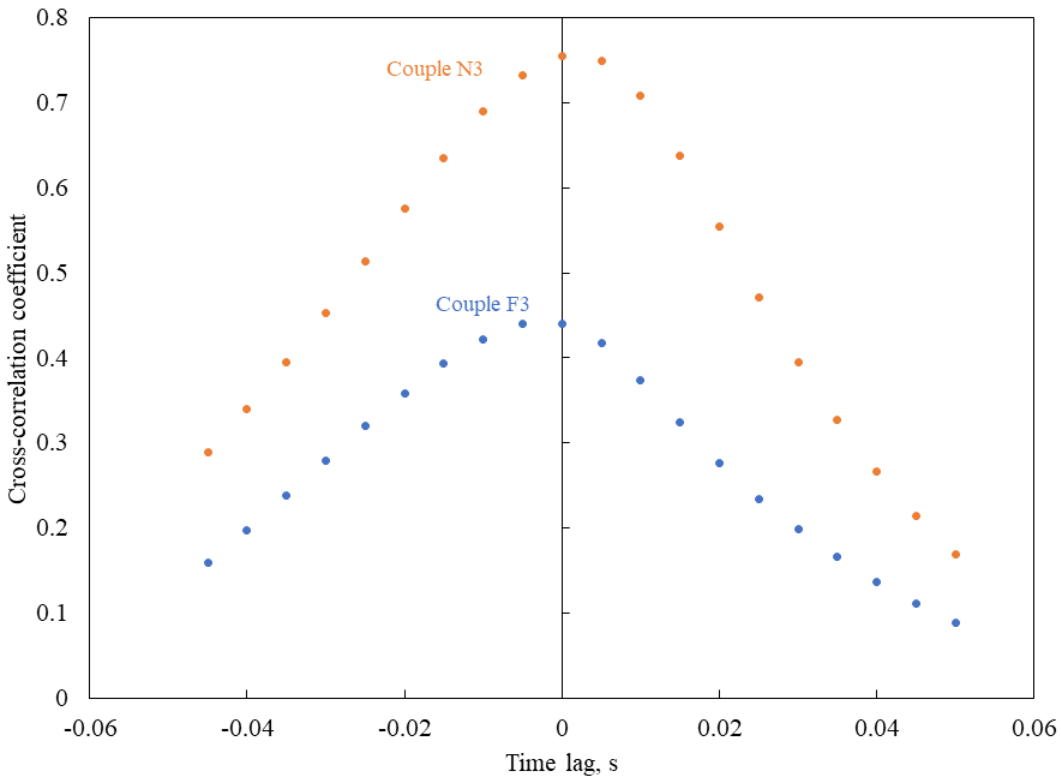

Figure 3.13 Examples of cross-correlation coefficient vs. time lag at different measuring locations (couple N3 and couple F3 are shown in Figure 3.12, $V_g = 1.56\ m/s$).

3.3.4 Example of results

The maximum cross-correlation coefficient was calculated for all configurations shown in Figure 3.12 at superficial gas velocities from 0.48 to 1.56 m/s. All 20 valves of the tuyeres in the gas distributor were open to provide the higher superficial gas velocity. In this research, the fluidized bed was normally operated below 1 m/s. Fluidization velocities up to 1.56 m/s were tested in this case, which was to ensure that the bubbles were not spanning the bed, even at very high fluidization velocities.

Figure 3.14 shows that with the experimental set-up shown in Figure 3.12, probes in the near configuration consistently gave much higher cross-correlation coefficients than probes in the far configuration, for all the gas velocities from 0.48 to 1.56 m/s. This meant that most bubbles did not span between the bed walls. Figure 3.14 also shows the

impact of increasing superficial gas velocity on the cross-correlation coefficients of near and far configurations.

With the near configuration, at lower superficial gas velocities, the cross-correlation coefficients were lower. This could be because the cross-correlation coefficients were obtained as a time-averaged value from three-minute runs. The lower maximum cross-correlation meant there might be fewer gas bubbles to give a very good correlation as the high gas velocities. Another possible reason was that the probability of several small bubbles coalescing to form a large bubble spanning the whole space between the back and front walls is more likely when there is more gas flowing through the column.

With the far configurations, the cross-correlation coefficients from lower and higher superficial gas velocities were mixed together. This was expected, because at either low or high superficial gas velocities, the probes from the far configurations did not measure the same bubbles.

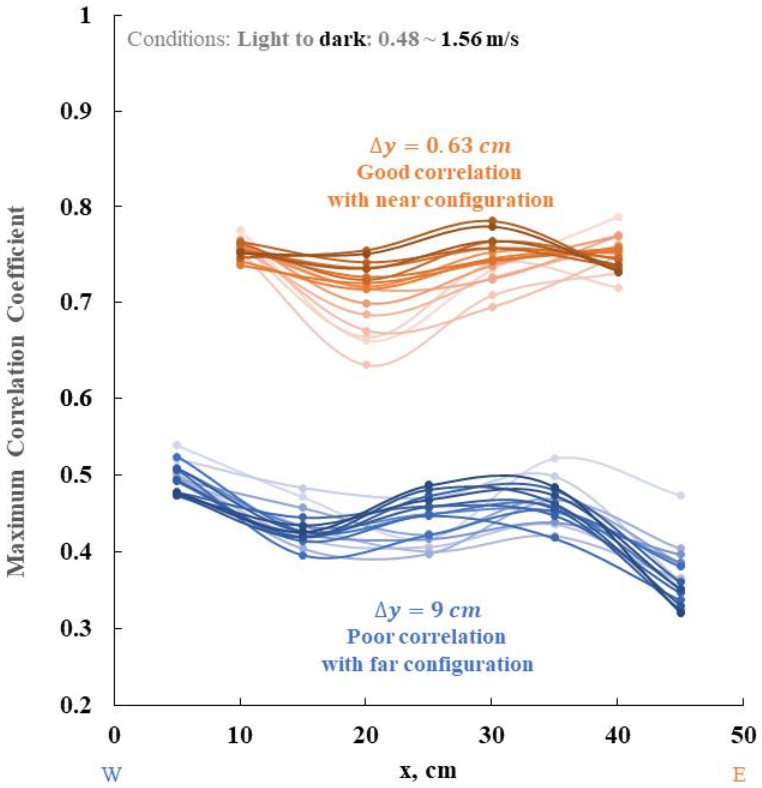

Figure 3.14 Bubble spanning check with maximum cross-correlation coefficient comparison (No baffle, inclined distributor, all twenty nozzles are open to provide high superficial gas velocity)

3.4 Liquid distribution quality

To reduce agglomerates formation during injection, we needed to develop tools to evaluate liquid distribution quality. In this research, the standard Gum Arabic method was used to create real agglomerates that can be retrieved from the bed mass and analyzed, as shown in section 1.3.1 of Chapter 1. We also developed two quick estimation methods to provide an initial selection of interesting conditions that can then be studied with the Gum Arabic method and provide information of agglomerates properties.

3.4.1 Introduction

The Gum Arabic method has been applied widely in many publications, as introduced in section 1.3.1. It provided information about actual agglomerates, such as agglomerate size distribution, liquid to solids ratio in agglomerates, and water trapped/ water injected in agglomerates. However, the Gum Arabic method was very time-consuming. It took about 2 days for each run, including the run itself, sieving the whole bed, and agglomerates analysis.

In this research, one objective is to study the impact of gas distribution on liquid distribution. This meant that the liquid distribution quality needed to be evaluated at as many different gas distributions as possible. Therefore, quick estimation methods were built to give the most general information from the Gum Arabic method: water trapped/ water injected.

Two quick estimation methods were developed:

- Freeboard pressure with water injection at 115 °C

  When injected liquid vaporizes, it created additional gas moles inside the bed, which increased the freeboard pressure. This method was originally developed by Silitonga et al.[22] to evaluate the vaporization rate. The bed temperature was set at 115 °C to instantaneously evaporate water coming in when directly contacted with hot bed particles. As liquid was injected into a fluidized bed, it built up until steady-state is achieved, with the evaporation rate equal to the injection flowrate. The vapor flowrate increased the cyclone pressure drop and, hence, the freeboard pressure. When the liquid injection was stopped, the freeboard pressure gradually decreased until all the accumulated liquid has been vaporized. If more liquid was trapped in agglomerates, more liquid accumulated in the bed at a steady state. We found a good correlation between freeboard pressure measurements and water trapped/ water injected from the Gum Arabic method.

- E-probe with water injection at 30 °C

This method was even more time-saving because it did not require pre-heating the bed to 115 °C, as with the freeboard pressure estimation method, at a bed temperature of 30 ºC, the free liquid that came out of wet agglomerates built up in the bed and then vaporized slowly. Because of the low bed temperature, there was a significant concentration of free moisture, i.e., water on the surface of non-agglomerated individual bed particles. The signal of the E-probes provided information on the local free moisture at different locations in the bed. The first five rows of E-probes were installed to cover above and below the spray region. Information was extracted from the E-probe signals to correlate with water trapped/ water injected from the Gum Arabic method. Another reason why we have two quick estimation methods was to use them to validate each other.

Runs with a quick estimation method were typically repeated three times to check for possible variability of the results. Good agreement was found between the results obtained with the three methods. The reproducibility of each method was given, respectively, in the examples provided below.

3.4.2 Equipment, material, standard procedure, and data processing

a. Gum Arabic method

The Gum Arabic method was a well-established method and validated with actual bitumen coking experiments [16]. The Gum Arabic solution consisted of 92 wt % water, 6 wt % Gum Arabic, and 2 wt % blue dye. The pH was adjusted to 3 to match the viscosity of bitumen in a coker. In this research, 200 g of Gum Arabic solution was consistently injected into the bed to avoid bogging [23].

The standard procedures used for the Gum Arabic method were shown in Figure 3.15:

1) The bed was pre-heated to 130 °C

2) The fluid bed was fluidized for 1 min before injection.

3) The injection of Gum Arabic solution was complete in 11.4 s (Figure 3.16)

4) The solenoid valve was closed 15 s after the start of the injection (Figure 3.16)

5) The bed was fluidized with a gas velocity below the minimum fluidization velocity (U_{mf}) for 10 min to avoid hot spots created in the bed.

6) The fluid bed was shut down and left for cooling overnight.

Sieving and agglomerates analysis:

1) The next day, the whole bed was sieved, and the agglomerates were retrieved in 9 size cuts (Figure 3.15) (details of the sieving procedure are given elsewhere [1, 2])

2) The agglomerates for each size cut were dissolved with DI water.

3) The dye concentration in the solution was measured with a UV-spectrum meter.

4) The mass of micro-agglomerates was corrected for the fines in the bed. (details of correction are given elsewhere [1, 2])

5) The agglomerates properties for each size-cut, such as the mass of agglomerate, liquid to solids ratio, initial liquid trapped, was measured using a mass balance, as the components of the Gum Arabic solution were given. (details of calculations are given elsewhere [1, 2])

6) The total initial water trapped/ water injected in agglomerates from the Gum Arabic solution was used as summary information of the agglomerates. It was used to build a correlation with the two quick estimation methods, respectively.

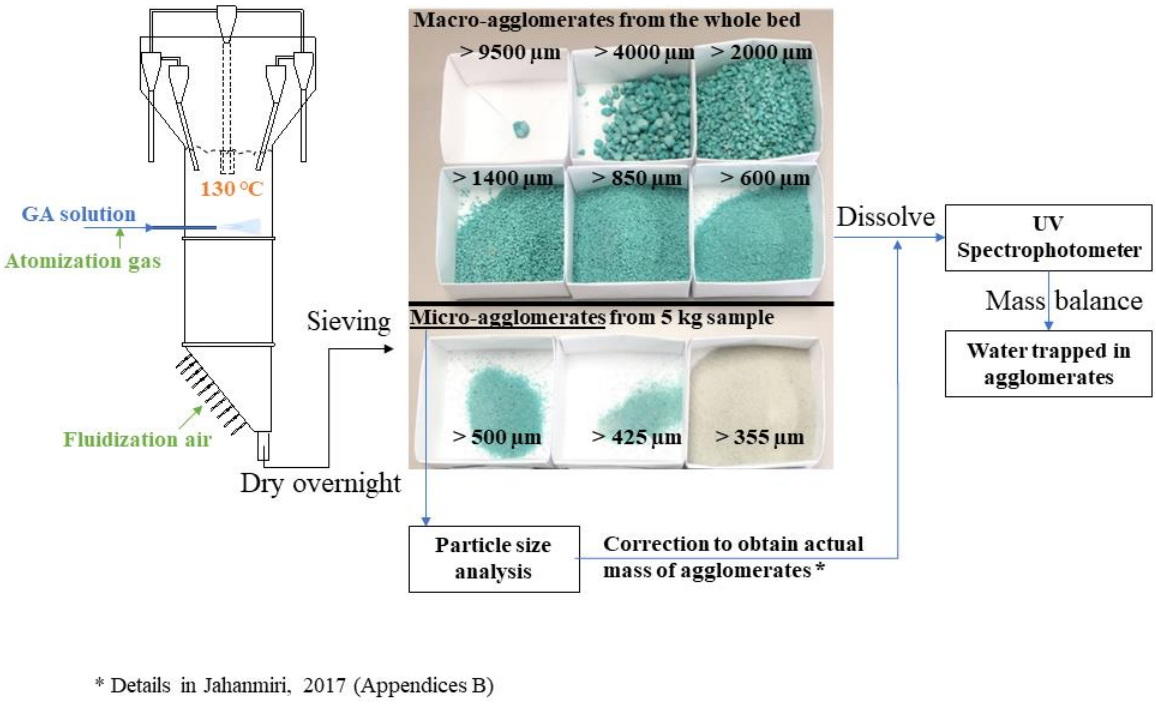

Figure 3.15 Process of Gum Arabic method procedure

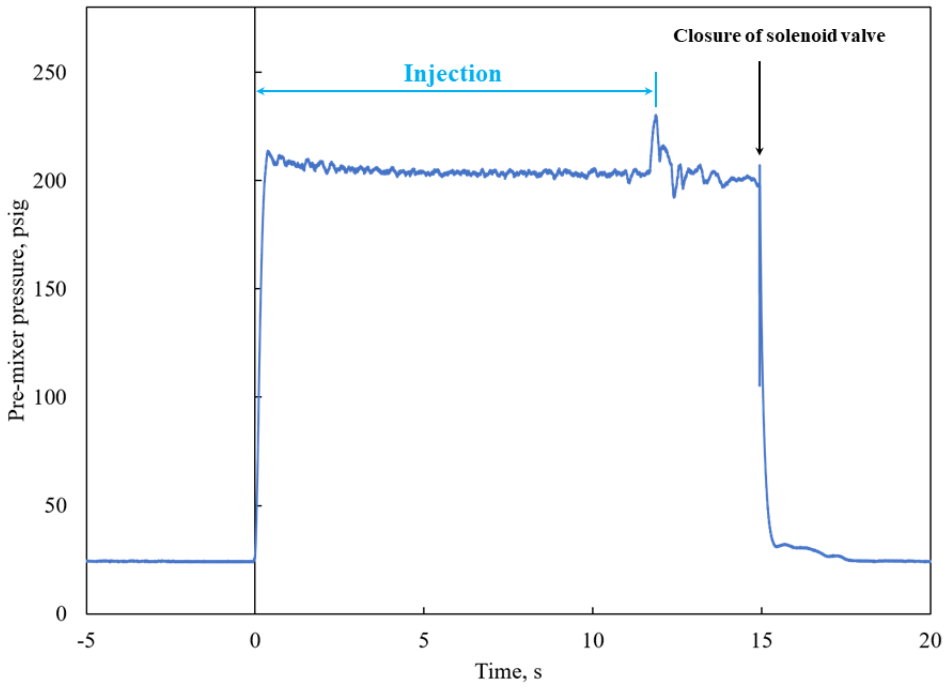

Figure 3.16 A typical example of pre-mixer pressure of a run with Gum Arabic

b. Freeboard pressure estimation method

The experimental setup was given in section 2.1. The standard procedures of the freeboard pressure estimation method were:

1) The bed was pre-heated to 115 °C
2) The fluid bed was fluidized for 1 min before injection.
3) The injection of water was complete in 11.4 s.
4) The solenoid valve was closed at 15 s
5) The bed was continuously fluidized for 10 min to dry the bed. (The drying time required was validated with conductance probes: section 3.5)

Figure 3.17 shows an example of data processing to prepare freeboard information to be correlated with initial water trapped/ water injected obtained with the Gum Arabic method. First, the excess value of freeboard pressure due to injection was obtained by eliminating the background freeboard pressure from the fluidization gas. Then the cumulative pressure at the end of injection was applied to build a correlation with initial liquid water trapped in agglomerates from the Gum Arabic method. Figure 3.17 shows that a significant fraction of the injected water had accumulated in the bed and vaporized after the end of the liquid injection.

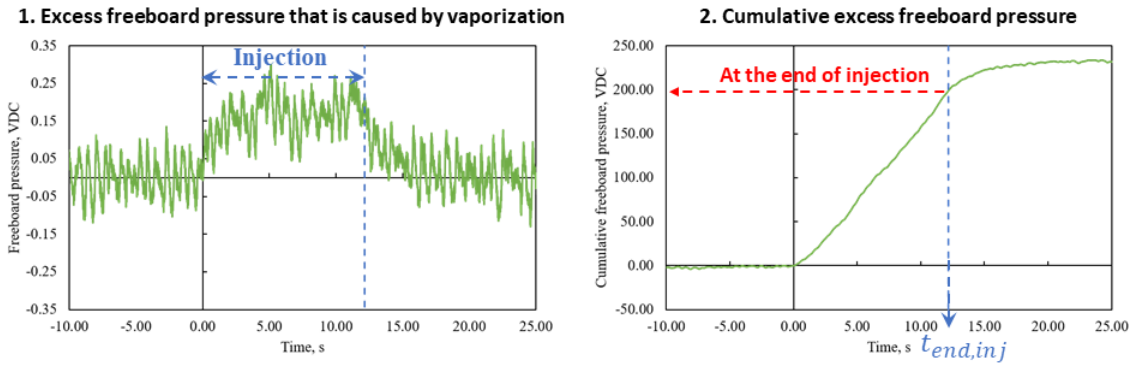

Figure 3.17 Example of using cumulative freeboard pressure at the end of injection to predict free moisture fraction (No baffle, even case, $T_{bed} = 115\ °C$, $V_g = 1\ m/s$,

1 mm TEB nozzle, $x_{inj} = 0.18\ m$, $z_{inj} = 0.67\ m$, $L_{jet} = 0.23\ m$, $m_{inj} = 200\ g$, $F_L = 17.5\ g/s$)

c. E-probe estimation method

A second quick estimation method was developed because the freeboard pressure measurement required high temperature, while the E-probe measurement could be implemented at room temperature. The two estimation methods could be used to validate each other. Figure 3.18 shows the top five rows of E-probes that were used to build a correlation with the initial water trapped fraction in agglomerates.

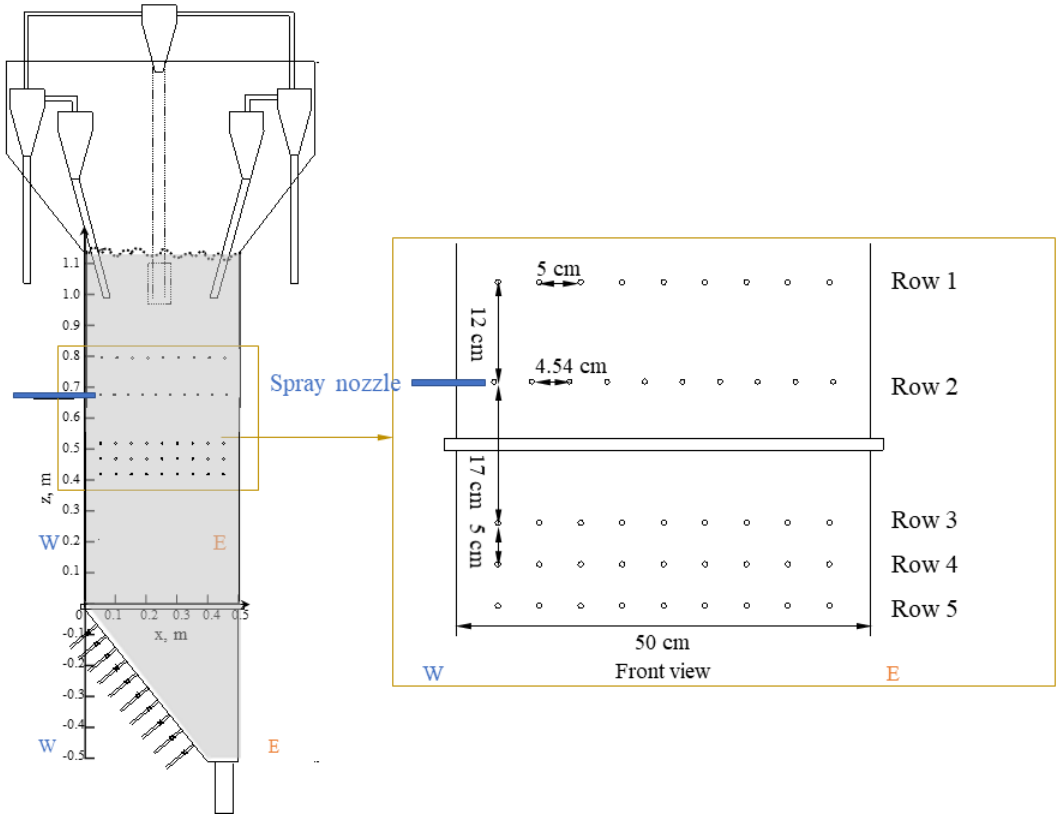

Figure 3.18 Measuring locations of E-probes for the quick estimation method to obtain initial water trapped/ water injected.

The standard procedures of the E-probe estimation method were:

1) The bed was pre-heated to 30 °C.

2) The fluid bed was fluidized at 1 m/s for 1 min before injection.

3) The injection of water was complete in 11.4 s.

4) The solenoid valve was closed at 15 s.

5) The bed was slumped for 30 s.

6) The bed was continuously fluidized for 10 min to dry the bed. (The drying time required was validated with conductance probes: section 3.5)

Figure 3.19 shows an example of data processing of the E-probe signal with liquid injection. This process was done to each probe shown in Figure 3.18. The average of each row from step 3 was obtained. Multilinear regression was applied to select the most interesting parameters (Eq.3-10) from E-probes correlated with initial water trapped fraction in agglomerates.

$$y(t) = \frac{\int_0^t |V| dt}{\int_0^{400} |V| dt} \qquad 3\text{-}9$$

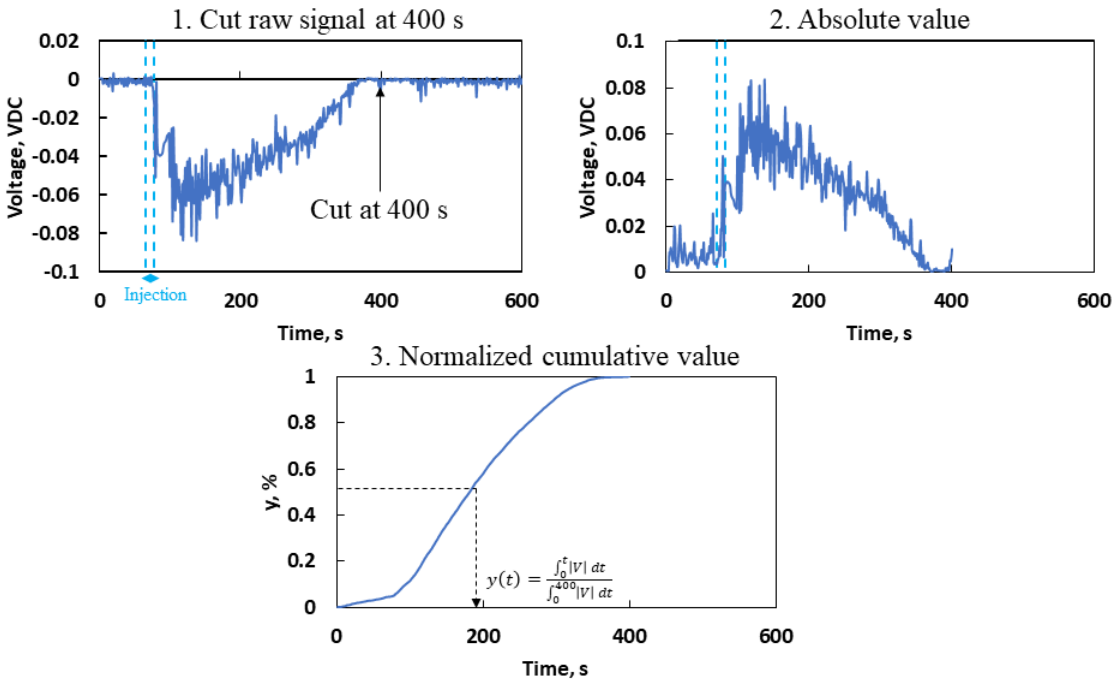

Figure 3.19 Data processing steps: use cumulative E-probe signal to predict free moisture fraction (1 m/s)

3.4.3 Example of results and reproducibility check

a. Gum Arabic method

Figure 3.20 shows the impact of superficial gas velocity during injection on the summary information about agglomerates: the total initial water trapped/ water injected in agglomerates. With the increase of the superficial gas velocity, the initial liquid trapped fraction in agglomerates dropped, which was also found by Li et al.[2]. It was also shown that the impact of superficial gas velocity on initial liquid distribution is non-linear and related to the regime transition from bubbling to turbulent (more details in section 5.1).

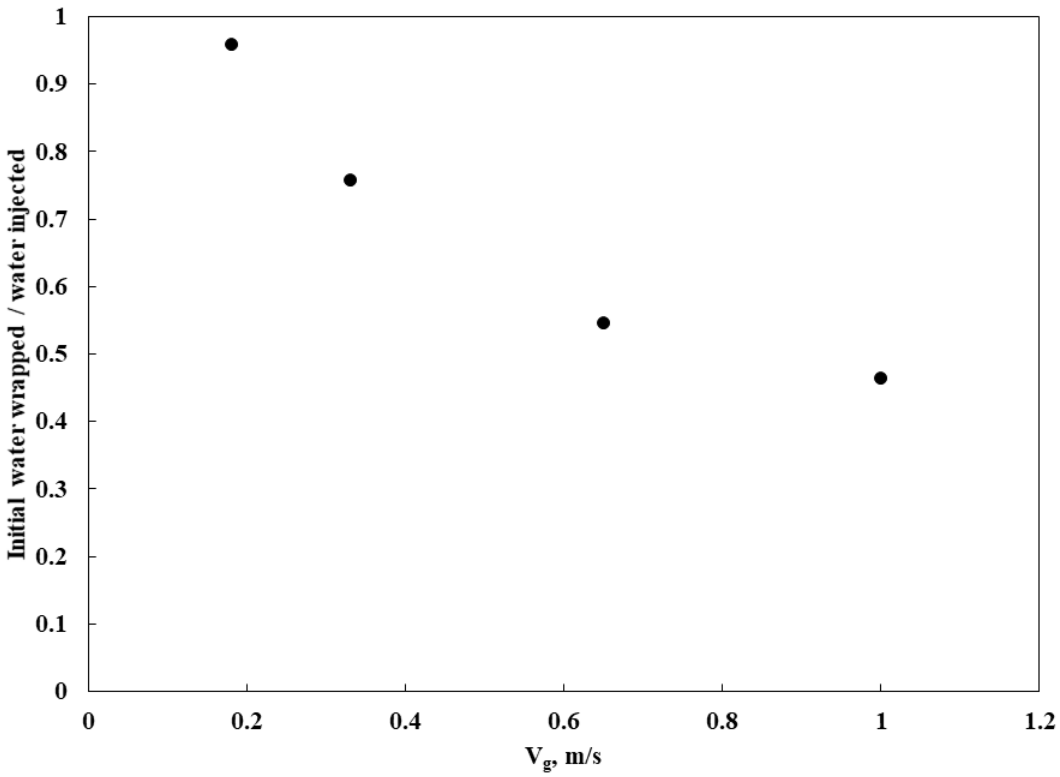

Figure 3.20 Effect of superficial gas velocity during injection (V_{gi}) on initial trapped liquid fraction, using the gum Arabic method. (Inclined distributor, even case, no baffle, $T_{initial} = 130\ °C$, $x_{inj} = 0.18\ m$, $z_{inj} = 0.67\ m$, $L_{inj} = 0.23\ m$, $F_L = 17.33\ g/s$, $m_{inj} = 200\ g$, $GLR = 2\ \%$, $V_{gd} < U_{mf}$, $t_{drying} = 10\ min$)

Figure 3.21 shows the cumulative fraction of water trapped in agglomerates in each size cut. These experiments showed that the method could detect expected changes in agglomerate production with increased fluidization velocity.

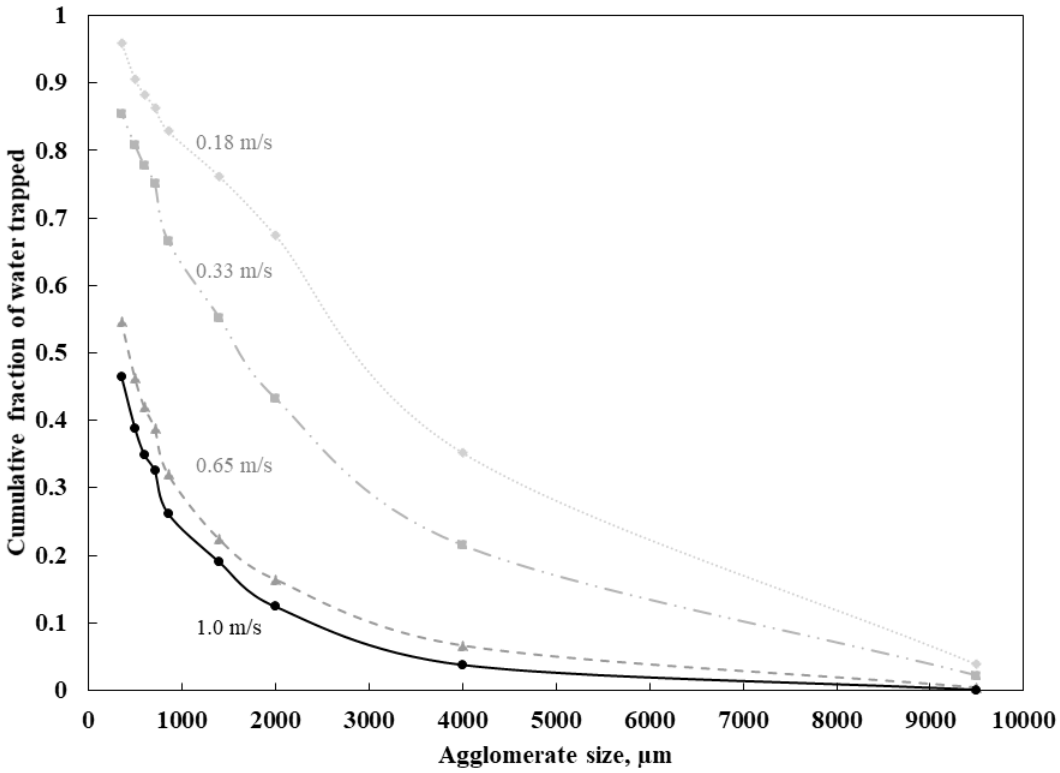

Figure 3.21 Cumulative fraction of water trapped in agglomerates for various superficial gas velocities during injection (V_{gi}) (Inclined distributor, even case, no baffle, $T_{initial} = 130\ °C$, $x_{inj} = 0.18\ m$, $z_{inj} = 0.67\ m$, $L_{inj} = 0.23\ m$, $F_L = 17.33\ g/s$, $m_{inj} = 200\ g$, $GLR = 2$ %, superficial gas velocity during drying: $V_{gd} < U_{mf}$, $t_{drying} = 10\ min$)

Figure 3.22 shows the cumulative mass of agglomerates in bed mass decreased with the increase of superficial gas velocity. The reduction was expected because with higher

superficial gas velocities, better jet-bed interaction was expected. Thus, fewer agglomerates were formed during the injection.

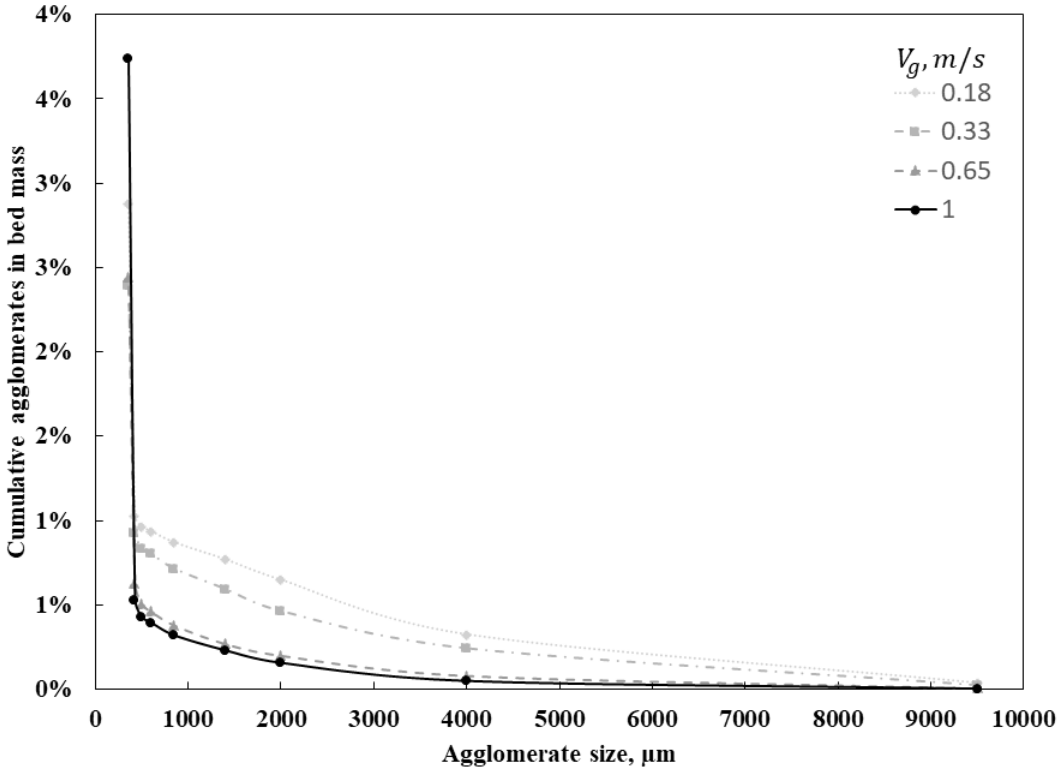

Figure 3.22 Cumulative fraction of water trapped in agglomerates for various superficial gas velocities during injection (V_{gi}) (Inclined distributor, even case, no baffle, $T_{initial} = 130\,°C$, $x_{inj} = 0.18\,m$, $z_{inj} = 0.67\,m$, $L_{inj} = 0.23\,m$, $F_L = 17.33\,g/s$, $m_{inj} = 200\,g$, $GLR = 2$ %, superficial gas velocity during drying: $V_{gd} < U_{mf}$, $t_{drying} = 10\,min$)

Figure 3.23 shows the agglomerates were generally drier (lower liquid to solid ratio (L/S)) with higher superficial gas velocity, agreed with results from Li et al. [2]. The

higher superficial gas velocity provided faster mass transfer because the wet agglomerates contacted dry gas bubbles more frequently.

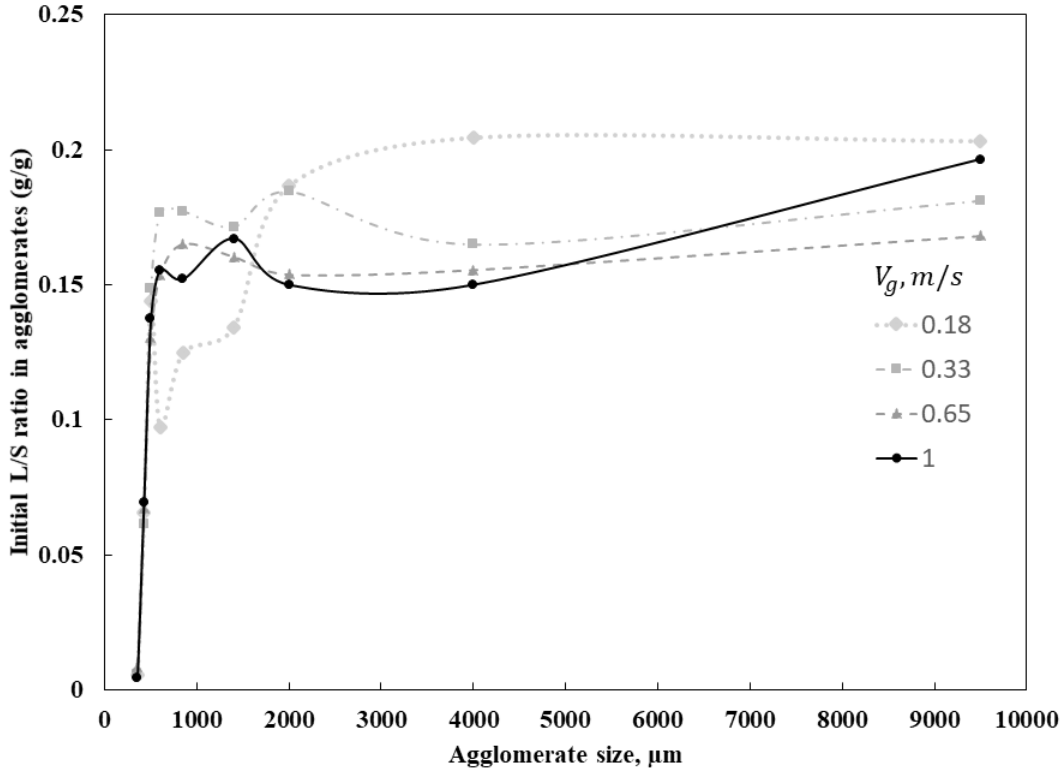

Figure 3.23 Liquid to solids ratio (L/S) in each agglomerate size cut for various superficial gas velocities during injection (V_{gi}) (Inclined distributor, even case, no baffle, $T_{initial} = 130\ °C$, $x_{inj} = 0.18\ m$, $z_{inj} = 0.67\ m$, $L_{inj} = 0.23\ m$, $F_L = 17.33\ g/s$, $m_{inj} = 200\ g$, $GLR = 2$ %, superficial gas velocity during drying: $V_{gd} < U_{mf}$, $t_{drying} = 10\ min$)

Table 3-2 shows that the Gum Arabic method showed good reproducibility. The differences between replicates are much smaller than the changes obtained when using baffles.

Conditions	Replicate 1	Replicate 2
No baffle	0.46	0.44
Baffle A1 (asymmetrical baffle without a flux-tube)	0.37	0.35
Baffle A2 (asymmetrical baffle with a flux-tube)	0.58	0.53

Table 3-2 Reproducibility of the Gum Arabic method

b. Freeboard pressure estimation method

The empirical correlation between excess freeboard pressure and initial water trapped fraction from Gum Arabic was given in Eq.3-10:

$$\frac{initial\ water\ trapped}{water\ injected} = 0.0017 \int_0^{t_{end\ inj}} P_{freeboard}\, dt + 0.2579 \qquad 3\text{-}10$$

Figure 3.24 shows the freeboard pressure estimation method agreed well with the general trend of the Gum Arabic method. The scatter from replicates may affect the determination of precise improvement. However, this method was used to find interesting conditions that can significantly improve, for example, a reduction of initial liquid trapped fraction in agglomerates from 0.6 to 0.3. Then the interesting conditions would first be confirmed with the other quick estimation method with E-probes. Then the most interesting conditions would be validated with the Gum Arabic method.

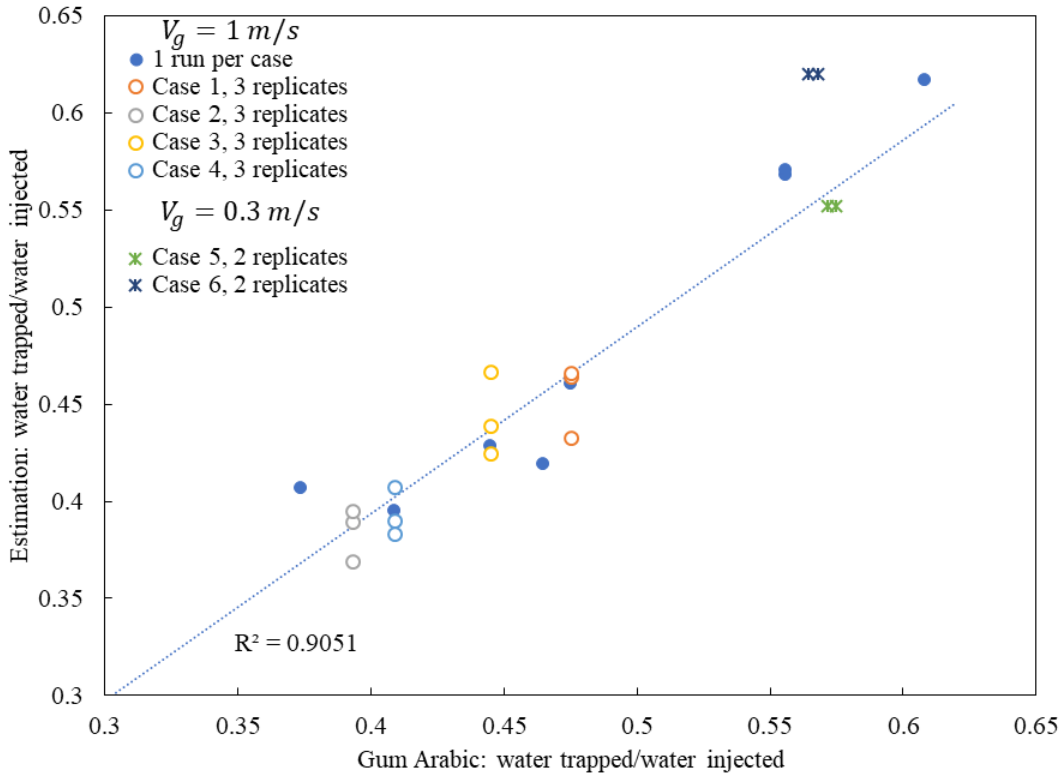

Figure 3.24 Initial water trapped/water injected in agglomerates from freeboard estimation method and Gum Arabic method

c. E-probe estimation method

The empirical correlation between the E-probe estimation method and initial water trapped fraction from Gum Arabic was given in Eq.3-11:

$$\frac{initial\ water\ trapped}{water\ injected} = 0.024 + 0.0043 \times t_{35\%,\,row4} - 0.0056 \times t_{55\%.\,row1} + 0.0026 \times t_{95\%,\,row5} \qquad 3\text{-}11$$

Figure 3.25 shows that the general trend from the E-probe estimation and the Gum Arabic results agreed. The empty markers were replicates with E-probe estimation methods. Different colors meant different conditions. This method was quick but created some scatter. Therefore, it was used to detect the most interesting cases, for example, which conditions could give water trapped/ water injected smaller than 0.3. The interesting conditions were also verified with the freeboard pressure estimation method, which gave less scatter between replicates but required pre-heating. As for the most

interesting condition, a Gum Arabic run was conducted to check the agglomerate characteristics.

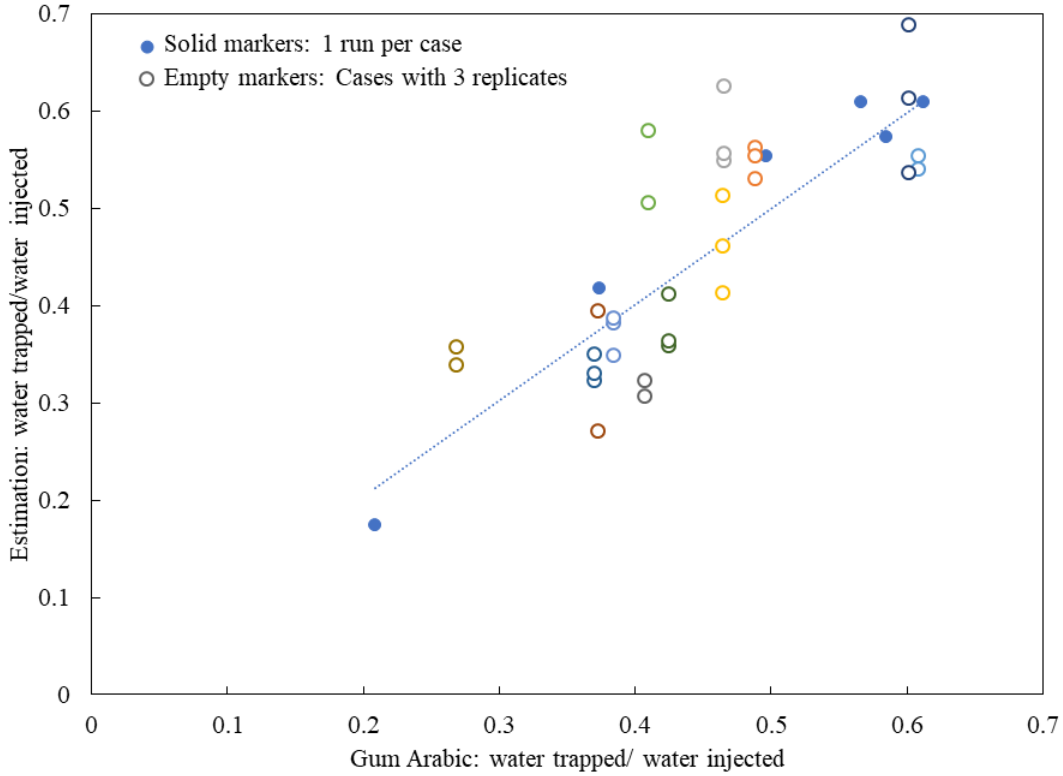

Figure 3.25 Reproducibility of E-probe estimation method comparing to the Gum Arabic method results (1 m/s)

d. Comparison among three liquid distribution quality evaluation methods

From previous calibration and reproducibility checks, it was known that both estimation methods could scatter the results. But they could clearly show which experimental conditions could give much less initial water trapped/water injected (Figure 3.26).

The gas distributor configuration concentrated gas bubbles to certain sides of the bed, i.e., the western case had more gas bubbles on the western side of the bed (Chapter 4). More gas bubbles near the injection location resulted in less water trapped in agglomerates (Chapter 5).

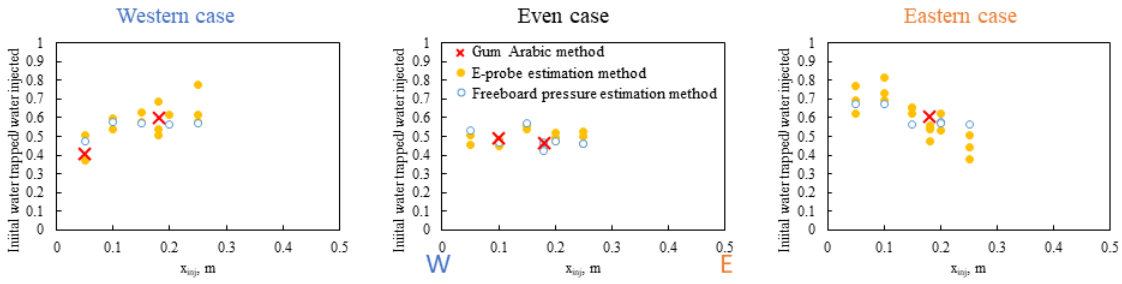

Figure 3.26 Comparison of three methods for liquid distribution quality evaluation: impact of injection location (x_{inj}) with different gas distributor configurations.

3.5 Liquid concentration in the bed

3.5.1 Introduction

It is essential to know if installing a baffle in a coker would be detrimental from the point of view of wet solids mixing and local evaporation rate. Past studies showed that the baffle created a staging effect on vertical solids mixing [24-26]. It is essential to know if the staging effect applies to vapors as well, as the wet solids mixing and local vaporization is highly connected with the local liquid concentration. This section shows the application of conductance probes to obtain liquid concentration.

Past studies showed other methods to obtain local liquid concentration, such as E-probes [27] and X-ray [28]. Farkhondehkavaki et al.[29] has proved with experiments (Karl-Fisher titration method) that the conductance probes measure the online local free-moisture concentration in the bed. In comparison, the E-probe measurement seemed to be affected by both discharges of the bed and evaporation. The shortcoming of the X-ray method was that it requires an expensive apparatus, and it would be beneficial to develop a method that can be widely applied.

3.5.2 The experimental set-up, material, and standard procedure

The conductance probes measured the online impact of local free moisture on the local conductivity from the measuring point to the ground. The measuring circuit was shown in Figure 3.27. A signal generator supplied an AC current to the circuit, with a frequency of

100 Hz and a total voltage of 7 V. When the resistance of the fluidized bed changes, the voltage on the resistor changed accordingly.

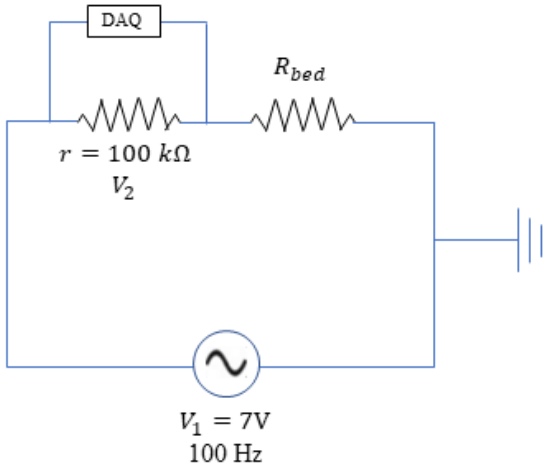

Figure 3.27 Conductance measurement electrical circuit

The fluid bed in this research was made of carbon steel. Therefore, each conductance probe measured the conductivity of the exposure area of the probe tip to the bed wall where it is attached to. Same as the E-probes, the conductance probes were insulated from the bed wall with Teflon fittings. Figure 3.28 shows the conductance probe locations with and without a symmetrical baffle. 46 locations could be measured simultaneously for each run, i.e., rows 1, 2 ,3, 4, and 5. The run could then be repeated while it measures rows 1, 2, 5, 6, and 7. Therefore, for each case, rows 1, 2, and 5 were replicates to check the reproducibility of the data.

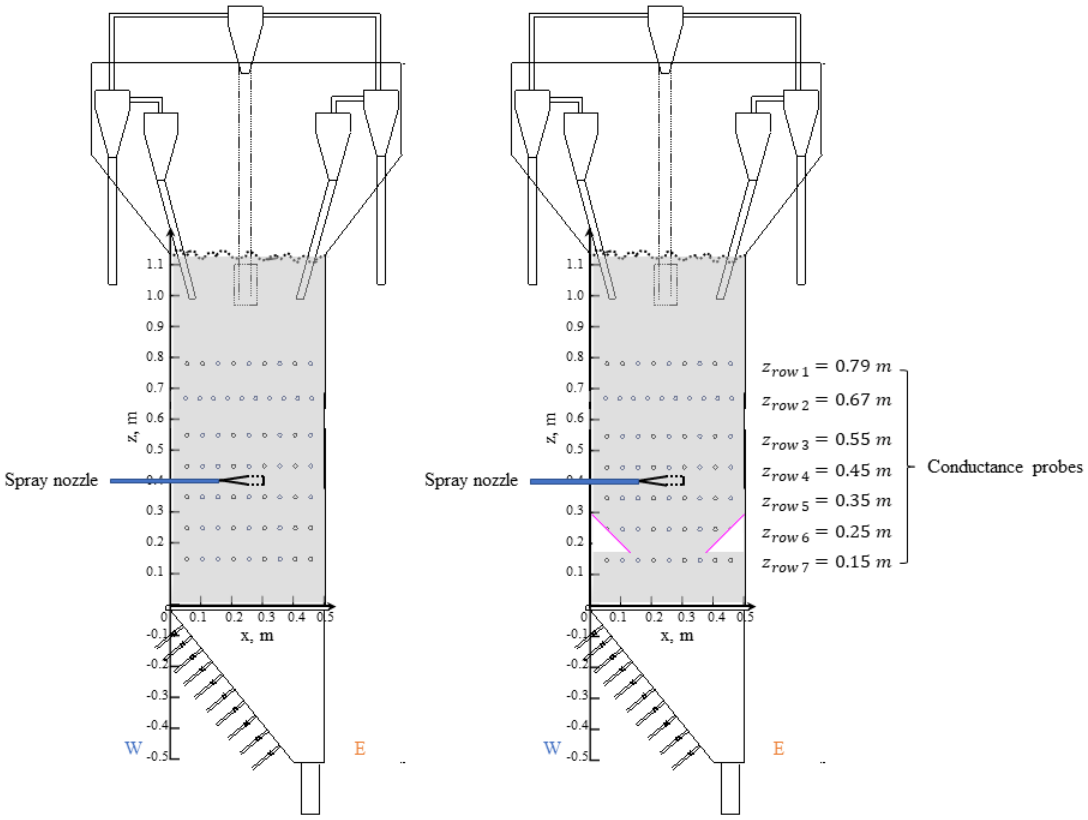

Figure 3.28 Schematic diagram of conductance probe, spray jet, and symmetrical baffle locations (Flat distributor, $x_{inj} = 0.15\ m$, $z_{inj} = 0.4\ m$, $L_{inj} = 0.15\ m$, $F_L = 1.6\ g/s$, GLR=107 %)

The standard procedures were:

1) The bed temperature was adjusted to 20 °C.

2) The fluid bed was fluidized for 1 min before injection.

3) The injection flowrate was kept at 1.6 g/s with a 107 % gas to liquid ratio (GLR).

4) The solenoid valve closes automatically just after the injection is completed.

5) The bed was continuously fluidized until the conductance probe signal dropped back to the same as before the injection. (The time it took to dry the bed was verified with the predicted end of evaporation, assuming the air coming out of the

bed is saturated. Also, the time it took to dry the bed was verified with thermocouples measurements in section 3.7.)

3.5.3 Data processing

For each probe, using Ohm's law, the resistance of the bed was:

$$R_{bed} = \frac{1}{\prod_{bed}} = r\left(\frac{V_1}{V_2} - 1\right) \quad \text{3-12}$$

Where $\prod_{bed}$ was the conductivity of the bed, r was the resistance of the resistor, $V_1$was the root-mean-square (RMS) voltage of the signal generator, V_2 was the root-mean-square voltage measured at the resistor (Figure 3.27).

The conductance of the bed was:

$$\prod_{bed} = \frac{1}{r}\frac{V_2}{V_1 - V_2} \quad \text{3-13}$$

Because from experiments, $V_1 \gg V_2$,

$$\prod_{bed} \propto \boldsymbol{V}_2 \quad \text{3-14}$$

Figure 3.29 shows an example of the average V_2 of the whole bed. It showed good agreement from experimental and theoretical end of evaporation calculated assuming the air coming out of bed is saturated.

Figure 3.29 shows it was a bit delayed to reach the maximum of $\boldsymbol{V_2}$ after the end of the injection because it took some time for the wet solids to disperse. To obtain the liquid concentration in the bed, we developed a correlation to get $C_{L\,\max,\,avg}$ from $V_{2,\,max}$.

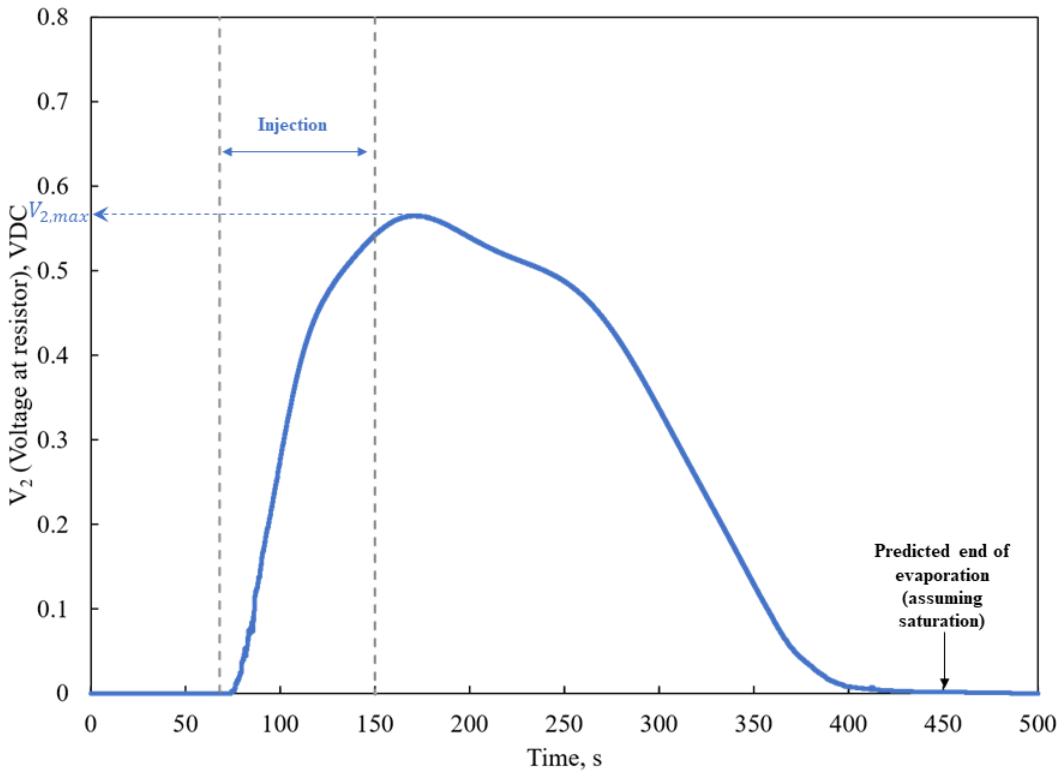

Figure 3.29 Typical result of the average of all the probes in bed (flat distributor, no baffle, $\boldsymbol{V_g = 0.5\ m/s,\ x_{inj} = 0.15\ m, z_{inj} = 0.4\ m, T_{initial} = 20\ °C, L_{inj} = 0.15\ m, F_L = 1.6\ g/s, m_{inj} = 125\ g, GLR = 107\ \%}$)

Figure 3.30 shows the calibration done with an ideal nozzle (a straight pipe with an outlet diameter of 4.94 mm). The high gas to liquid ratio (GLR=107 %) formed very fine droplets. Therefore, with this setup, there were no agglomerates created during the injection. Three linear calibration curves could give a good fit from the average voltage

of all conductance probes to average liquid concentration. The trend of 3 linear calibration curves was similar to what Farkhondehkavaki et al.[29] found.

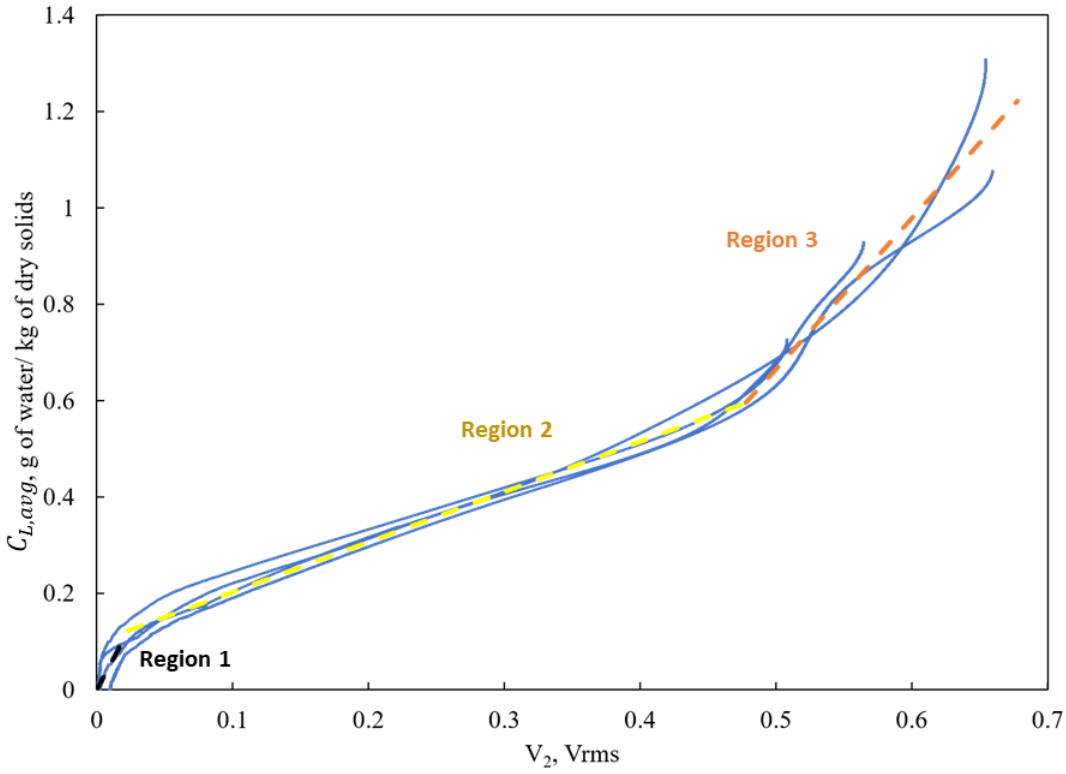

Figure 3.30 Calibration using average voltage, from all conductance probes in bed, to obtain average liquid concentration ($V_g = 0.5\ m/s$, $x_{inj} = 0.15\ m$, $z_{inj} = 0.4\ m$, $T_{initial} = 20\ °C$, $L_{inj} = 0.15\ m$, $F_L = 1.6\ g/s$, $m_{inj} = 100,\ 125,\ 150,\ 170\ g$, $GLR = 107$ %)

From three linear calibration curves, the average liquid concentration ($\overline{C_L}$) were given:

$$\overline{C_L} = a_1\bar{V},\ when\ 0 < \overline{C_L} < 0.1 \qquad 3\text{-}15$$

$$\overline{C_L} = a_2\bar{V} + b_2,\ when\ 0.1 \leq \overline{C_L} \leq 0.48$$

$$\overline{C_L} = a_3\bar{V} + b_3,\ when\ 0.48 < \overline{C_L} < 1.2$$

Figure 3.31 shows that the three linear calibration curves worked well one minute after the injection was complete for all masses of injection.

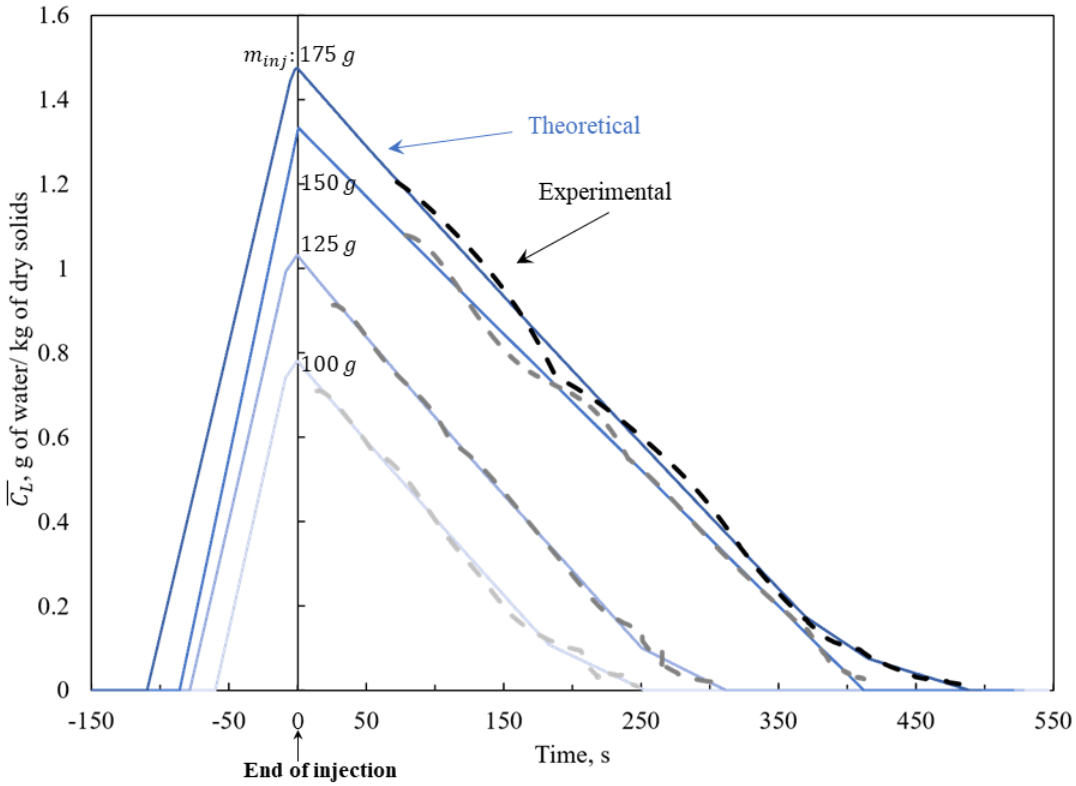

Figure 3.31 Comparison between theoretical and experimental bed-averaged free liquid concentration, applying the three linear calibration curves (107 % GLR, flat distributor, no baffle, V_g= 0.5 m/s, x_{inj}=0.15 m, z_{inj}=0.4 m, L_{inj}=0.15 m, F_L=1.6 g/s, $T_{initial}$=20 °C)

3.5.4 Example of results and reproducibility check

Figure 3.32 shows good agreement of 2 replicates with and without a baffle at different superficial gas velocities. There was a clear difference between with and without baffle groups.

Higher superficial gas velocity enhanced evaporation; therefore, the remaining liquid in the bed would be reduced at the end of injection. The higher maximum average liquid seen with baffle could be because the staging effect of the baffle made it much drier below the baffle, where there were no probes ($z < 0.15\ m$ in Figure 3.28). Therefore,

where there were probes, it became wetter. Normalized liquid concentration above and at the baffle region was discussed in detail in section 6.1.

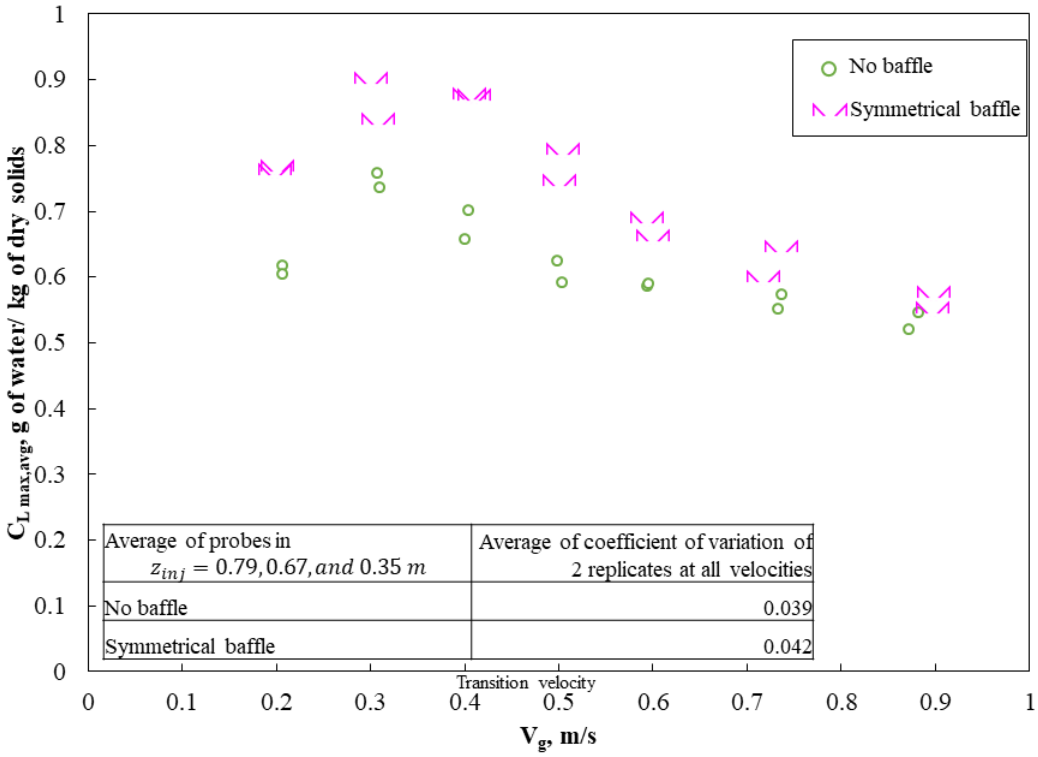

Figure 3.32 Reproducibility of maximum average liquid concentration in bed at different V_g with and without baffle (Flat distributor, 4.94 mm High GLR nozzle: $x_{inj} = 0.15\ m$, $z_{inj} = 0.4\ m$, $L_{jet} = 0.15\ m$, $m_{inj} = 100\ g$, $F_L = 1.6\ g/s$, $GLR = 107$ %, $T_{bed} = 20$ ℃)

3.6 Wet solids trajectory

3.6.1 Introduction

This section used the same setup as shown in section 3.5. This section shows another way to look at information from the same raw measurement data.

3.6.2 Data processing

The liquid of the spray was carried upward with the up-flowing gas bubbles first, then flowed down with the emulsion solids below the spray jet. So, it was expected that above

the spray (Figure 3.33 probe 1), the conductance probe detected liquid earlier than the probe below the spray (Figure 3.33 probe 2). By the time the wet solids reached the probe below the spray, they have been diluted with dry solids, and their concentration was lower.

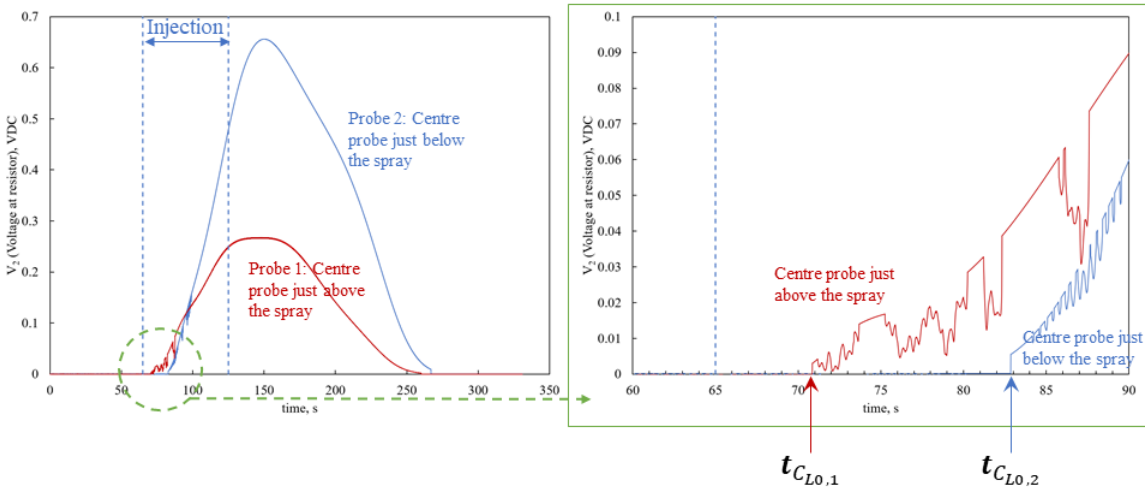

Figure 3.33 Example of the time it takes for the liquid to be detected by a conductance probe (Flat distributor, no baffle, $V_g = 0.9\ m$, No injection for normalized gas distribution, $T_{bed} = 30$ ℃; for normalized local liquid concentration: 4.94 mm High GLR nozzle: $x_{inj} = 0.15\ m$, $z_{inj} = 0.4\ m$, $L_{jet} = 0.15\ m$, $m_{inj} = 100\ g$, $F_L = 1.6\ g/s$, $GLR = 107$ %, $T_{bed} = 20$ ℃, Probe 1: $x = 0.25\ m$, $z = 0.45$; Probe 2: $x = 0.25\ m$, $z = 35\ m$)

3.6.3 Example of results and reproducibility check

Figure 3.34 (left) shows the local gas bubble distribution compared to the bed average. Similarly, Figure 3.34 (right) shows the normalized time for the wet solids to reach a certain area after the injection begins. The liquid from the spray jet first wetted the solids near itself. Then the wet solids were picked up by the upward flowing bubbles to be mixed with dry solids. Due to the mass transfer, the liquid was transported by solids mixing everywhere in the bed. Therefore, the liquid could be applied as a tracer to tell

where the wet solids went as time goes by. The approximate wet solids trajectory was shown by the arrow.

When the liquid was just sprayed into the bed, the gas bubble flow above the spray level helped distribute the liquid. While below the spray, the strong dry gas bubble flow below the spray prevented the liquid from reaching the section below the spray quickly.

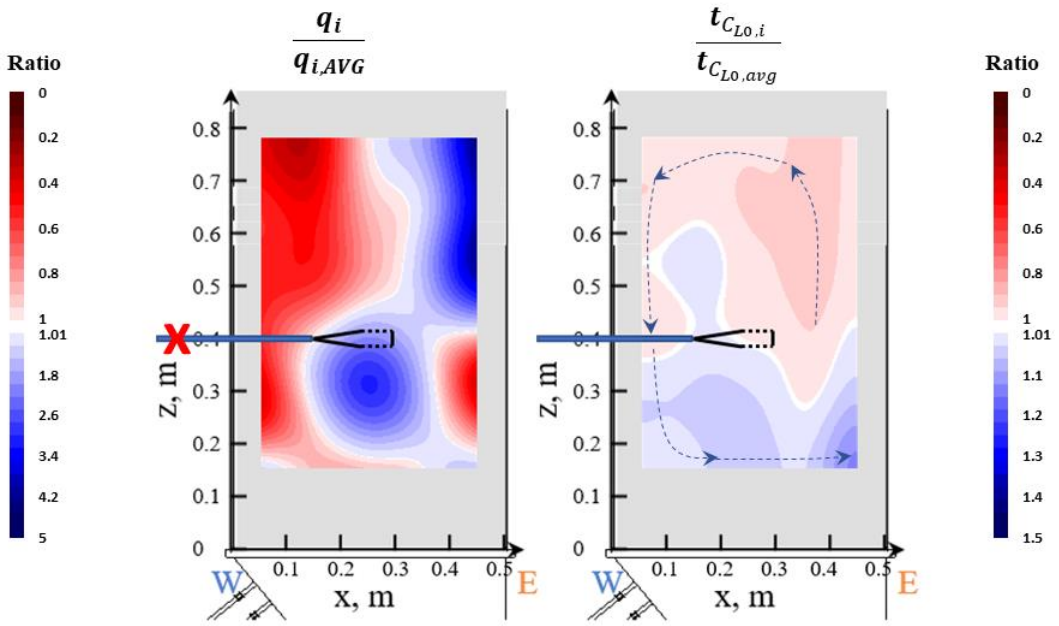

Figure 3.34 Impact of gas bubble flow on time it takes for the liquid to reach certain location in the bed (Flat distributor, no baffle, $V_g = 0.9\ m$, No injection for normalized gas distribution, $T_{bed} = 30$ ℃; for normalized local liquid concentration: 4.94 mm High GLR nozzle: $x_{inj} = 0.15\ m$, $z_{inj} = 0.4\ m$, $L_{jet} = 0.15\ m$, $m_{inj} = 100\ g$, $F_L = 1.6\ g/s$, $GLR = 107$ %, $T_{bed} = 20$ ℃, Arrow: approximate wet solids trajectory.)

Figure 3.35 shows good agreement of 2 replicates with and without a baffle at different superficial gas velocities. Without a baffle, the higher superficial gas velocity enhanced

wet solids mixing. Therefore, less time to reach certain probes at higher superficial gas velocities was expected.

Figure 3.35 shows, in most cases, although the baffle did not make much of a difference, there was usually enough accuracy to differentiate between these two cases. As for the impact of the baffle on the time it took to reach a certain area of the bed, it will be discussed in section 6.1.

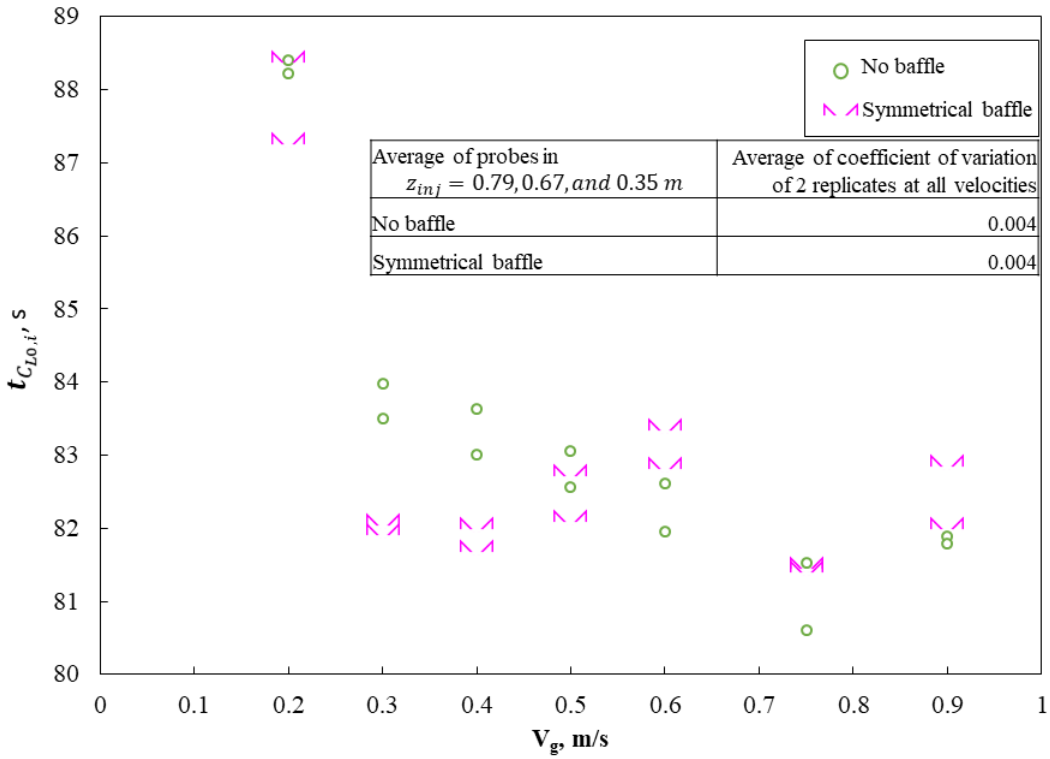

Figure 3.35 Reproducibility of maximum average liquid concentration in bed at different V_g with and without baffle (Flat distributor, 4.94 mm High GLR nozzle: $x_{inj} = 0.15\ m$, $z_{inj} = 0.4\ m$, $L_{jet} = 0.15\ m$, $m_{inj} = 100\ g$, $F_L = 1.6\ g/s$, $GLR =$ 107 %, $T_{bed} = 20$ ℃, average of all 28 probes in $z_{inj} = 0.79,\ 0.67,\ and\ 0.35\ m$)

3.7 Vaporization rate

3.7.1 Introduction

The purpose of these methods was to evaluate how quickly wet particles from the spray region were dispersed and mixed with the bed solids. Operating at a low bed temperature increased the mass of hot bed particles that must be brought in contact with the wet particles to provide enough heat for liquid vaporization.

Section 3.4 showed how changes in freeboard pressure could be used to estimate the amount of water trapped in agglomerates when using a regular spray nozzle at a bed temperature of 130 ºC. This section adapted the same method to determine whether the baffle had a significant impact on the vaporization rate at a temperature that was much lower than the boiling point of the water injected when using a spray nozzle with a very high atomization gas flowrate, to avoid agglomerate formation.

The excess freeboard pressure was used to measure the overall vaporization rate downstream of the unit. The drying time was obtained from conductance probes locally to evaluate the local vaporization rate. The shorter drying time required indicated a higher local vaporization rate. The results were validated with thermocouples that were measuring the temperature simultaneously.

3.7.2 The experimental set-up, material, and standard procedure

a. Overall vaporization rate: freeboard pressure method

The experimental set-up was shown in section 2.1, Figure 2.1.

The standard procedures were:

1) The fluid bed was fluidized for 1 min before injection.

2) 100 g of water was injected continuously with the same flowrate of 4 g/s with a 30 % gas to liquid ratio (GLR).

3) The solenoid valve closed automatically just after the injection is completed.

4) The bed was continuously fluidized for 10 min to dry the bed. (The drying time required was confirmed with conductance measurement, shown in section 3.5.)

b. Local vaporization rate: conductance probe method

This section used the same setup as shown in section 3.5. This section shows another way to look at the information contained in the same raw measurement data.

c. Local vaporization rate validation: thermocouple method

Figure 3.37 shows a photo of specially designed multi-purpose probes. They could be applied to measure the temperature and local bed conductivity at the same time. At the center, the thermocouple wire was fixed with sealant, and only the tips were exposed to the surrounding bed. The hollow stainless-steel probe was connected to the bed with Teflon fittings. The conductance measurement was introduced in section 3.5. The two data acquisitions were synchronized, measuring temperature and conductivity, with a shared signal from the pre-mixer pressure (Figure 3.16) of the injection system.

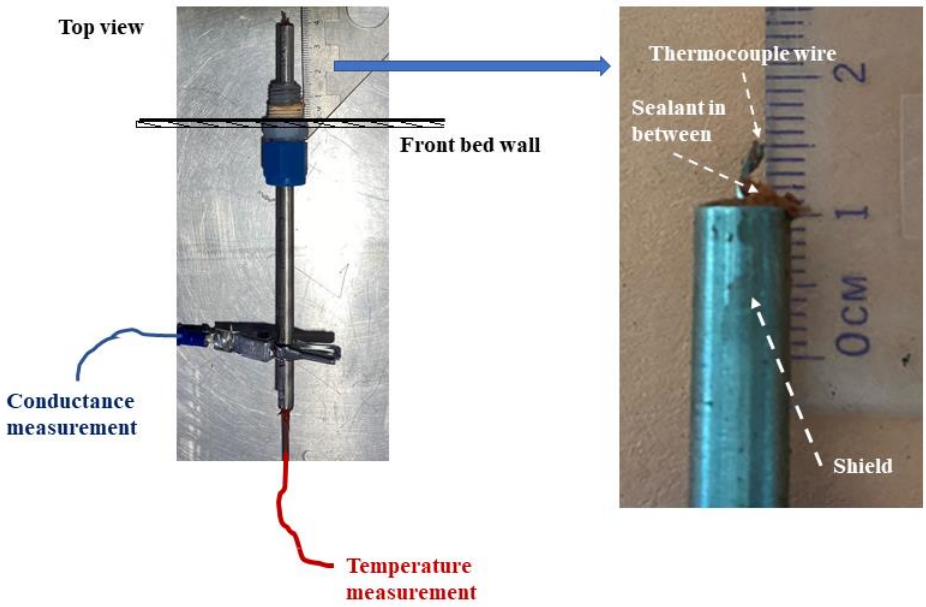

Figure 3.36 Photograph of multi-purpose probe design for both conductance and temperature measurement and thermocouple wire tip

Figure 3.37 shows the locations of the multi-purpose probes with and without the baffle.

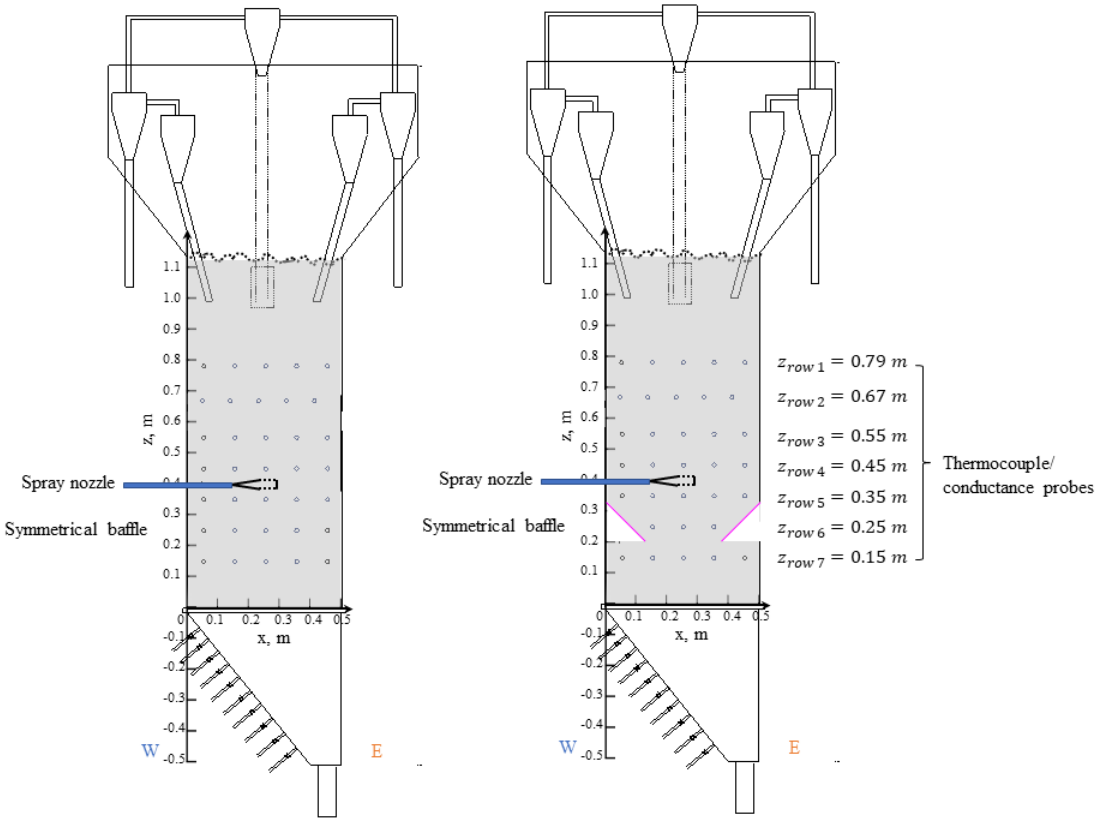

Figure 3.37 Schematic diagram of 36 thermocouple/conductance probe locations and spray jet locations with (right) and without (left) symmetrical baffle (Flat distributor, $x_{inj} = 0.15\ m$, $z_{inj} = 0.4\ m$, $L_{inj} = 0.15\ m$, $F_L = 1.6\ g/s$, GLR=107 %)

The standard procedures were the same as section 3.5.

3.7.3 Data processing

a. Overall vaporization rate: freeboard pressure method

The normalized cumulative fraction from the excess freeboard pressure was the "vaporized fraction." An example of "excess freeboard pressure" was given in section 3.4.2. At first, when the liquid injection was started, some injected liquid did not vaporize as soon as it was injected as it might, for example, take some time for the vapor to be built up in the bed.

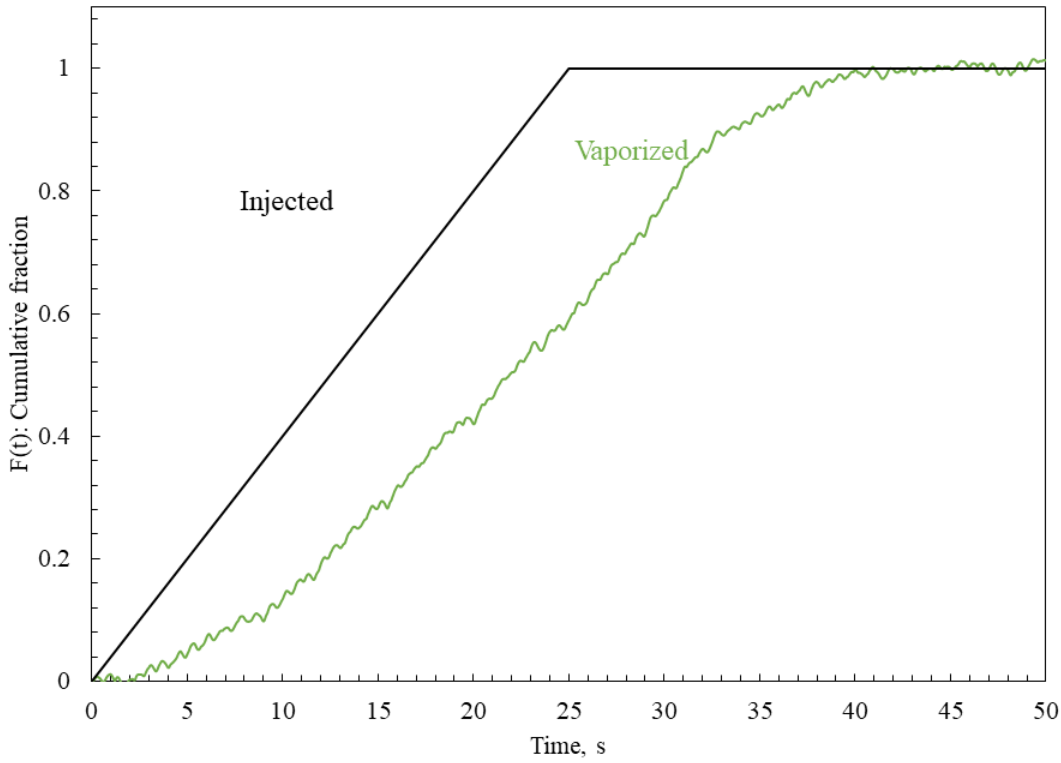

Figure 3.38 Typical results of experimental data processing: injection fraction, vaporized fraction from excess pressure. (Flat distributor, no baffle, $T_{initial} = 42\ °C, V_g = 0.8\ m/s, x_{inj} = 0.15\ m, z_{inj} = 0.4\ m, F_L = 4\ g/s, m_{inj} = 100\ g, GLR = 30$ %)

Figure 3.39 shows at the end of injection, it reached a steady state. The steady-state meant the rate of gas-liquid injection was equal to the rate for evaporation. In Figure 3.39, it was shown as the slope of the vaporized fraction was equal to the slope for the injected fraction (shown with a black dash line). Then, the accumulated liquid fraction (φ_{ac}) was obtained from the remaining liquid in the bed at the end of injection (Figure 3.39) [30].

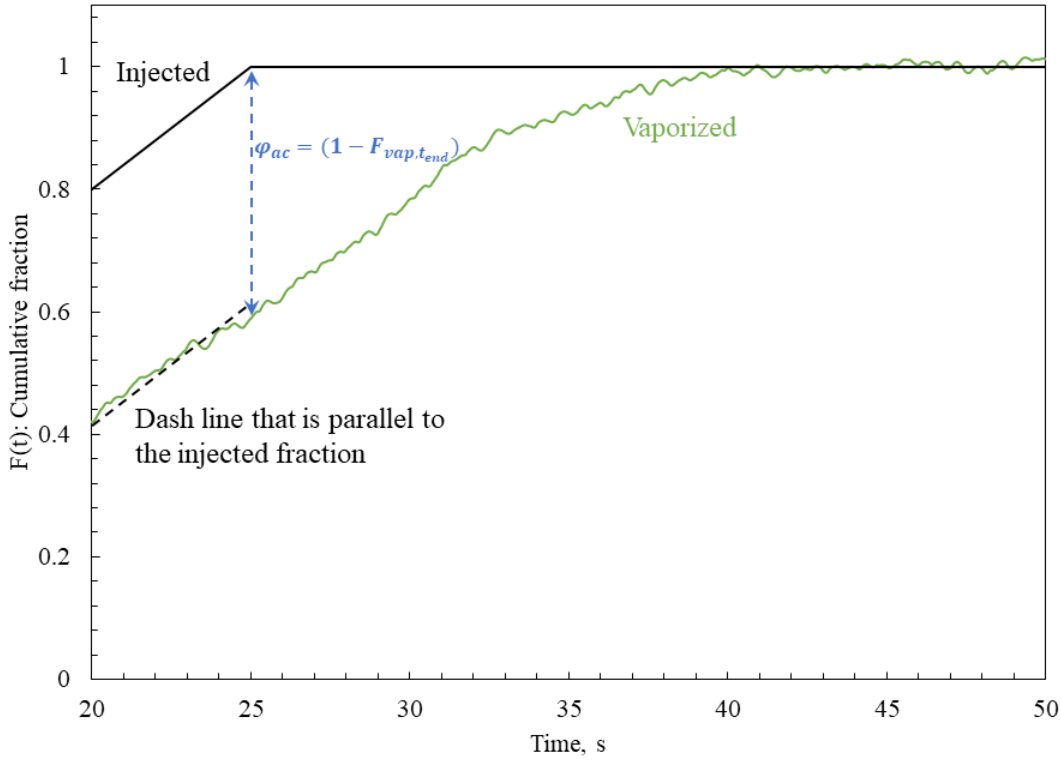

Figure 3.39 The vapor generation rate characterized by an accumulated liquid fraction at the end of the steady-state (Flat distributor, no baffle, $T_{initial} = 42\ °C$, $V_g = 0.8\ m/s$, $x_{inj} = 0.15\ m$, $z_{inj} = 0.4\ m$, $F_L = 4\ g/s$, $m_{inj} = 100\ g$, $GLR = 30$ %)

To confirm the results, at the freeboard, we installed a pipe tee fitting and connected two different types of pressure transducers to each side. One type was the absolute pressure transducer; the other type was the differential pressure transducer. As for the differential pressure transducer, one side was connected to the measuring location, while the other

side was exposed to the atmosphere. Figure 3.40 shows two different types of pressure transducers agreed well.

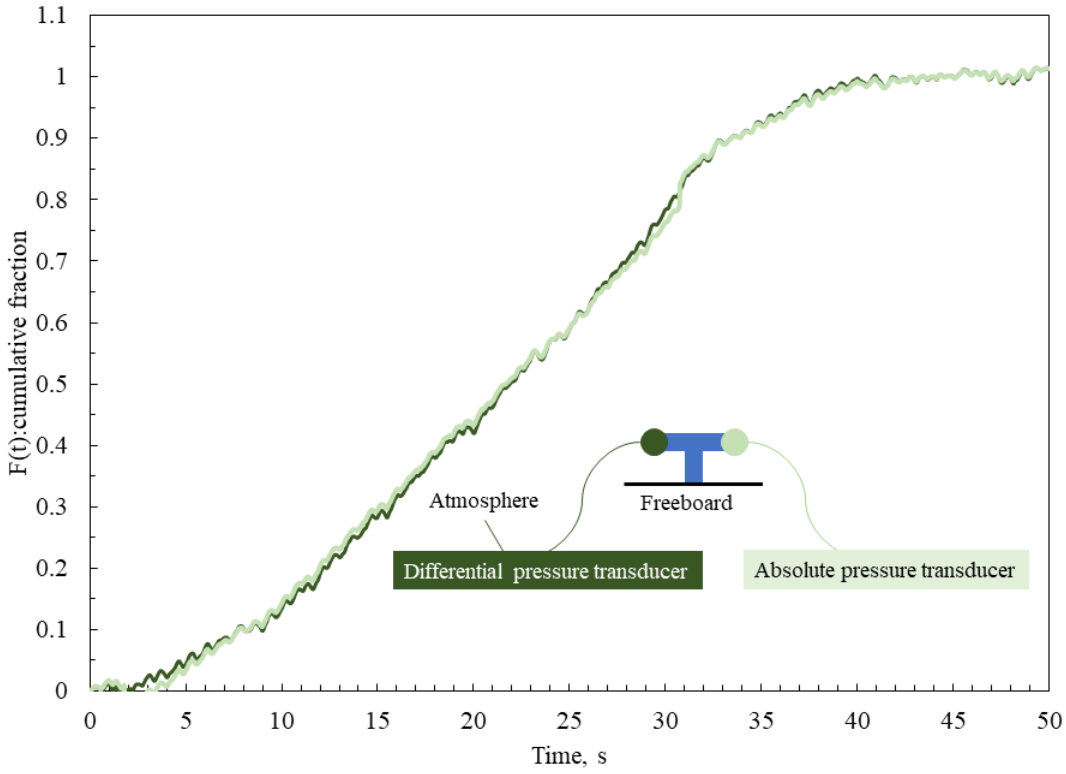

Figure 3.40 Cumulative exceed freeboard pressure measured with two different types of pressure transducers (Flat distributor, no baffle, $T_{initial} = 42\ °C$, $V_g = 0.8\ m/s$, $x_{inj} = 0.15\ m$, $z_{inj} = 0.4\ m$, $F_L = 4\ g/s$, $m_{inj} = 100\ g$, $GLR = 30$ %)

b. Local vaporization rate: conductance probe method

Figure 3.41 shows probe 1 dried faster than probe 2, because at probe 1, there were more gas bubbles. It was expected to dry faster with more gas bubbles because the more frequent dry gas bubbles helped to take away the liquid from the local area faster.

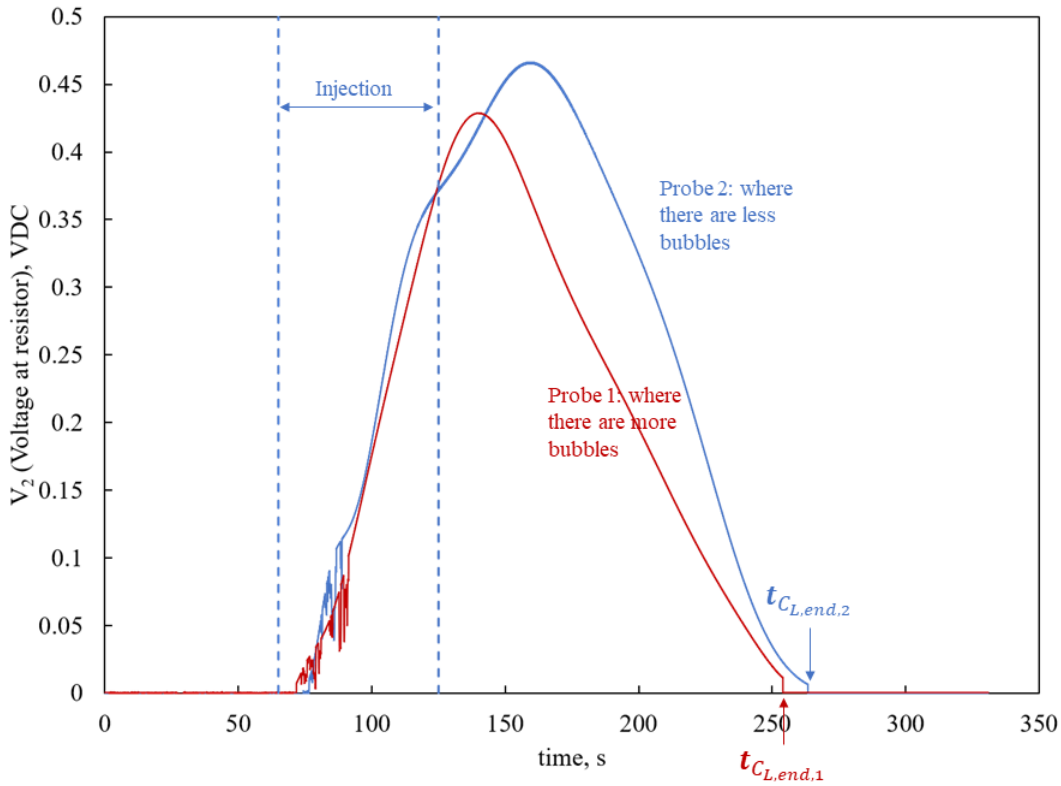

Figure 3.41 Examples of the time it takes for the liquid to be dried locally (Flat distributor, no baffle, $V_g = 0.9\ m$, No injection for normalized gas distribution, $T_{bed} = 30$ ℃; for normalized local liquid concentration: 4.94 mm High GLR nozzle: $x_{inj} = 0.15\ m$, $z_{inj} = 0.4\ m$, $L_{jet} = 0.15\ m$, $m_{inj} = 100\ g$, $F_L = 1.6\ g/s$, $GLR = 107$ %, $T_{bed} = 20$ ℃, Probe 1: $x = 0.45\ m$, $z = 0.55$; Probe 2: $x = 0.\ 05m$, $z = 0.55\ m$)

c. Local vaporization rate validation: thermocouple method

The data from two measurements, conductivity measurement, and temperature measurement, were obtained simultaneously at the same location, using the multi-purpose probe (Figure 3.36). Figure 3.42 shows the time required for local drying was very consistent with both measurements. The thermocouple method, which measured the cold

and hot solids mixing, validated the results obtained from the conductivity method, which measured the wet solids mixing.

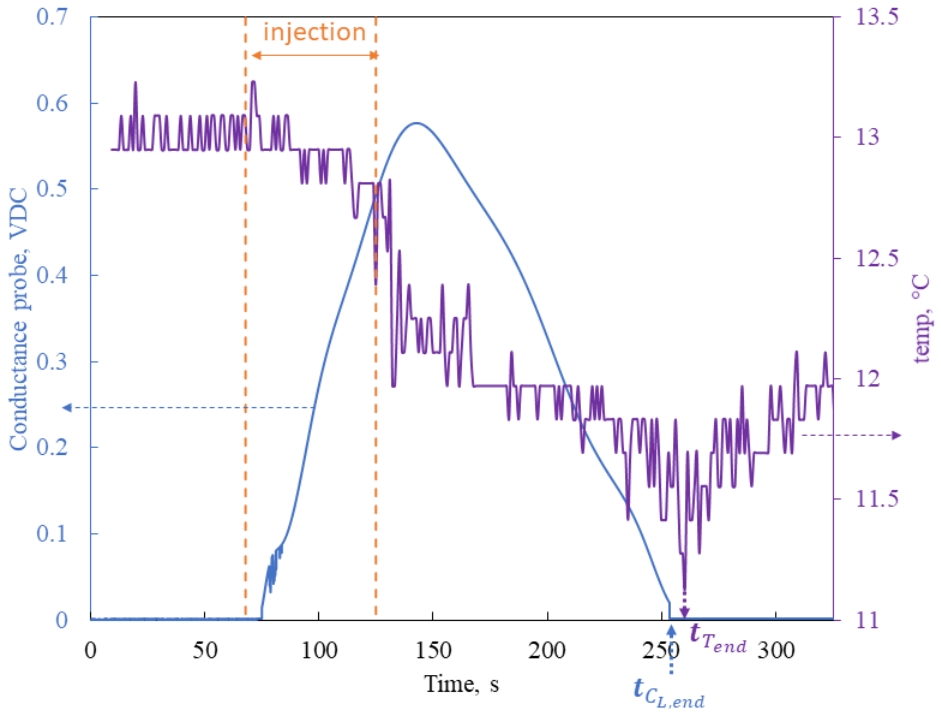

Figure 3.42 Examples of the time it takes for the liquid to be dried locally from thermocouple and conductance probe at the same location (Flat distributor, no baffle, $V_g = 0.9\ m$, No injection for normalized gas distribution, $T_{bed} = 30$ ℃; for normalized local liquid concentration: 4.94 mm High GLR nozzle: $x_{inj} = 0.15\ m$, $z_{inj} = 0.4\ m$, $L_{jet} = 0.15\ m$, $m_{inj} = 100\ g$, $F_L = 1.6\ g/s$, $GLR = 107$ %, $T_{bed} = 20$ ℃, Probe location: $x = 0.45\ m$, $z = 0.55$)

3.7.4 Example of results and reproducibility check

a. Overall vaporization rate: freeboard pressure method

Figure 3.43 shows that the increase of bed temperature before injection would improve evaporation. These results agreed with what Silitonga et al.[22] had found.

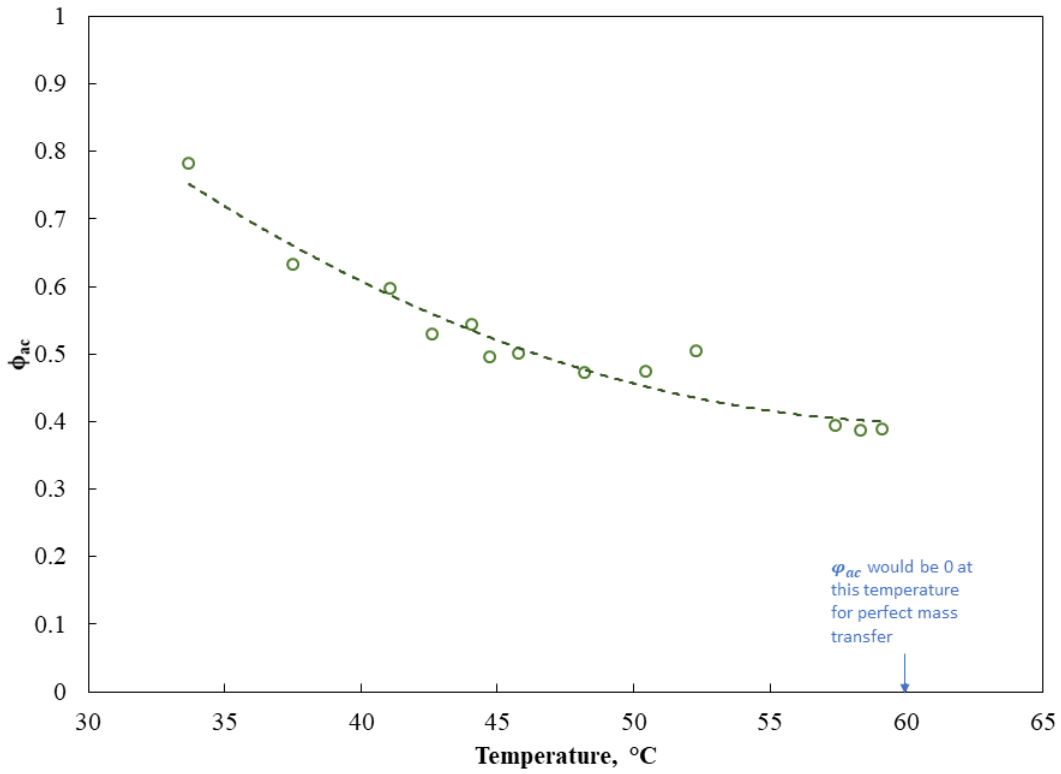

Figure 3.43 Impact of initial bed temperatures on vapor saturation (Flat distributor, no baffle, $V_g = 0.7\ m/s$, $x_{inj} = 0.15\ m$, $z_{inj} = 0.4\ m$, $L_{inj} = 0.15\ m$, $F_L = 4.5\ g/s$, $m_{inj} = 100\ g$, $GLR = 30$ %)

b. Local vaporization rate: conductance probe method and thermocouple method

Figure 3.44 shows that the average time it took to dry certain areas (where we had probes) from conductance probes, and temperature measurements agreed well with and without a baffle at different superficial gas velocities.

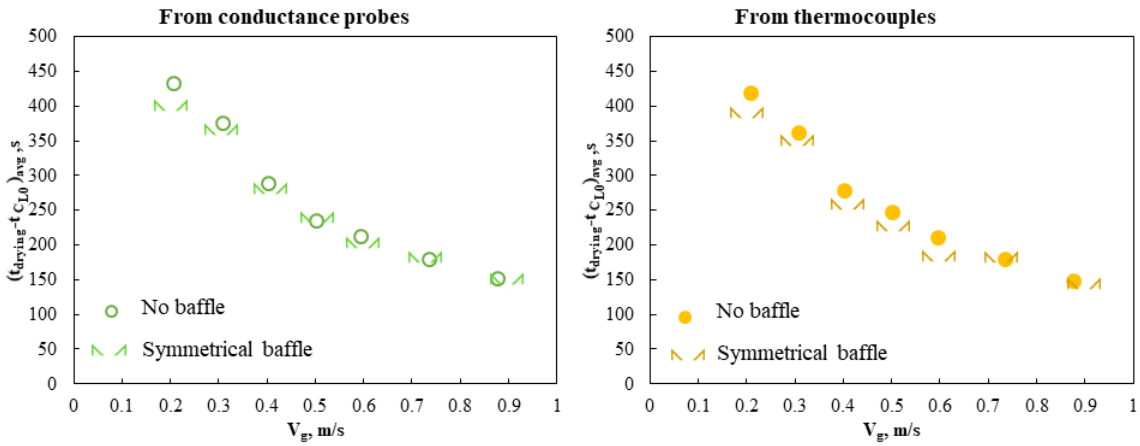

Figure 3.44 Impact of the symmetrical baffle on drying time from conductance probes and thermocouple method (Flat distributor, $T_{bed} = 20$ °C, $x_{inj} = 0.15$ m, $z_{inj} = 0.4$ m, $L_{jet} = 0.15$ m, $m_{inj} = 100$ g, $F_L = 1.6$ g/s, $GLR = 107$ %)

3.8 Minimum turbulent fluidization velocity (U_{mt})

3.8.1 Introduction

As shown in section 1.2.1, using pressure fluctuations to detect U_{mt} was applied as a standard method in quite a lot of publications. If a new method was applied to find U_{mt}, pressure fluctuation method was usually the validation method. Other methods to detect U_{mt} were introduced in section 1.2.1.

Instead of the frequently used parameters, standard deviation, or coefficient of variation of pressure fluctuations, we found another parameter that could be used to obtain U_{mt}: maximum value of V-statistic, which gave a better reproducibility among replicates.

In this section, the differential pressure fluctuations connecting from the freeboard to the lower level of the bed were used to obtain the U_{mt} of the bed. The results were then compared with a more local measurement: the radiation transmission method.

3.8.2 The experimental set-up, material, and standard procedure

a. Pressure fluctuation

Figure 3.45 shows the measuring location of differential pressure measurement location to obtain U_{mt}. No injection was involved in this method. The standard procedures were the same as section 3.1.2.

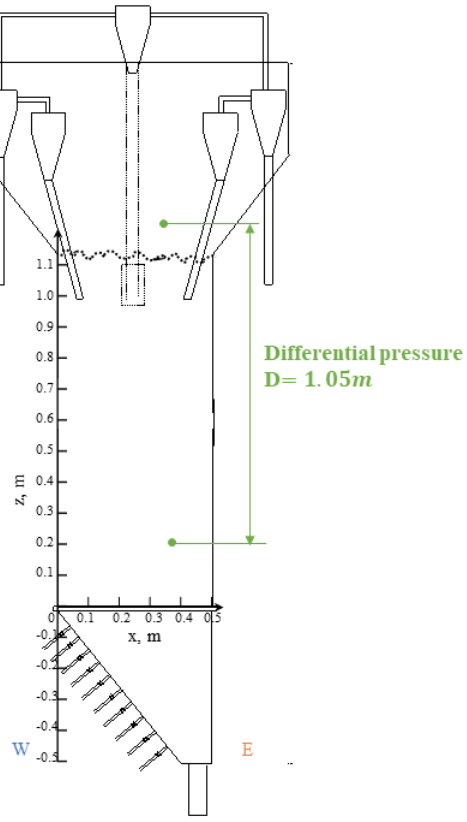

Figure 3.45 Measuring location of pressure fluctuation to obtain U_{mt}

b. Radiation transmission method

Figure 3.46 shows the measuring locations of the radiation transmission method. The green circles showed the locations of the radioactive source (same as the one used in section 3.1). Three sensors were fixed on the other side of the bed wall at different vertical locations (blue rectangular box in Figure 3.46). Then the radioactive particle

source was moved to obtain the average bed voidage from the front bed wall to the back bed wall along with the arrows in Figure 3.46.

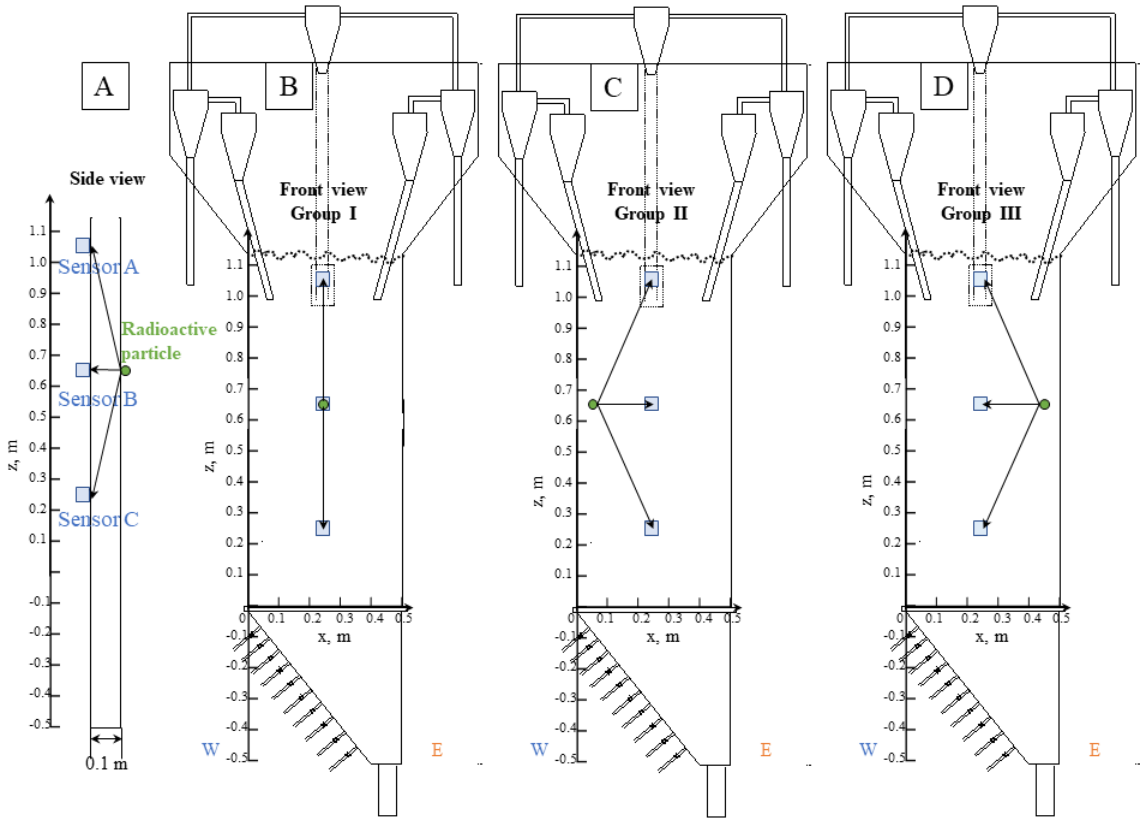

Figure 3.46 Measuring location of radiation transmission. A. Side view of radioactive particle stick to outside of the front bed wall and three sensors A (top, z=1.05 m), B (middle, z=0.65 m), and C (bottom, z=0.25 m) on the outside of back bed wall, B. Group I: Front view of the sensor at the center (x=0.25 m, z=0.65 m), C. Group II: Front view of the sensor at the western side (x=0.05 m, z=0.65 m), D. Group III: Front view of the sensor at eastern side (x=0.45 m, z=0.65 m).

3.8.3 Data processing

a. Pressure fluctuations

Figure 3.47 shows a typical way to obtain U_{mt} with the coefficient of variation (CV) of pressure fluctuations. The U_{mt} found for this condition was 0.36 m/s.

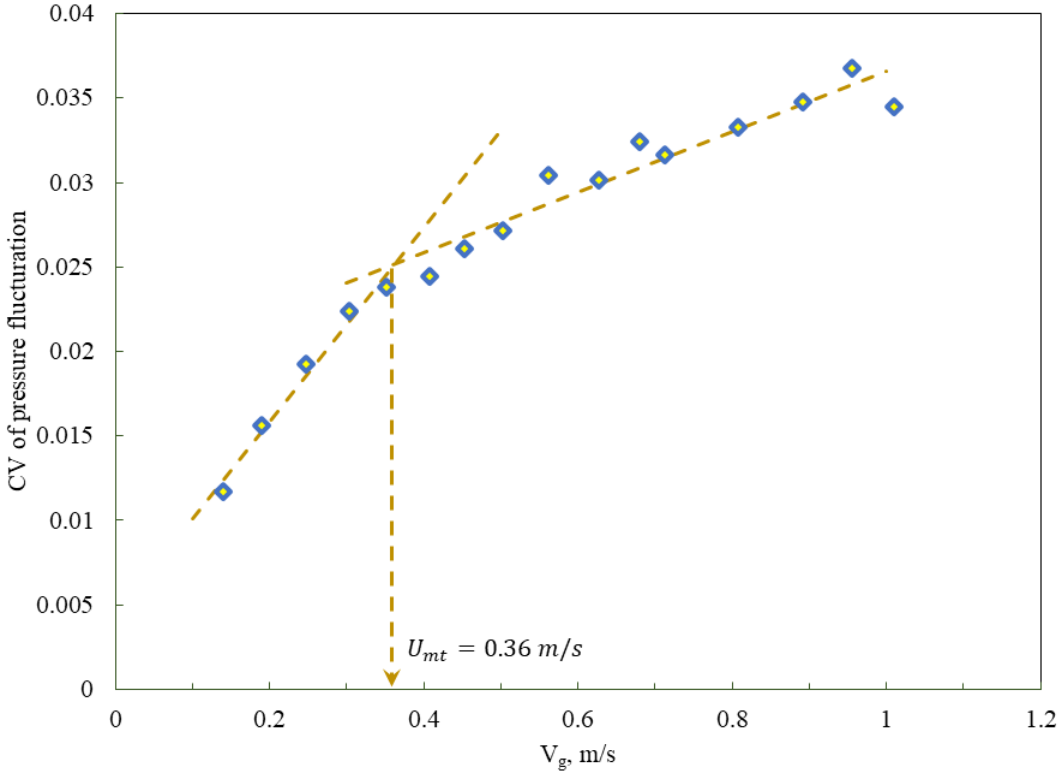

Figure 3.47 Example of coefficient of variation (CV) of pressure fluctuation vs. superficial gas velocity (V_g) to detect minimum turbulent velocity (U_{mt}) (inclined distributor, No baffle, western case, 25 °C)

Figure 3.48 shows that the variation of the values obtained from replicate runs might indicate there was be a better parameter(s) to give U_{mt} with smaller variations.

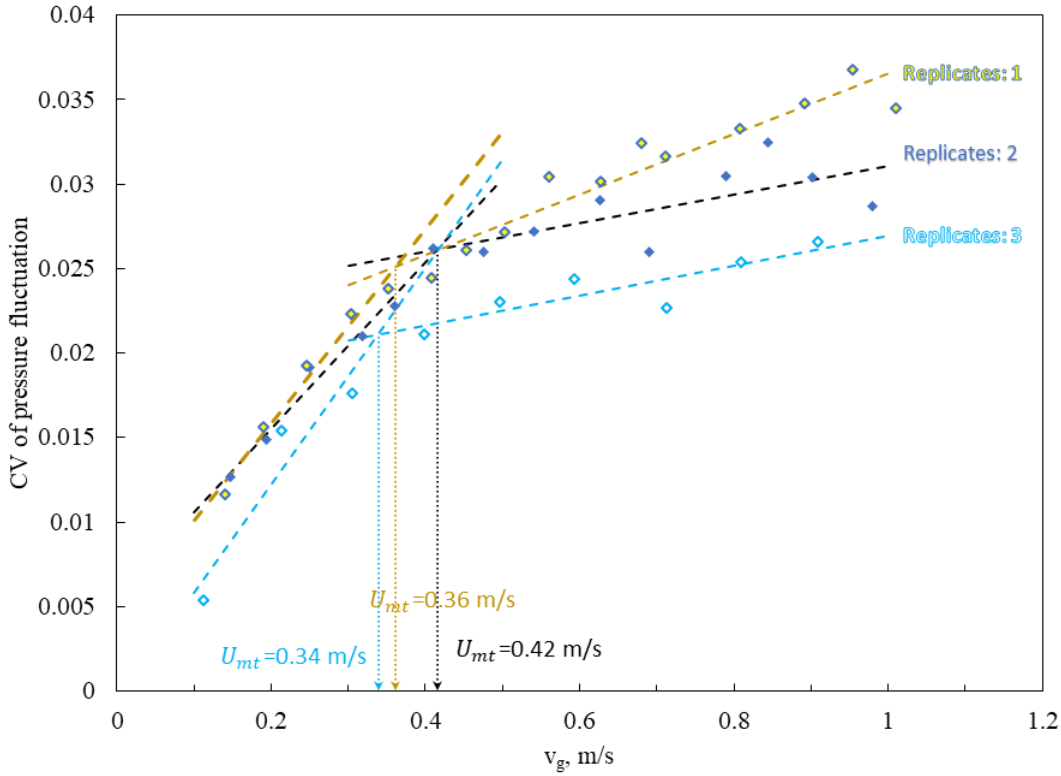

Figure 3.48 Coefficient of variation (CV) of pressure fluctuation vs. superficial gas velocity (V_g) to obtain U_{mt}, replicates with same conditions (inclined distributor, No baffle, western case, 25 °C)

Figure 3.49 shows that the variation of the values obtained from replicate runs became much smaller. The method used to obtain the maximum value of the V-statistic was given in Figure 3.3 in section 3.1.

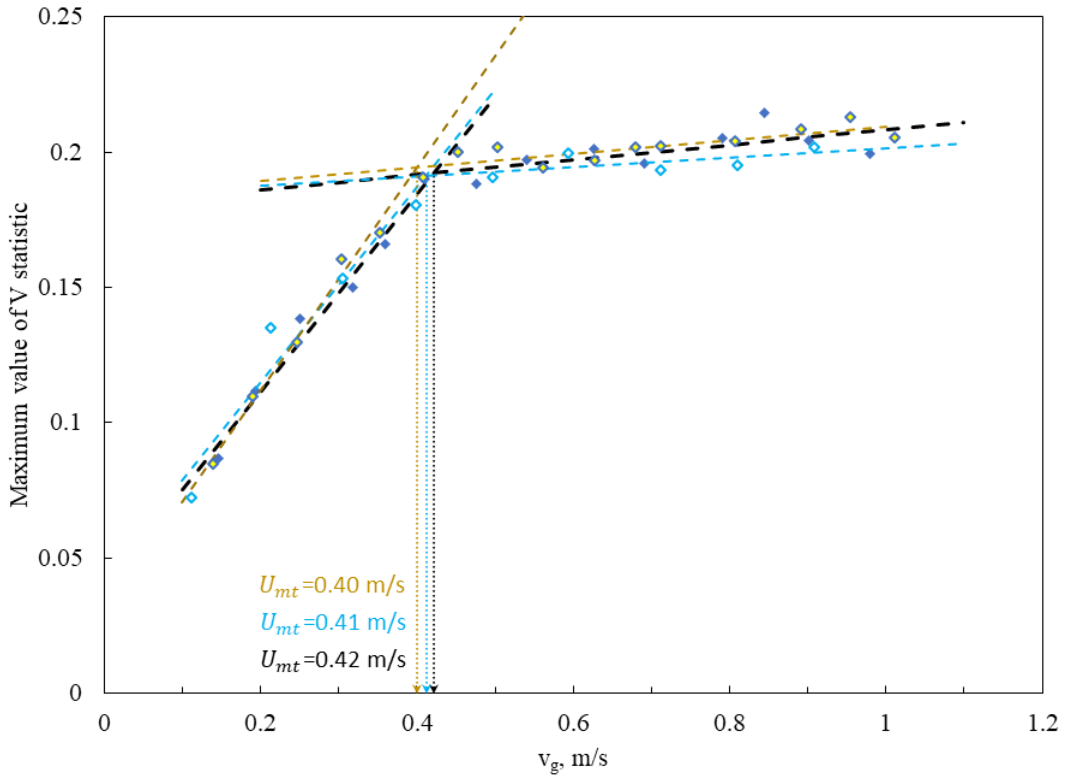

Figure 3.49 Maximum value of V-statistic of pressure fluctuation vs. superficial gas velocity (V_g) to obtain U_{mt}, replicates with same conditions (inclined distributor, No baffle, western case, 25 °C)

b. Radiation transmission method

Figure 3.50 shows the calibration curve using the radiation transmission method to obtain bed voidage. The calibration used the standard relationship between radiation absorption and bed density (i.e. bed voidage) and used experimental results obtained at two extreme conditions: when there are no solids in the bed, the signal was at the maximum value, the bed voidage was 1; when the bed was filled with sand particles and fluidized at the

minimum fluidization conditions, the signal was at the minimum value, the bed voidage is 0.4.

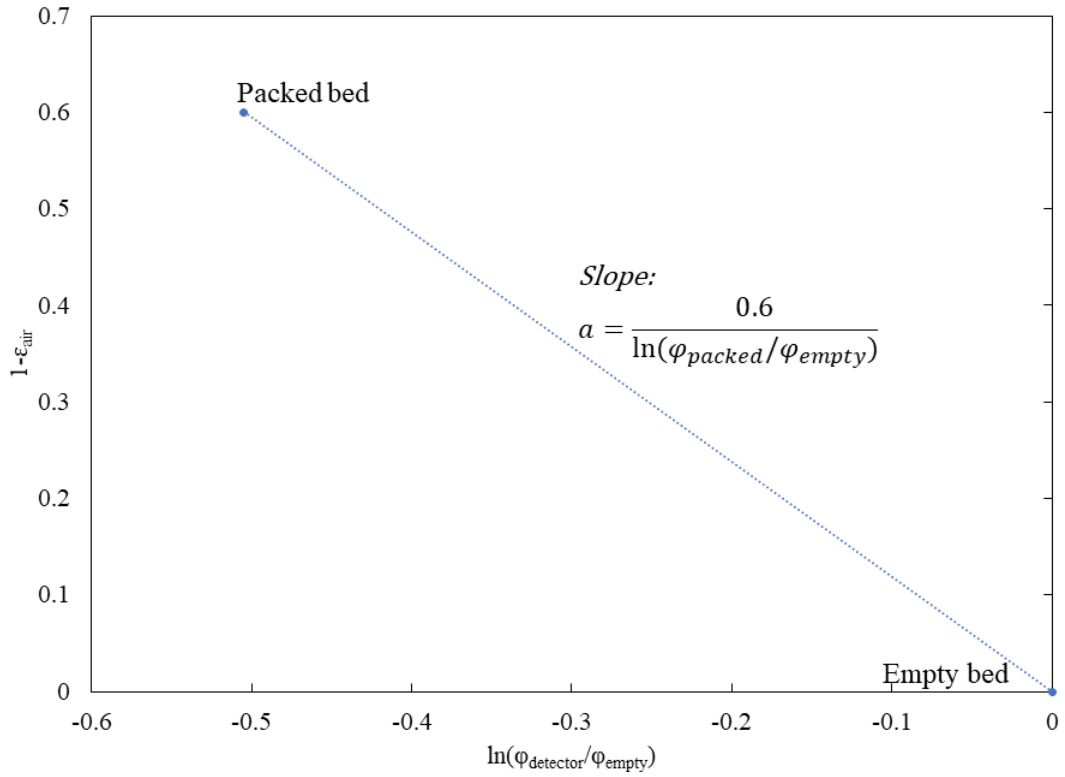

Figure 3.50 Example of calibration to obtain bed voidage (ε_{air}) from radiation transmission signal with packed bed and bed without solids. (Source location: x=0.25 m, z=0.65 m; Sensor location: x=0.25 m, z=1.05 m)

The calibration curve gave the slope:

$$a = \frac{0.6}{ln\ (\varphi_{packed}/\varphi_{empty})} \qquad 3\text{-}16$$

The bed voidage (ε_{air}) could be obtained from radiation transmission signal using Eq.3-17:

$$\varepsilon_{air} = 1 - \ a \cdot ln\ (\varphi_{detector}/\varphi_{empty}) \qquad 3\text{-}17$$

3.8.4 Example of results and reproducibility check

a. Pressure fluctuations

We tried to compare our results with the predicted results from the existing correlations and models. However, there was a significant spread in the predicted values (Table 3-3). The large variability of U_{mt} calculated with different correlations might be due to how the correlation was developed, such as how many factors a correlation included, as shown in section 1.2.1 b, in chapter 1. Therefore, in the rest of this section, we only compare our experimental results.

U_{mt}, m/s		Standard condition
Experimental results	Pressure fluctuation - Max value of V-statistic	0.36
	Pressure fluctuation – CV	0.41
Predicted value	Abba et al. [31]	0.89
	Bi et al. [32]	1.60
	Choi et al. [33]	1.83
	Ellis et al. [34]	3.55
	Gonzalez et al. [35]	0.64
	Seo et al. [36]	0.76
	Sun et al. [37]	2.59
	Yang et al. [38]	1.55

Table 3-3 Comparison between experimental results and predicted results with existing models (Standard condition: inclined distributor, no baffle, even case, 25 °C, $d_P = 190\ \mu m$, $\rho_P = 2650\ kg/m^3$)

Table 3-4 and Table 3-5 shows that coarser particles had a slightly larger U_{mt}, which agreed with past studies introduced in section 1.2.1.

	Particle size(d_P), μm	Apparent particle density (ρ_P), kg/m^3	U_{mt}, m/s Pressure fluctuation - Max value of V-statistic	U_{mt}, m/s Pressure fluctuation – CV
Silica sand	190	2650	0.36	0.41
Silica sand	310	2650	0.45	0.46

Table 3-4 Impact of particle size on U_{mt} found using pressure fluctuations (inclined distributor, no baffle, even case, 25 °C)

	Particle size(d_P), μm	Apparent particle density (ρ_P), kg/m^3	U_{mt}, m/s Pressure fluctuation - Max value of V-statistic	U_{mt}, m/s Pressure fluctuation – CV
Silica sand	190	2650	0.36	0.41
Coke	140	1450	0.32	No transition found

Table 3-5 Impact of particle properties on U_{mt} found using pressure fluctuations (inclined distributor, no baffle, even case, 25 °C)

Table 3-6 shows higher operating pressure gave slightly lower U_{mt}, which agreed with past studies introduced in section 1.2.1.

	Operating pressure, kPa	U_{mt}, m/s Pressure fluctuation - Max value of V-statistic	U_{mt}, m/s Pressure fluctuation – CV
Silica sand	101	0.36	0.41
	116	0.34	0.31

Table 3-6 Impact of operating pressure on U_{mt} found using pressure fluctuations (inclined distributor, no baffle, even case, 190 μm sand, 25 °C)

Table 3-7 shows that higher temperature would have a larger U_{mt}, which agreed with past studies introduced in section 1.2.1. In our case, the temperature variation was not large enough to show a significant increase. For example, Seo et al.[36] found that with a similar condition to this research, by increasing the bed temperature from 25 to 200 °C, the U_{mt} increased by only 0.1 m/s. But when the bed temperature increased from 25 to 600 °C, the U_{mt} increased by 0.7 m/s.

	Temperature, °C	U_{mt}, m/s Pressure fluctuation - Max value of V-statistic	U_{mt}, m/s Pressure fluctuation – CV
Silica sand	25	0.36	0.41
Silica sand	115	0.37	0.38

Table 3-7 Impact of temperature on U_{mt} found using pressure fluctuations (inclined distributor, no baffle, even case, 190 μm sand)

Table 3-8 shows the impact of gas distributor configuration on the U_{mt}. It indicated that the U_{mt} found with new and conventional parameters showed a slight difference. Therefore, it was difficult to conclude if the gas distributor configuration has a significant impact. From the point of view of operating in a commercial coker, what matters is the

impact of the regime transition on the bed hydrodynamics with liquid injection (for details, see section 5.1 and section 6.4).

U_{mt}, m/s	Pressure fluctuation - Max value of V-statistic	Pressure fluctuation - CV
Flat distributor	0.49	0.35
Western case	0.41	0.37
Even case	0.36	0.41
Eastern case	0.33	0.36

Table 3-8 Impact of gas distributor configuration on U_{mt} found using two parameters of pressure fluctuations. (No baffle, 190 μm sand, 25 °C)

b. Radiation transmission method

Figure 3.51 shows that bed voidage (ε_{air}) vs. superficial gas velocity (V_g) could be used to obtain U_{mt}. Two sets of tests were conducted: one where the superficial gas velocity was gradually increased and the other where the superficial gas velocity was gradually decreased. The ascending and descending order to change V_g did not affect results.

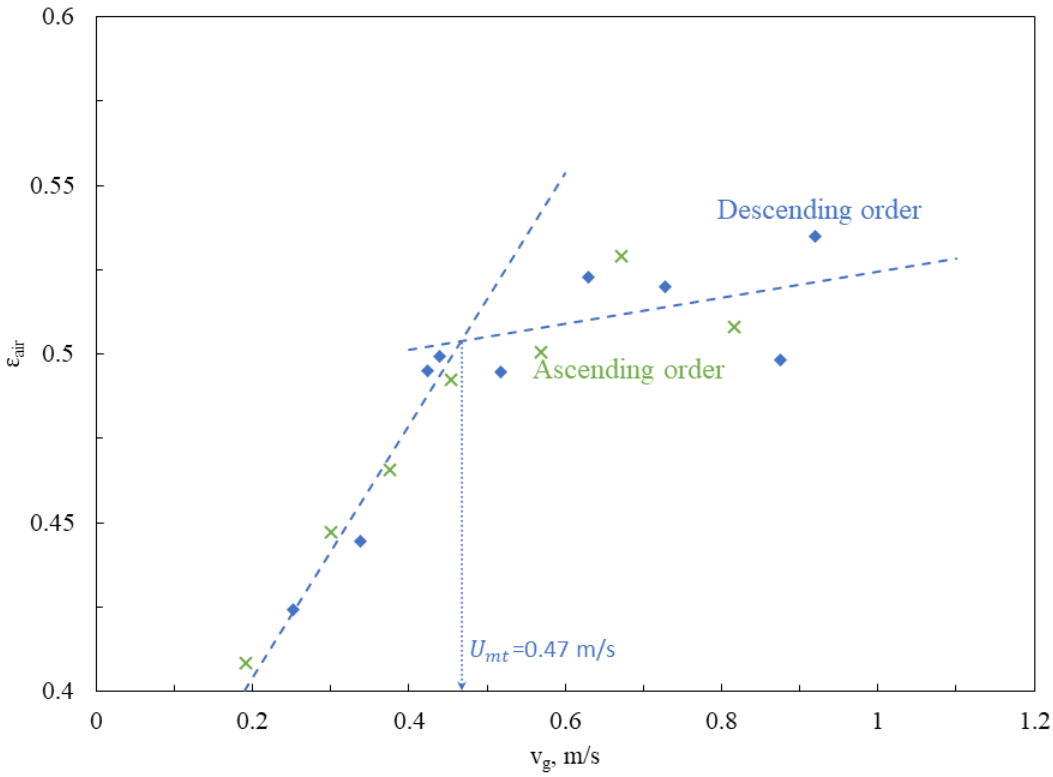

Figure 3.51 Example of bed voidage (ε_{air}) vs. superficial gas velocity (V_g) to obtain U_{mt}. (Source location: x=0.25 m, z=0.65 m; Sensor location: x=0.25 m, z=1.05 m; inclined distributor, No baffle, western case, 25 °C)

Table 3-9 shows that the radiation transmission method confirmed the little variation found with different gas distributor configurations. However, this method was not able to show which parameter from the pressure fluctuations was more accurate. Therefore, in the later chapters, when comparing the U_{mt} with transition velocity found with other

methods with injection, the U_{mt} obtained from both coefficient of variation and maximum value of V-statistic from pressure fluctuation method will be given.

U_{mt}, m/s	Pressure fluctuation - Max value of V-statistic	Pressure fluctuation - CV	Radiation transmission (at different locations) – bed voidage
Western case	0.41	0.37	0.33 – 0.48
Even case	0.36	0.41	0.32 – 0.47
Eastern case	0.33	0.36	0.3 – 0.57

Table 3-9 Summary of the impact of gas distributor configuration on U_{mt} found using two different methods and parameters. (No baffle, 190 μm sand, 25 °C)

3.9 Conclusion

This chapter introduced all methods applied in this research. For each method, validation experiments are conducted with at least one different method, which ensures the experimental data obtained are reliable. Therefore, the reliable, detailed experimental data in a scaled-down model can reach a fundamental understanding of how local hydrodynamics affects the initial liquid distribution. This will provide engineers designing or modifying commercial cokers with the tools required to improve liquid distribution.

3.10 Nomenclature

A	VDC	Cycle amplitude
B_i		Undefined signal characteristic
$\boldsymbol{C}$	$Counts/s$	Time-averaged counts

$\boldsymbol{C_{empty}}$	$Counts/s$	Time-averaged counts when there are no solids in the bed
$\boldsymbol{C_i}$		Undefined signal characteristic
$\overline{C_L}$	g/kg	Average liquid concentration in g of water/ kg of dry solids
$\boldsymbol{C_{L,k}}$	g/kg	Liquid concentration in g of water/ kg of dry solids of probe k in conductance method
C_{mf}	$Counts/s$	Time-averaged counts when the bed is fluidized with the minimum fluidization gas velocity
$\boldsymbol{C_{L\,max,i}}$	$\frac{g\ of\ water}{kg\ of\ dry\ solids}$	Maximum liquid concentration at location i
$\boldsymbol{C_{L\,max,\,AVG}}$	$\frac{g\ of\ water}{kg\ of\ dry\ solids}$	Average of maximum Liquid concentration at location i of the whole bed
$\boldsymbol{C_{L\,max,abv\,baffle,\,AVG}}$	$\frac{g\ of\ water}{kg\ of\ dry\ solids}$	Average of maximum Liquid concentration at locations above the baffle
$\boldsymbol{C_{L\,max,\,baffle,\,AVG}}$	$\frac{g\ of\ water}{kg\ of\ dry\ solids}$	Average of maximum Liquid concentration at locations at baffle region
d	m	Total bed length
d_P	μm	Particle Sauter-mean diameter
D	m	Distance between two points
f		Free moisture/ water injected

f_{avg}	Hz	Average frequency
F_L	g/s	Liquid flowrate
F_t		Cumulative fraction of freeboard pressure
$F_{vap,\,t_{end}}$		Cumulative fraction of freeboard pressure at the end of injection
GLR	%	Gas to liquid ratio
I	A	Electrical current
L_{jet}	m	Jet penetration in a fluidized bed
m_{inj}	g	Mass of liquid injection
$\overline{q_b}$	$kg/(s \cdot m^2)$	Average cross-sectional volumetric flux
q_{bi}	$kg/(s \cdot m^2)$	Local bubble volumetric flux
$\overline{q_{b,cal}}$	$kg/(s \cdot m^2)$	Calculated average cross-sectional volumetric flux
q_i		Normalized local bubble volumetric flux
r	Ω	Resistor
R_{bed}	Ω	Resistance of fluid bed
R^2		A statistical measure of fit indicates how much variation of a dependent variable is explained by the independent variable(s) in a regression model.

ΔT	$°C$	Temperature difference to the initial bed temperature
$T_{initial}$	$°C$	Bed temperature before injection
$\boldsymbol{t_{end,\,inj}}$	s	Time at the end of injection
$\boldsymbol{t_{\max avg,\,C_L}}$	s	The average time when the local liquid concentration reaches its maximum of all probes in the bed
$\boldsymbol{t_{max,\,C_L}}$	s	The time when the local liquid concentration reaches its maximum
$\boldsymbol{t_{C_{L,max,\,i}}}$	s	The time it takes to reach maximum liquid concentration at location i
$\boldsymbol{\left(t_{C_{L,max,\,i}} - t_{C_{L0,i}}\right)_{avg}}$	s	The average time it takes to reach maximum local liquid concentration since the conductance probe detects the liquid at location i of the whole bed
$\boldsymbol{t_{C_{L,max,\,abv\,baffle},i}}$	s	The time it takes to reach maximum local liquid concentration at location i above the baffle
$\boldsymbol{t_{C_{L,max,\,baffle},i}}$	s	The time it takes to reach maximum local liquid concentration at location i at the baffle region
$\boldsymbol{t_{C_{L0,i}}}$	s	The time it takes for the liquid to be detected for conductance probe at location i

$\boldsymbol{t_{C_{L0,\,avg}}}$	s	The average time it takes for the liquid to be detected for conductance probe at location i of the whole bed
$\boldsymbol{t_{C_{L0,\,abv\,baffle,avg}}}$	s	The average time it takes for the liquid to be detected for conductance probe at location i above the baffle
$\boldsymbol{t_{C_{L0,i}}}$	s	The time it takes for the liquid to be detected for conductance probe at location i
V_g	m/s	Superficial gas velocity
U_{mf}	m/s	Minimum fluidization gas velocity
U_{mt}	m/s	Minimum turbulent gas vel
$\bar{V}$	VDC	The average voltage of all conductance probes in bed
w	m	Total bed width
x_{bi}		Local fraction of the bed volume that is occupied by bubbles
x_i		Normalized local fraction of the bed volume that is occupied by bubbles
x_{inj}	m	Lateral injection location
x	m	Lateral location
$\overline{x_b}$		Average cross-sectional bubble concentration

$\Delta \boldsymbol{y}$	m	Distance between front and back bed wall E-probes for bubble spanning check
$z_{row\,1}$ to $z_{row\,7}$	m	The vertical location of each E-probe or conductivity row
z_{inj}	m	Vertical injection location
z	m	Vertical location

Greek

α		The coefficient for correlation of variable and local volumetric flux of bubble gas flow
$\boldsymbol{\beta}$		The coefficient for correlation of variable and local volumetric flux of bubble gas flow
$\boldsymbol{\gamma}$		The coefficient for correlation of variable and local volumetric flux of bubble gas flow
ε_{air}		Bed voidage
$\boldsymbol{\lambda_i}$	m^2	Local cross-sectional area for the volumetric flux of bubble gas
$\prod_{bed}$	S/m	The conductivity of the fluid bed
ρ_P	kg/m^3	Apparent particle density
φ_{ac}		The cumulated liquid fraction at the end of steady-state
$\boldsymbol{\varphi_{empty}}$	$counts/ms$	Bed without solids radiation counts changing rate

$\boldsymbol{\varphi_{detector}}$	$counts/ms$	The radiation counts changing rate in any condition
φ_{packed}	$counts/ms$	Packed bed radiation counts changing rate

3.11 References

1. Jahanmiri, M., *Use of a Baffle to Enhance Distribution of a Liquid Sprayed into a Gas-Solid Fluidized Bed*. 2017, MESc thesis, Western University.

2. Li, L., *Effect of Local Bed Hydrodynamics on the Distribution of Liquid in a Fluidized Bed*. 2016, MESc thesis, Western University.

3. Joness, A.M., *The Effect of Scale on Spray Nozzle Performance.* 2019.

4. Idowu, J., C. Briens, and D. Pjontek, *Spraying Slurries: Impact of Slurry Properties on Spray Characteristics and Agglomerate Formation in Fluidized Beds.* Mater. Sci., 2018.

5. Bhatti, M.O.I., *Study of Motion of Agglomerates Through a Fluidized Bed*. 2017, MESc thesis, Western University.

6. Ellis, N., et al., *Characterization of dynamic behaviour in gas-solid turbulent fluidized bed using chaos and wavelet analyses.* Chemical Engineering Journal, 2003. **96**(1-3): p. 105-116.

7. Saayman, J., et al., *Fast X-ray tomography for the quantification of the bubbling-, turbulent- and fast fluidization-flow regimes and void structures.* Chemical Engineering Journal, 2013. **234**: p. 437-447.

8. Xing, X., *Numerical study of the effect of gas distributors and baffles on the bubble distribution, gas and solid mixing in a fluidized bed,* in *Chemical and biochemical engineering*. 2020, Western University. p. 292.

9. Cochet, Y., *Impact of column geometry and internals on gas and particle flows in a fluidized bed with downward solids circulation*, in *Chemical and Biochemical Engineering*. 2021, Western University: unpublished.

10. Darton, R., et al., *BUBBLE GROWTH DUE TO COALESCENCE IN FLUIDISED BEDS.* 1977.

11. Hurst, H.E., *Long-term storage capacity of reservoirs.* Trans. Amer. Soc. Civil Eng., 1951. **116**: p. 770-808.

12. Briens, L. and C. Briens, *Cycle detection and characterization in chemical engineering.* AIChE journal, 2002. **48**(5): p. 970-980.

13. Peters, E.E., *Fractal market analysis: applying chaos theory to investment and economics*. Vol. 24. 1994: John Wiley & Sons.

14. Careaga, F.S., C. Briens, and F. Berruti. *Measurement of penetration and cycle time of jets from an industrial fluid coking spray nozzle*. in *Fluidization XV*. 2016. Montebello, Quebec, Canada: ECI.

15. Briens, C. and J. McMillan, *Review of Research Related to Fluid Cokers.* Energy & Fuels, 2021.

16. Reyes, L.A.P., *Effect of temperature and successive sprays on liquid distribution in fluidized beds*. 2015, School of Graduate and Postdoctoral Studies, University of Western Ontario.

17. Bruhns, S. and J. Werther, *An investigation of the mechanism of liquid injection into fluidized beds.* AIChE Journal, 2005. **51**(3): p. 766-775.

18. Ariyapadi, S., et al., *Horizontal penetration of gas-liquid spray jets in gas-solid fluidized beds.* International Journal of Chemical Reactor Engineering, 2004. **2**(1).

19. Bi, H.T., et al., *A state-of-the-art review of gas–solid turbulent fluidization.* Chemical Engineering Science, 2000. **55**(21): p. 4789-4825.

20. LEE, G.S. and S.D. KIM, *Gas mixing in slugging and turbulent fluidized beds.* Chemical Engineering Communications, 1989. **86**(1): p. 91-111.

21. Thiel, W.J. and O.E. Potter, *Slugging in Fluidized Beds.* Industrial & Engineering Chemistry Fundamentals, 1977. **16**(2): p. 242-247.

22. Silitonga, H.M., et al., *EVOLUTION AND FLOW OF VAPORS IN A FLUIDIZED BED*, in *CFB13*. 2020.

23. Hamidi, M., *Development And Study Of Measurement Methods For Jets And Bogging In A Fluidized Bed*. 2015, PhD thesis, Western University.

24. Cochet, Y., et al., *Impact of column geometry and internals on gas and particle flows in a fluidized bed with downward solids circulation: Effect of lateral injection profile and baffles.* Powder Technology, 2020. **372**: p. 275-289.

25. WYATT, J.e.a., *CIRCULATING FLUID BED REACTOR WITH IMPROVED CIRCULATION*, U.S.P.A. Publication, Editor. 2011: United States. p. 9.

26. Careaga, F.J.S., *Hydrodynamics in Recirculating Fluidized Bed Mimicking the Stripper Section of the Fluid Coker* in *Chemical and Biochemical Engineering* 2013, Western University.

27. Portoghese, F., F. Berruti, and C. Briens, *Use of triboelectric probes for on-line monitoring of liquid concentration in wet gas–solid fluidized beds.* Chemical Engineering Science, 2005. **60**(22): p. 6043-6048.

28. Ariyapadi, S., et al., *Digital X-ray imaging technique to study the horizontal injection of gas-liquid jets into fluidized beds.* International Journal of Chemical Reactor Engineering, 2003. **1**(1): p. A 56.

29. Farkhondehkavaki, M., *Developing Novel Methods to characterize Liquid Dispersion in a Fluidized bed.* 2012.

30. Silitonga, H., *EVOLUTION AND FLOW OF VAPORS IN A FLUIDIZED BED*. 2021, Western University.

31. Abba, I.A., et al., *Spanning the flow regimes: generic fluidized‐bed reactor model.* AIChE Journal, 2003. **49**(7): p. 1838-1848.

32. Bi, H., J. Grace, and K. Lim, *Transition from bubbling to turbulent fluidization.* Industrial & engineering chemistry research, 1995. **34**(11): p. 4003-4008.

33. Choi, J.-H., H.-J. Ryu, and C.-K. Yi, *A model for the temperature effect on onset velocity of turbulent fluidization of Geldart type A particles.* Korean Journal of Chemical Engineering, 2010. **28**(1): p. 304-307.

34. Ellis, N., *Hydrodynamics of gas-solid turbulent fluidized beds*. 2003, University of British Columbia: UBC.

35. Gonzalez, A., J. Chaouki, and A. Chehbouni. *Effect of temperature on the onset of turbulent fluidization*. in *Proc, of 8th International Symposium of the Engineering Foundation, Fluidization VIII, Tours, France*. 1995.

36. Seo, M.W., et al., *The transition velocities in a dual circulating fluidized bed reactor with variation of temperatures.* Powder Technology, 2014. **264**: p. 583-591.

37. Sun, G. *Transition to turbulent fluidization and its prediction*. in *Fluidization VI*. 1989. Banff, Canada: Engineering Foundation.

38. Yang, W.-C., *Mechanistic models for transitions between regimes of fluidization.* AIChE Journal, 1984. **30**(6): p. 1025-1027.

Chapter 4

4 Impact of gas distributor configurations and baffle(s) on bubble flow

The second objective of this thesis is to study the effect of distributor configuration and baffles on gas distribution. This chapter shows the gas distribution change due to the change of gas distributor configuration (section 2.1.2), baffles (section 2.1.3), superficial gas velocity, and bed temperature. This chapter also compares the experimental results from this thesis with the CFD modeling results from Xing et al.[1], to determine whether CFD modeling could be used to scale up the results of this study. This chapter will be used to build a connection with the results about initial liquid distribution and solids mixing in chapters 5 and 6.

4.1 Impact of gas distributor configuration

Figure 4.1 shows that the gas distributor configuration greatly affected the gas distribution at the spray level, using the E-probe method (introduced in section 3.1). As introduced in section 3.1, the q_i was the dimensionless gas flux profile, described in Eq.3-1: $q_i = \frac{q_{bi}}{\overline{q_b}}$, where the q_{bi} was the local bubble volumetric flux around each probe, and the $\overline{q_b}$ was the cross-sectional average volumetric flux. The flat distributor was a perforated plate gas distributor, one of the most commonly used gas distributors in fluid beds. As with most flat distributors, the gas bubbles concentrated to the bed center, displaying a symmetrical profile. After removing the perforated plate, modified the gas distributor configurations by turning on and off valves connected to the tuyeres of the gas distributor, as stated in section 2.1.2. For each gas distributor configuration, 10 valves were open. The western case concentrated gas bubbles to the western side of the bed. The eastern case concentrated on the eastern side of the bed. The even case concentrated gas bubbles to the center of the bed, but a higher gas bubble profile was seen on the western side. The possible reason is that, in Figure 2.4, at the bottom of the unit, there was a pipe for solids drainage to retrieve agglomerates easily. However, there was no incoming fluidization gas from this pipe, which could be why the gas bubble profile for the even

case was lower on the eastern side of the bed.

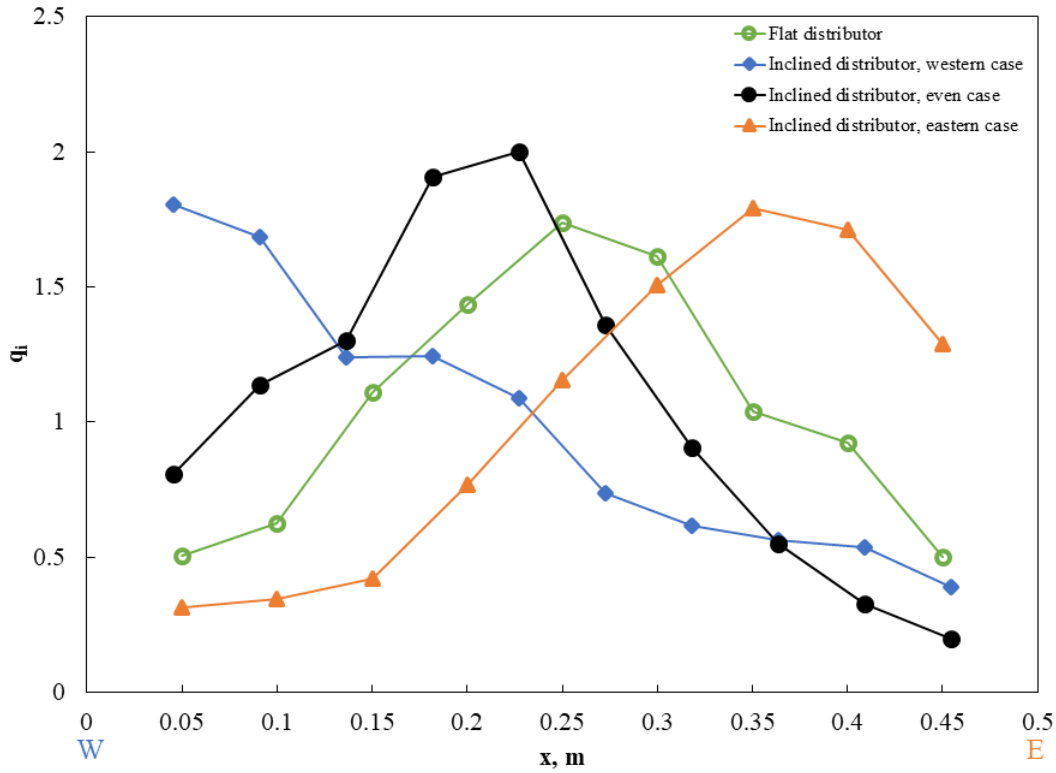

Figure 4.1 Impact of gas distributor configurations (Figure 2.4) on gas distribution at spray level (No baffle, x = 0 – 0.5 m, inclined distributor: $z = 0.67\ m$, flat distributor: $z = 0.35\ m$; $V_g = 1\ m/s$, $T_{bed} = 30\ °C$)

Figure 4.2 shows with the inclined distributor, different gas distributor configurations successfully concentrated gas bubbles to different sides of the bed for the whole column. As for the eastern case, the break at around $z = 0.45\ m$ could be related to original gas bubble direction. The gas bubbles hit the eastern side bed wall then come back. Then they merged with new bubbles coming in from tuyeres that were near the center of the inclined distributor.

The gas distribution was symmetrical with the flat distributor, and the gas bubbles concentrated to the center near and below the injection level. However, the gas bubbles above the injection level concentrated on the eastern side of the bed. This result has been

confirmed with another three methods: the radiation transmission method, pressure measurement with a bubbler tube (provided by a fellow student, Jessica Godin), and solids entrainment to two cyclones on the western and eastern sides of the bed. Many attempts were made to correct the potential issue that created it, such as leveling the unit, adjusting the cyclone pressure, and opening the unit to check for possible reasons. Unfortunately, the above effort did not change the gas distribution observed in Figure 4.2. Because the gas distribution at the bottom section was very symmetrical and similar to the core-annular gas flow in a commercial coker (introduced in section 1.3.3), we decided to move the injection level to $z = 0.4\ m$ for this distributor, as shown in Figure 4.2.

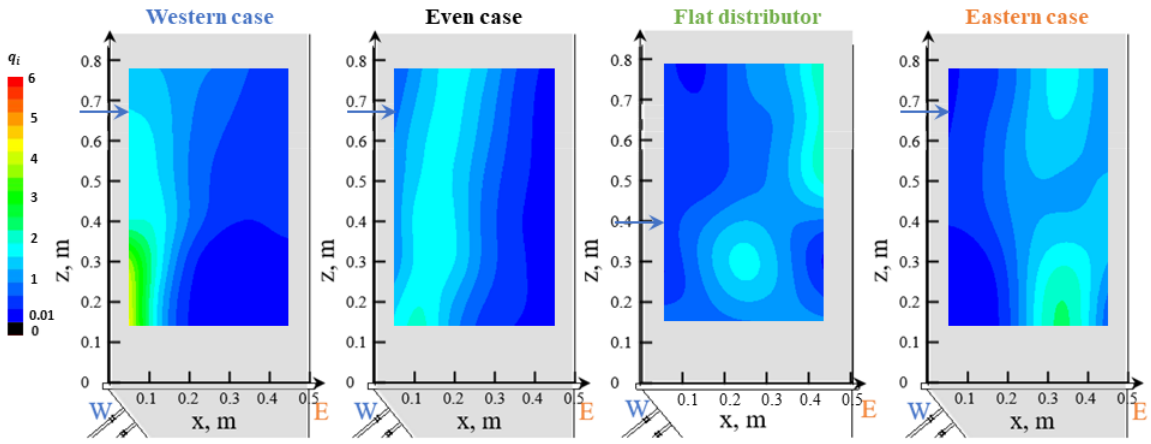

Figure 4.2 The impact of gas distributor configuration (Figure 2.4) on gas distribution (no baffle, $V_g = 1\ m/s$, $T_{bed} = 30\ °C$) (The spray nozzle level is shown with a horizontal blue arrow on the West side).

4.2 Impact of a baffle

Figure 4.3 shows that the asymmetrical baffle without a flux-tube significantly reduced the gas bubbles fraction above the baffle and redirected gas bubbles near the baffle tip region. The above finding was consistent with all three gas distributor configurations.

In the western and even cases, the gas bubbles had to detour to avoid the baffle. Therefore, it is understandable that the gas bubbles were concentrated in the baffle tip region. As for the eastern case, although the flow of bubbles below the baffle was small, there were enough large bubbles coming out of the lip of the baffle that acted as a "magnet" for the bubbles elsewhere in the bed. Because the bubbles created a local zone with a relatively low pressure, which could "suck in" gas near it, they would suck the gas from both the western and eastern sides.

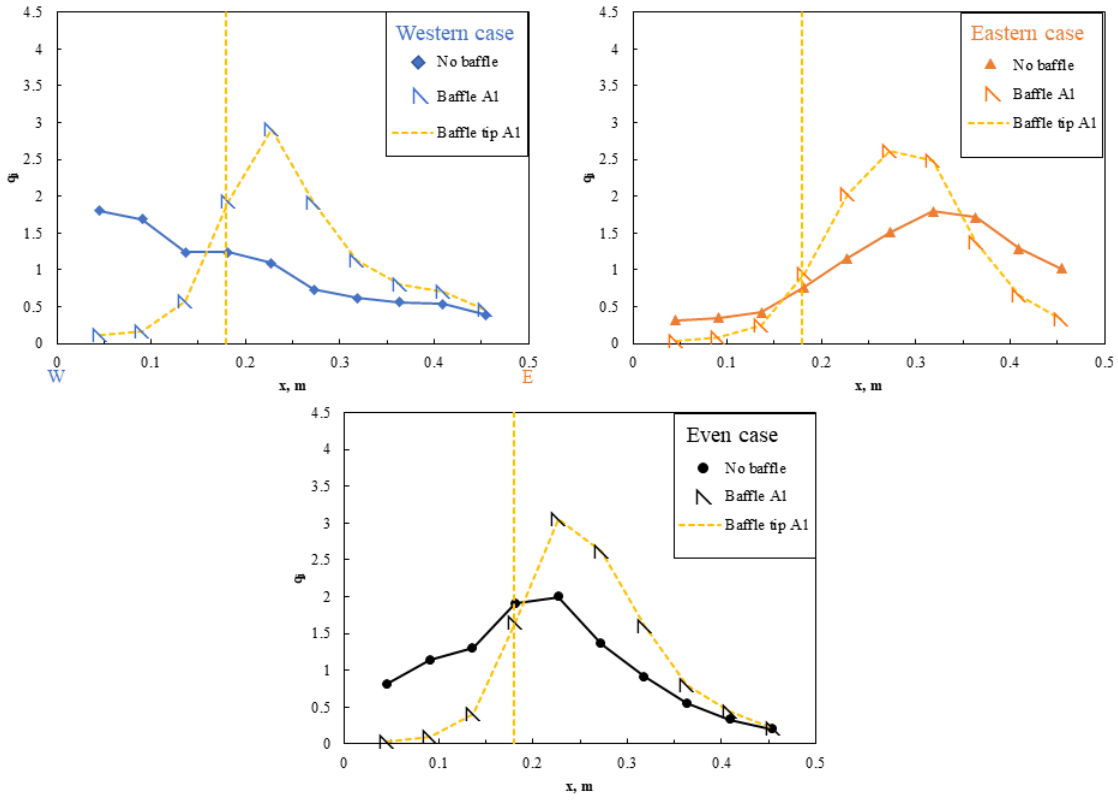

Figure 4.3 Impact of baffle A1 (asymmetrical baffle without flux-tube, 36 % blocking cross-sectional area (Figure 2.6 A)) on gas distribution at spray level (Inclined distributor, x = 0 – 0.5 m, $z = 0.67\ m$; $V_g = 1\ m/s$, $T_{bed} = 30\ °C$)

Figure 4.4 shows that the asymmetrical baffle without a flux-tube and with a larger, 50 % blocking cross-sectional area redirected gas bubbles to the near baffle tip region at the spray level. The above finding was consistent with all three gas distributor configurations. Compared to the smaller asymmetrical baffle with a 36 % blocking cross-sectional area (baffle A1 in Figure 4.3), the larger baffle showed a more vigorous gas bubble flow at the baffle tip region. Near the western side bed wall, the normalized local volumetric flux was very low for all three cases with the baffle A4, because the large size of the baffle prevented the gas from reaching most of the zone above the baffle. Because of this reason, the baffle may not be suitable to be installed in a commercial coker. We tested this baffle because we wanted the variation of gas distribution at spray level to be as large as possible to be able to cover more possible gas distributions in a coker.

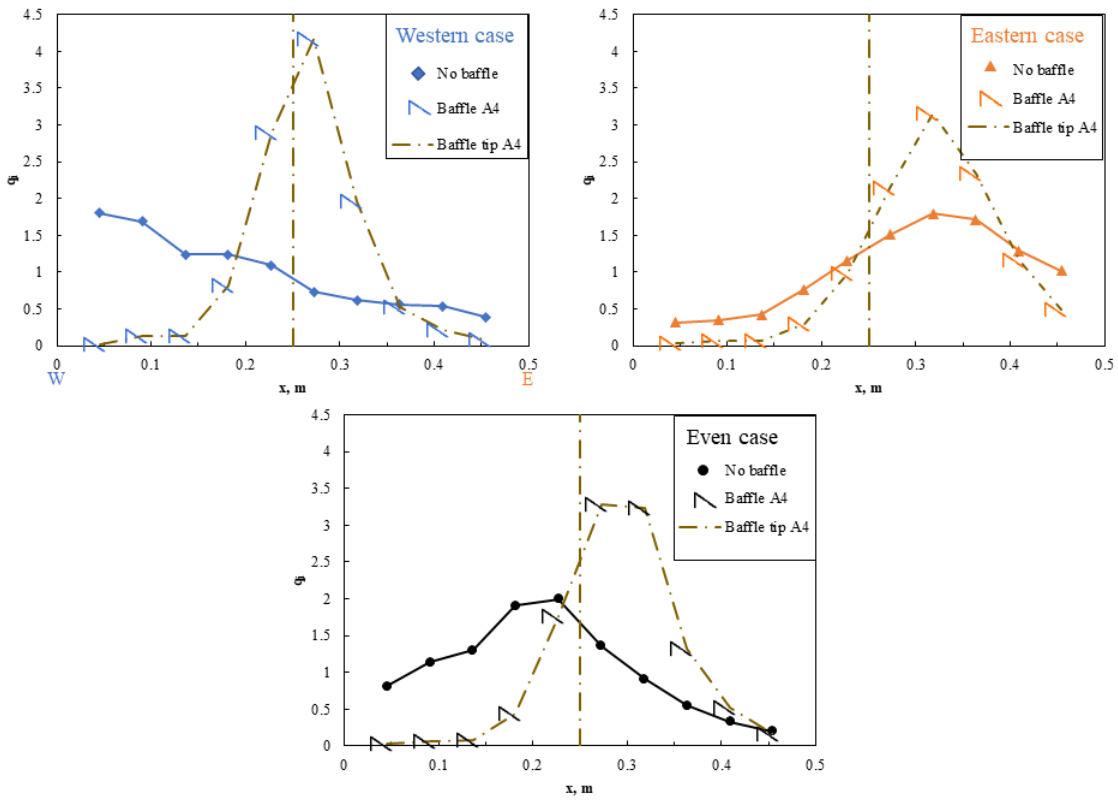

Figure 4.4 Impact of baffle A4 (asymmetrical baffle without flux-tube, 50 % blocking cross-sectional area (Figure 2.6 D)) on gas distribution at spray level (Inclined distributor, x = 0 – 0.5 m, $z = 0.67\ m$; $V_g = 1\ m/s$, $T_{bed} = 30\ °C$)

Figure 4.5 shows that an asymmetrical baffle with a flux-tube had a minor impact on gas distribution at the spray level with all three gas distributor configurations. It can be seen that the normalized local gas bubble volumetric flux was slightly higher above the flux-tube region, because the flux-tube allows gas bubbles to pass through.

As for the even case, a baffle on the western side moved gas bubbles to the eastern wall region. It could be because the baffle tip redistributed the gas bubbles. Large bubbles that coming out from the lip of the baffle acted as a “magnet” for the bubbles elsewhere in the bed.

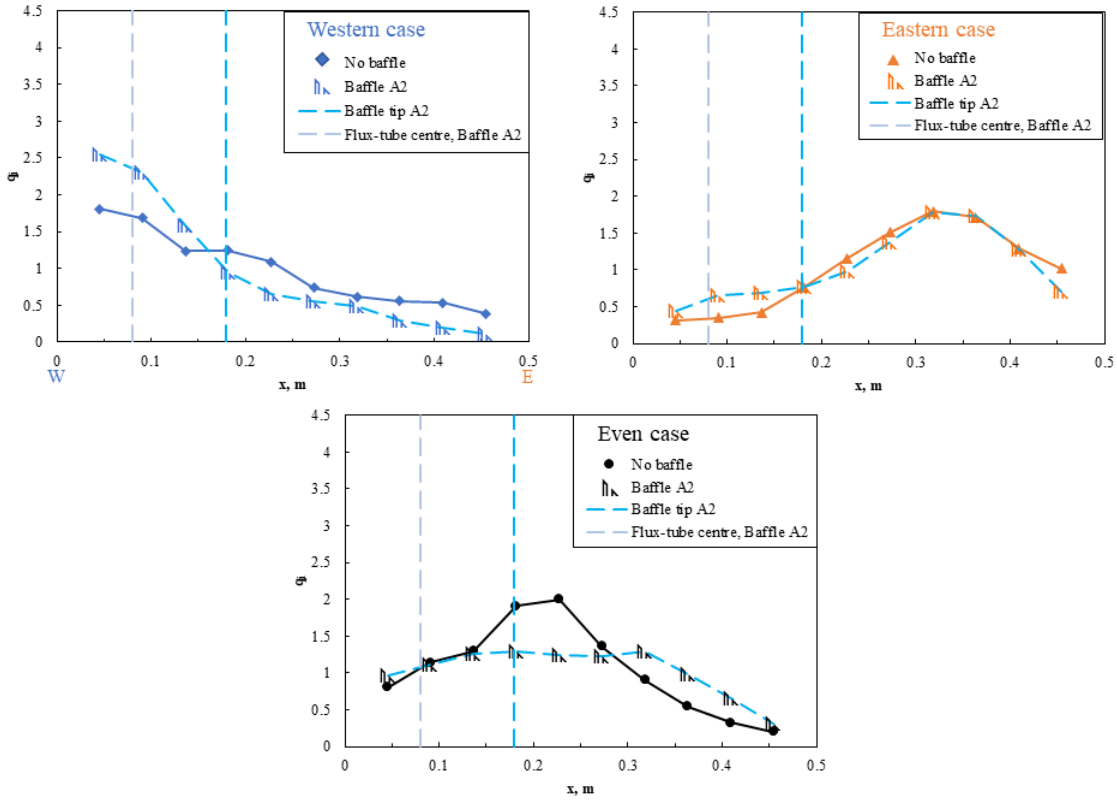

Figure 4.5 Impact of baffle A2 (asymmetrical baffle with a flux-tube (Figure 2.6 B)) on gas distribution at spray level (Inclined distributor, x = 0 – 0.5 m, $z = 0.67\ m$; $V_g = 1\ m/s, T_{bed} = 30\ °C, T_{bed} = 30\ °C$)

Figure 4.6 shows that the slightly shorter flux-tube had a minor impact on gas distribution at the spray level.

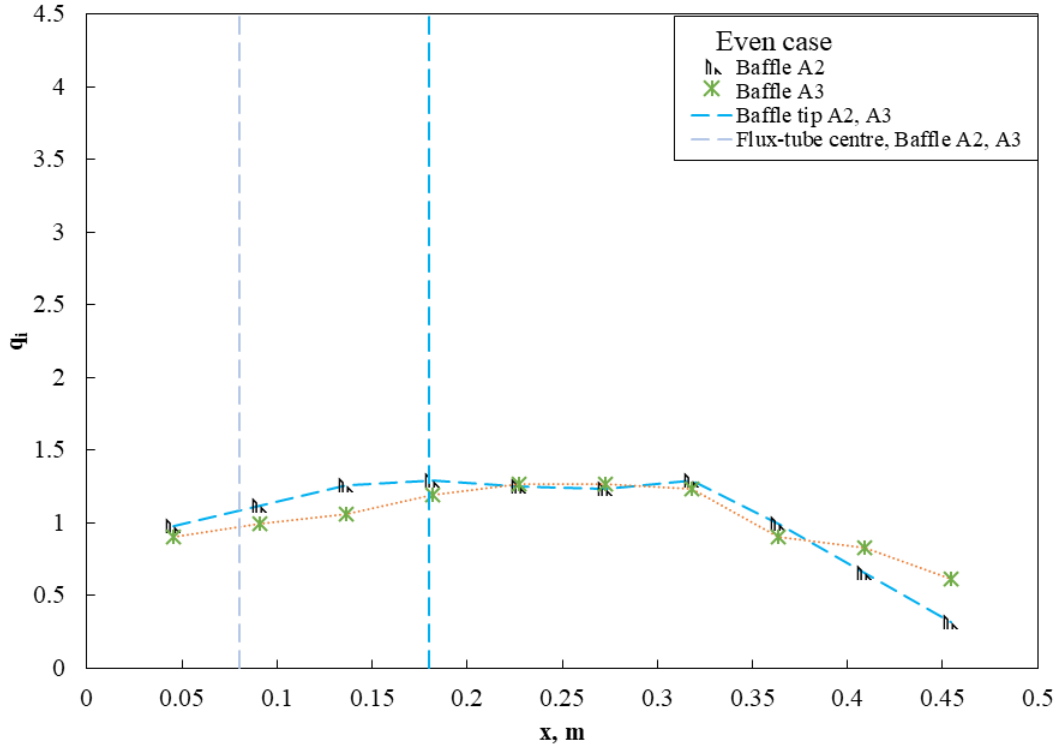

Figure 4.6 Impact of flux-tube length (asymmetrical baffle with a standard flux-tube (Figure 2.6 B) & a shorter flux-tube (Figure 2.6 C)) on gas distribution at spray level (Inclined distributor, even case, x = 0 – 0.5 m, $z = 0.67\ m$; $V_g = 1\ m/s$, $T_{bed} = 30\ °C$)

Figure 4.7 shows that the symmetrical baffle reduced the gas bubbles within the baffle regions and redirected the gas bubbles to the gap between the baffle tips.

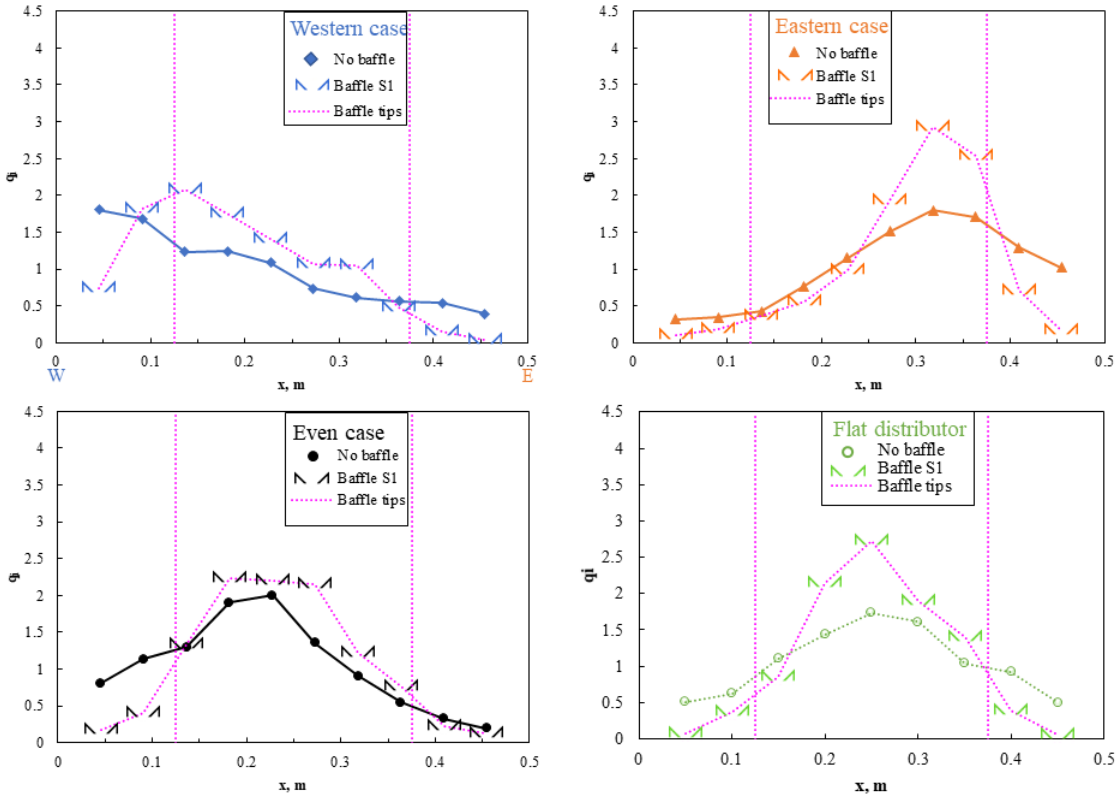

Figure 4.7 Impact of baffle S1 (symmetrical baffle without flux-tube (Figure 2.7 A)) on gas distribution at spray level (x = 0 – 0.5 m, $V_g = 1\ m/s$, $T_{bed} = 30\ °C$, inclined distributor: $z = 0.67\ m$; flat distributor: $z = 0.4\ m$)

In section 2.1.3, Figure 2.7, a symmetrical baffle with a connector was introduced. The objective of the connector was to connect the two baffle pockets of baffle Type S1 to equilibrate the pressures in the pockets under each half baffle, because in the cylindrical industrial coker, there is a single pocket under the whole baffle, where the pressure is the

same. Figure 4.8 shows that this connector had a minor impact on gas distribution at the spray level.

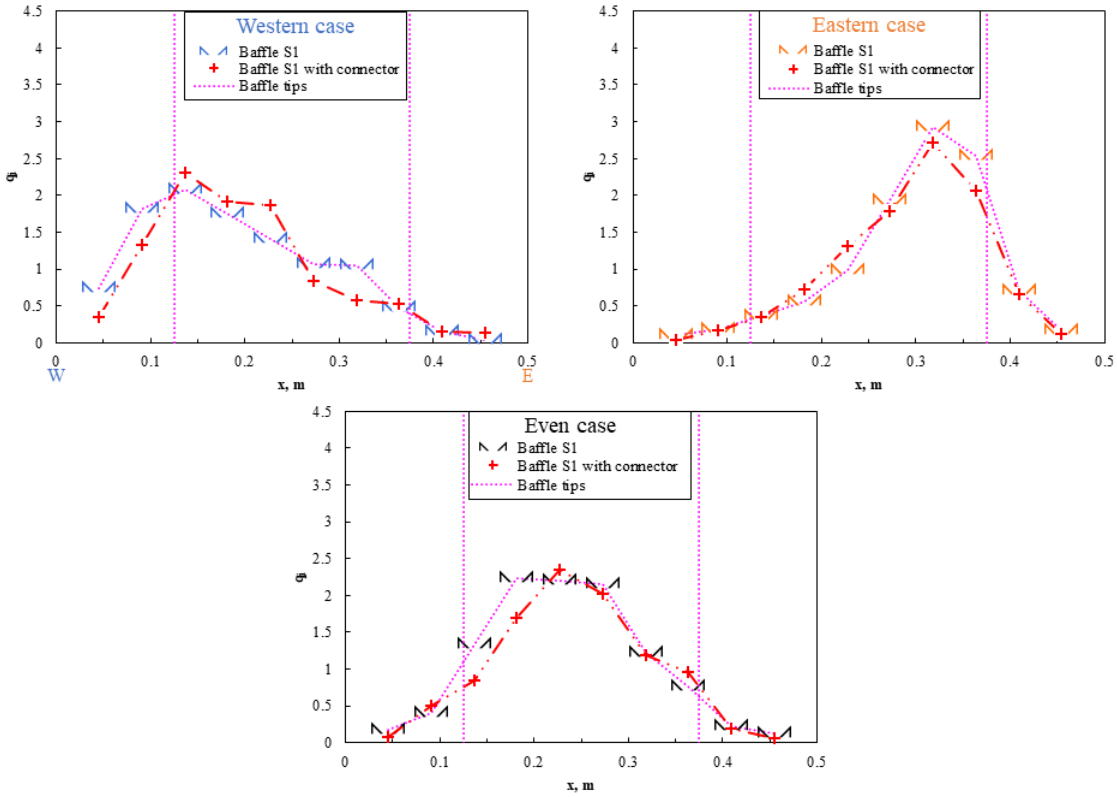

Figure 4.8 Impact of baffle S1 with a connector (symmetrical baffle without flux-tube (Figure 2.7 B)) on gas distribution at spray level (Inclined distributor, x = 0 – 0.5 m, $z = 0.67\ m$; $V_g = 1\ m/s$, $T_{bed} = 30\ °C$)

Figure 4.9 shows that the asymmetrical baffle without flux-tube reduced gas bubbles just below the baffle, and redirected gas bubbles to the baffle tip. As for the eastern case, the gas bubbles did not "hit the wall" with the existence of the baffle. This is consistent with the hypothesis that the large bubbles coming out from the lip of the baffle acted as a "magnet" for the bubbles elsewhere, because the large bubble created a relatively low-pressure zone. The baffle did not change the gas distribution below the baffle

significantly. This was confirmed with data obtained in a smaller fluid bed by Jahanmiri et al.[2].

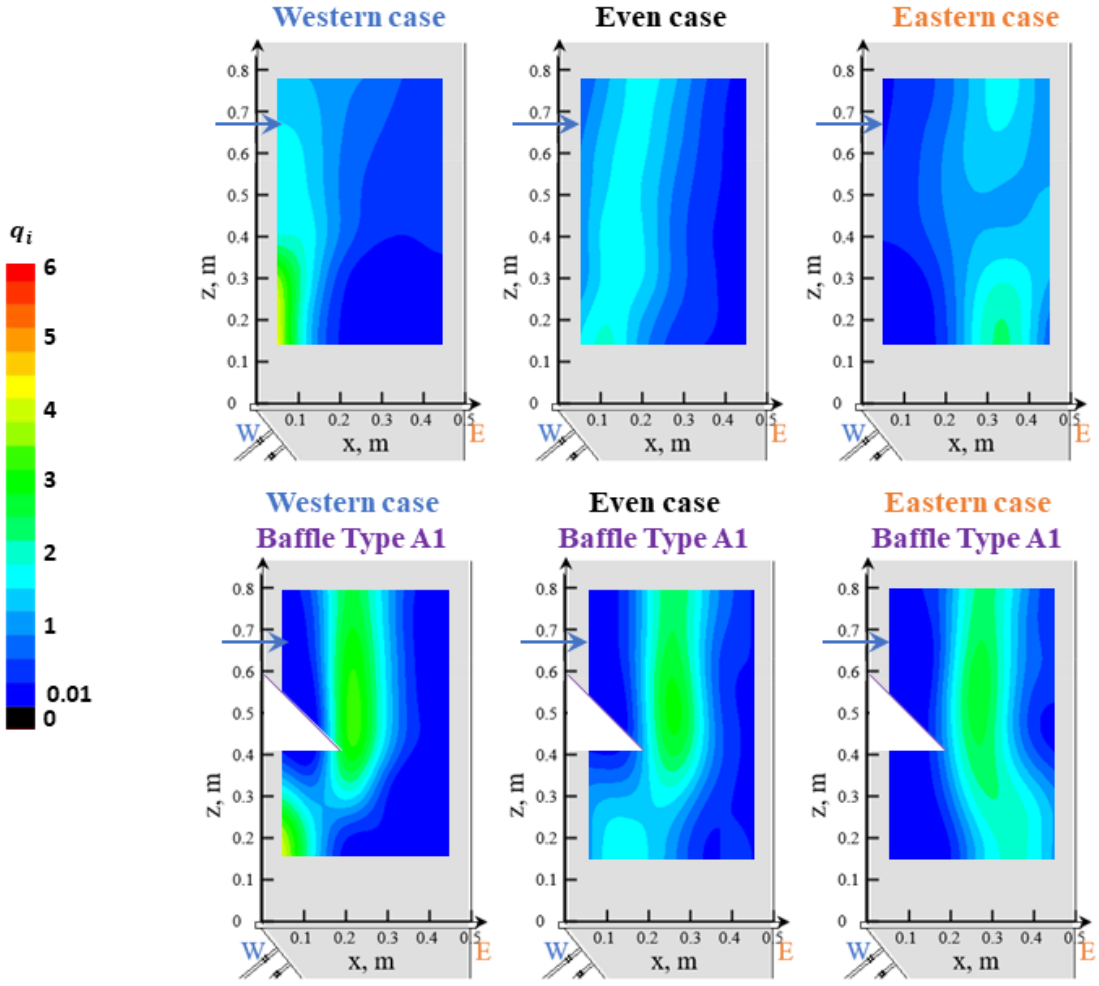

Figure 4.9 The impact of baffle type A1 on gas distribution with different gas distributor configurations (inclined distributor, $V_g = 1\ m/s$, $T_{bed} = 30\ °C$) (The spray nozzle level is shown with a horizontal blue arrow on the West side).

Figure 4.10 shows that the asymmetrical baffle with a larger cross-sectional area reduced gas bubbles just below the baffle and significantly changed the gas distribution above the baffle. The larger value of q_i above the baffle, compared to the no baffle cases, indicated a much stronger gas bubble flow was created due to the baffle partially blocking the

cross-sectional area of the bed, which increased the local gas bubble velocity at the baffle tip.

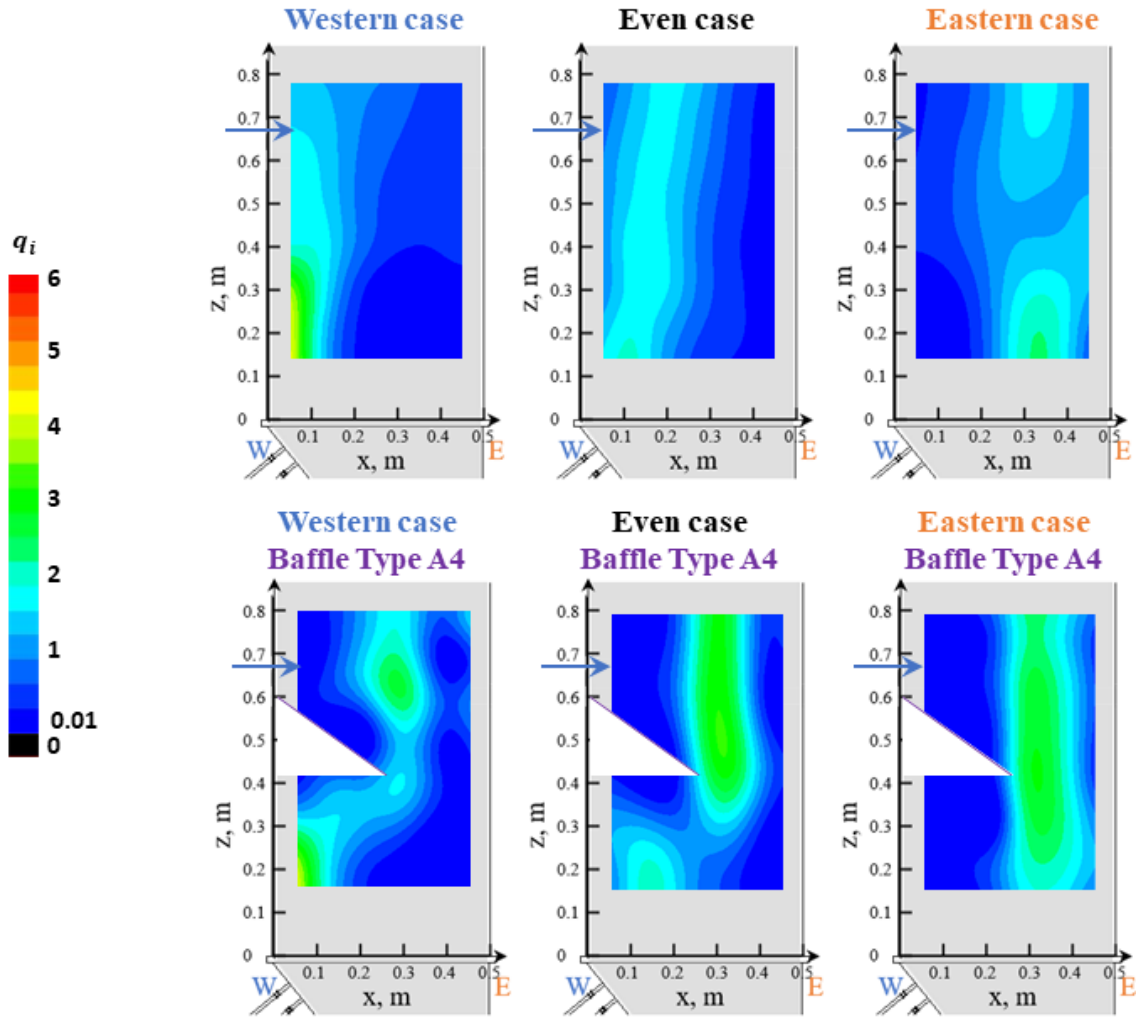

Figure 4.10 The impact of baffle type A4 on gas distribution with different gas distributor configurations (inclined distributor, $V_g = 1\ m/s$, $T_{bed} = 30\ °C$) (The spray nozzle level is shown with a horizontal blue arrow on the West side).

Figure 4.11 shows that the asymmetrical baffle without a flux-tube redirected gas bubbles to the baffle tip region, compared to the no baffle cases. However, the asymmetrical baffle with a flux-tube had a minor impact on redirecting gas bubbles, when compared to the asymmetrical baffle without flux-tube cases. The flux-tube allowed gas bubbles to

pass through, which reduced the concentrating effect of gas bubbles at the baffle tip region.

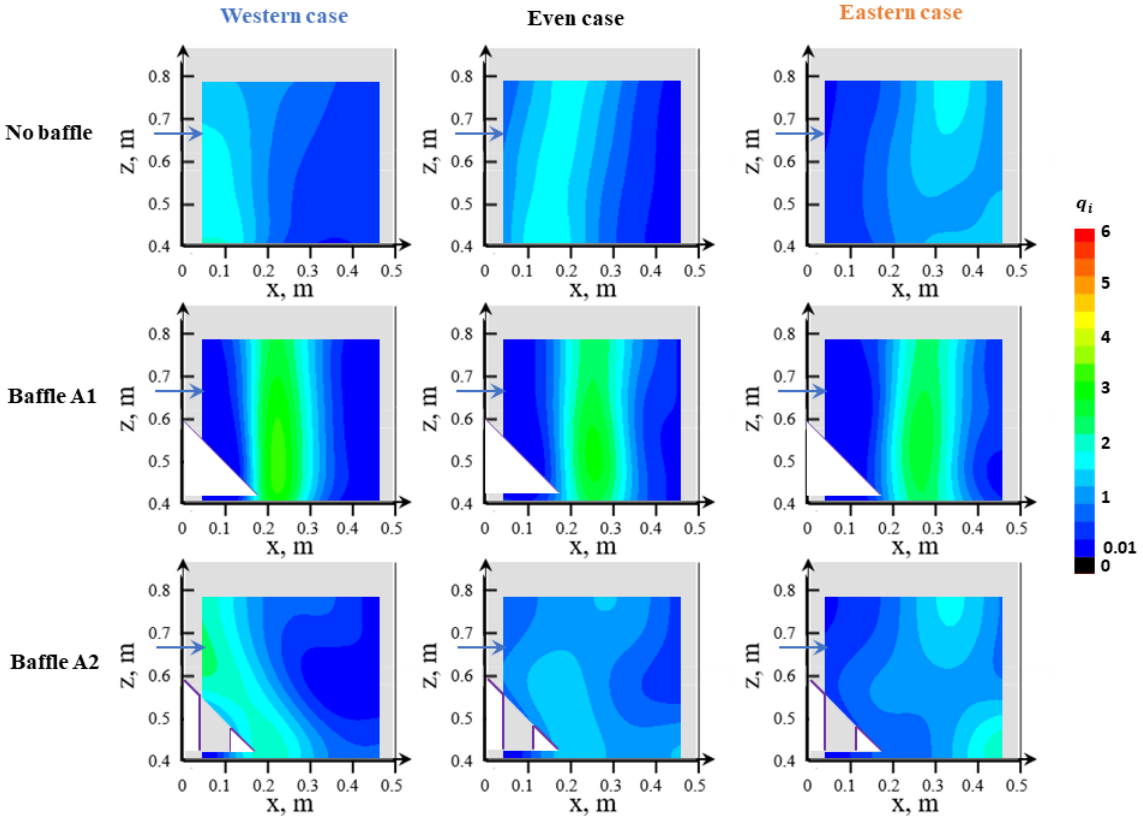

Figure 4.11 The impact of baffle type A1 and A2 on gas distribution above the baffle with different gas distributor configurations comparing to no baffle cases (inclined distributor, $V_g = 1\ m/s, T_{bed} = 30\ °C$) (The spray nozzle level is shown with a horizontal blue arrow on the West side).

Figure 4.12 shows that the symmetrical baffle reduced the gas bubbles within the baffle tip to be bed wall regions and redirected the gas bubbles to the gap between baffle tips. It seems that the redirecting effect from the baffle to above the baffle region was strong because it corrected the unexpected gas concentrating to the eastern regions of the flat distributor. For other gas distributor configurations with the inclined distributor, Figure 4.12 shows the initial inlet gas distribution still had a minor impact in the region above the baffle. For example, the gas bubbles from the western case with the baffle were redirected by the baffle. However, bubbles still concentrated more on the western side of

the bed above the baffle region. This was consistent with all three gas distributor configurations. Again, the possible reason is that had there were more gas bubbles as the initial gas sources created larger gas bubbles. The larger gas bubbles created relatively low pressure to suck in the gas bubbles near it. Therefore, even if there was a baffle, the impact of initial gas distribution still had some impact.

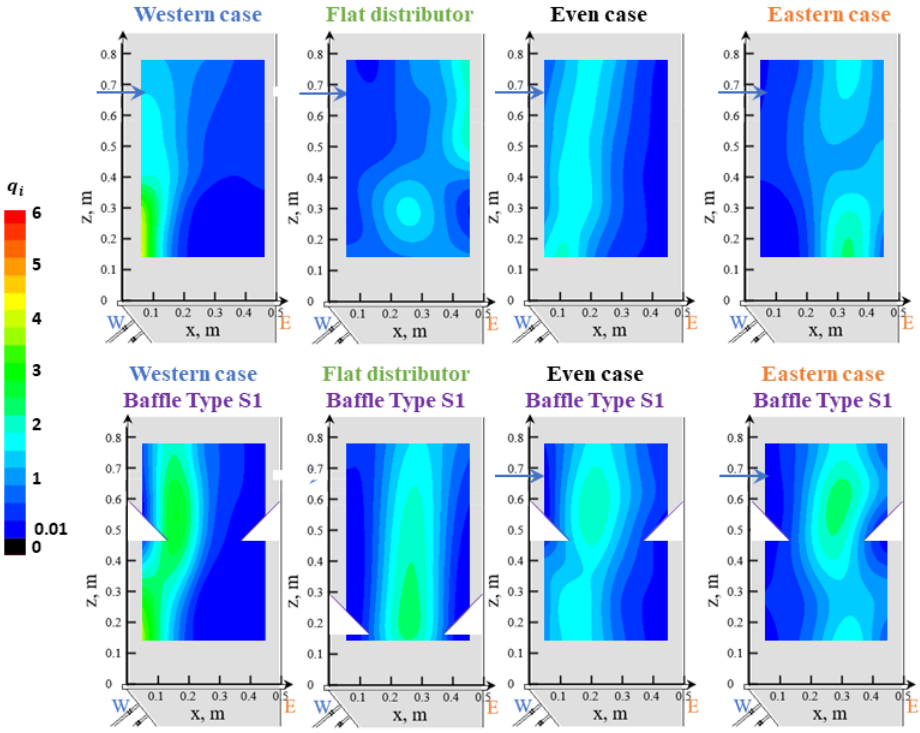

Figure 4.12 The impact of baffle type S1 on gas distribution with different gas distributor configurations (inclined distributor, $V_g = 1\ m/s, T_{bed} = 30\ °C$) (The spray nozzle level is shown with a horizontal blue arrow on the West side).

Figure 4.13 confirms that the connector of the symmetrical baffle had a minor impact on gas distribution to the whole bed.

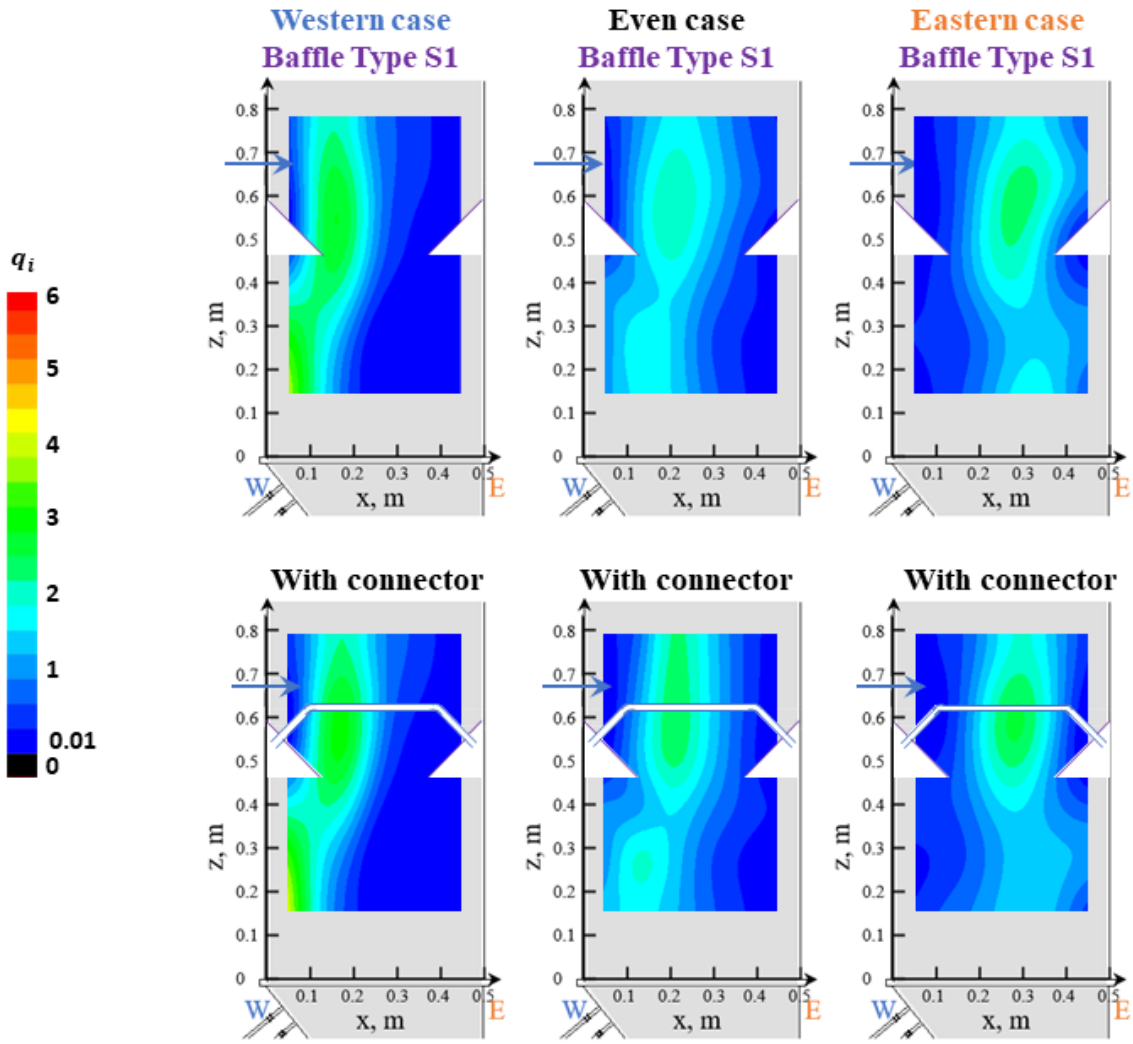

Figure 4.13 The impact of the connector on gas distribution with baffle type S1 with different gas distributor configurations (inclined distributor, $V_g = 1\ m/s$, $T_{bed} = 30\ °C$) (The spray nozzle level is shown with a horizontal blue arrow on the West side).

4.3 Impact of superficial gas velocity and bed temperature on gas distribution

4.3.1 Impact of superficial gas velocity on gas distribution

Figure 4.14 shows that with the flat distributor, without a baffle, the gas distribution was symmetrical and concentrated to the bed center for all gas velocities. The superficial gas velocity had a minor impact on the gas distribution profile at the spray level, with higher velocities resulting in a higher fraction of bubbles in the center of the bed.

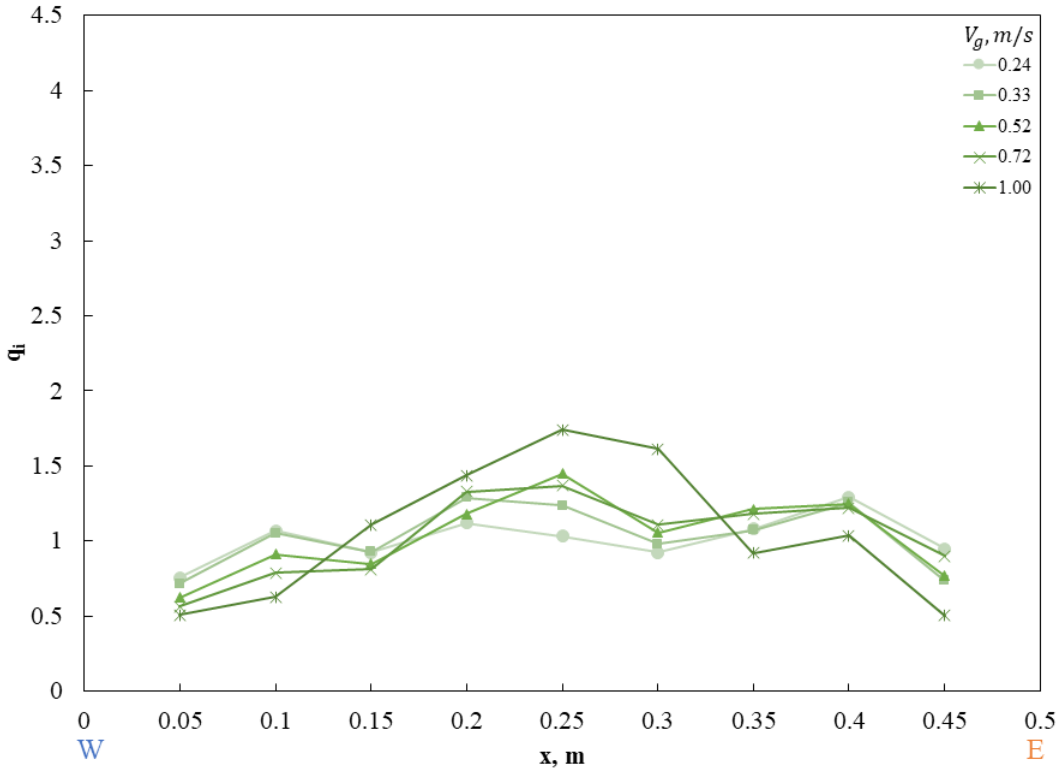

Figure 4.14 Impact of superficial gas velocity (V_g) on gas distribution at spray level (No baffle, flat distributor, x = 0 – 0.5 m, $z = 0.35\ m$)

Figure 4.15 shows that with the inclined distributor, no baffle, western case, the gas bubbles concentrated to the western side of the bed for all tested velocities. The superficial gas velocity had a minor impact on the gas distribution profile at the spray

level. With the increase of superficial gas velocity, the lateral profile became less pronounced.

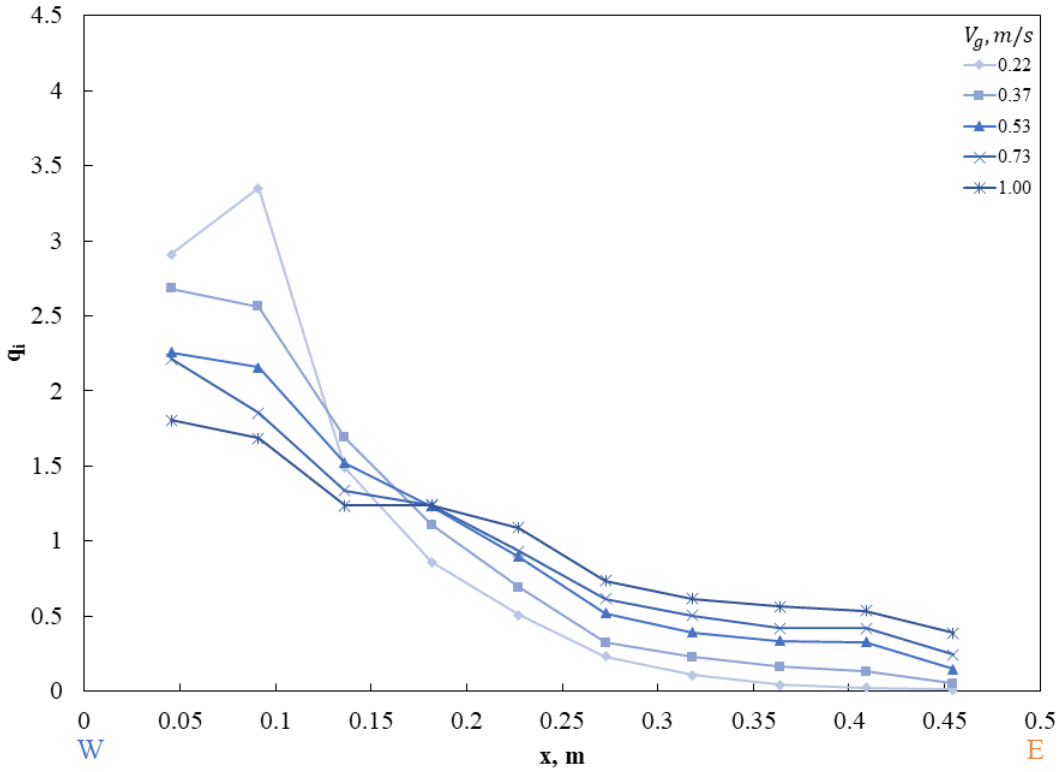

Figure 4.15 Impact of superficial gas velocity (V_g) on gas distribution at spray level (No baffle, inclined distributor, western case, x = 0 – 0.5 m, $z = 0.67\ m$)

Figure 4.16 shows that with the inclined distributor, no baffle, even case, the gas bubbles concentrated to bed center for all velocities tested. The superficial gas velocity had a minor impact on the gas distribution profile at the spray level. When compared

normalized gas bubble flux at 1 m/s and 0.23 m/s, it shows that more gas concentrated to the center ($x = 0.2\ to\ 0.25\ m$).

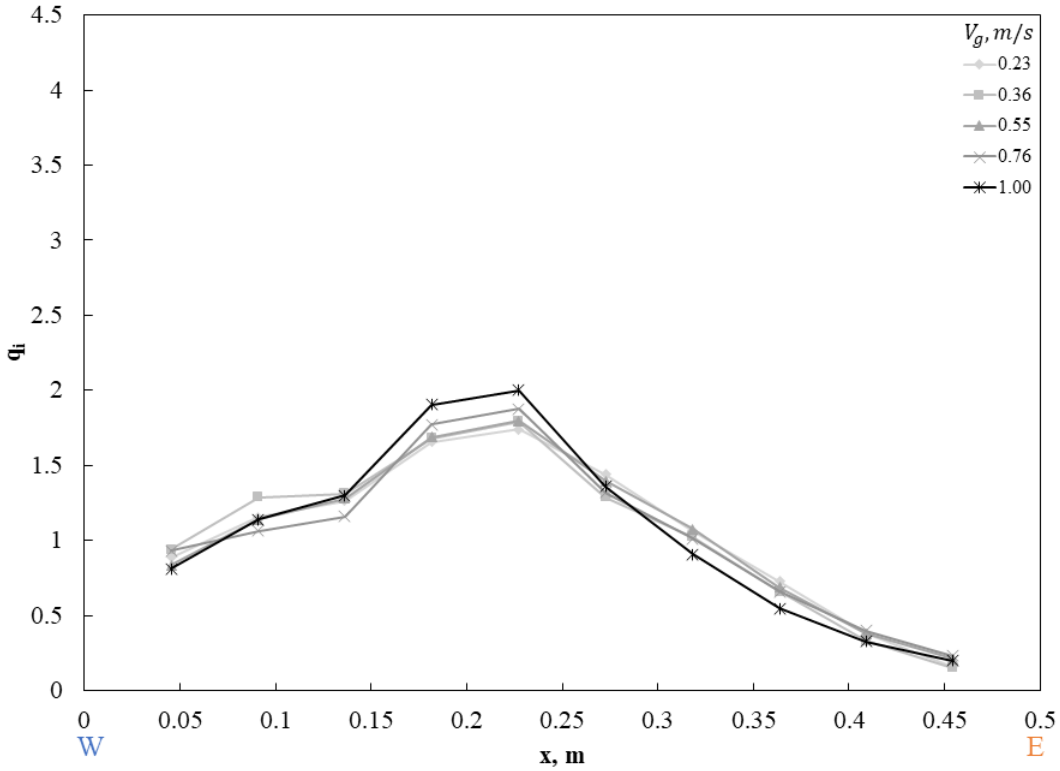

Figure 4.16 Impact of superficial gas velocity (V_g) on gas distribution at spray level (No baffle, inclined distributor, even case, x = 0 – 0.5 m, $z = 0.67\ m$)

Figure 4.17 shows with the inclined distributor, no baffle, eastern case, the gas bubbles concentrated to the eastern side of the bed. The superficial gas velocity had a minor impact on the gas distribution profile at the spray level. Similar to the western case, with

a higher superficial gas velocity, the dimensionless lateral gas flux profile became less pronounced at 1 m/s, comparing to that of 0.24 m/s.

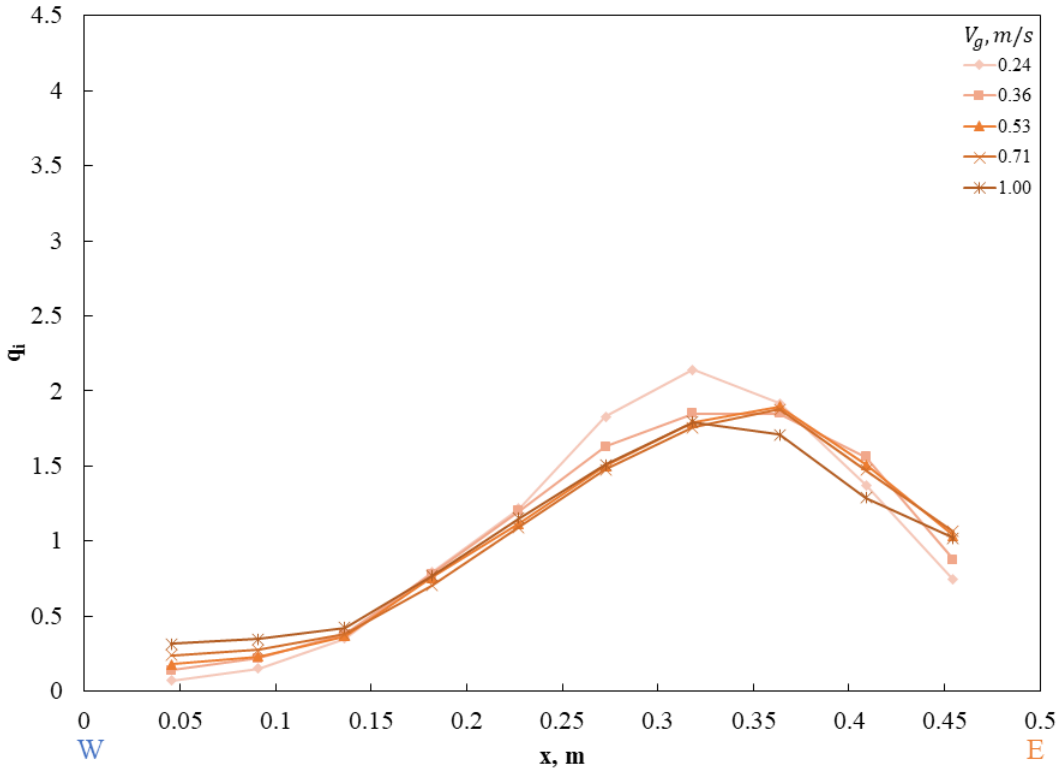

Figure 4.17 Impact of superficial gas velocity (V_g) on gas distribution at spray level (No baffle, inclined distributor, even case, x = 0 – 0.5 m, $z = 0.67\ m$)

Figure 4.18 shows with the inclined distributor, baffle A1, even case, which significantly redirected gas bubble flow comparing to no baffle case, the gas bubbles concentrated to

the center of the bed. The superficial gas velocity had an insignificant impact on the gas distribution profile at the spray level.

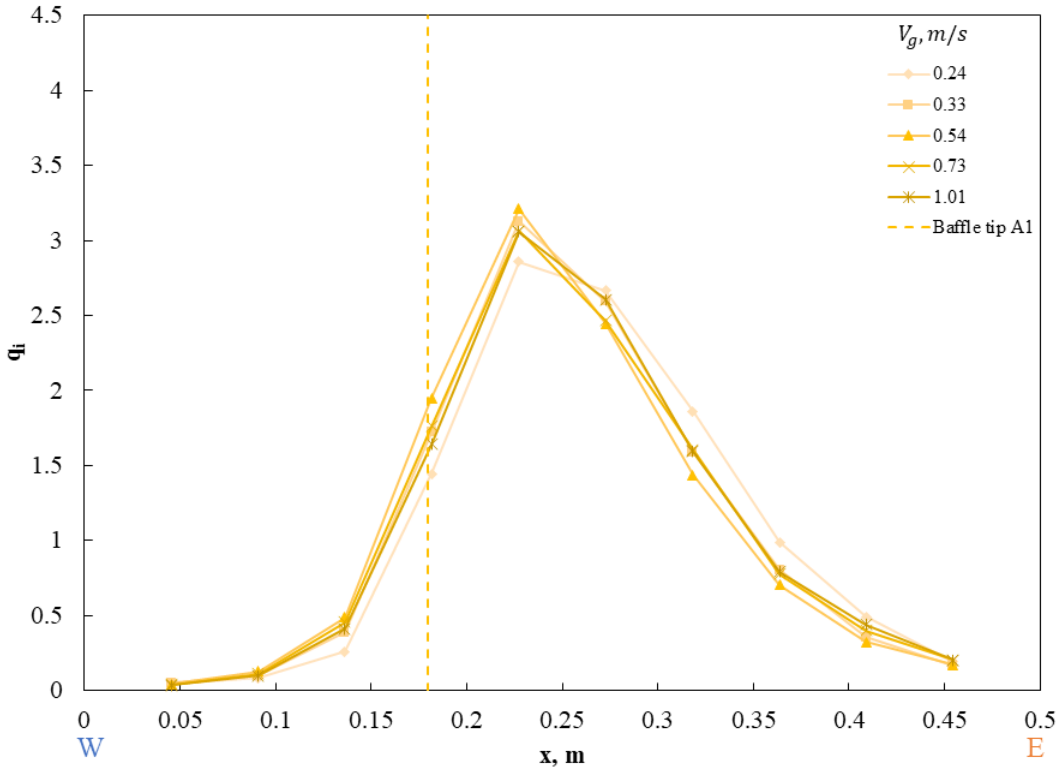

Figure 4.18 Impact of superficial gas velocity (V_g) on gas distribution at spray level (Baffle A1 (asymmetrical baffle without flux-tube, 36 % blocking cross-sectional area (Figure 2.6 A)), inclined distributor, even case, x = 0 – 0.5 m, $z = 0.67\ m$)

Figure 4.19 shows the inclined distributor, baffle S1, even case, which had a minor impact on gas bubble flow compared to the no baffle case. The gas distribution was

symmetrical for all velocities. The superficial gas velocity had an insignificant impact on the gas distribution profile at the spray level.

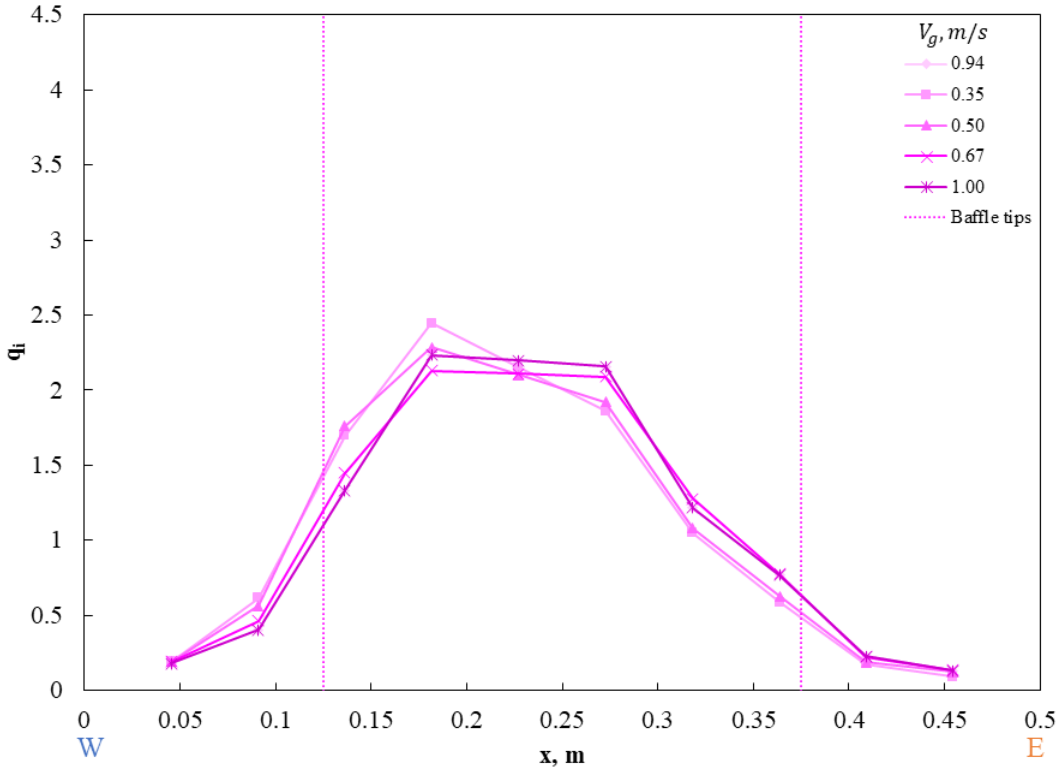

Figure 4.19 Impact of superficial gas velocity (V_g) on gas distribution at spray level (Baffle S1 (symmetrical baffle without flux-tube (Figure 2.7 A)), inclined distributor, even case, x = 0 – 0.5 m, $z = 0.67\ m$)

Figure 4.20 shows that more gas bubbles concentrated to the western side for all cases. With the increase of V_g, the gas bubbles tended to migrate to the bed center at the higher

vertical locations. But no clear impact from bubbling to turbulent transition change could be seen.

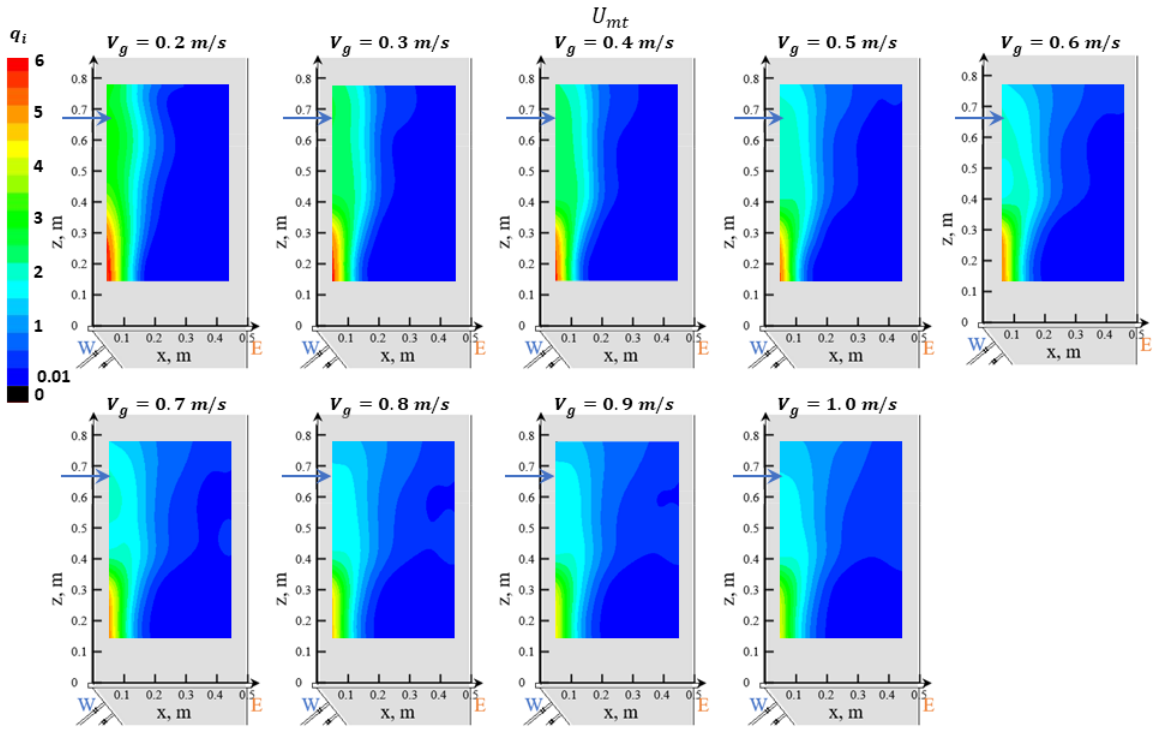

Figure 4.20 The impact of V_g on gas distribution (inclined distributor, no baffle, western case, $T_{bed} = 30\ °C$) (The spray nozzle level is shown with a horizontal blue arrow on the West side).

4.3.2 Impact of bed temperature on gas distribution

Figure 4.21 shows that increasing the bed temperature from 30 °C to 130 °C had no impact on gas distribution at the spray level. The impact of baffle type A4 on gas

distribution at the spray level was much more significant than the bed temperature change from 30 to 130 °C.

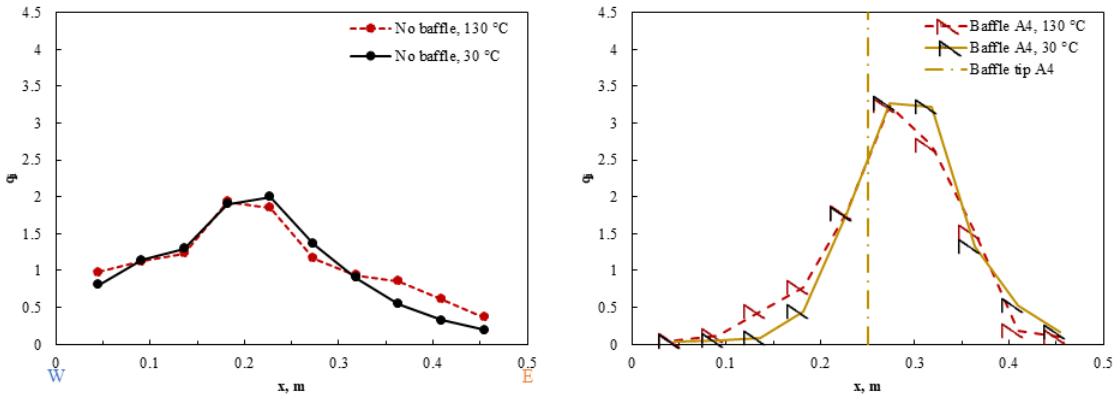

Figure 4.21 Impact of temperature (T_{bed}) on gas distribution with and without baffle at spray level (Inclined distributor, even case, x = 0 – 0.5 m, $z = 0.67\ m$)

Figure 4.22 shows that increasing the temperature from 30 to 120 °C had an insignificant impact on gas distribution without a baffle in the whole bed.

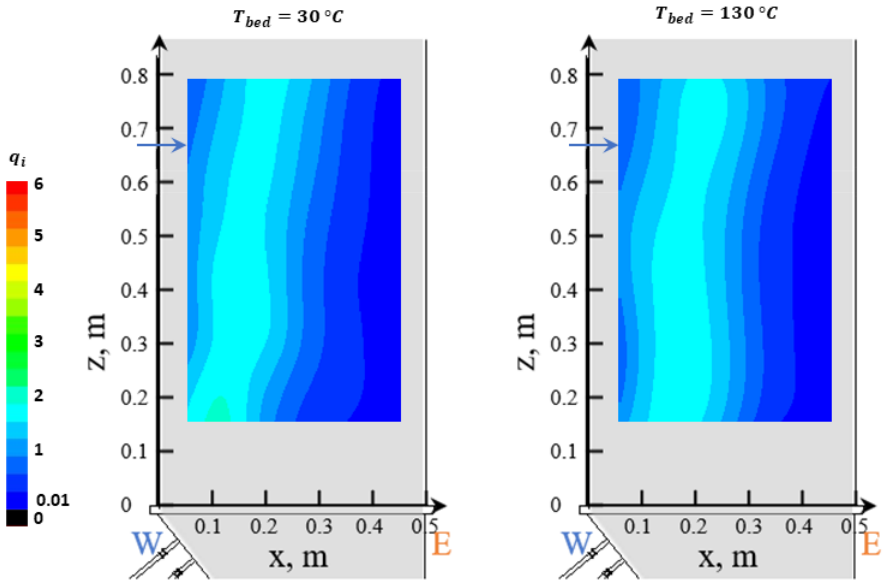

Figure 4.22 The impact of temperature on gas distribution (inclined distributor, no baffle, even case, V_g=1 m/s) (The spray nozzle level is shown with a horizontal blue arrow on the West side).

Figure 4.23 shows that the temperature from 30 to 120 °C had an insignificant impact on gas distribution with baffle A4.

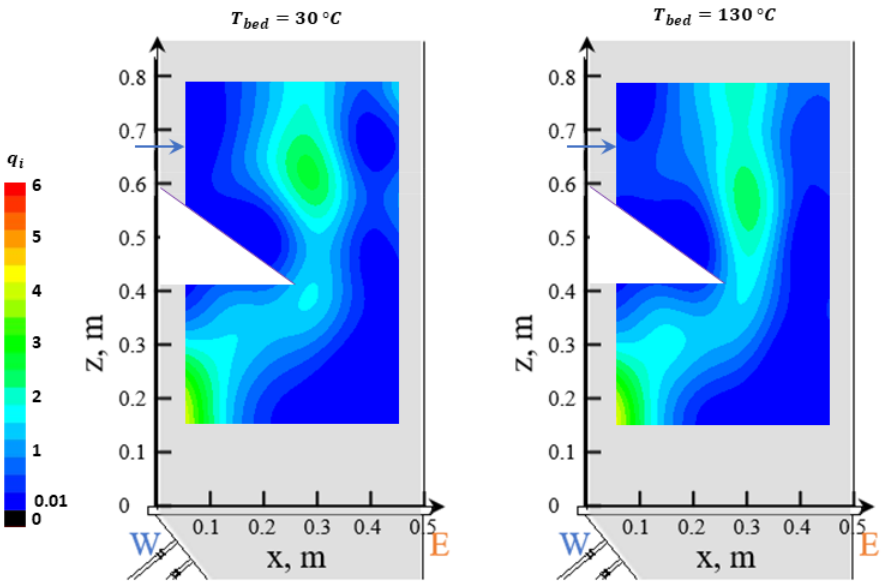

Figure 4.23 The impact of temperature on gas distribution (inclined distributor, western case, baffle type A4, Vg=1 m/s) (The spray nozzle level is shown with a horizontal blue arrow on the West side).

4.4 Comparison of experimental and numerical results

Figure 4.24 shows that CFD modeling (Xing et al.[1]) could predict the general trends measured with E-probes at the spray level with the 4 distributors. The minor differences could be because the CFD modeling results combined the bed voidage and gas velocity.

It suggested that CFD could be used to scale up the experimental results to a commercial coker, confirming results obtained with other column configurations [3].

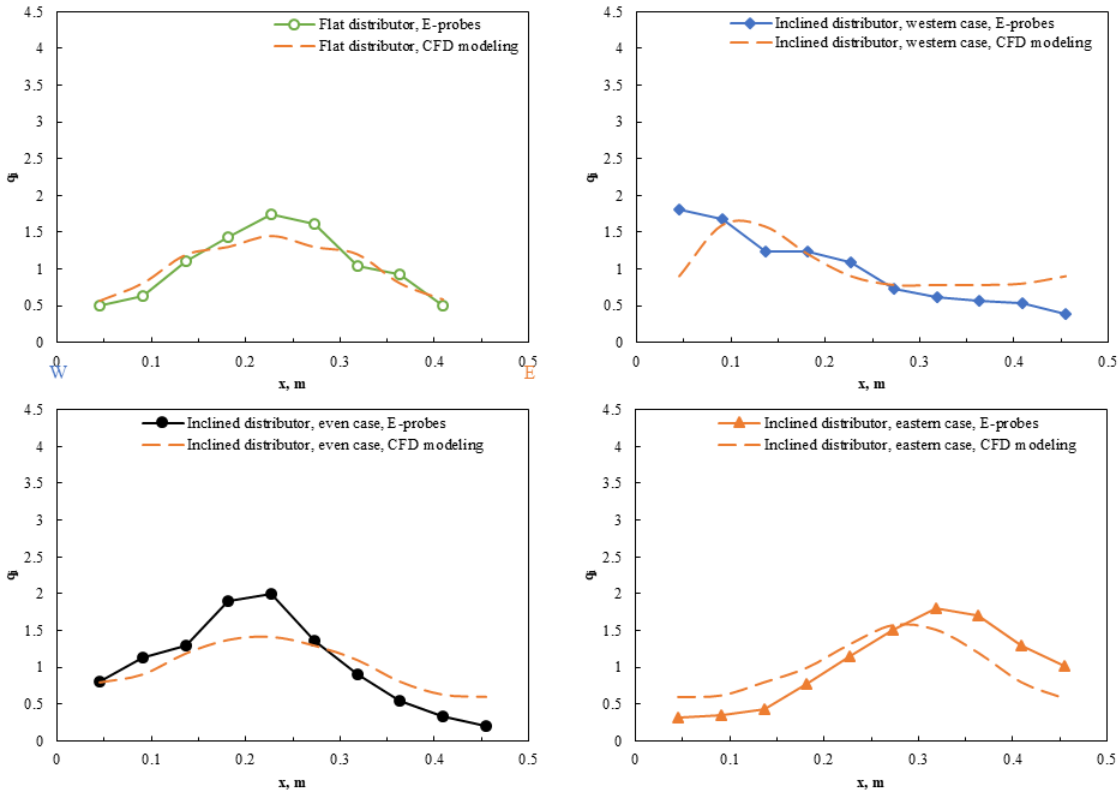

Figure 4.24 Comparison of gas distribution at spray level between experimental and numerical (Xing, 2020) results (No baffle, x = 0 – 0.5 m, inclined distributor: $z = 0.67\ m$, flat distributor: $z = 0.35\ m$; $V_g = 1\ m/s$)

Figure 4.25 shows the CFD modeling (Xing et al.[1]) predictions of the normalized local gas bubble flux at spray level (z=0.67 m), with a flat distributor by concentrating gas bubbles at the bottom of the reactor to different sides of the bed. The results indicate that the impact of inlet gas distribution is dissipated at the spray level with a flat distributor. It

shows how an inclined distributor was needed to modify the bubble gas distribution at the spray level.

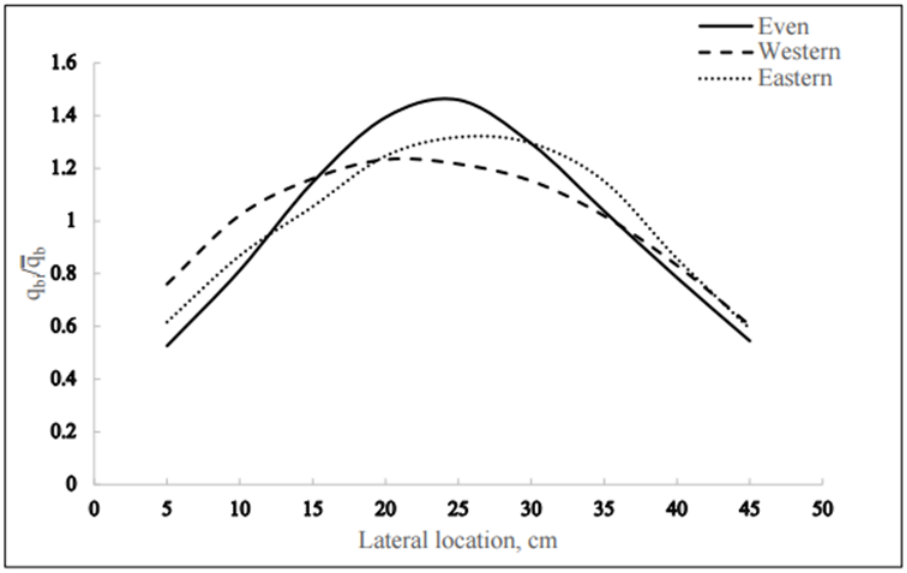

Figure 4.25 Comparison of the lateral gas bubble distribution at the injection level ($z = 0.67\ m$) using three different inlet distributor configurations under the superficial velocity of 0.4 m/s and the flat inlet gas distributor.

4.5 Conclusions

Without a baffle, the initial gas distribution with an inclined distributor has a strong impact on the gas distribution of the whole bed.

With a baffle, the baffles redirect gas bubbles to the baffle tip region, while their impact on gas distribution quickly dissipates below the baffle.

- The asymmetrical baffles without a flux-tube (baffle A2, A4) significantly redirect gas bubbles at the spray level near the baffle tip region.
- The asymmetrical baffles with a flux-tube (baffle A2 and A3) and the symmetrical baffle (S1 and S1 with connector) have a minor impact on gas distribution at the spray level.

The superficial gas velocity and bed temperature have an insignificant impact on gas distribution at the spray level.

The CFD modeling results (from Xing, 2020) agree well with experimental results, suggesting that CFD could be used to scale up the results from this research to commercial cokers.

4.6 Nomenclature

q_i		Normalized local bubble volumetric flux
$\overline{q_b}$	$kg/(s \cdot m^2)$	Average cross-sectional volumetric flux
q_{bi}	$kg/(s \cdot m^2)$	Local bubble volumetric flux
V_g	m/s	Superficial gas velocity
T_{bed}	°C	Bed temperature
U_{mt}	m/s	Minimum turbulent gas vel
x	m	Lateral location
z	m	Vertical location

4.7 References

1. Xing, X., *Numerical study of the effect of gas distributors and baffles on the bubble distribution, gas and solid mixing in a fluidized bed*, in *Chemical and biochemical engineering*. 2020, Western University. p. 292.

2. Jahanmiri, M., *Use of a Baffle to Enhance Distribution of a Liquid Sprayed into a Gas-Solid Fluidized Bed*. 2017, MESc thesis, Western University.

3. Li, T., et al., *Numerical investigation of FLUID COKING™ units, Part I: Hydrodynamics of a scaled cold flow model.* The Canadian Journal of Chemical Engineering, 2012. **90**(2): p. 442-456.

Chapter 5

5 Impact of bubble flow on liquid distribution quality with a practical nozzle

In this chapter, we use a practical nozzle (TEB nozzle) that was scaled down from a commercial coker to provide a stable spray with the same liquid flux as a commercial nozzle (introduced in section 2.1.1). In this chapter, we show a correlation found between the local gas distribution at the jet cavity and the initial liquid trapped/ water injected in agglomerates. Based on the correlation found, recommendations are proposed to improve initial feed jet-bed interaction in a coker to reduce agglomerates formation. This chapter also shows the impact of gas distribution near the spray jet on the mass of macro and micro agglomerates generated and the liquid to solids ratio in agglomerates.

At the end of the chapter, the shrinking core model [1] is applied to predict the remaining liquid fraction in agglomerates. And a new model is developed to predict the effect of local bed hydrodynamics on the average liquid concentration in the wet solids released from the spray region.

5.1 Impact of superficial gas velocity on liquid distribution

Figure 5.1 shows that the increase of V_g decreased water trapped/water injected in agglomerates, which indicated better liquid distribution was achieved by increasing V_g. Figure 5.1 also shows no clear change of trend could be found from the aspect of water trapped/water injected with the flat distributor without a baffle. However, when looking

from a more regional basis, there was a transition seen with the solids mixing below and above the baffle (Chapter 6).

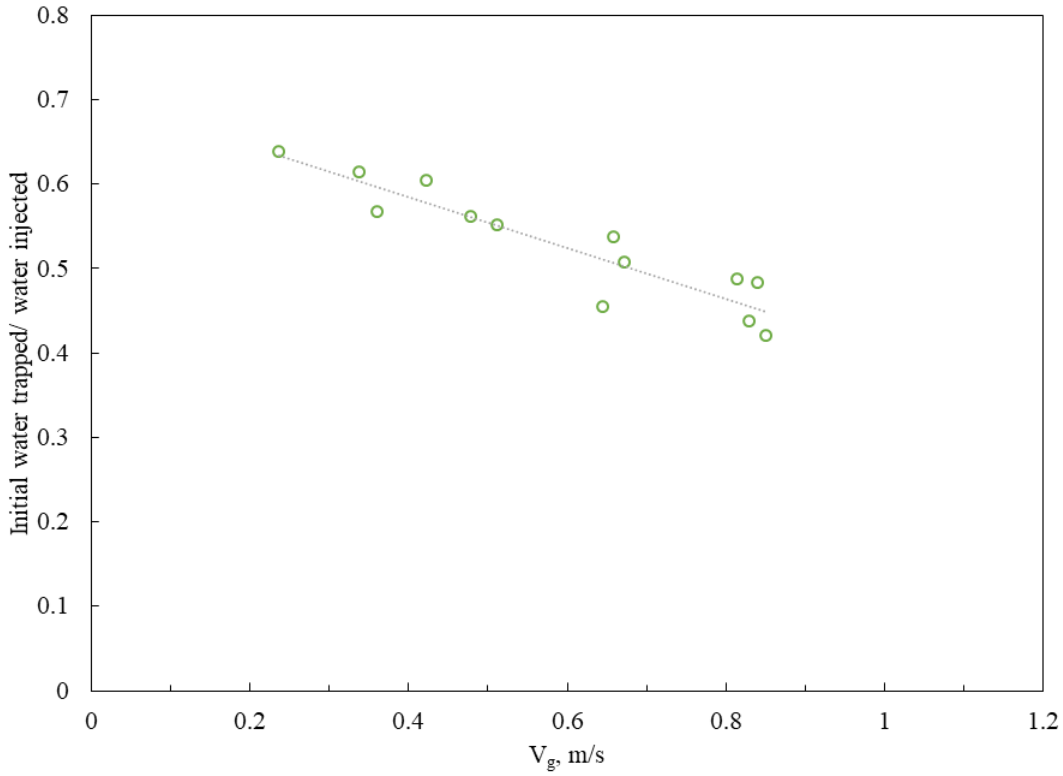

Figure 5.1 Impact of V_g on water trapped/water injected in agglomerates (Flat distributor, no baffle, 1 mm TEB nozzle, $x_{inj} = 0.05\ m$, $z_{inj} = 0.4\ m$, $L_{jet} = 0.23\ m$, $m_{inj} = 200\ g$, $F_L = 17.5\ g/s$, method: freeboard pressure estimation in section 3.4)

Figure 5.2 shows that the eastern case showed more water trapped in agglomerates than that of other gas distributor configurations. This could be related to the gas distribution near the spray region. The nozzle penetrated 5 cm from the western bed wall. The eastern case concentrated the gas bubbles to the eastern side of the bed (Figure 4.1). It suggests that the initial water trapped fraction is affected by the gas distribution near the jet cavity.

Compared to solids mixing (shown in Chapter 6), the transition velocities obtained from the initial water trapped/ water injected were much larger. This suggests that solids mixing was not a limiting factor for liquid distribution with a practical spray nozzle.

When the best performance from the point of view of water trapped/ water injected was reached, it had already been at the most efficient solids mixing conditions: because the solids mixing reached its best performance much earlier. Instead of the solids mixing, agglomerates breakup could be the limiting step. Agglomerates distributed the liquid to other bed regions before they could break up, so that once they broke up, the wet fragments were surrounded by lots of dry, hot solids. Even if the 2D fluidized bed is not suitable to provide realistic conditions to simulate the agglomerates break-up process in a coker, Cochet et al.[2] studied the impact of baffle and injections on agglomerates break-up, applying a 3D column and modeling.

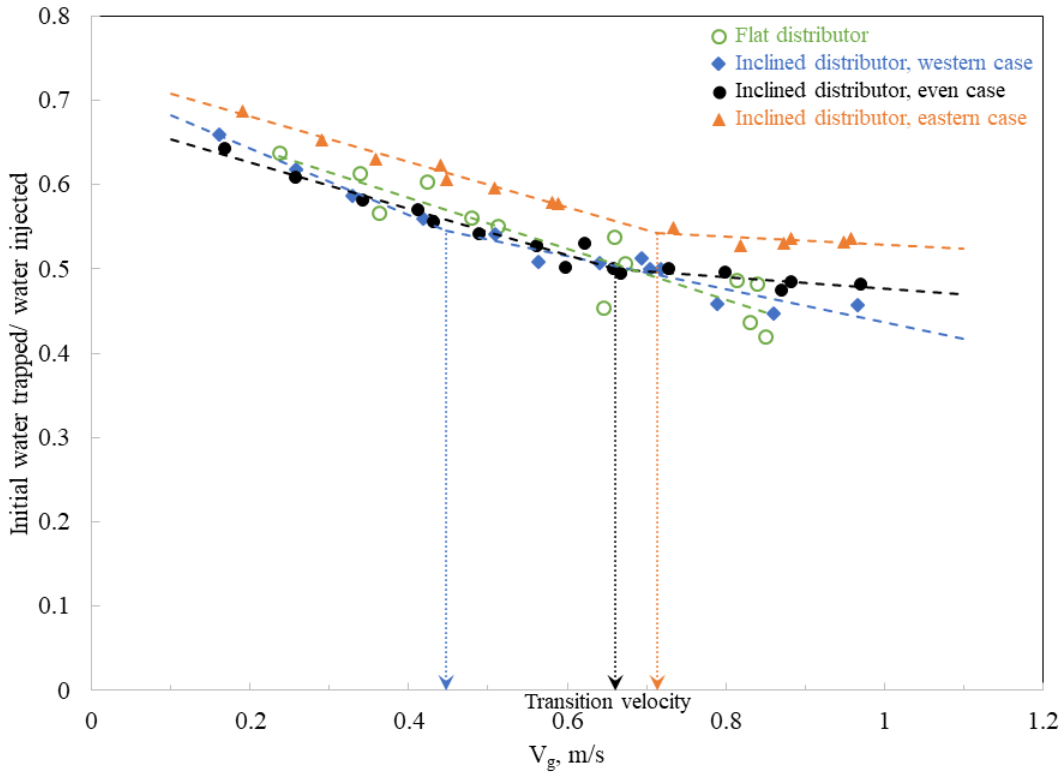

Figure 5.2 Impact of gas distributor configuration on water trapped/water injected in agglomerates at different V_g (No baffle, 1 mm TEB nozzle, $x_{inj} = 0.05\ m$, flat distributor: $z_{inj} = 0.4\ m$, inclined distributor: $z_{inj} = 0.67\ m$, $L_{jet} = 0.23\ m$, $m_{inj} = 200\ g$, $F_L = 17.5\ g/s$, method: freeboard pressure estimation in section 3.4)

Figure 5.3 shows that, with the western distributor configuration, there was slightly more water trapped in agglomerates when the symmetrical baffle was installed than without the symmetrical baffle installed. This could be because the symmetrical baffle redirected gas bubbles to the bed center and reduced the gas bubbles near the injection location ($x = 0.05\ m$) (Figure 4.7).

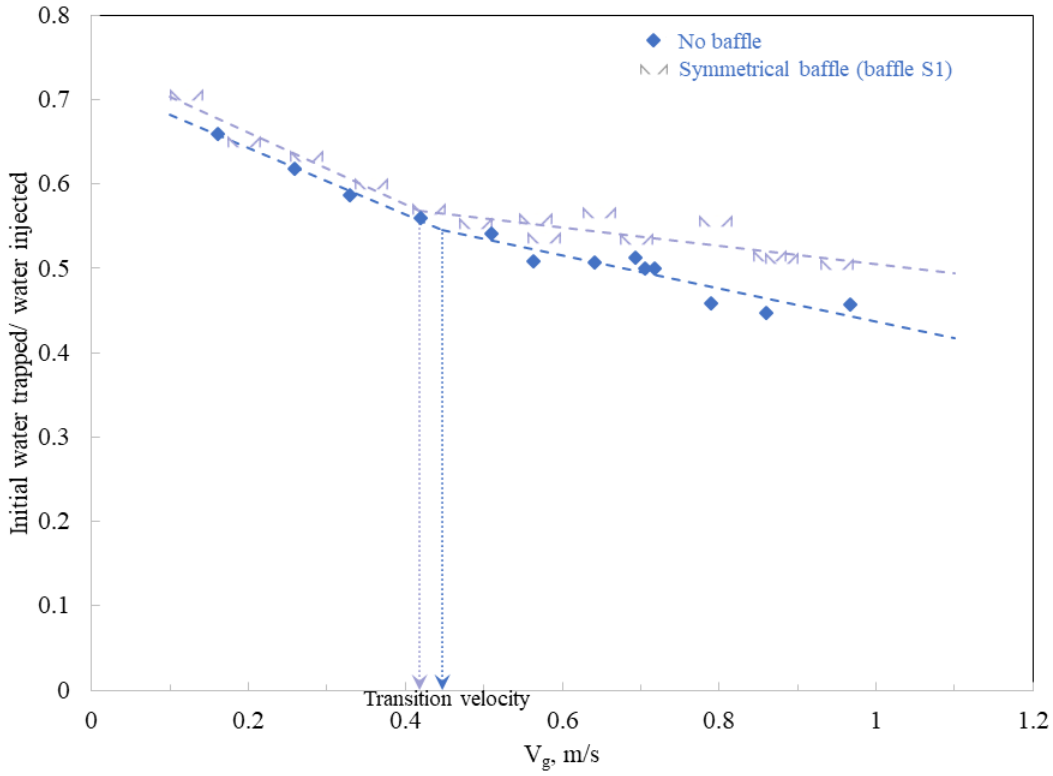

Figure 5.3 Impact of the symmetrical baffle on water trapped/water injected in agglomerates at different V_g (Inclined distributor, western case, 1 mm TEB nozzle, $x_{inj} = 0.05\ m$, $z_{inj} = 0.67\ m$, $L_{jet} = 0.23\ m$, $m_{inj} = 200\ g$, $F_L = 17.5\ g/s$, method: freeboard pressure estimation in section 3.4)

Figure 5.4 also shows that, with the even distributor configuration, slightly more water was trapped in agglomerates with the symmetrical. Similarly, this could be due to at this injection location ($x = 0.05\ m$), the gas bubbles were reduced comparing to the no

baffle case, because the symmetrical baffle redirected gas bubbles to the bed center (Figure 4.7).

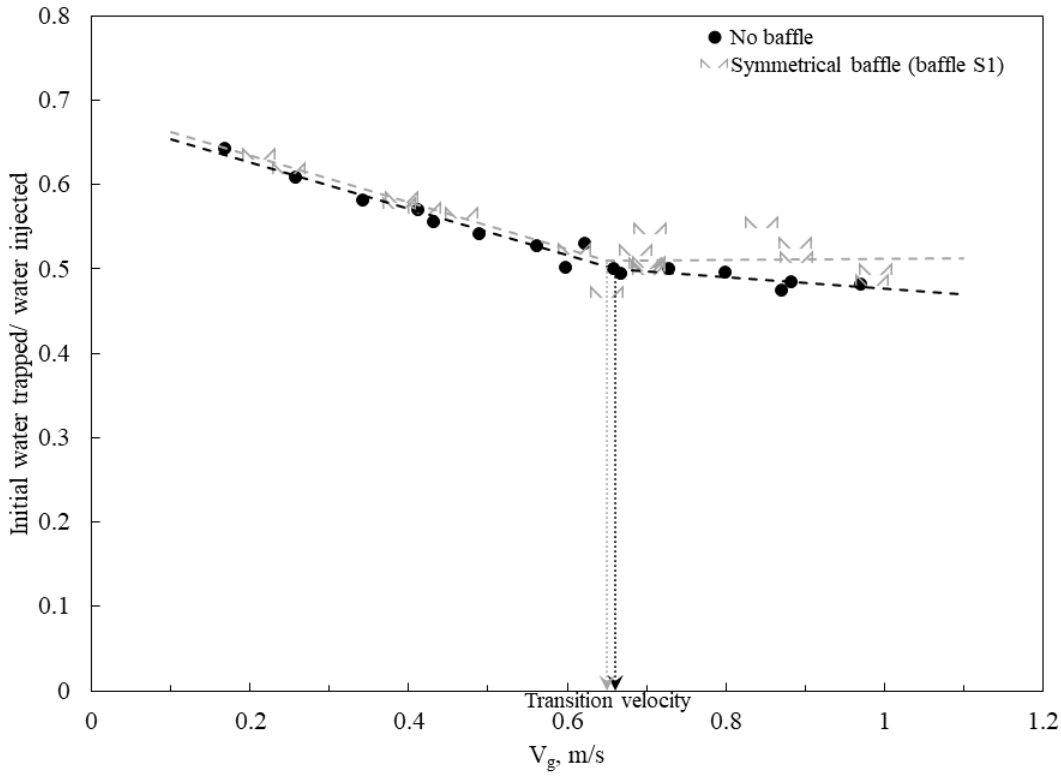

Figure 5.4 Impact of the symmetrical baffle on water trapped/water injected in agglomerates at different V_g (Inclined distributor, even case, 1 mm TEB nozzle, $x_{inj} = 0.05\ m$, $z_{inj} = 0.67\ m$, $L_{jet} = 0.23\ m$, $m_{inj} = 200\ g$, $F_L = 17.5\ g/s$, method: freeboard pressure estimation in 3.4)

Figure 5.5 shows that, with the eastern distributor configuration, there was an insignificant impact at lower velocities of the symmetrical baffle on the initial water

trapped fraction. This could be because the baffle has an insignificant impact on gas distribution at the spray region (Figure 4.7).

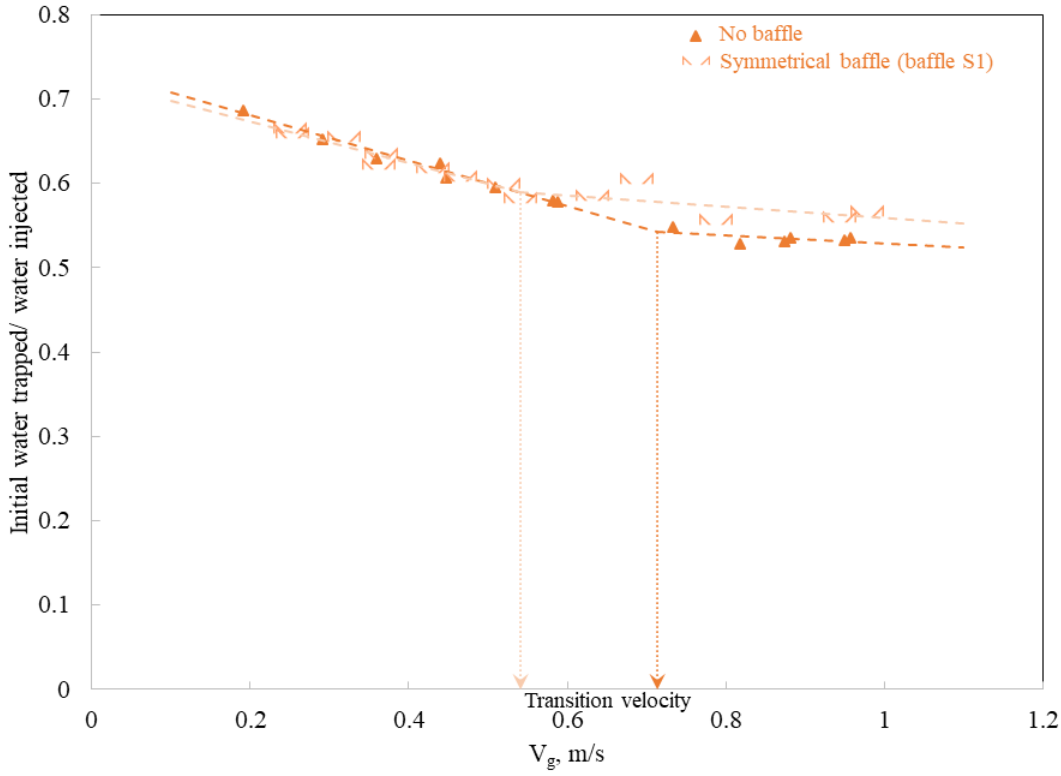

Figure 5.5 Impact of the symmetrical baffle on water trapped/water injected in agglomerates at different V_g (Inclined distributor, eastern case, 1 mm TEB nozzle, $x_{inj} = 0.05\ m$, $z_{inj} = 0.67\ m$, $L_{jet} = 0.23\ m$, $m_{inj} = 200\ g$, $F_L = 17.5\ g/s$, method: freeboard pressure estimation in section 3.4)

Table 5-1 shows that the transition velocity of water trapped/water injected in agglomerates were generally larger than the U_{mt} found by pressure fluctuations. This could be due to the fact that the agglomerates created were larger than the sand particles. As shown in section 3.9.4 and the literature review in section 1.2.1, the minimum turbulent velocity for larger particles was expected to be larger.

When there were more gas bubbles near the spray region (western case), the transition velocity was closer to the U_{mt} found without injection, which indicates better jet-bed

interaction. While when there were fewer gas bubbles near the spray region (eastern case), the transition velocity was much larger than the U_{mt} found without injection, which indicates insufficient jet-bed interaction. This agreed with the impact of gas distribution on the initial liquid distribution shown in section 5.2.

	U_{mt}, m/s Pressure fluctuation – Max value of V-statistic	U_{mt}, m/s Pressure fluctuation - CV	Transition velocity of water trapped/water injected, m/s
Flat distributor	0.35	0.49	N/A
No baffle, western case	0.41	0.37	0.44
Symmetrical baffle, western case	0.49	0.44	0.42
No baffle, even case	0.36	0.41	0.66
Symmetrical baffle, even case	0.44	0.43	0.64
No baffle, eastern case	0.33	0.36	0.71
Symmetrical baffle, eastern case	0.37	0.34	0.54

Table 5-1 Minimum turbulent velocity (U_{mt}) without injection vs. transition velocity with injection

Figure 5.6 shows with any drying gas velocity, there was a significant reduction of the water trapped fraction (about 30 - 50 %) by increasing the gas velocity during injection from 0.18 to 1 m/s. Therefore, we would expect less water trapped in agglomerates by

modifying the velocity in the injection zone only. The results agreed with what Li et al.[3] found.

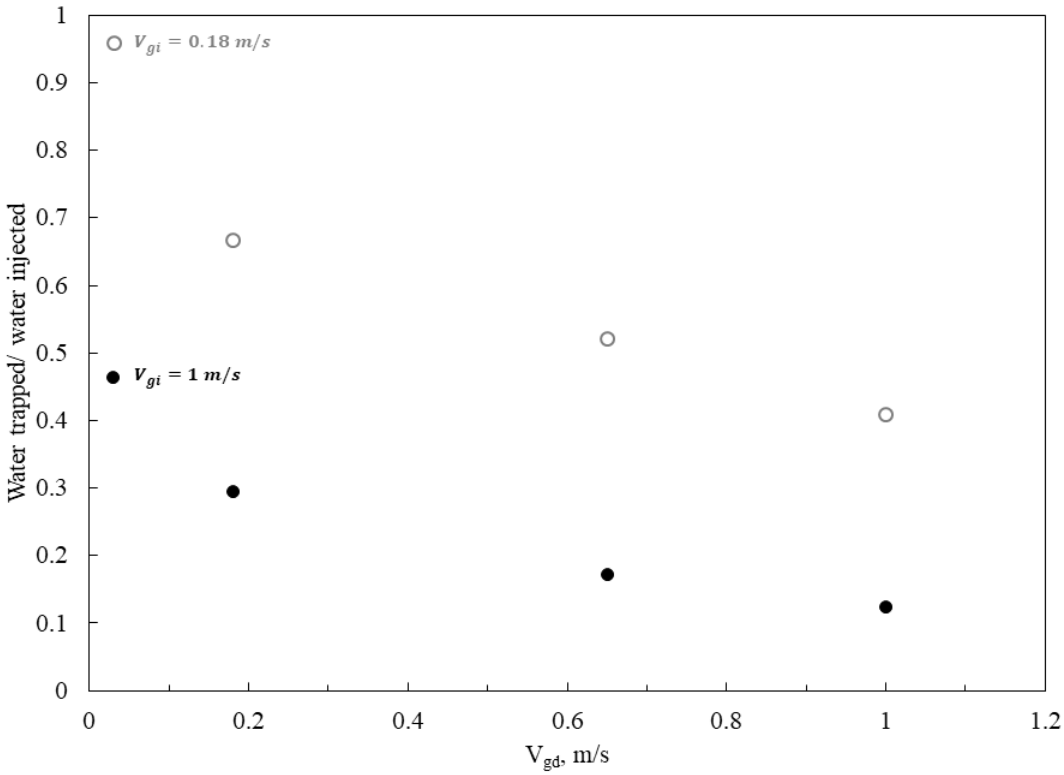

Figure 5.6 Impact of V_{gd} (superficial gas velocity during drying) on water trapped/water injected in agglomerates (Inclined distributor, even case, 1 mm TEB nozzle, $x_{inj} = 0.18\ m$, $z_{inj} = 0.67\ m$, $L_{jet} = 0.23\ m$, $m_{inj} = 200\ g$, $F_L = 17.5\ g/s$, method: Gum Arabic in section 3.4)

Figure 5.7 shows that the injection location significantly affected the water trapped/water injected in agglomerates. The injection location impact was stronger at lower superficial gas velocities. When the spray jet was exposed to more gas bubbles, lower water trapped/water injected in agglomerates was observed. This indicates that there would be a

correlation between liquid distribution quality and the gas bubble flow at the spray jet region.

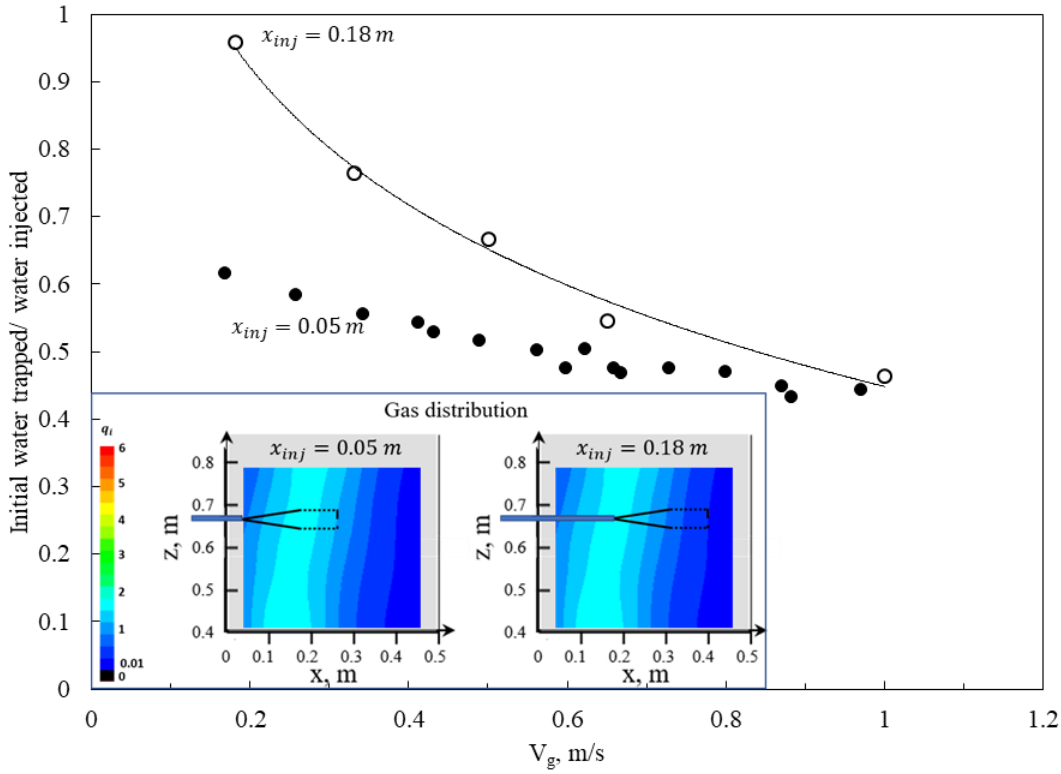

Figure 5.7 Impact of injection location on water trapped/water injected in agglomerates at different V_g (No baffle, inclined distributor, even case,1 mm TEB nozzle, $z_{inj} = 0.67\,m$, $L_{jet} = 0.23\,m$, $m_{inj} = 200\,g$, $F_L = 17.5\,g/s$, method: $x_{inj} = 0.18\,m$ with Gum Arabic method and $x_{inj} = 0.05\,m$ with freeboard pressure estimation in section 3.4)

Figure 5.8 shows that when the nozzle position was at the same injection location, the asymmetrical baffle redirected gas bubbles to where the spray jet was located. This

effectively reduced the water trapped fraction in agglomerates at all velocities tested.

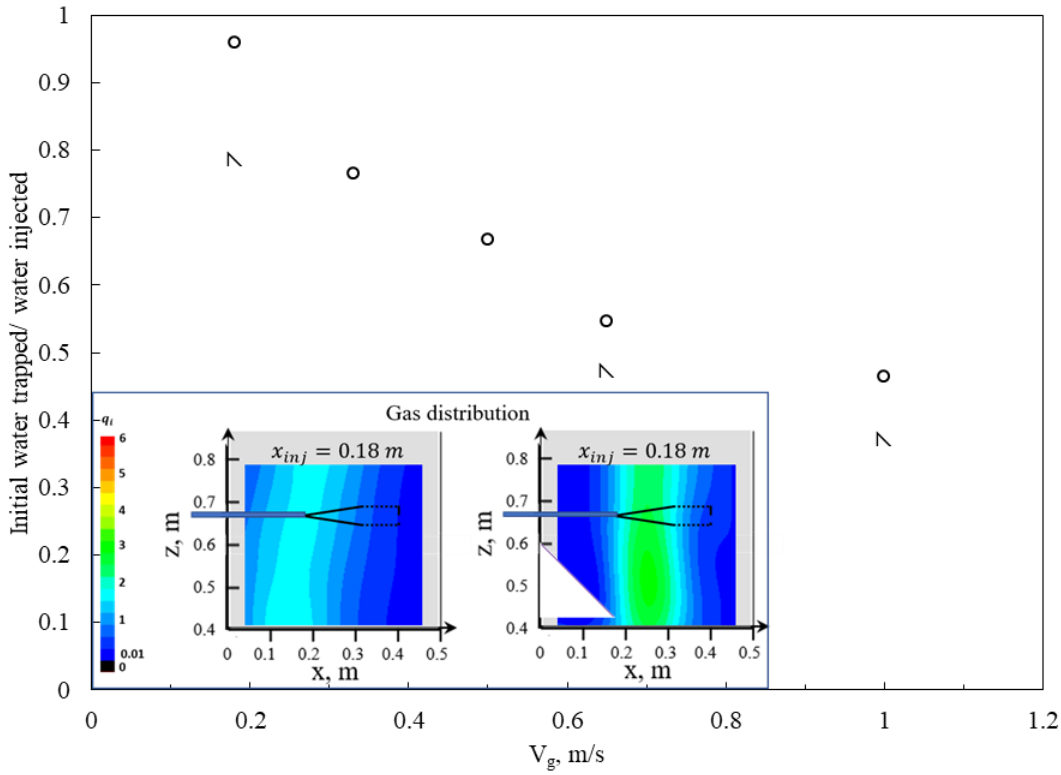

Figure 5.8 Impact of baffle A1 (asymmetrical baffle without a flux-tube) on water trapped/water injected in agglomerates at different V_g (Inclined distributor, even case, 1 mm TEB nozzle, $x_{inj} = 0.18\ m$, $z_{inj} = 0.67\ m$, $L_{jet} = 0.23\ m$, $m_{inj} = 200\ g$, $F_L = 17.5\ g/s$, method: Gum Arabic in section 3.4)

Figure 5.9 shows that when the nozzle positions were at the same location, the asymmetrical baffle with a flux-tube had a minor impact on the initial liquid distribution. Because, at this certain injection location, the geometry of the asymmetrical baffle with a

flux-tube had a minor impact on the gas distribution at the spray region.

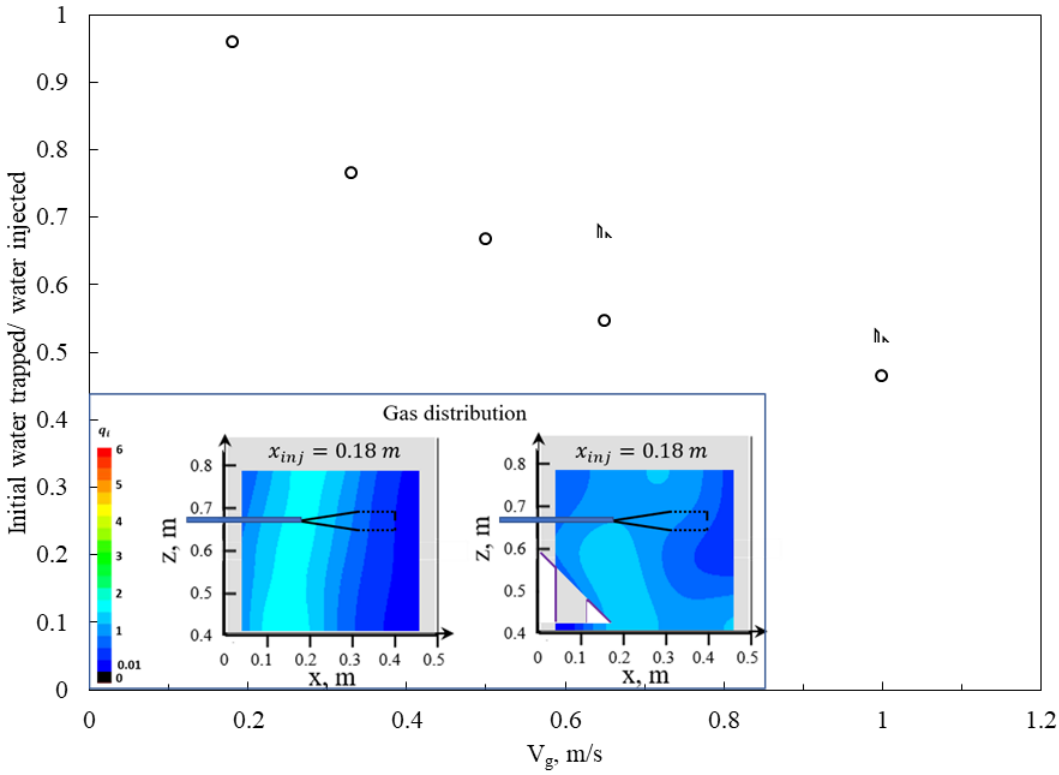

Figure 5.9 Impact of baffle A2 (asymmetrical baffle with a flux-tube) on water trapped/water injected in agglomerates at different V_g (Inclined distributor, even case,1 mm TEB nozzle, $x_{inj} = 0.18\ m$, $z_{inj} = 0.67\ m$, $L_{jet} = 0.23\ m$, $m_{inj} = 200\ g$, $F_L = 17.5\ g/s$, method: Gum Arabic in section 3.4)

5.2 Correlation between gas distribution and liquid distribution

Figure 5.10 shows the highest and lowest initial water trapped fraction from Gum Arabic runs. It indicates that there would be a correlation between the gas distribution in the first half of the spray jet and the water trapped/ water injected in agglomerates.

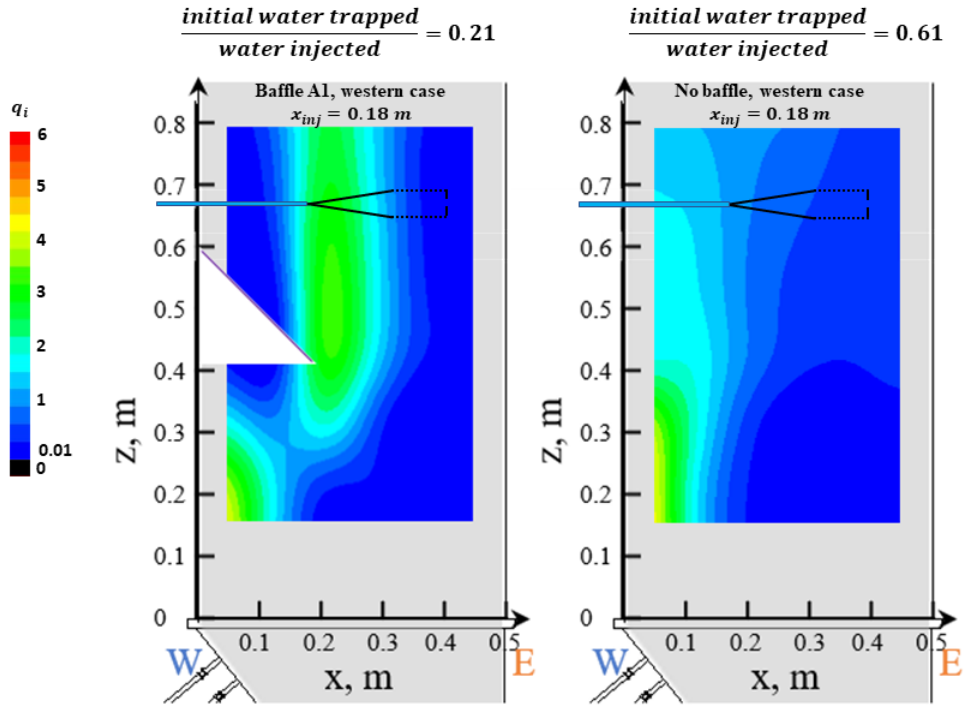

Figure 5.10 Best and worst case with Gum Arabic method: gas distribution vs. water trapped/ water injected ($V_{gi} = 1\ m/s, V_{gd} < U_{mf} = 0.03\ m/s$, 1 mm TEB nozzle, $L_{jet} = 0.23\ m, m_{inj} = 200\ g, F_L = 17.5\ g/s$)

Figure 5.11 shows the correlation found between local gas distribution at the jet cavity and the initial water trapped fraction in agglomerates with 18 Gum Arabic runs. The correlation (Eq.5-1) shows that the initial liquid-solid contact could be enhanced by directing gas bubbles to two regions: the first region is near the nozzle tip, the second region is the region at the transition between the stable jet core, and the fluctuating part of

the jet (details see section 5.5.3). The arrows show where there should be more gas bubbles.

$$\frac{initial\ water\ trapped}{water\ injected} = \mathbf{1} - \boldsymbol{free\ moisture}\ \% \qquad 5\text{-}1$$

$$= \mathbf{1} - \left(0.26\ q_{avg,\ -0.02\ to\ 0.01\ m}^{1.1} + \mathbf{0.09}\ \boldsymbol{q}_{avg,\ 0.12\ to\ 0.16\ m}^{1.68}\right)$$

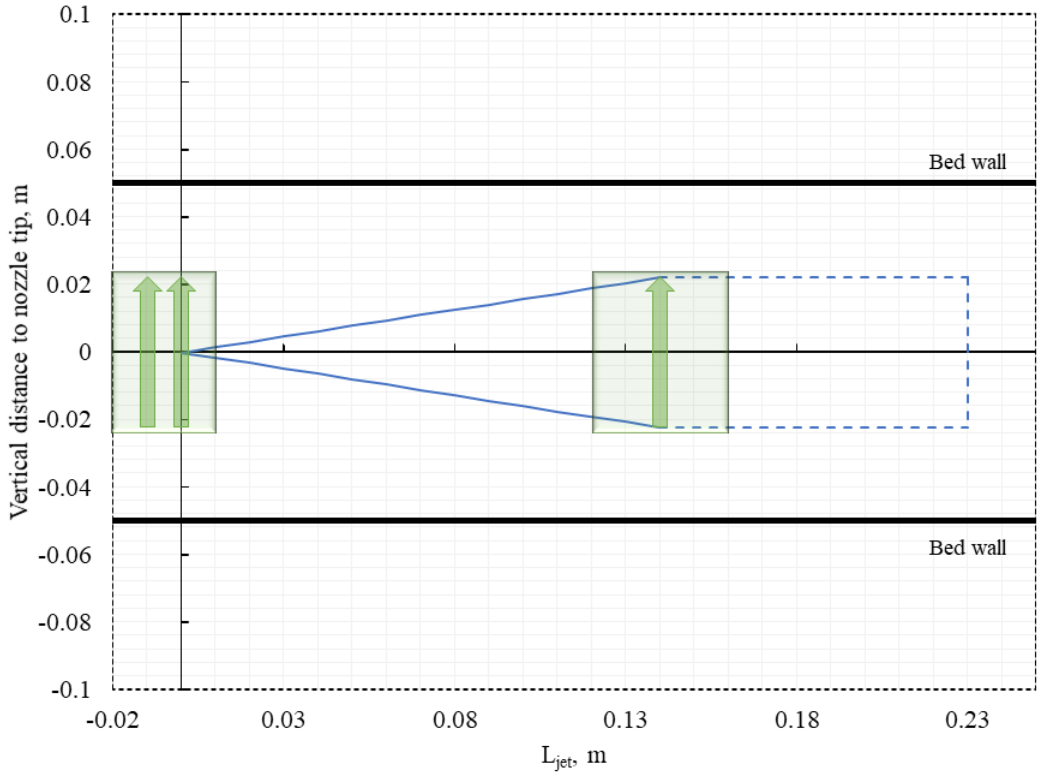

Figure 5.11 Graph shows where to direct gas bubbles to decrease water trapped/ water injected ($V_{gi} = 1\ m/s$, $V_{gd} < U_{mf} = 0.03\ m/s$, 1 mm TEB nozzle, $L_{jet} = 0.23\ m$, $m_{inj} = 200\ g$, $F_L = 17.5\ g/s$, method: E-probe method for gas distribution in section 3.1 and chapter 4; Gum Arabic method in section 3.4)

Figure 5.12 shows a good correlation was found using the empirical correlation found at 1 m/s. The points included a wide range of initial water trapped/water injected in agglomerates from 0.21 to 0.61.

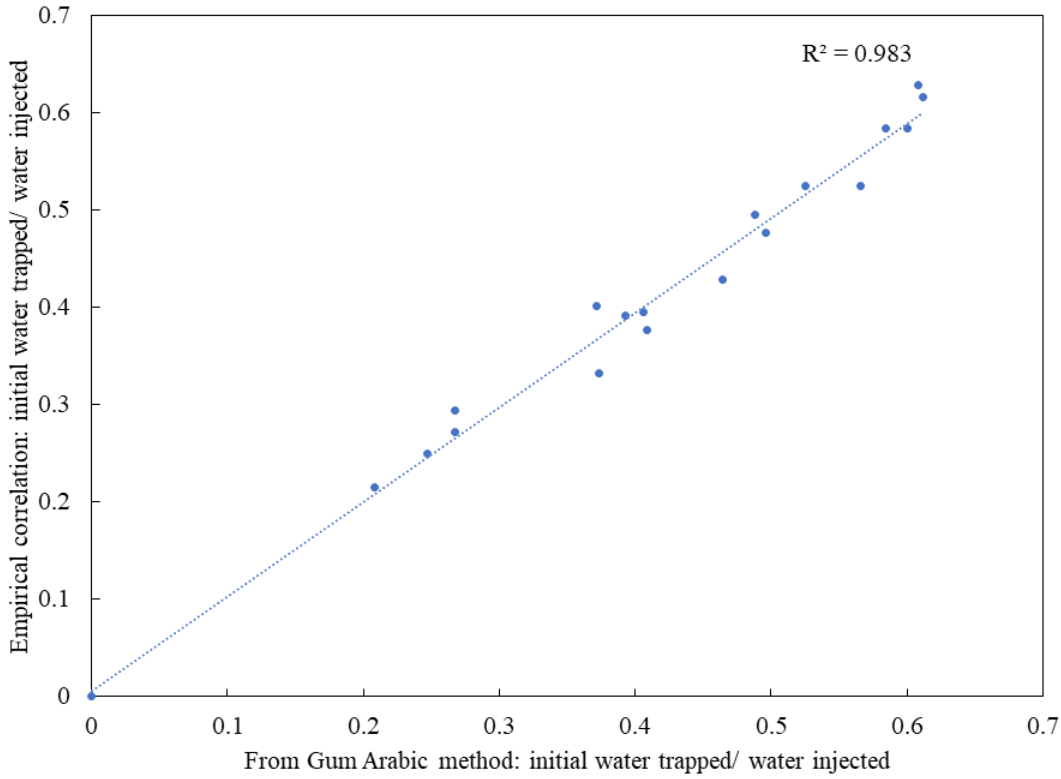

Figure 5.12 Water trapped/ water injected from Gum Arabic method vs. from empirical correlation built with gas distribution near the spray jet ($V_{gi} = 1\ m/s$, $V_{gd} < U_{mf} = 0.03\ m/s$, 1 mm TEB nozzle, $L_{jet} = 0.23\ m$, $m_{inj} = 200\ g$, $F_L = 17.5\ g/s$, method: Gum Arabic method in section 3.4)

5.3 Impact of gas distribution on liquid distribution at different horizontal injection locations

With the correlation found (Eq.5-1) and experimental methods developed to evaluate initial liquid distribution quality (details see section 3.4), we showed that the impact on

the fraction of the injected liquid that is initially trapped in agglomerates results from modifying the gas distributor configuration or adding baffle(s).

For the future scale-up purpose, we first needed to define the base case by comparing our lab-scaled unit with the typical commercial coker. The first part was about the scaling factor, which is shown in Table 5-2. It shows that our unit can be considered as the scaled-down version of the radius of the commercial coker. The scaling factors, such as jet penetration and nozzle penetration, were around an order of magnitude. Due to the taper geometry (Figure 5.13), the coker diameter varies from 7 to 10 m, from the top to the bottom injection locations. The maximum nozzle penetration means, if one were to inject beyond this point, the spray jet tip would interact with the opposing feed jet in a coker. Interactions between feed jets should be avoided to minimize the risk of wet agglomerates generated from a spray jet being captured by another spray jet, as previous publications showed that agglomerates entering a spray jet acted as a seed for stronger agglomerates [4-6].

To find the injection location in the lab-scaled unit for the base case, we first needed to know the nozzle penetration in a coker. In a coker, “At run start” means the time when the coke on the wall is cleaned, and the new run just started. During the run, the feed is injected into a coker continuously, while the coke on the wall keeps building up. “At the end of run” means the time when the coker is shut down for unplugging or maintenance purposes. At that time, the coke on the wall can build up to the average thickness of 0.91

m. If we take an average, the average nozzle penetration is about 0.45 m. In our unit, we selected 0.05 m as the nozzle location for the base case.

	Typical fluid coker	Lab unit	Scaling factor
Reactor Diameter	7-10 m	1 m*	0.07 – 0.1
Nozzle jet penetration	2 m	0.23 m	0.115
Nozzle penetration	0.45 m**	0.05 m	0.11
Maximum nozzle penetration	1.5-3 m	0.15-0.25 m	0.083-0.1

* Assuming 0.5 m width corresponding to radius
** Average of 0.91 m at run start and 0 m at end of run

Table 5-2 Scaling factors from lab-scaled bed to commercial coker.

The second part was to match the gas distribution profile at the spray jet region. Figure 5.13 shows that the eastern case with the inclined distributor in our lab-scaled unit

matched half of the core-annular gas structure in a coker. Therefore, the eastern case was applied to provide gas distribution for the base case.

To summarize, injecting at 0.05 m, with the eastern case without a baffle, provided the closest match to simulate the initial liquid distribution in a coker. Therefore, we called it the "base case."

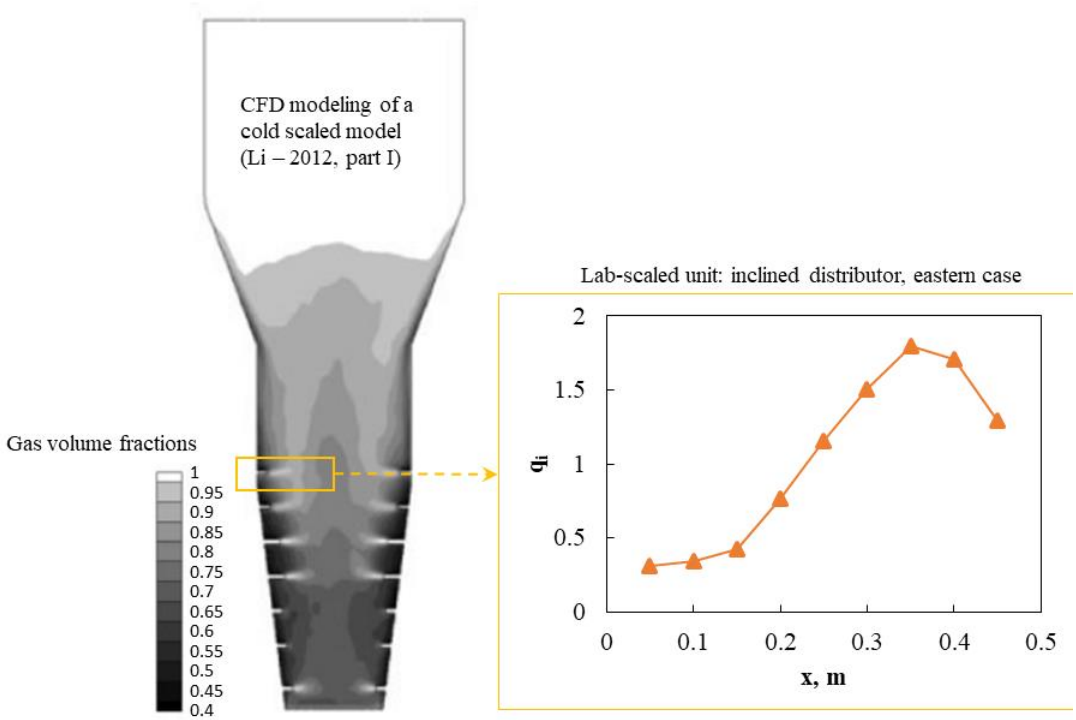

Figure 5.13 Typical gas volume fraction distribution in a coker (Li, 2012a) and the case to simulate it in this research.

Table 5-3 shows the baffle tip location of a coker with a reactor diameter of 10 m [7]. In the patent about baffle [8], they indicated that the best baffle geometry needed to be

further investigated. Therefore, we modified the baffle designs in this research. The detailed dimension and drawings of the baffles can be found in Figure 2.6 and Figure 2.7.

	Baffle tip location	Scaling factor
Baffle in typical fluid coker (Figure 2.5)	1.45 m	
Lab-scaled unit:		
Baffle A1 (asymmetrical baffle without flux-tube)	0.18 m	0.12
Baffle A2 (asymmetrical baffle with flux-tube)	0.18 m	0.12
Baffle A4 (larger asymmetrical baffle without flux-tube)	0.25 m	0.17
Baffle S1 (symmetrical baffle without flux-tube)	0.125 m (from both sides)	0.086

Table 5-3 Scaling factors of baffle (s) from lab-scaled bed to commercial coker.

Figure 5.14 shows that by concentrating the gas bubbles to the bed wall (western case), one could decrease the initial water trapped fraction by 25 % when injecting near the bed wall. Injecting near the bed wall is desired in a coker to avoid opposing spray jets from hitting each other, especially lower in the coker where the diameter is smaller.

The injection locations were within 0.25 m because the jet penetration was 0.23 m. The eastern side bed wall corresponded to the furthest location where the jet tip can reach;

beyond this point, it means the jet tip would interact with the opposing spray jet in a coker.

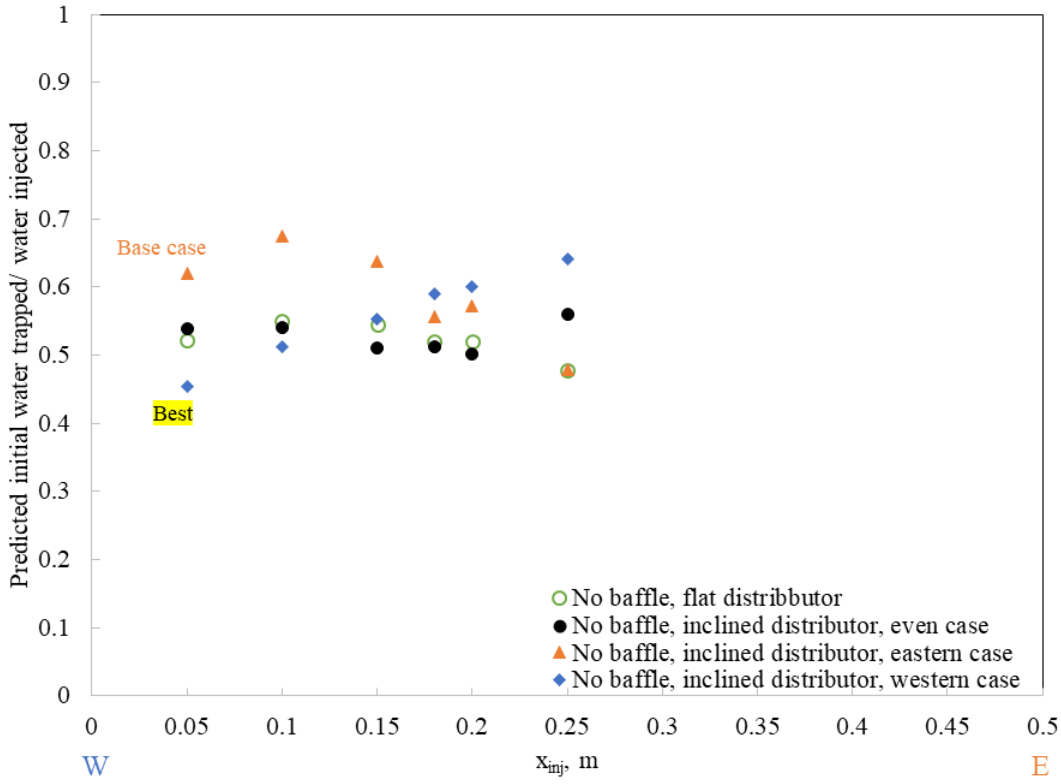

Figure 5.14 Impact of gas distributor configuration on initial water trapped/ water injected in agglomerates at different injection locations (x_{inj}) ($V_{gi} = 1\ m/s$, $z_{inj} = 0.67\ m$, 1 mm TEB nozzle, $L_{jet} = 0.23\ m$, $m_{inj} = 200\ g$, $F_L = 17.5\ g/s$, values predicted from the correlation in Eq. 5-1, using measured gas distributions from Chapter 4)

Figure 5.15 shows that the asymmetrical baffle without a flux-tube can reduce the water trapped fraction by 30 % near the bed wall compared to the base case. It was slightly better compared to the best case without a baffle.

When increasing the nozzle penetration, a further decrease of water trapped in agglomerates could be observed by 80 % compared to the base case. This baffle was highly recommended to be installed just below the top injection rings, where the nozzle could penetrate beyond the baffle tip. At deeper injection locations, the beneficial impact

from the baffle was even less sensitive to the initial gas distribution (western, even, and eastern cases) because the gas bubbles were concentrated and redirected to the baffle tip region.

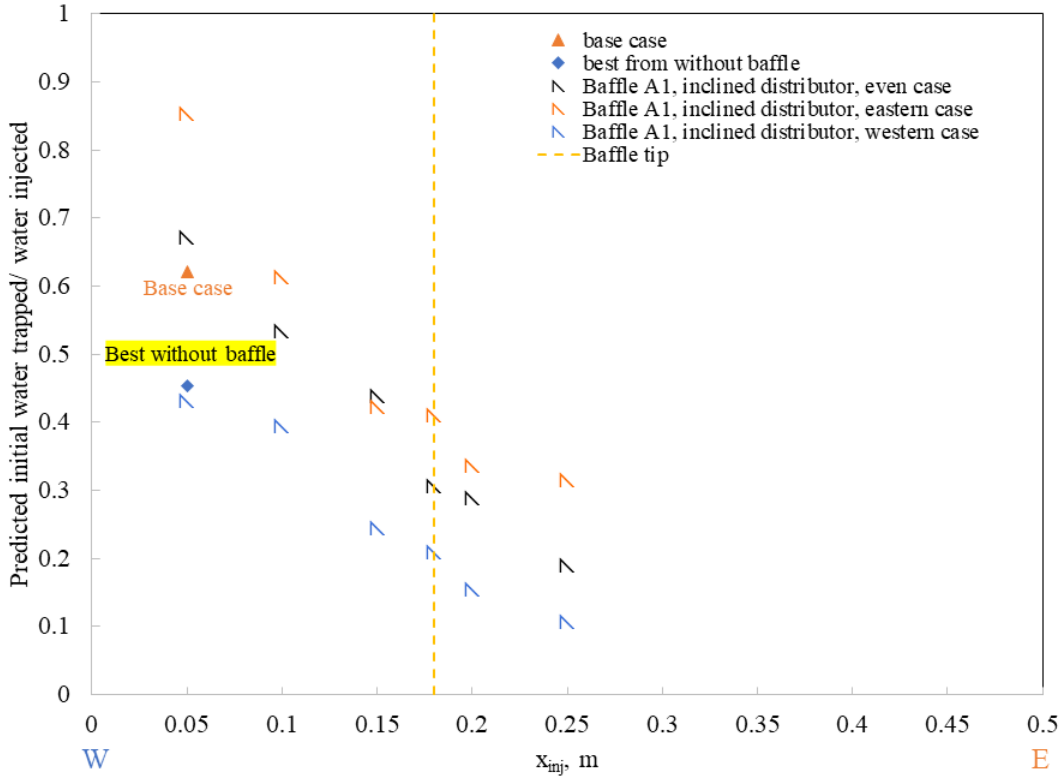

Figure 5.15 Impact of baffle A1 (Figure 4.3) with different gas distributor configurations on initial water trapped/ water injected in agglomerates at different injection locations (x_{inj}) when injecting from above the baffle ($V_{gi} = 1\ m/s$, $z_{inj} = 0.67\ m$, 1 mm TEB nozzle, $L_{jet} = 0.23\ m$, $m_{inj} = 200\ g$, $F_L = 17.5\ g/s$, values predicted from the correlation in Eq. 5-1, using measured gas distributions from Chapter 4)

Figure 5.16 shows that near the bed wall, the baffle A4 was non-beneficial, as the baffle was too big and resulted in much fewer gas bubbles and poor fluidization in regions near the bed wall. At deeper injection locations, with the asymmetrical baffle, which blocks

more cross-sectional area (baffle A4), similarly good performance as the baffle A1 was observed.

When comparing baffle A2 (Figure 5.15) and A4 (Figure 5.16) (36 % and 50 % blocking cross-sectional area, respectively), the smaller baffle (baffle A2) was recommended. Because the reduction of gas bubbles at the wall region from the smaller baffle was not as severe as that of the larger baffle, the smaller baffle showed better performance when injecting at the bed wall compared to the larger baffle. Both smaller and larger baffles highly concentrated and redirected gas bubbles to the baffle tip region. Therefore, the strong gas bubble flow there enhanced the jet-bed interaction.

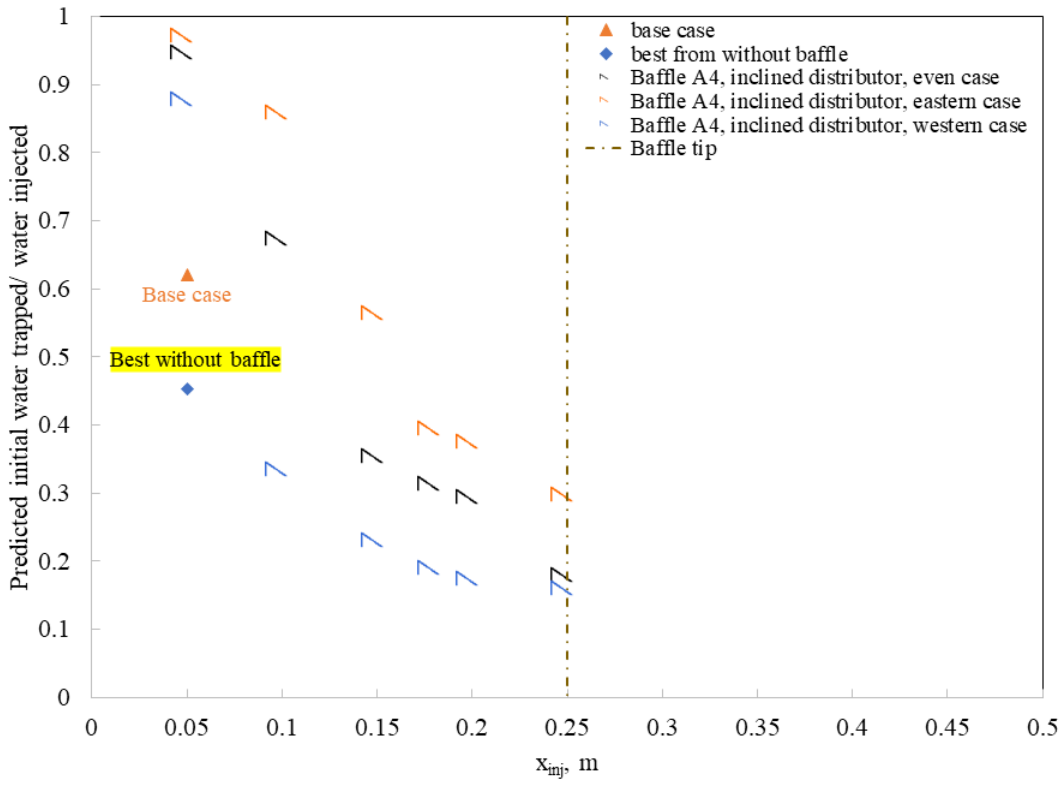

Figure 5.16 Impact of baffle A4 (Figure 4.4) with different gas distributor configurations on initial water trapped/ water injected in agglomerates at different injection locations (x_{inj}) when injecting from above the baffle ($V_{gi} = 1\ m/s$, $z_{inj} = 0.67\ m$,1 mm TEB nozzle, $L_{jet} = 0.23\ m$, $m_{inj} = 200\ g$, $F_L = 17.5\ g/s$, values predicted from the correlation in Eq. 5-1, using measured gas distributions from Chapter 4)

Figure 5.17 shows that with the asymmetrical baffle with the flux-tube, only one location with the western case gave a slightly better initial liquid distribution than the best case without a baffle. However, the asymmetrical baffle with flux-tube had a strong potential to be adjusted to become the best baffle (details in recommendations in section 7.2). For example, the flux-tube and baffle tip could be used to concentrate gas bubbles to the critical two regions shown in Eq. 5-1: at the nozzle tip; and at the transition between the stable jet core and the fluctuating part of the jet (details see section 5.5.3).

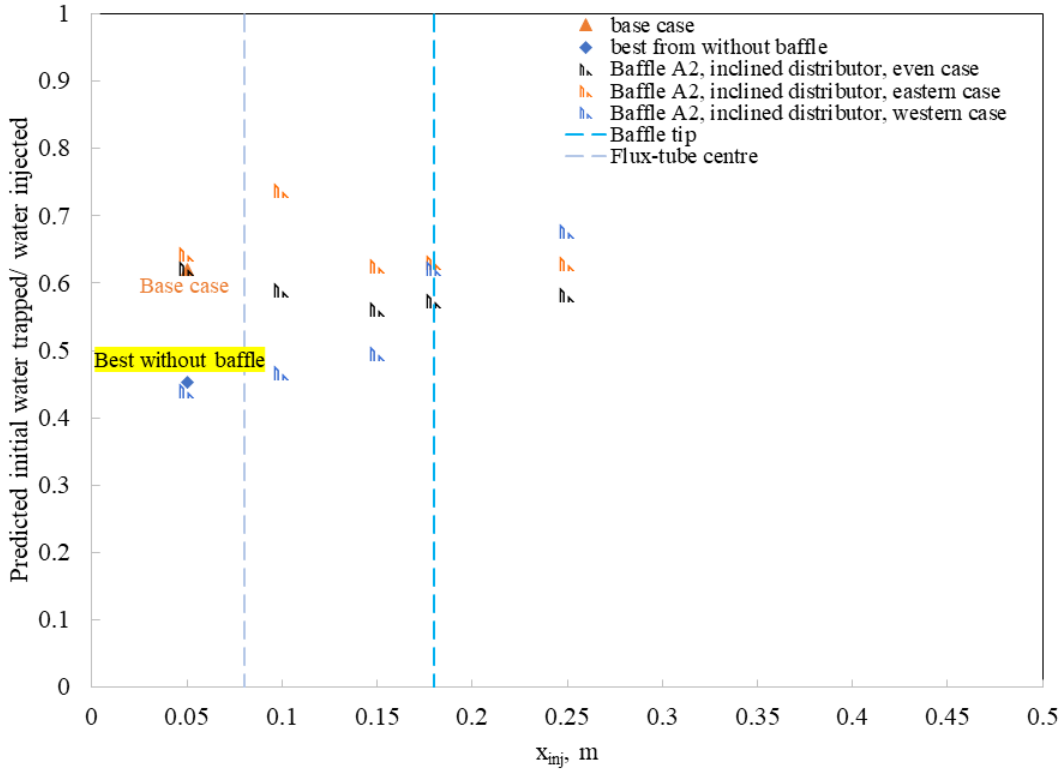

Figure 5.17 Impact of baffle A2 (Figure 4.5) with different gas distributor configurations on initial water trapped/ water injected in agglomerates at different injection locations (x_{inj}) when injecting from above the baffle ($V_{gi} = 1\ m/s$, $z_{inj} = 0.67\ m$,1 mm TEB nozzle, $L_{jet} = 0.23\ m$, $m_{inj} = 200\ g$, $F_L = 17.5\ g/s$, values predicted from the correlation in Eq. 5-1, using measured gas distributions from Chapter 4)

Figure 5.18 shows that with the symmetrical baffle, the slight beneficial impact from the baffle could be reached in baffle regions, as the gas bubble flow was stronger there

(Figure 4.7). This baffle was not highly recommended because the reduction of water trapped fraction is not that attractive.

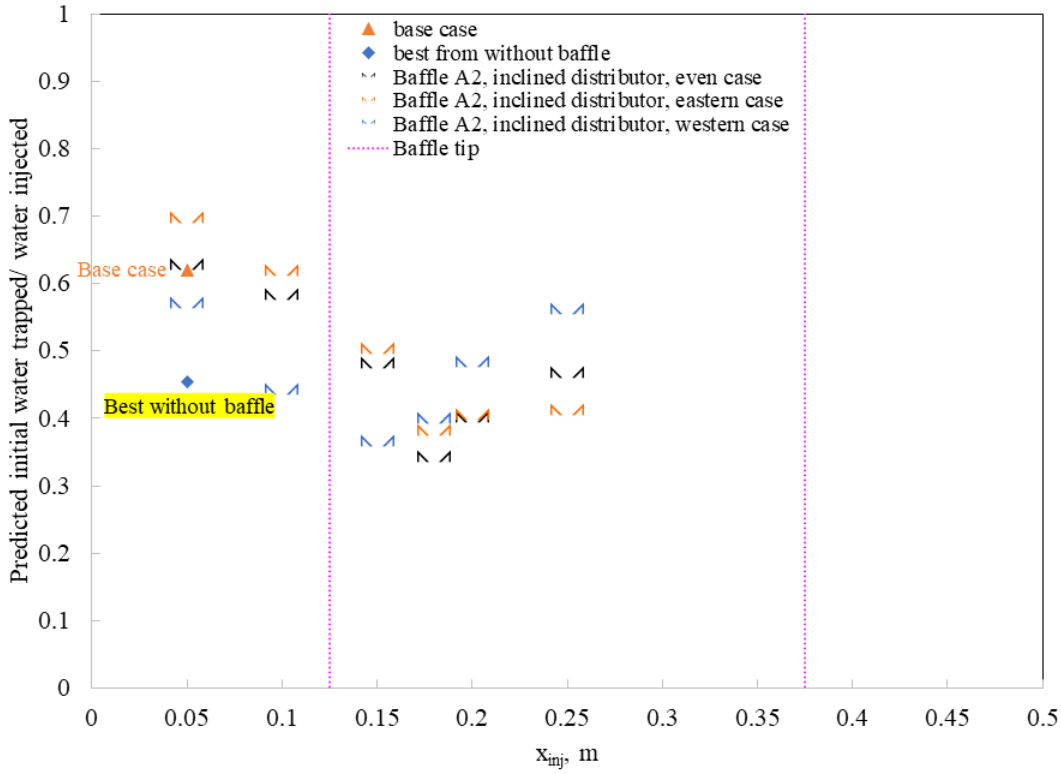

Figure 5.18 Impact of baffle S1 (Figure 4.7) with different gas distributor configurations on initial water trapped/ water injected in agglomerates at different injection locations (x_{inj}) when injecting from above the baffle ($V_{gi} = 1\ m/s$, $z_{inj} = 0.67\ m$,1 mm TEB nozzle, $L_{jet} = 0.23\ m$, $m_{inj} = 200\ g$, $F_L = 17.5\ g/s$, values predicted from the correlation in Eq. 5-1, using measured gas distributions from Chapter 4)

5.4 Impact of baffle on liquid distribution at different injection locations

Figure 5.19 shows the beneficial impact of the baffle dissipated with the increased vertical distance from the spray nozzle to the baffle.

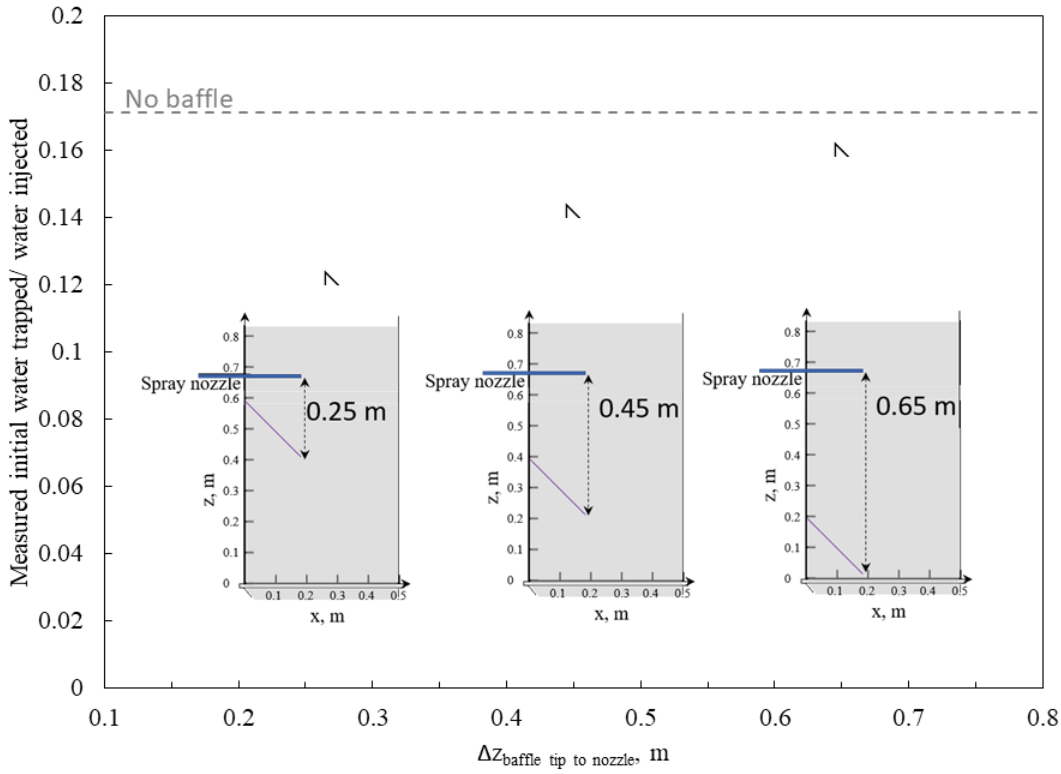

Figure 5.19 Impact of increase of distance between the spray nozzle and baffle A1 on initial water trapped/ water injected in agglomerates ($V_{gi} = 1\ m/s$, $V_{gd} = 0.65\ m/s$, $t_{drying} = 10\ min$, $z_{inj} = 0.67\ m$,1 mm TEB nozzle, $L_{jet} = 0.23\ m$, $m_{inj} = 200\ g$, $F_L = 17.5\ g/s$, method: Gum Arabic method in section 3.4)

Figure 5.20 shows that when injecting inside the baffle, when gas bubbles came in from below the baffle, lower water trapped/water injected could be reached. The best case reduced the water trapped fraction by 67 %, compared to the base case.

Injecting inside the baffle pocket is recommended when deep nozzle penetration is not applicable, such as in the lower injection rings.

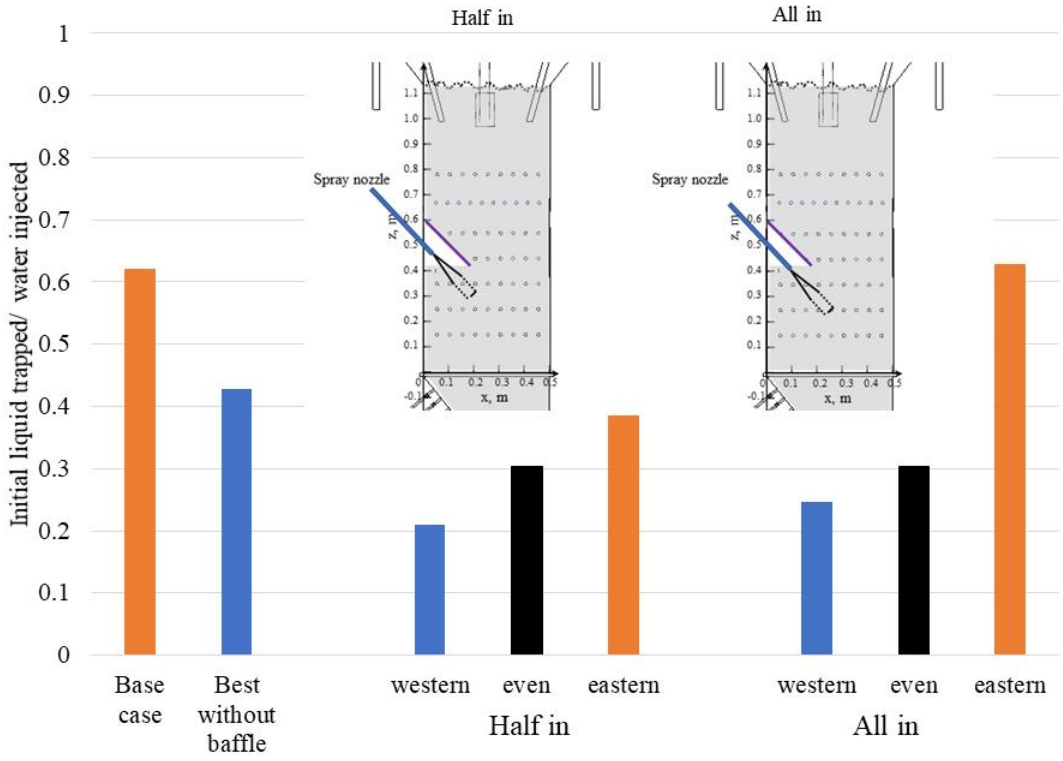

Figure 5.20 Impact of injecting from baffle pocket with different gas distributor configurations on initial water trapped/ water injected in agglomerates at different horizontal injection locations (x_{inj}) ($V_{gi} = 1\ m/s$, 1 mm TEB nozzle, $L_{jet} = 0.23\ m$, $m_{inj} = 200\ g$, $F_L = 17.5\ g/s$, method: E-probe estimation in section 3.4)

Figure 5.21 shows that when injecting just below the baffle, near the bed wall, water reduction trapped in agglomerates could be reached. It could be the benefit from the

turbulent flow, as just below the baffle, the gas bubbles direction was about to be modified by the baffle. Some bubbles could enter the baffle pocket and break up.

Injecting below the baffle was also recommended when deep nozzle penetration would not be applicable, such as lower injection rings. Even if it was not as effective as injecting inside the baffle, it could avoid the possible interaction of the spray jet to the lower feed jet.

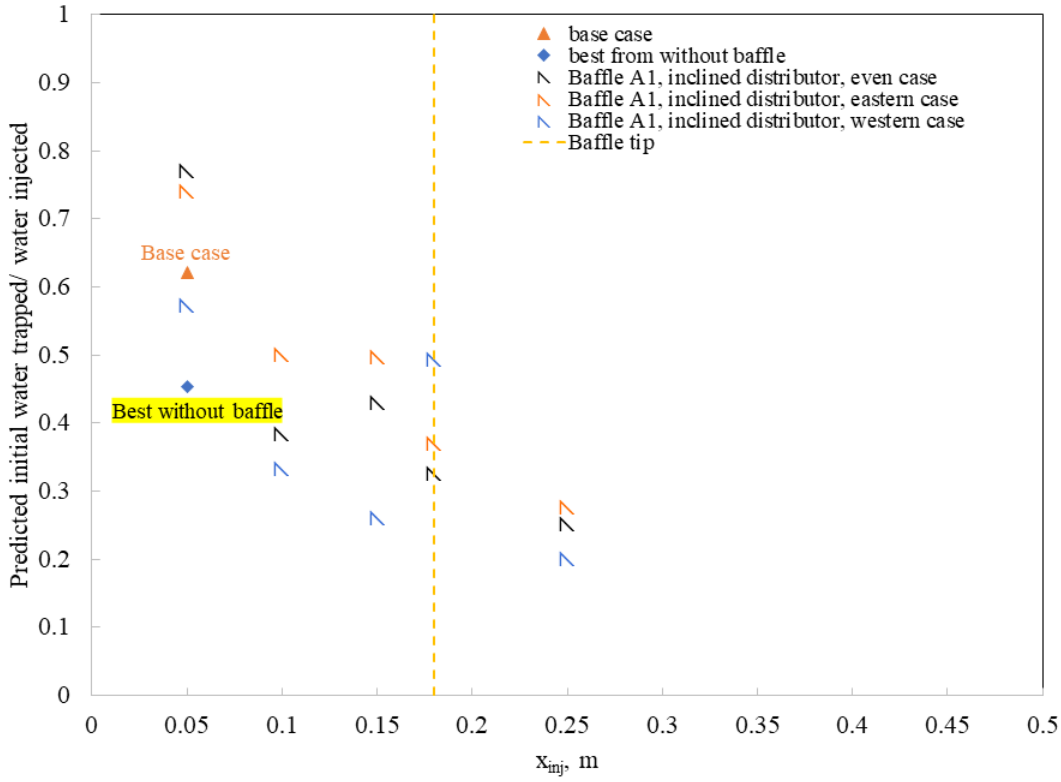

Figure 5.21 Impact of baffle A1 with different gas distributor configurations on initial water trapped/ water injected in agglomerates at different injection locations (x_{inj}) when injecting from below the baffle (Figure 2.9 B) ($V_{gi} = 1\ m/s$, $z_{inj} = 0.4\ m$, 1 mm TEB nozzle, $L_{jet} = 0.23\ m$, $m_{inj} = 200\ g$, $F_L = 17.5\ g/s$, values predicted from the correlation in Eq. 5-1, using measured gas distributions from Chapter 4)

5.5 Impact of gas distribution on liquid reaching stripper section

5.5.1 Impact of gas distribution on agglomerates properties

Figure 5.22 shows that directing the gas bubbles to the nozzle tip and the region between the stable jet core and the fluctuating part (best case with and without baffle) helped to reduce the fraction of water trapped in agglomerates for each size cut. Less water trapped in agglomerates indicated drier agglomerates, which agreed with the liquid to solid ratio in agglomerates shown in Figure 5.24.

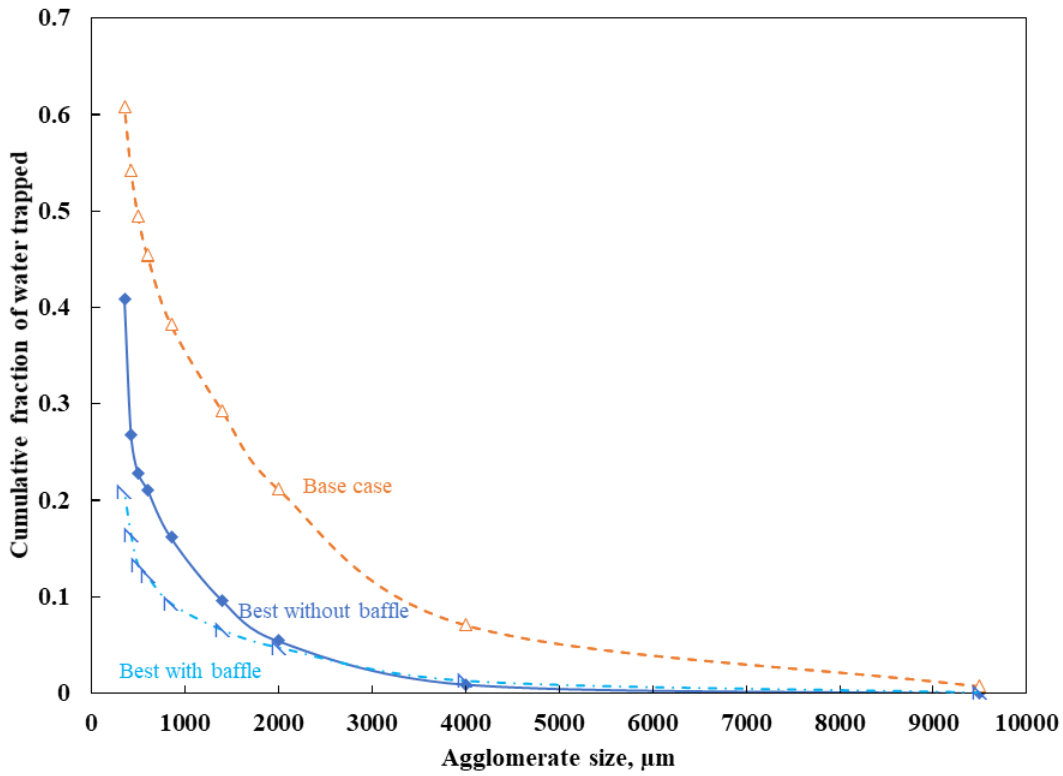

Figure 5.22 Best baffle (asymmetrical baffle A1), best case without baffle, and base case (Figure 5.17): cumulative fraction of water trapped/ water injected in agglomerates ($V_{gi} = 1\ m/s$, $z_{inj} = 0.4\ m$, 1 mm TEB nozzle, $L_{jet} = 0.23\ m$, $m_{inj} = 200\ g$, $F_L = 17.5\ g/s$, method: Gum Arabic in section 3.4)

Figure 5.23 shows that directing the gas bubbles to the nozzle tip and the first half of the spray helped to reduce the mass of agglomerates. However, it may not be very effective in reducing the mass of micro-agglomerates (agglomerates smaller than 500 μm). It

agrees with the information provided from Figure 5.22 that less liquid was trapped in agglomerates with the best case with and without baffle compared to the based case. The liquid was essential to form agglomerates (introduced in section 1.1.2): the wet agglomerates were formed as the binder solution connects particles. When the solvent was evaporated due to the heat convection from agglomerates to particles, strong agglomerates are formed [9].

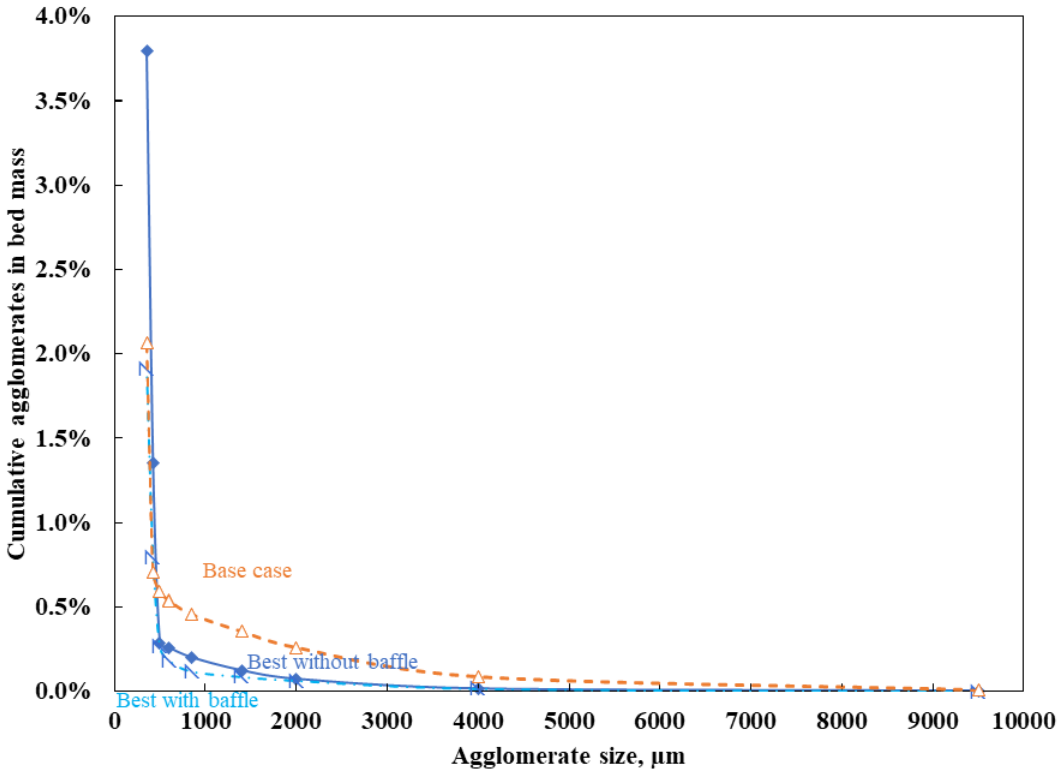

Figure 5.23 Best baffle (asymmetrical baffle A1), best case without baffle, and base case (Figure 5.17): cumulative fraction of water trapped/ water injected in agglomerates ($V_{gi} = 1\ m/s$, $z_{inj} = 0.4\ m$, 1 mm TEB nozzle, $L_{jet} = 0.23\ m$, $m_{inj} = 200\ g$, $F_L = 17.5\ g/s$, method: Gum Arabic in section 3.4)

Figure 5.24 shows that directing the gas bubbles to the nozzle tip and the first half of the spray helped to reduce the liquid to solid ratio (L/S) in agglomerates. The drier agglomerates were weaker and more easily broken [5]. The increase of broken up of agglomerates was desired as it reduced the risk of agglomerates reaching the stripper

section to foul and plug it [2]. The L/S in larger size cut of agglomerates, for instance, 9500 μm, was always a bit of tricky, as there was small number of agglomerates formed at 1 m/s. Figure 5.24 shows that generally, the cases had less total amount of liquid trapped in agglomerates is drier, which was expected.

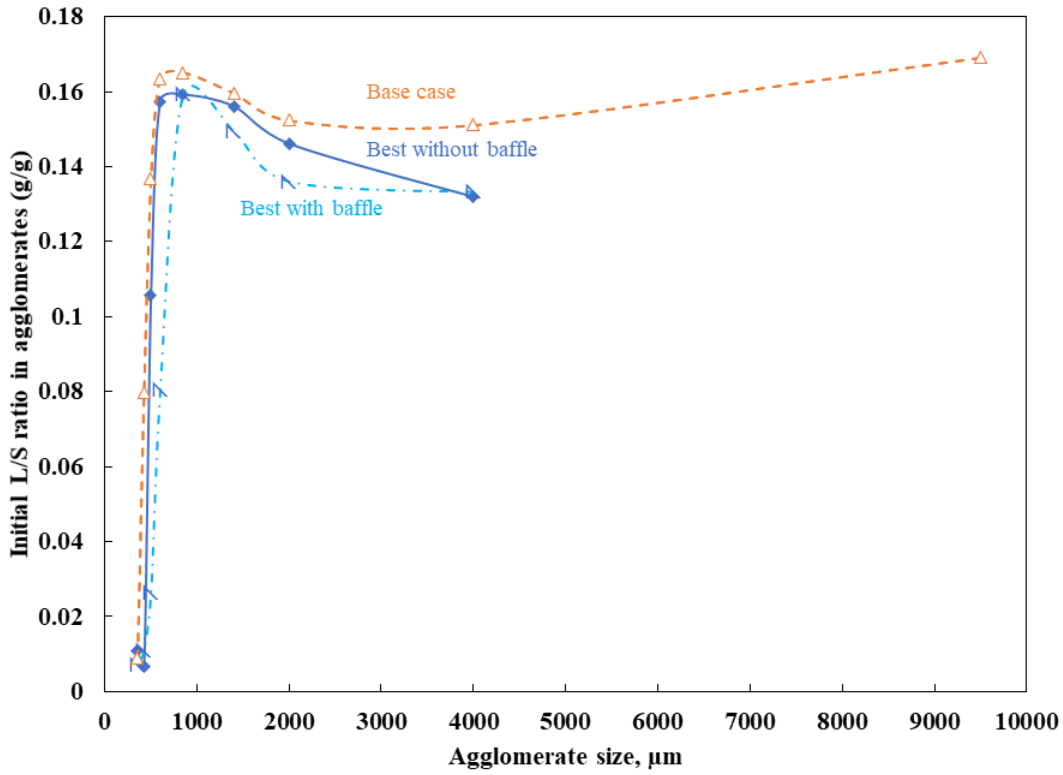

Figure 5.24 Best baffle (asymmetrical baffle A1), best case without baffle, and base case (Figure 5.17): initial liquid to solid ratio in each agglomerate size cut ($V_{gi} = 1\ m/s$, $z_{inj} = 0.4\ m$, 1 mm TEB nozzle, $L_{jet} = 0.23\ m$, $m_{inj} = 200\ g$, $F_L = 17.5\ g/s$, method: Gum Arabic in section 3.4)

5.5.2 Application of shrinking core model

Knowing the above agglomerate properties, we can calculate the remaining liquid fraction in agglomerates at any time, using a shrinking core model established by Sanchez Careaga et al.[1]. Therefore, one could predict the time required for the agglomerates created during injection to be dried before they reach the stripper section.

a. Model

Figure 5.25 shows the wet agglomerates behavior during drying:

1) At $t = 0$, it was assumed that the liquid trapped in an agglomerate is uniformly distributed throughout the agglomerate. At $t = \infty$, it was assumed that all the liquid is evaporated.
2) The surface temperature of agglomerates was equal to the bed temperature. It was assumed that the thermal cracking reaction was only limited by conduction heat transfer from the agglomerate outer surface to the reaction front.

Therefore, in the beginning, the thermal cracking reaction was faster. As time goes by, the amount of liquid being consumed was "shrinking." So, the thermal cracking reaction became slower.

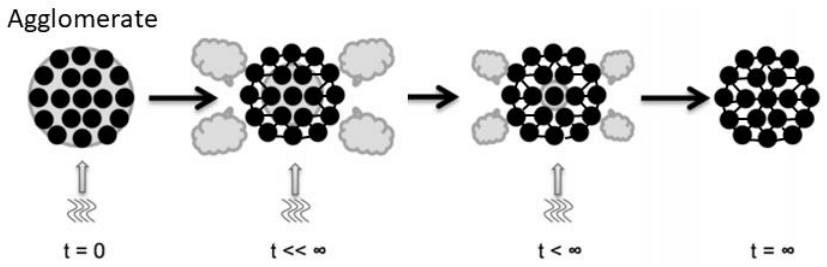

Figure 5.25 Wet agglomerate behavior during drying

b. Model equations

1) For each agglomerate, the initial liquid concentration (L/S) was C_0 and the radius was R.
2) If T_B was the bed temperature (typical is 550 °C), one can calculate ΔH, which was affected by C_0.

   ΔH was the enthalpy change when the liquid reacted. Considering the new coke forming from the thermal cracking reaction, we modified the enthalpy formula and presented it in Eq.5-2:

$$\Delta H = \Delta H_{Liq}(1 + \frac{C_P(T_B - T_R)}{C_0 \Delta H_{Liq}} + \frac{C_P(T_B - T_R)y_C}{C_0 \Delta H_{Liq}}) \quad 5\text{-}2$$

Where:

- ΔH_{Liq} was the enthalpy change when the liquid reacts (1152.41 kJ/kg[1])
- C_P was the bitumen heat capacity (2.72142 kJ/(kg °C)[1])
- y_C was the coke yield (20 %)

The only unknown parameter from this set of equations was the temperature at the reaction front (T_R). This temperature was obtained by comparing and minimizing the standard deviation of the model data presented by House et al.[10]. This yielded a value of 520 °C for T_R, which was reasonable given that the bed temperature of commercial Fluid Cokers is usually between 530 and 560 °C.

3) Then calculate γ:

$$\gamma = \frac{k(T_B - T_R)}{\rho_S \Delta H} \quad 5\text{-}3$$

Where:

- ρ_S was the particle density (1450 kg/m^3)
- k was the thermal conductivity of coke layers (1 $W/(m \cdot K)$ according to House et al.[10])
- T_B was the temperature of the bed (550 °C)
- T_R was the temperature at the reaction front (there the thermal cracking was taking place)

4) Then t_c:

t_c was the time for full conversion, that was, the total time required for full conversion of all the liquid within the agglomerate; this parameter was presented in Eq.5-4:

$$t_c = \frac{R^2 C_0}{6\gamma} \quad 5\text{-}4$$

5) Once t_c was calculated, the shrinking core model [1] could be used to calculate the fractional evaporation of the initial liquid vs. time for each agglomerate size cut. The overall fractional evaporation for all the agglomerates at time t was:

$$Y = \frac{\sum_{i=1}^{n}(C_{0i}x_i y_i)}{\sum_{i=1}^{n}(C_{0i}x_i)} \quad 5\text{-}5$$

6) Water remaining in agglomerates after injection at time t was given in Eq.5-6:

$$water\ remaining\ in\ agglomerates\ fraction = \frac{initial\ liquid\ trapped}{water\ injected}(1 - Y) \quad 5\text{-}6$$

c. Predicted results

Figure 5.26 shows a quick and significant reduction of the remaining liquid in agglomerates after the injection by changing the gas distribution. In a commercial coker, the agglomerates would be expected to be much larger, as much larger feed nozzles are applied [11]. Therefore, the drying of the agglomerates would be longer (10 to 30 s [12]). When compared to the base case, the best with baffle and the best without baffles cases shows a lower liquid fraction remaining in the agglomerates at any time. In industrial applications, drier agglomerates could result in less risk of fouling to the stripper section

or less liquid loss to the burner. Moreover, according to Reyes et al. [5], drier agglomerates are easier to be broken up.

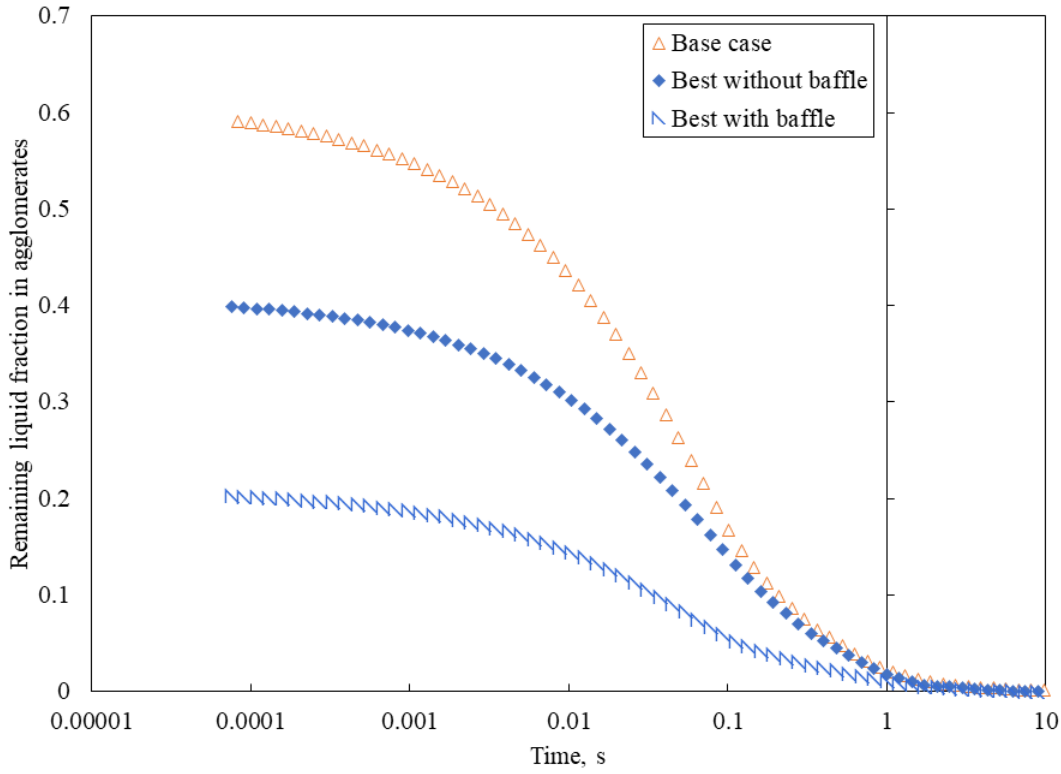

Figure 5.26 Best baffle (asymmetrical baffle A1), best case without baffle, and base case (Figure 5.17): remaining liquid fraction in agglomerates vs. time after injection($V_{gi} = 1\ m/s$, $z_{inj} = 0.4\ m$, 1 mm TEB nozzle, $L_{jet} = 0.23\ m$, $m_{inj} = 200\ g$, $F_L = 17.5\ g/s$, method: shrinking core model)

5.5.3 Model for the liquid concentration in wet solids

The purpose of this model was to predict the effect of local bed hydrodynamics on the average liquid concentration in the wet solids released from the spray region. This model was built from a basic model proposed by Mohagheghi et al. [13], which considered that all bubbles interacting with the jet cavity were equally likely to bring solids into the jet cavity; in this study, it was improved by modeling the mechanisms through which solids

from gas bubbles interacted with the jet cavity. Thus, the redirecting of gas bubbles to the jet cavity could be targeted more precisely.

a. Model

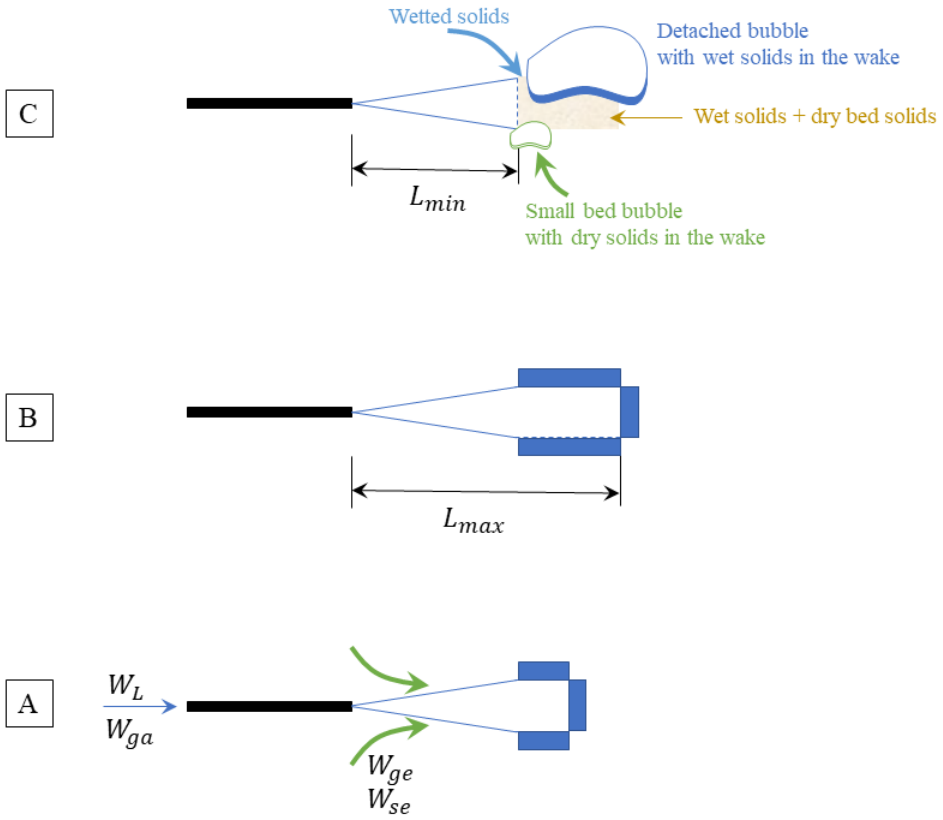

Figure 5.27 Spray jet cycle

Figure 5.27 shows the spray jet expansion cycle:

- Figure 5.27A shows the jet while it was expanding. Liquid (W_L) and atomization gas (W_{ga}) entered the jet cavity through the nozzle. Gas (W_{ge}) and solids (W_{se}) were entrained from the surrounding bed into the jet cavity because of the low-pressure zone in the jet cavity just downstream of the nozzle tip [14]. Wet solids accumulated at the tip of the jet cavity and were moved aside as the jet expands [15]. The wetted solids were a combination of solids entrained into the jet cavity and wetted emulsion phase solids at the jet tip.

- Figure 5.27B shows the fully expanded jet, with its maximum penetration length, L_{max}. Wetted solids have accumulated around the jet cavity.
- Figure 5.27C shows a large gas bubble detaching from the tip of the jet cavity. The jet had contracted by a volume equal to the volume of the detached bubble, and the jet penetration length was at its minimum value, L_{min}. The bubble detaching from the jet tip carried was away from the spray jet region, where some of the wet solids were at the periphery of the full expanded jet (Figure 5.27B); these solids were carried in its wake (Figure 5.27C). The volume previously occupied by the full expanded jet was filled in by solids: near L_{min}, the solids were wet solids that were previously at the periphery of the full expanded jet cavity. In contrast, further down, the wet solids from the periphery have mixed with dry solids that have replaced the wet solids carried in the wake of the detached bubble (Figure 5.27C).

b. Model equations

Local bed hydrodynamics had two separate impacts on the liquid concentration (c) of the wet solids carried from the spray region by the detached bubble:

Gas bubbles flowing near the nozzle tip help increased the flowrate of gas entrained into the jet cavity. The extra gas volume speeded up the jet expansion and increased the frequency at which bubbles detach from the region at the transition between the stable jet core and the fluctuating part of the jet. This increased the flowrate of solids carried in the wake of the detached bubbles (W_{st}) so that the injected liquid was diluted with more solids.

Just after the jet contraction, gas bubbles carried dry solids from the rest of the bed to the wet zone in the collapsed jet tip region (Figure 5.27C). These dry solids were exchanged with wet solids from this region that were carried by the bubbles rising away from the jet tip region. This was especially important for the region just beyond L_{min}, where the solids were wetter, with the same liquid concentration (c) as the wet solids removed in

the wake of the detached bubble. The flowrate of the exchanged solids (W_{sex}) could be obtained from the flowrate of solids carried by bubbles into the region just beyond L_{min}.

A liquid mass balance around the jet region provides:

$$W_L = c(W_{st} + W_{sex}) \quad 5\text{-}7$$

From which the liquid concentration of the wet solids carried from the jet region could be obtained:

$$c = \frac{W_L}{(W_{st} + W_{sex})} \quad 5\text{-}8$$

This section shows how the solids flowrate carried in the wake of the detached bubbles (W_{st}) and exchanged with small bubbles from the bed (W_{sex}) can be estimated.

i. Solids flowrate carried in the wake of detached bubbles

The solids flowrate carried in the wake of the bubbles detaching from the jet tip could be obtained from the gas flowrate flowing from the jet tip (W_{st}), the wake to bubble volumetric ratio and the density of the solids in the wake (ρ_{mf}):

$$W_{st} = f_W \frac{\rho_{mf}}{\rho_g} W_{gt} \quad 5\text{-}9$$

The density of the wake solids was assumed to be the bed density at minimum fluidization conditions and the wake to bubble volume ratio (f_W) can be assumed to be 0.1 [16, 17].

The gas flowrate flowing from the jet tip could be obtained by mass balance:

$$W_{gt} = W_{ga} + W_{ge} \quad 5\text{-}10$$

The atomization gas flowrate could be obtained from the GLR and the liquid flowrate (W_L):

$$W_{gs} = (GLR)W_L \quad 5\text{-}11$$

Because the bed was operated at velocities that are much larger than the minimum fluidization velocity, all the gas entering the jet cavity might be assumed to be in the form of gas bubbles. The gas flowrate entrained into the jet cavity could, thus, be obtained from the superficial gas velocity near the nozzle tip (q_N), and the cross-sectional area (a_N) from which bubbles are entrained:

$$W_{ge} = \rho_g q_N a_N \quad 5\text{-}12$$

The area from which bubbles were captured can be estimated from the nozzle diameter (d_N) and the bubble diameter (d_N):

$$a_N = \frac{\pi}{4}(d_N + d_B)^2 \quad 5\text{-}13$$

The bubble diameter was estimated to be about 4 cm, based on measurements conducted for this work.

Gas bubbles entering the jet cavity carried their wake solids into the jet cavity, and the corresponding entrained solids flowrate could be obtained from:

$$W_{se} = f_W \frac{\rho_{mf}}{\rho_g} W_{ge} \quad 5\text{-}14$$

Ariyapadi [14] provided a model to calculate the maximum solid flowrate ($W_{se,max}$) that can entrained by a spray from be gas-liquid jet from the surrounding fluidized bed, and which has been experimentally validated [18]. One should verify that:

$$W_{se} \leq W_{se,max} \quad 5\text{-}15$$

This condition was verified for all the conditions of this study.

ii. Solids flowrate exchanged with small bubbles from the bed

The flowrate of the exchanged solids (W_{sex}) could be obtained from the flowrate of solids carried by bubbles into the region just beyond L_{min}, which could be obtained from the flowrate of gas ($W_{g,min}$) from these bubbles:

$$W_{sex} = f_W \frac{\rho_{mf}}{\rho_g} W_{g,min} \quad 5\text{-}16$$

The gas flowrate associated with the bubbles entering the collapsed jet region just beyond L_{min} could be obtained from the local superficial gas velocity (q_{min}), the cross-sectional area (a_{min}) of the corresponding collapsed jet region and the fraction of the time during which this region is affected by bubbles (η):

$$W_{g,min} = \eta \rho_g q_{min} a_{min} \quad 5\text{-}17$$

The cross-sectional area of the corresponding collapsed jet region could be estimated from the bubble diameter (d_B) and the jet diameter (D):

$$a_{min} = 2 d_B D \quad 5\text{-}18$$

The fraction of the time during which the collapsed jet region was affected by bubbles can be obtained from the ratio of the time required for a bubble to traverse the jet height to the total jet cycle time:

$$\eta = \frac{\left(\frac{D}{U_B}\right)}{t_{jc}} \quad 5\text{-}19$$

The bubble velocity could be obtained from [19]:

$$U_B = 0.711\sqrt{g d_B} \quad 5\text{-}20$$

The jet diameter could be obtained from the full jet expansion angle (θ), the nozzle diameter (d_N) and minimum jet penetration (L_{min}):

$$D = d_N + 2L_{min} tan\left(\frac{\theta}{2}\right) \quad 5\text{-}21$$

The ratio of the minimum jet penetration (L_{min}) to maximum jet penetration (L_{max}) could range from 1.6 to 2 [5]. In this study, a ratio of 2 was selected. The expansion angle of a spray jet cavity was about 18 degrees [5, 20]. In this study, the maximum jet penetration (L_{max}) was obtained from measurements but it could also be predicted with a model [21, 22] or CFD studies [23].

The jet cycle time could be obtained from the volume of the jet tip region, between the minimum and maximum jet penetrations, and the gas flowrate through the jet:

$$t_c = \frac{\rho_g \frac{\pi}{4} D^2 (L_{max} - L_{min})}{W_{ga} + W_{ge}} \quad 5\text{-}22$$

c. Predicted results

i. The concentration of liquid in wet solids

Figure 5.24 shows that for the base case, the average liquid concentration in the recovered agglomerates is about $0.16\ g/g$. For this base case, Figure 5.22 shows that 60 % of the injected liquid is trapped in agglomerates so that the measured liquid concentration should not be much larger than the actual liquid concentration in the solids carried from the spray region. The model predicts a liquid concentration of $0.15\ g/g$.

ii. Comparison of predicted liquid concentration with liquid trapped in agglomerates

Figure 5.28 shows the predicted liquid concentration in solids leaving the spray jet with the model of 15 Gum Arabic runs. Table 5-4 shows the wide range of conditions of the 15 runs. Figure 5.28 shows that measurements found less liquid trapped in agglomerates under conditions for which the model predicted a lower liquid concentration in the wet solids leaving the spray jet. The objective of this research is to reduce the amount of liquid trapped in agglomerates by modifying local bed hydrodynamics, and the model can

help identify the most promising hydrodynamics, as shown by Table 5-4.

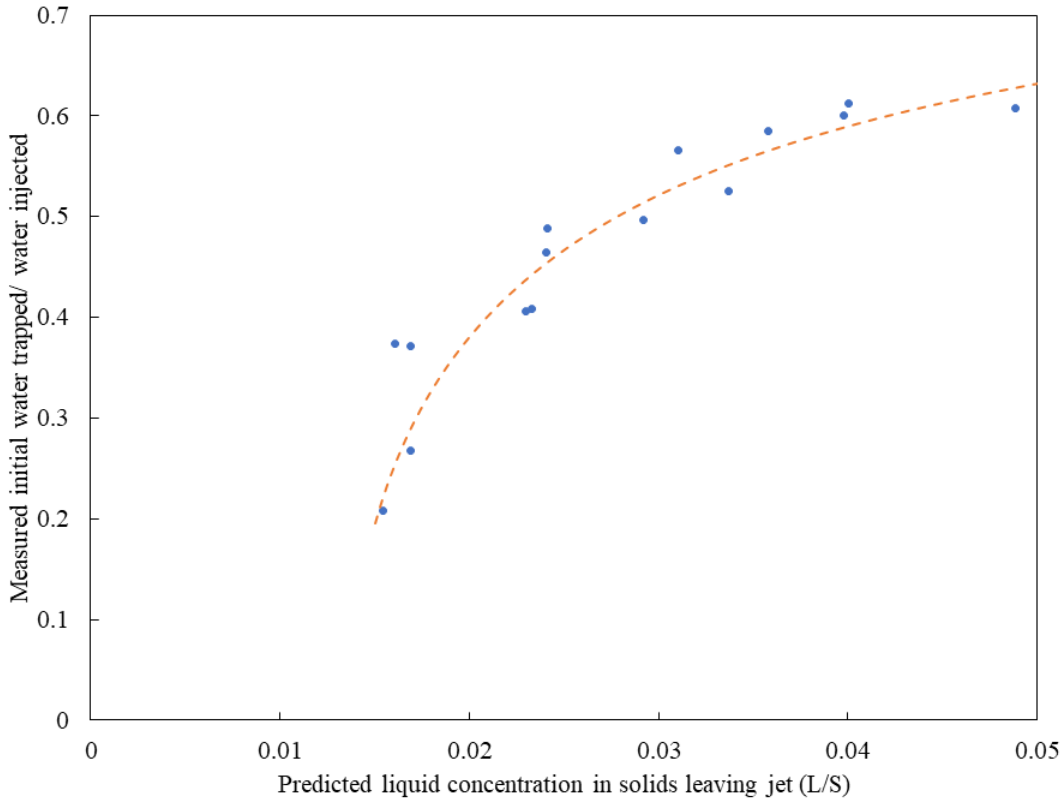

Figure 5.28 Comparison of experimental measured and model predicted results: initial water trapped/ water injected vs. liquid concentration in solids leaving the jet ($V_{gi} = 1\ m/s$, 1 mm TEB nozzle, $L_{jet} = 0.23\ m$, $m_{inj} = 200\ g$, $F_L = 17.5\ g/s$, method: Gum Arabic method (section 3.4), Model: model for the liquid concentration in wet solids)

Baffle	Gas distributor configuration	x_{inj}, m
No	Flat distributor	0.125
No	Inclined - even case	0.18
No	Inclined - western case	0.05
No	Inclined - western case	0.18
No	Inclined - eastern case	0.18
Baffle Type A1 (no flux-tube)	Inclined - even case	0.18
Baffle Type A1(no flux-tube)	Inclined - eastern case	0.18
Baffle Type A1(no flux-tube)	Inclined - eastern case	0.25
Baffle Type A1(no flux-tube)	Inclined - western case	0.18
Baffle Type A3 (short flux-tube)	Inclined - even case	0.04
Baffle Type A3 (short flux-tube)	Inclined - even case	0.08
Baffle Type A3 (short flux-tube)	Inclined - even case	0.18
Baffle Type A2 (long flux-tube)	Inclined - even case	0.18
Baffle Type S1 (symmetrical baffle)	Inclined - even case	0.125
Baffle Type S1(symmetrical baffle)	Inclined - even case	0.2

Table 5-4 Conditions of runs shown in Figure 5.28 ($V_{gi} = 1\ m/s$, 1 mm TEB nozzle, $L_{jet} = 0.23\ m$, $m_{inj} = 200\ g$, $F_L = 17.5\ g/s$, method: Gum Arabic method (section 3.4))

Table 5-5 shows that the model could correctly predict which bed hydrodynamic conditions in the spray region will minimize agglomerate formation: the measured fraction of injected liquid that is trapped in agglomerates correlates well with the liquid concentration in the wet solids carried from the spray jet region that is predicted by the model.

Condition	**Predicted liquid concentration in wet solids carried from the spray jet region**	**Measured fraction of injected liquid that is trapped in agglomerates**
Base case	0.15	0.61
Best case without baffle	0.023	0.41
Best case with baffle	0.015	0.21

Table 5-5 Comparison between predicted liquid concentration of solids carried from the spray region and measured liquid trapped in agglomerates.

5.6 Conclusions

To reduce agglomerates formation during injection in a coker:

a. Increase the superficial gas velocity:

This agrees with the previous publication from Li et al. 2016; the initial water trapped/water injected decreases by about 53.65 % with the increase of superficial gas velocity from 0.18 to 1 m/s.

The asymmetrical baffle without a flux-tube (corresponding to a ring baffle without a flux-tube in a coker) is even more effective at the lower fluidization velocities corresponding to the bottom region of cokers.

b. Change the gas distribution:

Concentrating gas bubbles to two regions can significantly reduce the initial liquid trapped fraction in agglomerates: the first region is the nozzle tip; the second region is the region at the transition between the stable jet core and the fluctuating part of the jet. This reduces the water trapped fraction in agglomerates for each size cut, the mass of macro-agglomerates, and the liquid to solids ratio in agglomerates. This can be achieved, for example, by:

i. Modifying the fluidization gas distributor. In the experiments, this could reduce the water trapped fraction in agglomerates by 25 %.

   It might be difficult to modify the gas distributor in a coker. However, there are other ways to achieve the same goal. For example, one can move the steam to the desired regions. As for the local gas distribution in a coker, one can use numerical modeling to determine where to direct the steam and how much steam is needed.

ii. Use a baffle:

A ring baffle without a flux-tube is more suitable to be applied at the top of a reactor because there is more room to locate the spray nozzle tip at the desired location. In these experiments, the water trapped fraction could be reduced by 80 % compared to the base case (current injection conditions in a coker).

When scaled up to commercial coker conditions, a nozzle penetration of 2.5 m will not be an issue at higher injection locations, where the bed diameter is 10 m, while at lower injection banks, where the bed diameter is only 7 m, the spray jets could hit each other. Another potential issue is that the agglomerates created at the jet tip could quickly move to another spray jet and get rewetted. The rewetted agglomerates are wetter and stronger [5], which is not preferred.

At lower nozzle banks, benefits can be achieved by injecting from inside a baffle pocket or from below the baffle. In these experiments, the reduction of water trapped compared to the base case can be reduced by 67 % and 40 %, respectively, when injected near the bed wall. The nozzle penetration is preferred to be 0.05 m in the laboratory unit, corresponding to the current nozzle penetration in a coker.

The model to predict liquid concentration in wet solids released from the spray region shows that by directing gas bubbles to the nozzle tip and region at the transition between the stable jet core and the fluctuating part of the jet, the liquid in the agglomerates can be easily evaporated. The shrinking core model shows that with such conditions, the remaining liquid in the agglomerates is easier to be completely evaporated. Thus, the local bed hydrodynamics near the jet cavity can be modified to reduce the risk of fouling in the stripper section and the loss of valuable liquid to the burner.

5.7 Nomenclature

a_N	m^2	Cross-sectional area
a_{min}	m^2	Cross-sectional area at collapsed jet region just beyond L_{min}
c	g/g	The liquid concentration of the wet solids carried from the jet region
C_0	g/g	Initial liquid concentration
C_P	$kJ/(kg\,°C)$	Bitumen heat capacity
d_N	m	Nozzle diameter
d_B	m	Bubble diameter
D	m	Jet diameter
f_W		Wake to bubble volume ratio
k	$W/(m \cdot K)$	Thermal conductivity of coke layers
F_L	g/s	Liquid flowrate
g	m/s^2	Gravitational acceleration, 9.81
GLR	%	Gas to liquid ratio in the gas-liquid spray jet
ΔH	kJ/kg	Enthalpy change when the liquid reacts, taking into account the new coke forming from the thermal cracking reaction
ΔH_{Liq}	kJ/kg	Enthalpy change when the liquid reacts
L/S	g/g	Liquid to solid ratio

L_{jet}	m	Jet penetration
L_{max}	m	Maximum jet penetration
L_{min}	m	Minimum jet penetration
m_{inj}	g	Mass of injection
q_N	m/s	The superficial gas velocity near the nozzle tip
q_{min}	m/s	Superficial gas velocity at collapsed jet region just beyond L_{min}
$q_{avg,\ -0.02\ to\ 0.01\ m}$		Average normalized local gas bubble flux between -0.02 to 0.01 m, while nozzle tip is set at 0.
$q_{avg,\ 0.12\ to\ 0.16\ m}$		Average normalized local gas bubble flux between 0.12 to 0.16 m, while nozzle tip is set at 0.
R	m	Radius
T_B	$°C$	Bed temperature
T_R	$°C$	The temperature at the reaction front (where the thermal cracking is taking place)
t_c	s	Time for full conversion
t_{jc}	s	Total jet cycle time
U_{mt}	m/s	Minimum turbulent velocity
U_{mf}	m/s	Minimum fluidization velocity

U_B	m/s	Gas bubble velocity
V_g	m/s	Superficial gas velocity
V_{gd}	m/s	Superficial gas velocity during drying
V_{gi}	m/s	Superficial gas velocity during injection
W_L	g/s	The mass flowrate of liquid
W_{st}	g/s	The flowrate of solids carried in the wake of the detached bubbles
W_{sex}	g/s	The flowrate of the exchanged solids
W_{gt}	g/s	Gas flowrate flowing from the jet tip
W_{ge}	g/s	Gas flowrate entrained from surrounding bed into the jet cavity
W_{ga}	g/s	Atomization gas flowrate
W_L	g/s	Liquid flowrate in the gas-liquid spray jet
W_{se}	g/s	The flowrate of the exchanged solids
$W_{se,max}$	g/s	Maximum solid flowrate ($W_{se,max}$) that can entrain by a spray from a fluidized bed
$W_{g,min}$	g/s	The flowrate of gas from these bubbles
x_{inj}	m	Horizontal injection location
y_C	%	Coke yield

γ		A constant that is independent of size and initial liquid concentration that is described in Eq.5-3.
Y	%	Overall fractional evaporation for all the agglomerates at time t
z_{inj}	m	Vertical injection location

Greek

η		The fraction of the time during which the collapsed jet region is affected by bubbles
θ	°	The full jet expansion angle
ρ_S	kg/m^3	Particle density
ρ_g	kg/m^3	Gas density
ρ_{mf}	kg/m^3	The density of the solids in the wake

5.8 References

1. Careaga, F.J.S., *Hydrodynamics in Recirculating Fluidized Bed Mimicking the Stripper Section of the Fluid Coker* in *Chemical and Biochemical Engineering* 2013, Western University.

2. Cochet, Y., *Impact of column geometry and internals on gas and particle flows in a fluidized bed with downward solids circulation*, in *Chemical and Biochemical Engineering*. 2021, Western University: unpublished.

3. Li, L., *Effect of Local Bed Hydrodynamics on the Distribution of Liquid in a Fluidized Bed*. 2016, MESc thesis, Western University.

4. Briens, C., et al., *Effect of successive sprays on liquid distribution in fluidized beds.* Particuology, 2021. **54**: p. 17-24.

5. Reyes, L.A.P., *Effect of temperature and successive sprays on liquid distribution in fluidized beds*. 2015, School of Graduate and Postdoctoral Studies, University of Western Ontario.

6. Briens, C. and J. McMillan, *Review of Research Related to Fluid Cokers.* Energy & Fuels, 2021.

7. Kamienski, P., et al. *FLEXICOKING™ Resid Upgrading Technology*. in *11th International BBTC Conference*. 2013. Dubrovnik.

8. WYATT, J.T., et al., *Circulating fluid bed reactor with improved circulation*. 2013, Google Patents.

9. Jacob, M., *Granulation equipment*, in *Handbook of powder Technology*. 2007, Elsevier. p. 417-476.

10. House, P., *Interaction of gas-liquid jets with gas-solid fluidized beds: Effect on liquid-solid contact and impact on fluid coker operation*. 2007, Faculty of Graduate Studies, University of Western Ontario.

11. Joness, A.M., *The Effect of Scale on Spray Nozzle Performance.* 2019.

12. Wormsbecker, M., et al. *Phosphorescent tracing to study solids mixing in fluidized beds*. in *AIChE Annual Meeting, Conference Proceedings*. 2012.

13. Mohagheghi Dar Ranji, M., *Impact of Local Bed Hydrodynamics on Jet-Bed Interaction*. 2014, PhD thesis, Western University.

14. Ariyapadi, S., et al., *Modeling the injection of gas-liquid jets into fluidized beds of fine particles.* Canadian Journal of Chemical Engineering, 2003. **81**(3-4): p. 891-899.

15. Ariyapadi, S., et al., *Digital X-ray imaging technique to study the horizontal injection of gas-liquid jets into fluidized beds.* International Journal of Chemical Reactor Engineering, 2003. **1**(1): p. A 56.

16. Pemberton, S.T. and J.F. Davidson, *Elutriation from fluidized beds—I. Particle ejection from the dense phase into the freeboard.* Chemical Engineering Science, 1986. **41**(2): p. 243-251.

17. Briens, C.L., M.A. Bergougnou, and T. Baron, *Prediction of entrainment from gas-s̄olid fluidized beds.* Powder Technology, 1988. **54**(3): p. 183-196.

18. Hulet, C., et al., *Entrainment and stability of a horizontal gas-liquid jet in a fluidized bed.* International Journal of Chemical Reactor Engineering, 2003. **1**(1).

19. Grace, J.R., X. Bi, and N. Ellis, *Essentials of Fluidization Technology*. 2020: Wiley Online Library. 604.

20. Berruti, F., M. Dawe, and C. Briens, *Study of gas–liquid jet boundaries in a gas–solid fluidized bed.* Powder Technology, 2009. **192**(3): p. 250-259.

21. Ariyapadi, S., et al., *Horizontal penetration of gas-liquid spray jets in gas-solid fluidized beds.* International Journal of Chemical Reactor Engineering, 2004. **2**(1).

22. Careaga, F.S., C. Briens, and F. Berruti. *Measurement of penetration and cycle time of jets from an industrial fluid coking spray nozzle*. in *Fluidization XV*. 2016. Montebello, Quebec, Canada: ECI.

23. Pougatch, K., M. Salcudean, and J. McMillan, *Three-dimensional numerical modelling of interactions between a gas–liquid jet and a fluidized bed.* Chemical Engineering Science, 2012. **68**(1): p. 258-277.

Chapter 6

6 Impact of gas bubble flow and baffle on wet solids mixing

Chapter 5 indicated that a baffle can improve the initial distribution of injected liquid on bed particles by redirecting gas bubbles to the nozzle tip and the region at the transition between the stable jet core and the fluctuating part of the jet. However, it is unknown whether it is helpful to install a baffle in a coker from the point of view of wet solids mixing.

Wet solids mixing is important in Fluid Coking. Rapid dispersion of wet particles from the spray region to other regions of the fluidized bed is essential to achieve efficient heat transfer from the hot, dry bed particles to the wet particles, and provide the heat required for reaction and vaporization; because a typical Fluid Coker uses about 100 spray nozzles distributed through the reactor volume, this requires intense local wet solids mixing [1]. It is also important to prevent the rapid transfer of wet particles from the spray region to the lower bed regions, commonly referred to as solids by-passing, where they would foul the stripper sheds or result in undesirable liquid losses to the burner.

Chapter 4 showed that a baffle can redirect gas bubbles to the baffle region. In a previous study by Cochet et al.[2], a baffle created a staging effect for vertical solids mixing. The baffle would likely provide staging for vapors as well [1]. Wyatt et al.[3] showed that the baffle increased the time available for drying the solids by reducing solids by-passing.

This chapter aims to show how the symmetrical baffle affects wet solids mixing and local evaporation rate with an ideal spray that does not produce agglomerates.

6.1 Impact of gas bubble flow and a baffle on wet solids trajectory from the spray zone

Figure 6.1 B shows that the liquid from the spray jet first wetted the solids near itself. Then the wet solids were picked up by the upward flowing bubbles to be mixed with dry solids. The liquid was transported by mixing solids everywhere in the bed. Therefore, the

liquid could be applied as a tracer to tell where the wet solids traveled from the spray region. The approximate wet solids trajectory was shown with the arrow.

When the liquid was sprayed into the bed, the gas bubble flow from the spray level helped distribute the liquid (Figure 6.1 A). Below the spray region, the strong dry gas bubble flow prevented liquid from reaching the lower section quickly.

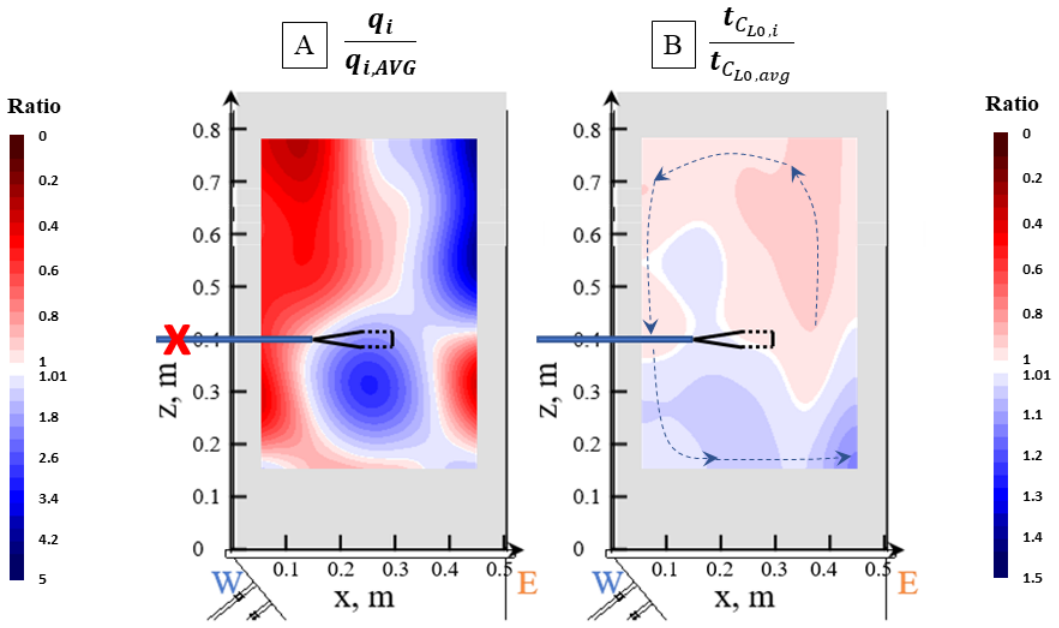

Figure 6.1 Impact of gas bubble flow (A) on time it takes for the liquid to reach certain location in the bed (B) without a baffle (Flat distributor, $V_g = 0.9\ m$, No injection for normalized gas distribution, $T_{bed} = 30$ ℃; for normalized local liquid concentration: 4.94 mm High GLR nozzle: $x_{inj} = 0.15\ m$, $z_{inj} = 0.4\ m$, $L_{jet} = 0.15\ m$, $m_{inj} = 100\ g$, $F_L = 1.6\ g/s$, $GLR = 107$ %, $T_{bed} = 20$ ℃, Arrow: approximate wet solids trajectory. Method: gas distribution in section 3.1, liquid concentration in section 3.6)

Figure 6.2 shows that with a symmetrical baffle, the gas bubbles (Figure 6.2 A) helped liquid distribution above the spray jet (Figure 6.2 B), similar to the no baffle case. And

below the spray, the strong gas bubbles prevented the liquid from reaching the lower region of the bed.

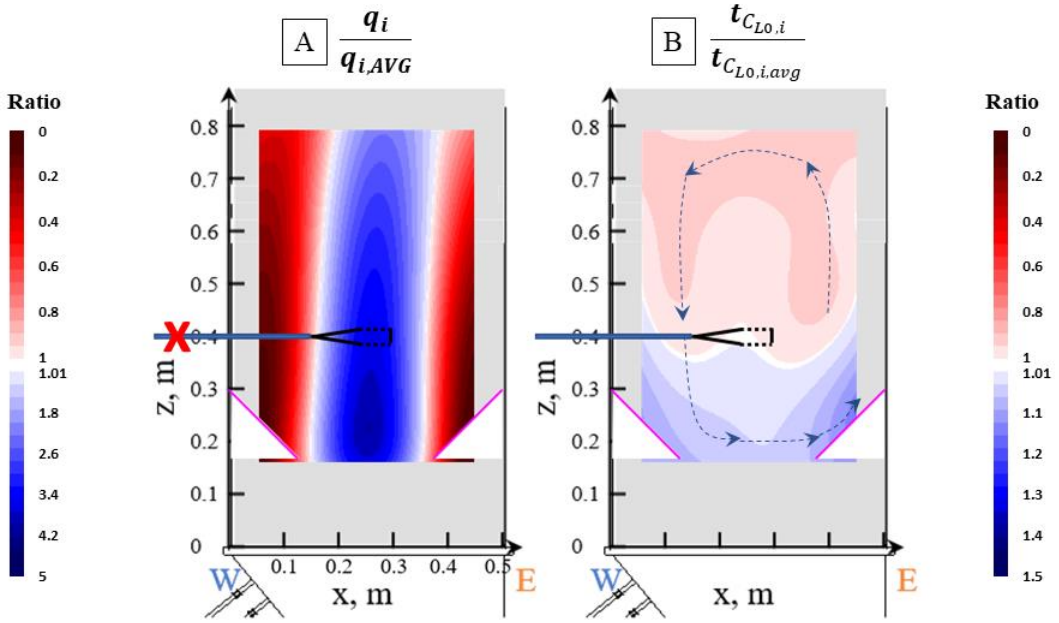

Figure 6.2 Impact of gas bubble flow (A) on time it takes for the liquid to reach certain location in the bed (B) with symmetrical baffle (Flat distributor, $V_g = 0.9\ m$, No injection for normalized gas distribution, $T_{bed} = 30$ ℃; for normalized local liquid concentration: 4.94 mm High GLR nozzle: $x_{inj} = 0.15\ m$, $z_{inj} = 0.4\ m$, $L_{jet} = 0.15\ m$, $m_{inj} = 100\ g$, $F_L = 1.6\ g/s$, $GLR = 107$ %, $T_{bed} = 20$ ℃, Arrow: approximate wet solids trajectory. Method: gas distribution in section 3.1, liquid concentration in section 3.6)

Figure 6.3 shows that when the superficial gas velocity was increased, the liquid was distributed more quickly everywhere in the bed for both cases with and without a baffle.

Figure 6.3 shows that the baffle had an insignificant impact on the overall time it took to wet the whole bed. This indicates that the baffle did not hinder wet solids dispersion.

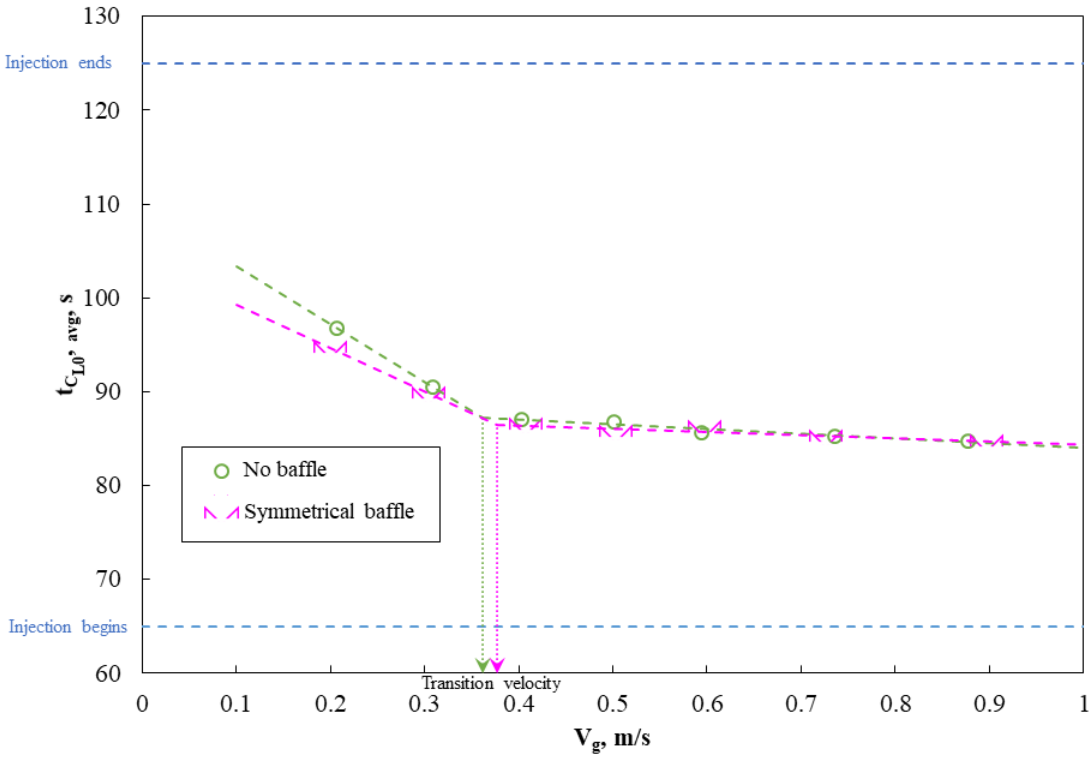

Figure 6.3 Impact of the symmetrical baffle on bed average time it takes to each all probes in the bed (Flat distributor, symmetrical baffle, 4.94 mm High GLR nozzle: $x_{inj} = 0.15\ m$, $z_{inj} = 0.4\ m$, $L_{jet} = 0.15\ m$, $m_{inj} = 100\ g$, $F_L = 1.6\ g/s$, $GLR = 107$ %, $T_{bed} = 20$ ℃, method: liquid concentration in section 3.6)

Figure 6.4 shows that for both with and without baffle cases, when increasing the superficial gas velocity, the time it took to wet the region both above the spray, and below the spray became closer to the bed average, which indicated better mixing. The transition velocities from above the spray, below the spray, and the average of the whole bed, were consistent. The transition velocity was believed to have a connection with the bubbling to turbulent fluidization regime transition. The comparison between the

transition velocity with injection and the minimum turbulent velocity without injection was discussed in section 6.4.

Figure 6.1 and Figure 6.2 show that near the feed jets, in the beginning, the liquid tended to go upward. The symmetrical baffle installed just under the spray accelerated the mixing above the baffle; thus, wet solids were dispersed relatively more quickly in the bed above the baffle (Figure 6.4 A). While below the spray, the symmetrical baffle was

slightly more efficient in preventing the liquid from reaching below the baffle region than the no baffle case (Figure 6.4 B).

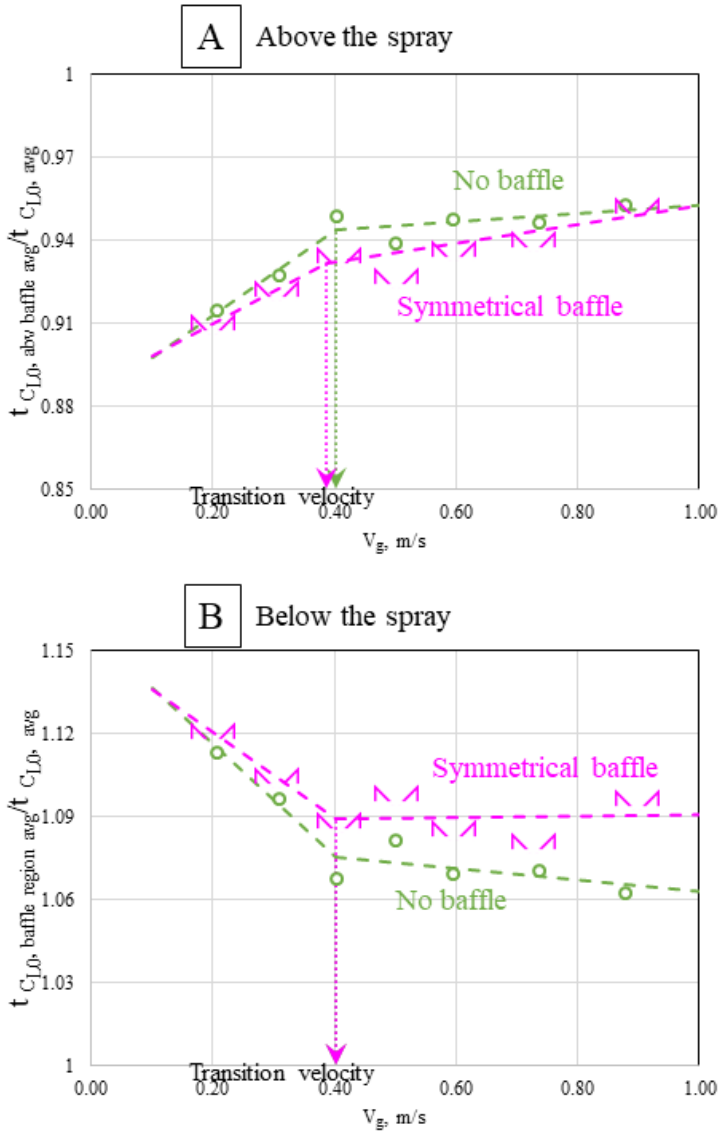

Figure 6.4 Impact of the symmetrical baffle on the average time it takes for the liquid to reach (A) above the spray and (B) below the spray, comparing to the average time of the whole bed (Flat distributor, 4.94 mm High GLR nozzle: $x_{inj} = 0.15\ m$, $L_{jet} = 0.15\ m$, $m_{inj} = 100\ g$, $F_L = 1.6\ g/s$, $GLR = 107$ %, $T_{bed} = 20$ ℃, spray level: z=0.4 m, above baffle: $z > 0.45\ m$; baffle region: $z < 0.35\ m$)

6.2 Impact of gas bubble flow and a baffle on maximum liquid concentration

$C_{L,max}$ was the local maximum liquid concentration. With 100 g of water injection, the local maximum liquid concentration was usually seen within 10 s after the injection is complete. Figure 6.5 shows that where there were more gas bubbles (Figure 6.5 A), there was less liquid (Figure 6.5 B). More gas bubbles resulted in more frequent mixing between the wet solids and the dry solids carried in the wake of gas bubbles. The gas bubbles would then carry the wet solids from the surrounding emulsion phase. Therefore, the local liquid concentration was lower where there are more gas bubbles, as shown in Figure 6.5.

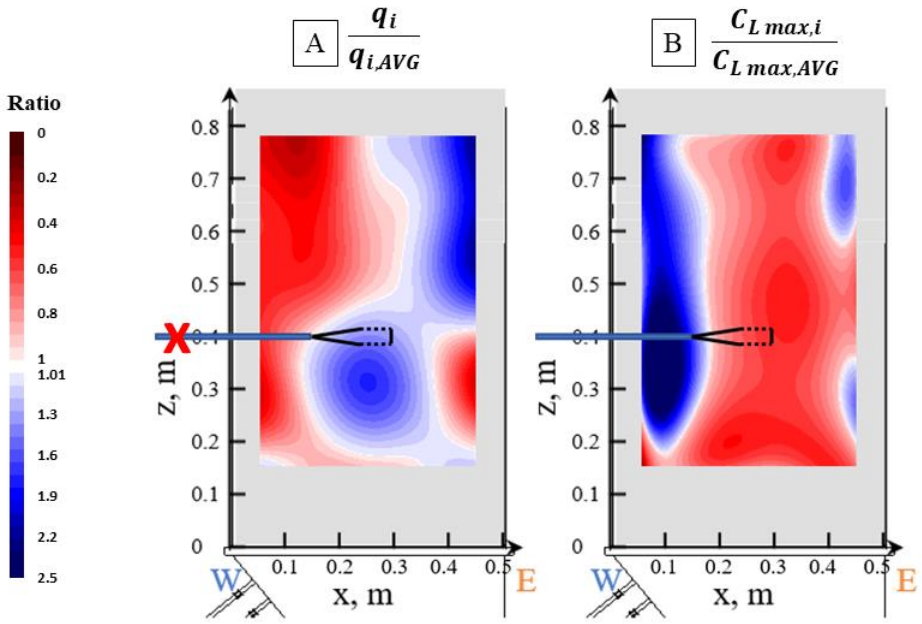

Figure 6.5 Impact of gas bubble flow (A) on local liquid concentration (B) without a baffle (Flat distributor, $V_g = 0.9\ m$, No injection for normalized gas distribution, $T_{bed} = 30$ ℃; for normalized local liquid concentration: 4.94 mm High GLR nozzle: $x_{inj} = 0.15\ m$, $z_{inj} = 0.4\ m$, $L_{jet} = 0.15\ m$, $m_{inj} = 100\ g$, $F_L = 1.6\ g/s$, $GLR = 107$ %, $T_{bed} = 20$ ℃, method: gas distribution in section 3.1, liquid concentration in section 3.5)

Figure 6.6 also shows, at the bed center, there was less liquid (Figure 6.6 B) comparing to the average of the bed, because there were more gas bubbles (Figure 6.6 A) redirected by the symmetrical baffle. It was notable that, without a baffle, the gas concentrated to the eastern side (discussed in section 4.1) at higher vertical locations, which resulted in less liquid there. While with the symmetrical baffle, the gas bubbles were concentrated to the bed center; thus, only the bed center showed less liquid. It indicated that the local liquid concentration is highly related to the gas bubble distribution in the bed.

Also, the baffle created a staging effect so that less liquid, compared to the average of the bed, can be seen near the baffle region. It indicated that the baffle tended to prevent liquid from reaching the baffle region. As a result, there would be less liquid that can reach below the baffle region. In a coker, if a ring baffle was installed just below the feed nozzles, our results suggest there would be less liquid entrain the lower section. Therefore, it reduced the risk of wet solids or agglomerates being rewetted by lower injections and create or strengthen the agglomerates [4]. Moreover, to prevent the liquid from reaching the stripper section, installing a ring baffle just above the stripper section is also recommended.

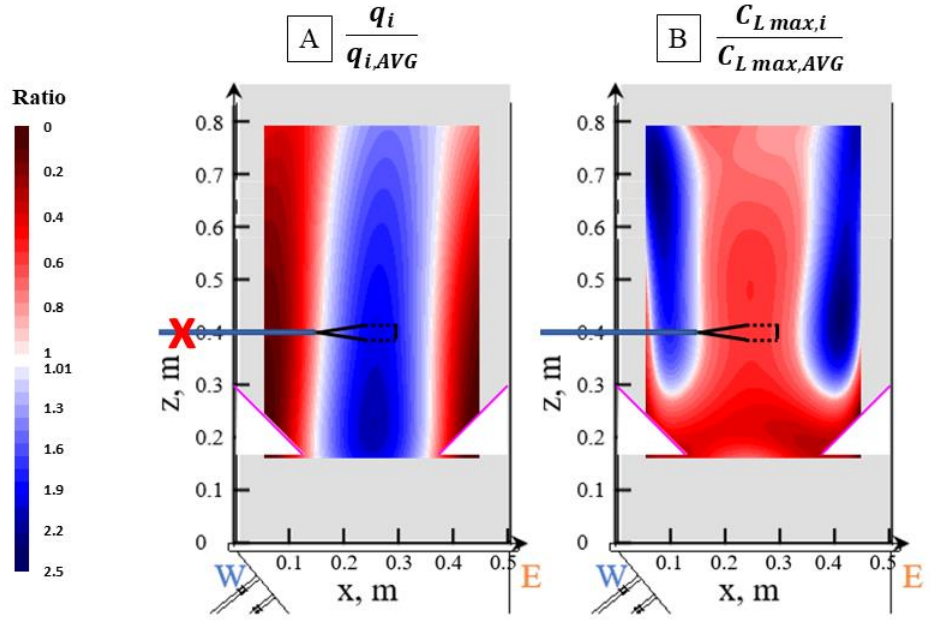

Figure 6.6 Impact of gas bubble flow (A) on local liquid concentration (B) with symmetrical baffle (Flat distributor, $V_g = 0.9\ m$, No injection for normalized gas

distribution, $T_{bed} = 30$ ℃; for normalized local liquid concentration: 4.94 mm High GLR nozzle: $x_{inj} = 0.15\ m$, $z_{inj} = 0.4\ m$, $L_{jet} = 0.15\ m$, $m_{inj} = 100\ g$, $F_L = 1.6\ g/s$, $GLR = 107$ %, $T_{bed} = 20$ ℃, method: gas distribution in section 3.1, liquid concentration in section 3.5)

Figure 6.7 shows that without a baffle, the liquid concentration above and below the baffle got closer to the bed average when increasing the superficial gas velocity (V_g). This means that when increasing the superficial gas velocity, the liquid was better dispersed. Also, it can be seen that the impact of the superficial gas velocity was stronger at lower superficial gas velocities. After it reached the transition velocity, above which the enhancement of liquid dispersion with further increases in superficial gas velocity became minor. In the turbulent regime, the gas flows as small, elongated voids that constantly appear and disappear, which also contributed to the more uniform liquid concentration. The size of bubbles in turbulent regime did not further decrease significantly [5]; thus, after the transition velocity, the beneficial impact from increasing superficial gas velocity was not as significant as that from the lower superficial gas velocities.

Figure 6.7 shows that with the symmetrical baffle, the region above the baffle became relatively wetter with increasing superficial gas velocity, while the baffle region became relatively drier. This meant that the baffle created a staging effect to prevent the liquid from reaching the stripper section. The transition velocities from above the spray, below

the spray, were consistent, although they were not as sharp as that without the baffle cases.

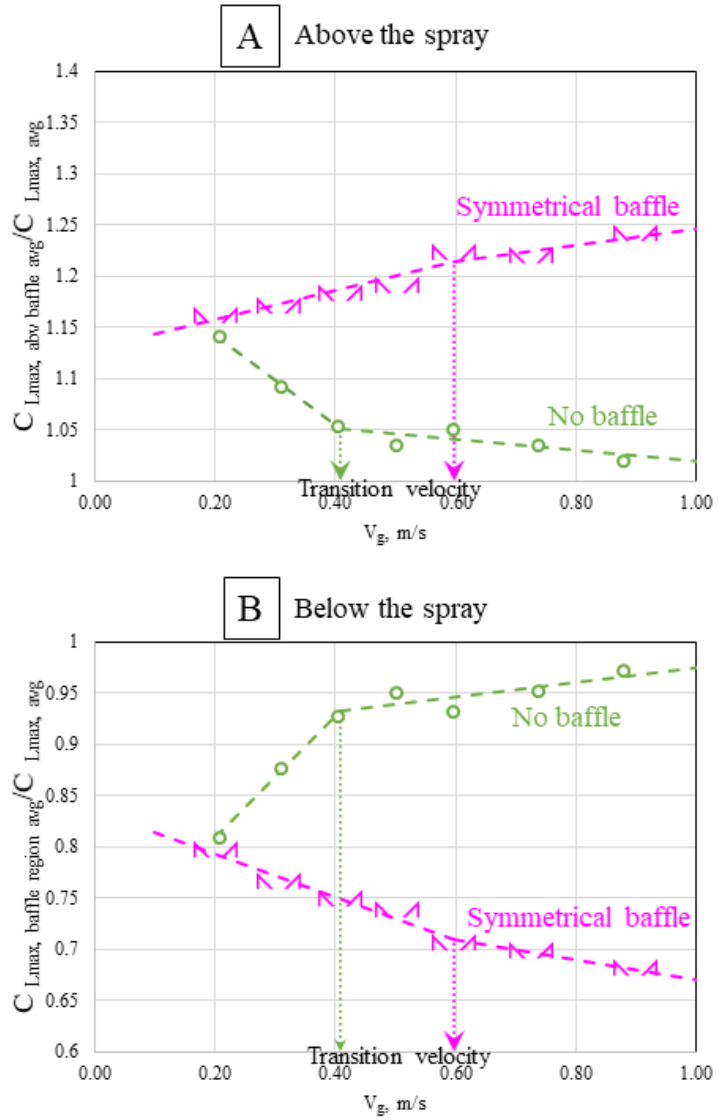

Figure 6.7 Impact of the symmetrical baffle on the average local maximum liquid concentration (A) above the spray and (B) below the spray, compared to the average time of the bed (Flat distributor, 4.94 mm High GLR nozzle: $x_{inj} = 0.15\ m$, $L_{jet} = 0.15\ m$, $m_{inj} = 100\ g$, $F_L = 1.6\ g/s$, $GLR = 107$ %, $T_{bed} = 20$ ℃, spray level: $z = 0.4\ m$, above baffle: $z > 0.45\ m$; baffle region: $z < 0.35\ m$)

6.3 Impact of gas bubble flow and a baffle on evaporation rate

Figure 6.8 shows that with an ideal spray, the symmetrical baffle had an insignificant impact on the remaining liquid in the bed at the end of injection (φ_{ac}) at different temperatures. The relevant method can be found in section 3.7 (Chapter 3). It indicated that the symmetrical baffle had no detrimental impact on the overall vaporization rate in the bed.

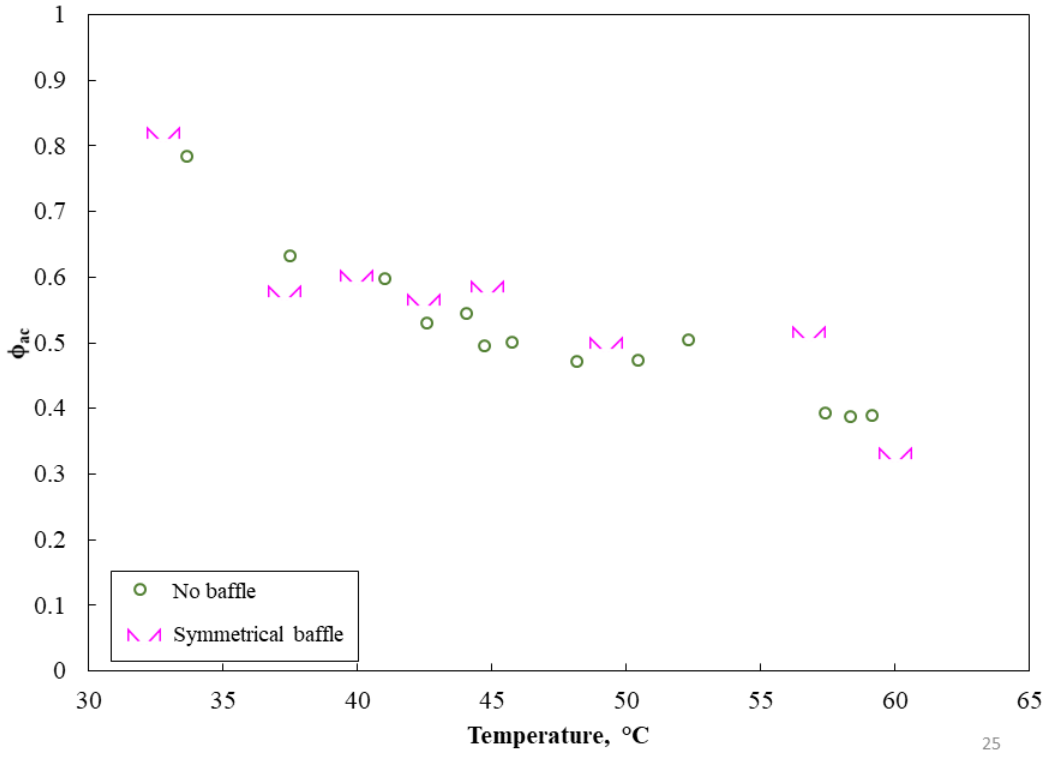

Figure 6.8 Impact of the symmetrical baffle on vapor saturation at different temperatures (Flat distributor, $V_g = 0.7$ m/s, $x_{inj} = 0.05$ m, $z_{inj} = 0.4$ m, $m_{inj} = 100$ g, $F_L = 4.5$ g/s, $GLR = 30$ %, Method: freeboard pressure method)

6.4 Impact of gas bubble flow and a baffle on fluidization regime

Table 6-1 shows that the transition velocity found with injection was close to the U_{mt} found using the pressure fluctuation measurements without injection. In section 5.1, it

was found that the transition velocity with injection was larger than the U_{mt} found with the pressure measurements. The possible reason was that with a TEB nozzle, agglomerates were created, which increased the average particle size. In this chapter, an ideal nozzle that does not create agglomerates was used; therefore, the transition velocity was close to the U_{mt} found with the pressure fluctuation measurements without injection.

Larger gas bubbles were created at the baffle region, as the symmetrical baffle concentrated gas bubbles to the baffle region, which caused the staging effect. With the baffle, it needed more turbulence in the bed to break up the large bubbles created at the baffle region to the small voids' characteristic of the turbulent regime. When a gas-liquid spray was injected into the bed, parameters that were affected by the staging effect of the baffle, such as $\frac{C_{L\,max,i}}{C_{L\,max,\,AVG}}$, resulting in a larger transition velocity when the baffle was present.

However, the staging effect did not hinder the rapid wet solids mixing in the bed (section 6.1). Therefore, the parameter to evaluate mixing, $\frac{t_{C_{L0,i}}}{t_{C_{L0,\,avg}}}$ gave very similar transition velocity to the U_{mt}.

In general, it suggests that the transition velocity with gas-liquid spray jet was highly connected with the local bed hydrodynamics, such as agglomerates formation (section 5.1), staging effect (section 6.2), and wet solids mixing (section 6.1).

Method	Parameter	No baffle	Symmetrical baffle
Pressure fluctuation without injection	U_{mt} from max value of V-statistic, m/s	0.35	0.37
	U_{mt} from coefficient of variation, m/s	0.40	0.43
With gas-liquid spray	Transition velocity from $\frac{C_{L\,max,i}}{C_{L\,max,AVG}}$, m/s	0.44	0.62
	transition vel from $\frac{t_{C_{L0,i}}}{t_{C_{L0,avg}}}$, m/s	0.39	0.39

Table 6-1 Minimum turbulent velocity without injection vs. transition velocity with injection

6.5 Conclusion

It helps to install a baffle in a coker even when no agglomerates are created during injection because the baffle:

1. Creates a strong local gas bubble flow near the baffle:
    - A strong gas bubble flow helps to:
        - Reduce local liquid concentration.
        - Prevent liquid from reaching below the spray region when the feed is just sprayed into the bed.
        - Provide better mixing between wet solids and dry gas bubbles.
2. Creates a staging effect:
    - Reduces liquid reaching below the baffle region: which is desired at the stripper section, and helpful between injection banks
    - It does not hinder the local rapid wet solids dispersion
    - It does not compromise the overall evaporation rate

6.6 Nomenclature

$C_{L\,max,i}$	$\frac{g\ of\ water}{kg\ of\ dry\ solids}$	Maximum liquid concentration at location i
$C_{L\,max,\,AVG}$	$\frac{g\ of\ water}{kg\ of\ dry\ solids}$	Average of maximum Liquid concentration at location i of the whole bed
$C_{L\,max,abv\ baffle,\,AVG}$	$\frac{g\ of\ water}{kg\ of\ dry\ solids}$	Average of maximum Liquid concentration at locations above the baffle

$C_{L\,max,\,baffle,\,AVG}$	$\frac{g\ of\ water}{kg\ of\ dry\ solids}$	Average of maximum Liquid concentration at locations at baffle region
F_L	g/s	Liquid flowrate
GLR	%	Gas to liquid ratio
L_{jet}	m	Jet length
m_{inj}	g	Mass of injection
q_i		Normalized gas bubble distribution
$q_{i,\,AVG}$		Normalized gas bubble distribution of the bed
$t_{C_{L0,i}}$	s	The time it takes for the liquid to be detected for conductance probe at location i
$t_{C_{L0,\,avg}}$	s	The average time it takes for the liquid to be detected for conductance probe at location i of the whole bed
$t_{C_{L0,\,abv\,baffle,avg}}$	s	The average time it takes for the liquid to be detected for conductance probe at location i above the baffle
$t_{C_{L0,\ baffle,avg}}$	s	The average time it takes for the liquid to be detected for conductance probe at location i at baffle region
T_{bed}	℃	Bed temperature
V_g	m/s	Superficial gas velocity

x_{inj}	m	Horizontal injection location
x	m	Horizontal location
z_{inj}	m	Vertical injection location
z	m	Vertical location

Greek

ϕ_{ac}	Cumulated vapor fraction at the end of injection

6.7 References

1. Briens, C. and J. McMillan, *Review of Research Related to Fluid Cokers.* Energy & Fuels, 2021.

2. Cochet, Y., *Impact of column geometry and internals on gas and particle flows in a fluidized bed with downward solids circulation*, in *Chemical and Biochemical Engineering*. 2021, Western University: unpublished.

3. WYATT, J.T., et al., *Circulating fluid bed reactor with improved circulation*. 2013, Google Patents.

4. Reyes, L.A.P., *Effect of temperature and successive sprays on liquid distribution in fluidized beds*. 2015, School of Graduate and Postdoctoral Studies, University of Western Ontario.

5. Brink, H.G., J. Saayman, and W. Nicol, *Two dimensional fluidised bed reactor: Performance of a novel multi-vortex distributor.* Chemical Engineering Journal, 2011. **175**(1): p. 484-493.

Chapter 7

7 Conclusions and recommendations

This chapter summarizes the major findings and contributions of the research, followed by recommendations for future research work.

7.1 Conclusions

- Measurement methods were successfully improved and adapted several to study local gas flow, initial liquid-solid contact, wet solids mixing, and evaporation rate.
- Each of these methods was validated with another method to ensure reliable results.
- The gas distribution in a fluid bed can be modified by changing the initial gas distributor or by using a baffle. An inclined distributor is an effective tool to concentrate gas bubbles to a specific area of the bed. A baffle can also be used to concentrate and redirect gas bubbles to the region just above the baffle tip. Experimental results agree well with CFD modeling [1], which indicates the potential of scaling up the major findings in this research.
- Concentrating gas bubbles to two regions can significantly reduce the initial liquid trapped fraction in agglomerates: the first region is the nozzle tip; the second region is the region at the transition between the stable jet core and the fluctuating part of the jet. We first defined a base case with our lab unit, which corresponds to the current injection location in a typical commercial coker. By just changing the initial fluidization gas distribution, without the addition of a baffle, the fraction of the injected liquid trapped in agglomerates could be reduced by 25 %, compared to the base case. With a symmetrical baffle, blocking 36 % of the cross-sectional area, the fraction of the injected liquid trapped in agglomerates could be reduced by up to 80 %. Injecting from below the baffle can reduce the fraction of liquid trapped by 40 %, compared to the base case. One can select these methods to reduce agglomerates formation based on the flexibility of available nozzle positions and associated jet penetration in the bed. A simple

shrinking core model [2] showed that this would result in significant improvements in commercial fluid cokers.

- We developed a simple, scalable model to predict how to modify the local bed hydrodynamics to enhance the initial liquid distribution.
- We confirmed that if the perfect initial liquid distribution is achieved when no agglomerates are created, the baffle is still helpful, as the staging effect can reduce liquid losses to the stripper section, leading to fouling, and to the burner, resulting in yield losses. In addition, the baffle does not hinder wet solids dispersion.

7.2 Recommendations

- Instead of modifying the fluid gas distribution or using a baffle, it may also be possible to add steam just below the two critical regions of the jet cavity identified in this thesis.
- A special baffle design could be developed to enhance the initial liquid distribution. For example, a flux tube could be positioned to direct additional gas to the nozzle tip region, while bubbles from the baffle tip would provide gas to the region at the transition between the stable jet core and the fluctuating jet part. An example that integrates an additional steam supply is shown below in Figure 7.1.

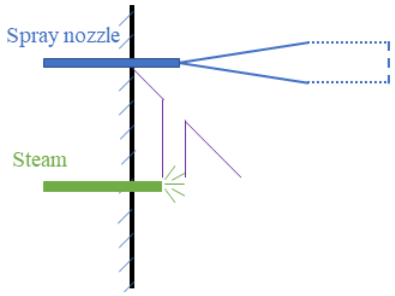

Figure 7.1 Recommendation to modify baffle geometry with additional steam to baffle flux-tube to reduce agglomerates formation during the injection.

- X-ray studies could be performed to visualize the impact of gas addition at different locations on the jet cavity dynamics. They could also be used to understand the impact of different baffle geometries on bubble flow patterns.
- The relationship between transition velocity with injection and minimum turbulent velocity without injection may be further investigated.

7.3 References

1. Xing, X., *Numerical study of the effect of gas distributors and baffles on the bubble distribution, gas and solid mixing in a fluidized bed*, in *Chemical and biochemical engineering*. 2020, Western University. p. 292.

2. Careaga, F.J.S., *Hydrodynamics in Recirculating Fluidized Bed Mimicking the Stripper Section of the Fluid Coker* in *Chemical and Biochemical Engineering* 2013, Western University.

Appendices

Appendix A: Comparison of particle size before and after operating for two months.

In this thesis, we proceeded a lot of three-min runs with silica sand for measurements, such as gas distribution, obtaining minimum turbulent velocity (U_{mt}). It was essential to ensure the silica sand in the bed did not change much. Therefore, we did particle size analysis with new sand particles and sand particles after being used for two months. Two operators tested both samples to eliminate errors.

New silica sand particles:

Sample 1, operator: Sanchez.

Main characteristics of the sample:

x_{10} = 120.68 µm x_{50} = 209.23 µm x_{90} = 342.76 µm SMD = 189.25 µm VMD= 221.93 µm

x_{16} = 136.84 µm x_{84} = 305.40 µm x_{99} = 473.40 µm S_V = 0.03 m²/cm³ S_m = 119.64 cm²/g

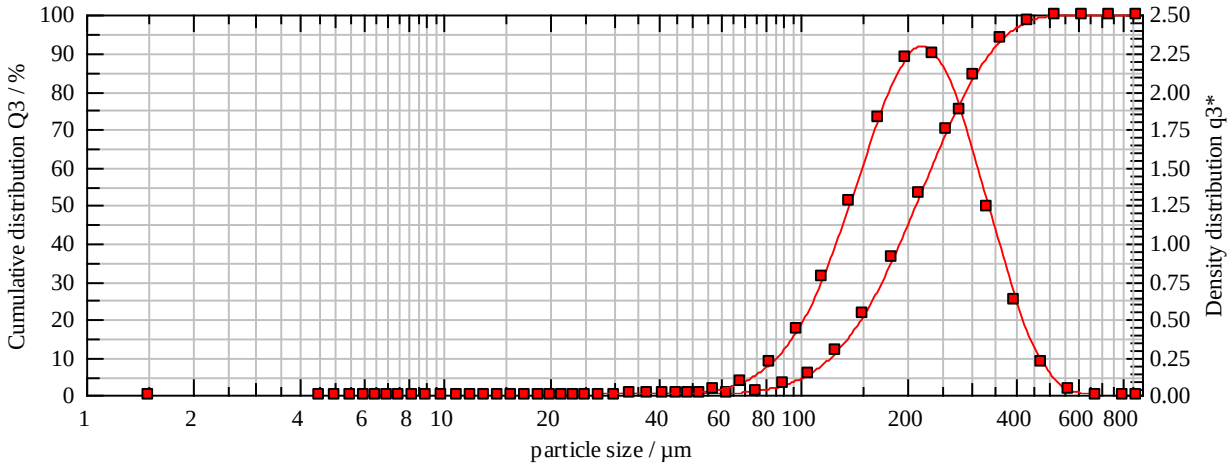

Figure A- 1 Particle size analysis of new silica sand (operator: Sanchez)

Sample 2, operator: Li.

Main characteristics of the sample:

x_{10} = 123.67 µm x_{50} = 209.26 µm x_{90} = 336.37 µm SMD = 190.27 µm VMD= 220.44 µm

x_{16} = 139.05 µm x_{84} = 301.76 µm x_{99} = 436.22 µm S_V = 0.03 m²/cm³ S_m = 119.00 cm²/g

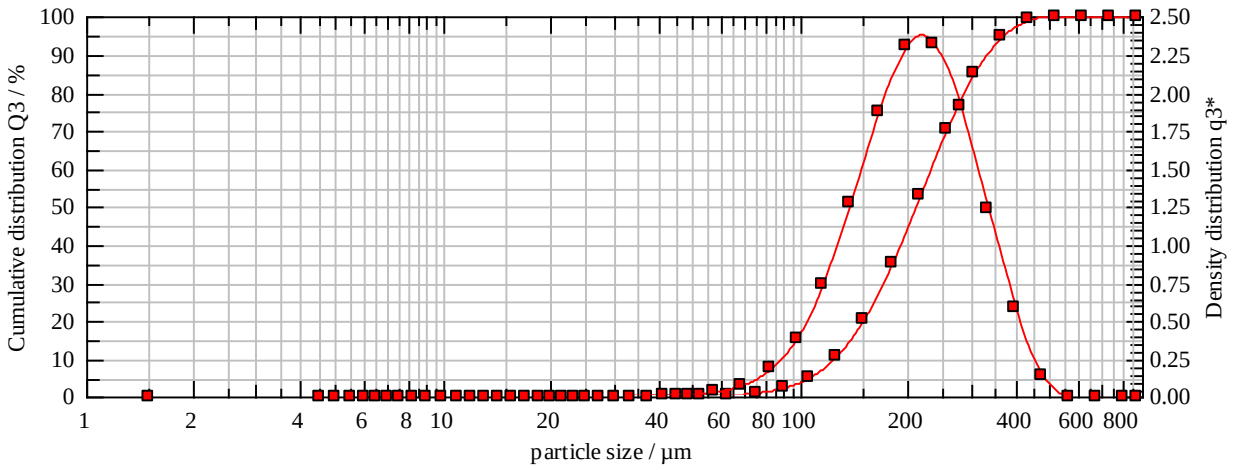

Figure A- 2 Particle size analysis of new silica sand (operator: Li)

Figure A- 1and Figure A- 2 gave the information that the average Sauter mean diameter of original silica sand at original condition is 189.76 μm.

After the bed of sand has been used for 2 months, the whole bed of sand was drained from the bottom of the bed. The mixture of 2 g of sands from the first and last part of the draining process was selected for particle size analysis.

After runs for 2 months

Sample 3, 2 months later, operator: Sanchez

x_{10} = 130.43 µm x_{50} = 214.67 µm x_{90} = 341.99 µm SMD = 197.48 µm VMD= 226.54 µm

x_{16} = 146.51 µm x_{84} = 306.77 µm x_{99} = 452.90 µm S_V = 0.03 m²/cm³ S_m = 114.65 cm²/g

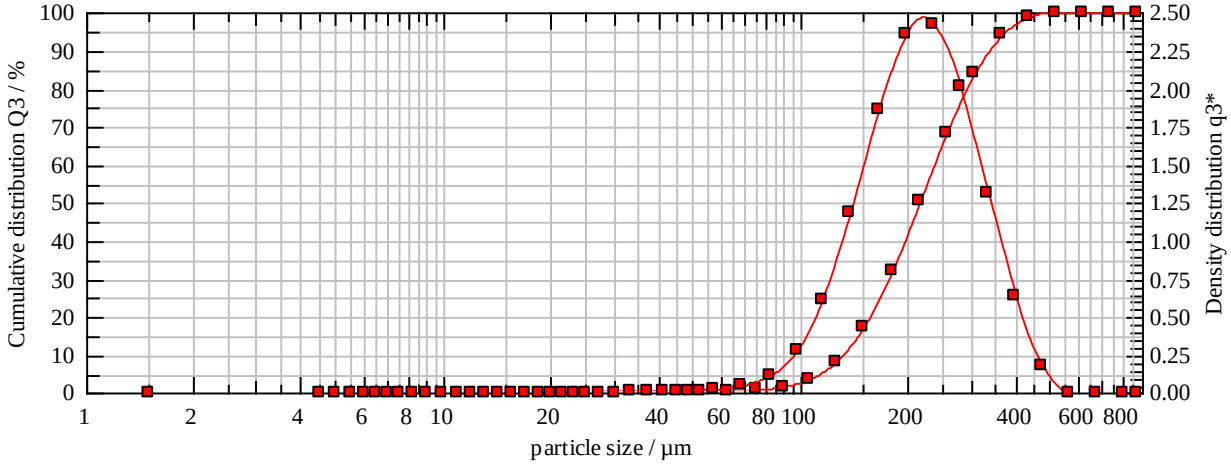

Figure A- 3 Particle size analysis of silica sand that has been operated for two months (operator: Sanchez)

Sample 4, 2 months later, operator: Li

x_{10} = 130.99 µm x_{50} = 213.07 µm x_{90} = 337.44 µm SMD = 197.39 µm VMD= 224.67 µm

x_{16} = 146.49 µm x_{84} = 302.99 µm x_{99} = 434.80 µm S_V = 0.03 m²/cm³ S_m = 114.70 cm²/g

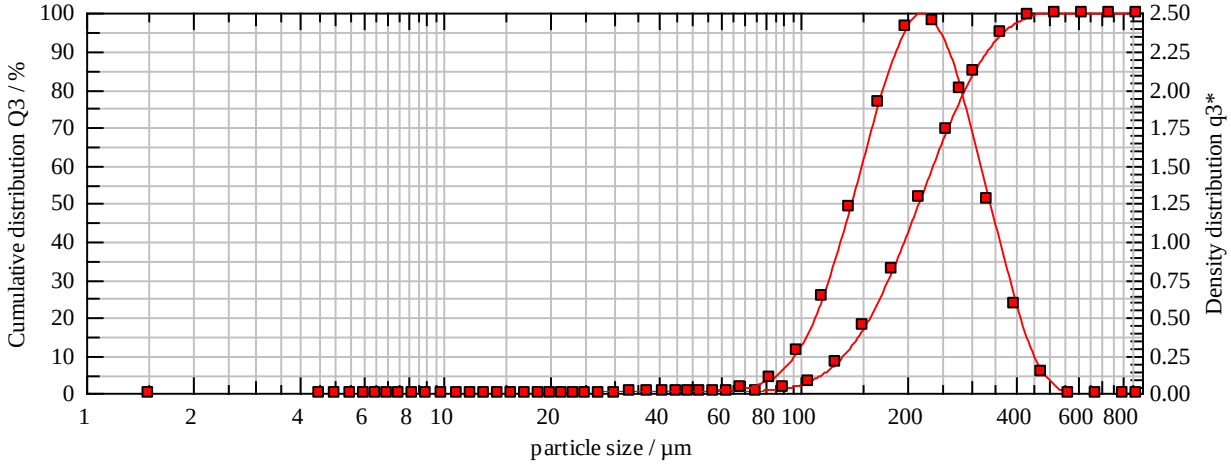

Figure A- 4 Particle size analysis of silica sand that has been operated for two months (operator: Li)

Figure A- 3 and Figure A- 4 gave the information that the average Sauter mean diameter of silica sand that has been used for 2 months was 197.44 μm.

A slight increase of the average Sauter mean diameter of silica sand by approximately 8 μm for 2-month operation, probably due to part of fines from original sand, was removed by cyclones. The minor change of particle Sauter mean diameter was considered as not significant.

Appendix B: Impact of superficial gas velocity on the gas distribution of the whole bed

We showed one example of superficial gas velocities (V_g) on the gas distribution of the whole bed with the western case without a baffle in Figure 4.2. In this section, we show the impact of V_g with the more gas distributor configurations, such as even and eastern case, and with a baffle.

Figure B- 1shows that the superficial gas velocity had a minor impact on the gas distribution of the whole bed with even case without a baffle, which was consistent with the case we presented in section Figure 4.2. With the increase of V_g, the gas bubbles tended to migrate to the bed center at the higher vertical locations. But no clear impact from bubbling to turbulent transition change could be seen. The even case has more gas bubbles concentrate to the western side of the bed was discussed in section Figure 4.2.

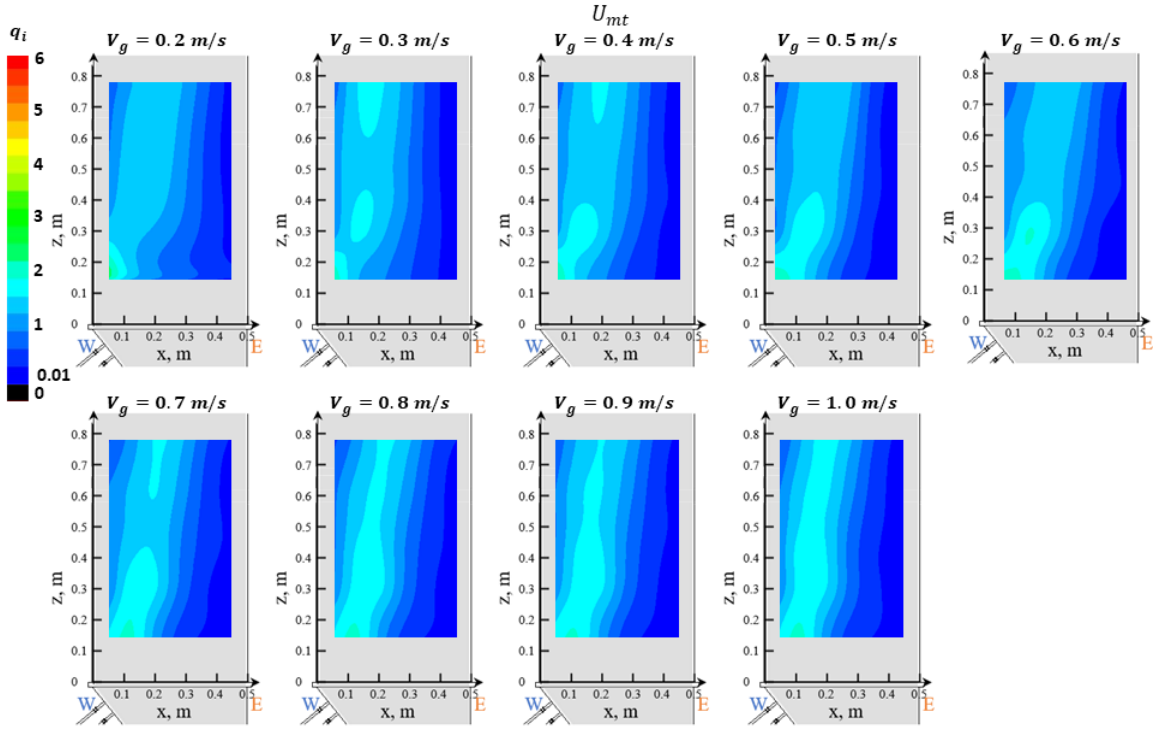

Figure B- 1 The impact of V_g on gas distribution (inclined distributor, no baffle, even case, $T_{bed} = 30\ °C$) (The spray nozzle level: $z = 0.67\ m$).

Figure B- 2 shows that the superficial gas velocity had a minor impact on the gas distribution of the whole bed with the eastern case without a baffle, which was consistent with the case we presented in Figure 4.2.

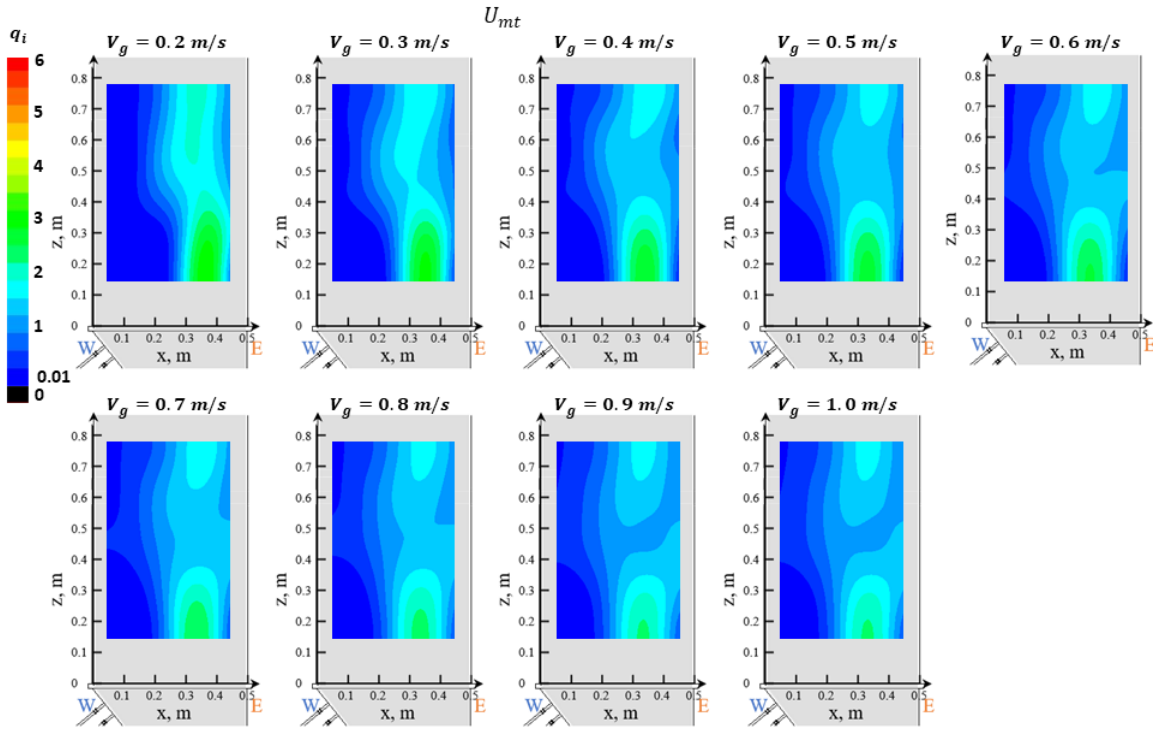

Figure B- 2 The impact of V_g on gas distribution (inclined distributor, no baffle, eastern case, $T_{bed} = 30\ °C$) (The spray nozzle level: $z = 0.67\ m$).

Figure B- 3 confirms that with baffle A1, which significantly modified the gas distribution, compared to the no baffle case, the superficial gas velocity had a minor

impact on gas distribution above the baffle, which was consistent with the case we presented in section Figure 4.2.

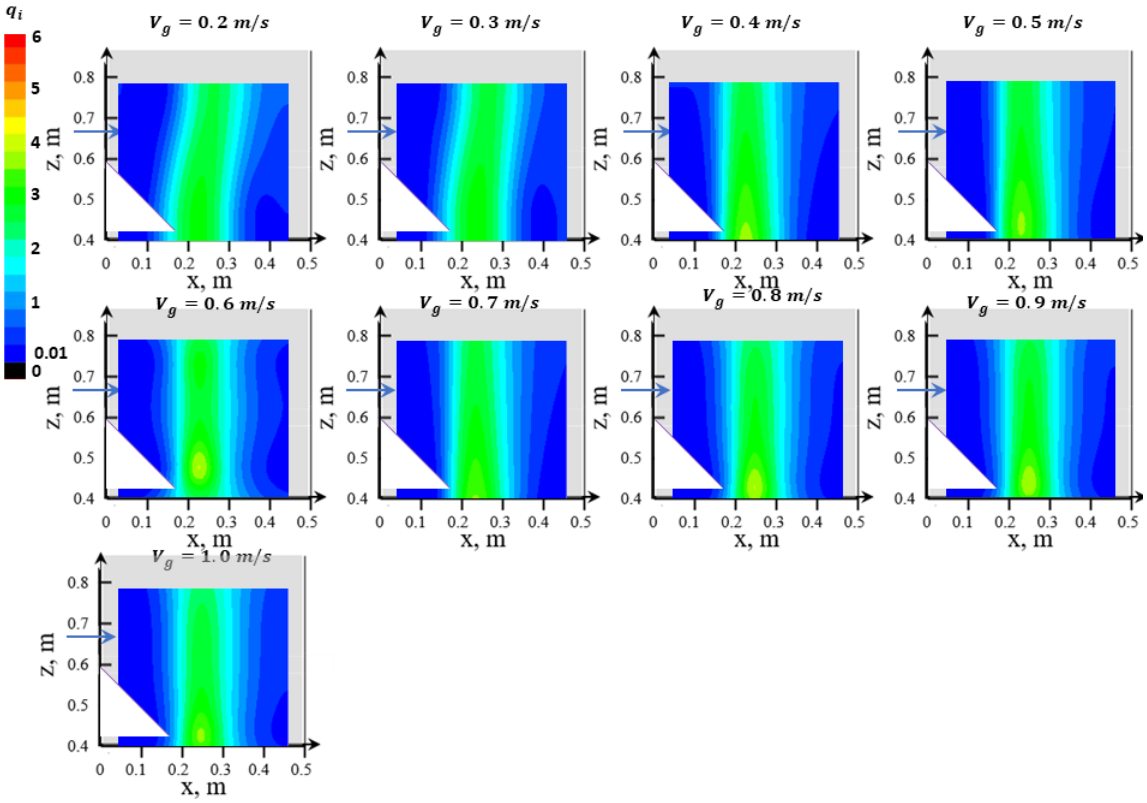

Figure B- 3 The impact of V_g on gas distribution (inclined distributor, baffle A1, even case, $T_{bed} = 30\ °C$) (The spray nozzle level: $z = 0.67\ m$).

Appendix C: Flat distributor gas distribution above the injection level

Figure 4.2 shows the gas bubbles above the injection level concentrated on the eastern side of the bed. This result has been confirmed with another three methods: the radiation transmission method, pressure measurement with a bubbler tube (provided by a fellow student, Jessica Godin), and solids entrainment to two cyclones on the western and eastern sides of the bed. Many attempts were made to correct the potential issue that created it, such as leveling the unit, adjusting the cyclone pressure, and opening the unit to check for possible reasons. Unfortunately, the above effort did not change the gas distribution observed in Figure 4.2.

This section shows the details of the results of the confirmation methods and the results from attempts to correct the potential issue with flat distributor gas distribution on the top section.

Confirmation methods:

a. Radiation transmission method

Figure C- 1 shows at a higher vertical location ($z = 0.79\ m$), the volume that was occupied by gas bubbles on the eastern side ($x = 0.4\ m$) was higher than that of the central location ($x = 0.25\ m$) and on the western side ($x = 0.1\ m$). While below the injection ($z = 0.35\ m$), the volume that was occupied by gas bubbles was similar from the eastern side ($x = 0.4\ m$) and western side ($x = 0.1\ m$), while it was higher at the central location ($x = 0.25\ m$). These results were consistent with what we saw with E-probe measurements that were presented in Figure 4.2.

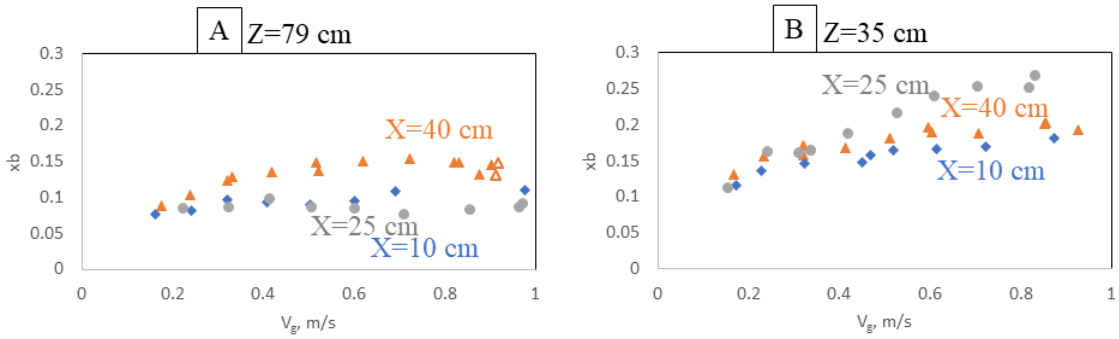

Figure C- 1 Bed volume that was occupied by bubbles (x_b) at different superficial gas velocities (V_g) (Flat distributor, no baffle, $T_{bed} = 30\ °C$, spray level: $z = 40\ cm$, Method: radiation transmission method)

b. Pressure measurement with a bubbler tube

Figure C- 2 shows that there were four measuring locations of the pressure measurements. They covered the area from the E-probe measurements. We measured differential pressure from top west to top east locations and from bottom west to bottom east locations.

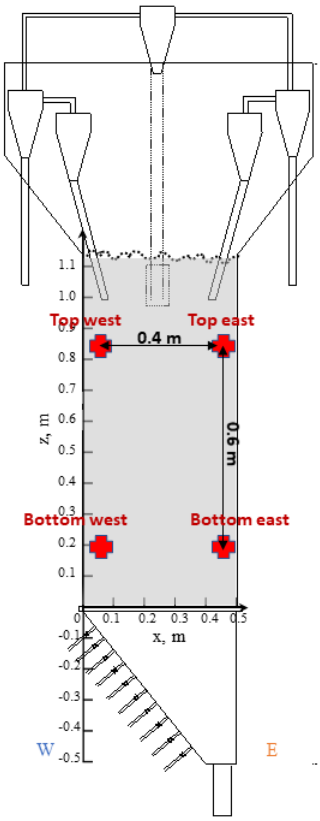

Figure C- 2 Measuring locations (in the red cross) of pressure measurements with a bubbler tube (Flat distributor, no baffle, $T_{bed} = 30\ °C$, measuring locations: top west: $x = 0.05\ m, z = 0.85\ m$, top east: $z = 0.45\ m, z = 0.85\ m$, bottom west: $x = 0.05\ m, z = 0.2\ m$, bottom east: $x = 0.45\ m, z = 0.2\ m$)

Figure C- 3 shows the experimental setup of the bubbler tube. The compressed air was connected to the measuring location with a small orifice with a diameter of 0.106 mm to avoid the measuring location being plugged by the particles. Figure C- 3 shows one measuring location was connected to a differential pressure transducer. We connected the

other measurement location to the other side of the differential pressure transducer as described previously.

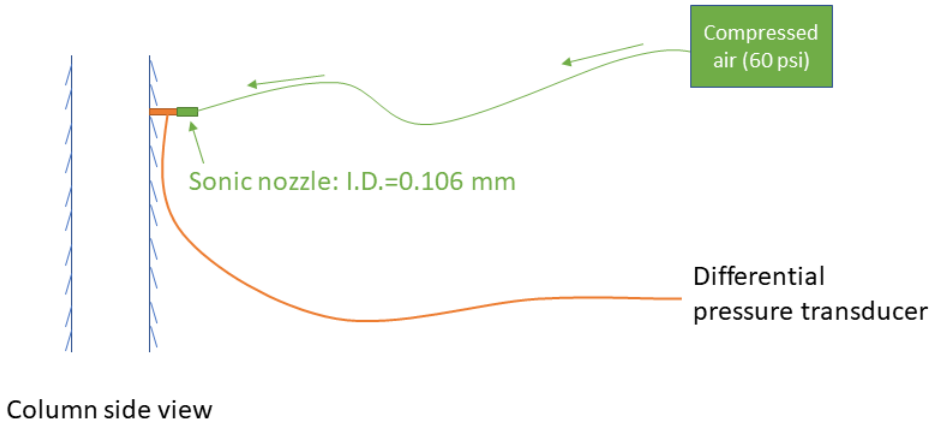

Figure C- 3 Pressure measurement with a bubbler tube

Figure C- 4 A shows that at the top measuring locations, the eastern side pressure was higher, resulting from more gas bubbles or more solids (higher bed density). From results from the radiation transmission method, we know it was caused by more gas bubbles. Figure C- 4 B shows that at the bottom measuring locations, at lower gas velocity, the western side pressure was higher. After 0.42 m/s, the eastern side was slightly higher, while comparing to results from the top measuring locations, they are closer to zero. Zero meant there was no pressure difference between the western and eastern sides.

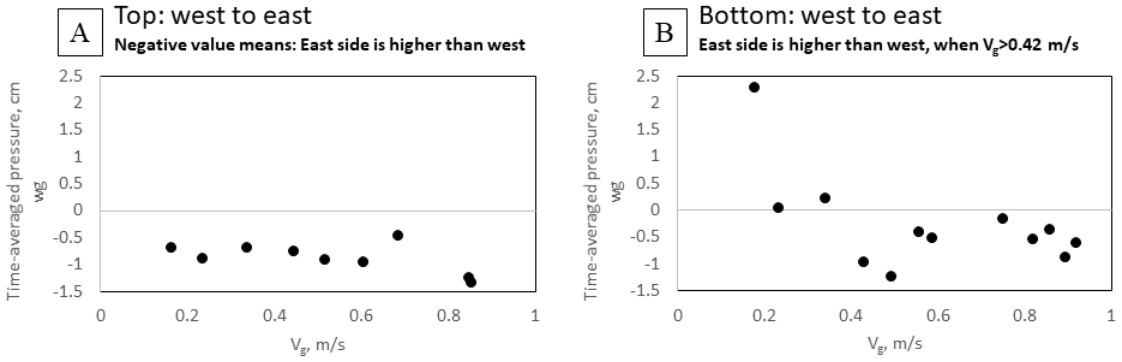

Figure C- 4 Time-averaged pressure from pressure measurements (Flat distributor, no baffle, $T_{bed} = 30\ °C$,)

c. Solids entrainment to cyclones

Because the lower fixed bed height (0.85 m) was below the cyclone diplegs, entrained solids to both cyclones could quickly reach a significant amount to be compared. We checked the mass of solids from both cyclones after each group, then put them back to the bed. Each experiment took about 40 min.

Table C- 1 shows that more gas bubbles concentrated on the eastern side at the top region, resulting in a higher solids entrainment.

M_{sand}, kg	Western side cyclone	Eastern side cyclone
Replicate 1	3.85	5.11
Replicate 2	4.54	5.42
Replicate 3	2.88	3.76
Replicate 4	2.26	2.78
Replicate 5	2.95	3.86
Replicate 6	2.93	3.73

Table C- 1 Solid entrainment to cyclones on the western and eastern side of the bed with lower fixed bed height with six replicates (Bed height:0.85 m, flat distributor, no baffle, $T_{bed} = 30\ °C$,)

Results from attempts to correct the potential issue:

Figure C- 5 shows that many attempts were made to correct the potential issue that created it, such as adding solids, leveling the unit, adjusting the cyclone pressure, and opening the unit to check for possible reasons. Unfortunately, the above effort did not change the gas distribution observed in Figure 4.2.

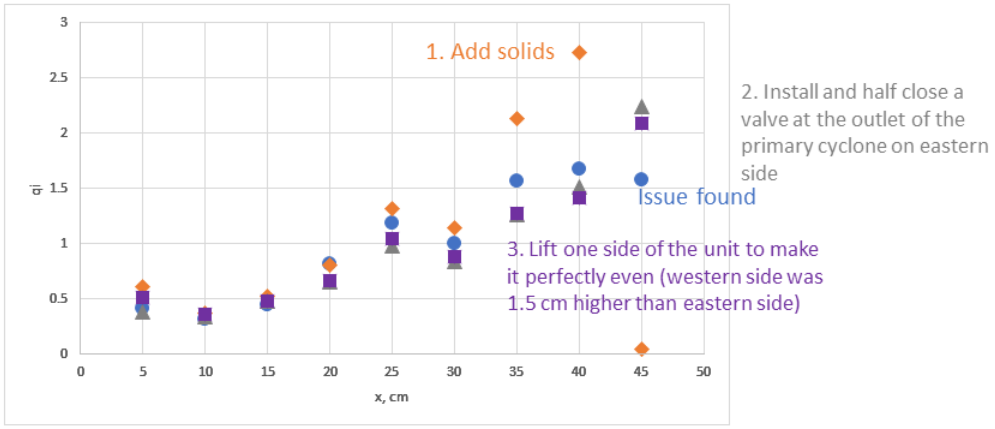

Figure C- 5 Impact of several attempts on the horizontal gas distribution (Flat distributor, no baffle, $T_{bed} = 30\ °C$)

Curriculum Vitae

Name: Yuan Li

Post-secondary Education and Degrees:
Northwest University
Xi'an, Shaanxi, China
2011-2015 Bachelor of Science

Related Work Experience
Teaching Assistant
The University of Western Ontario
2019

Publications:

Li, Y., Careaga, F. S., Briens, C., Berruti, F., & McMillan, J. (2020). Impact of local fluidized bed hydrodynamics on the distribution of liquid sprayed into the bed. Powder Technology, 367, 326-335.

Li, Y., Jahanmiri, M., Careaga, F. S., Briens, C., Berruti, F., & McMillan, J. (2020). Applications of electrostatic probes in fluidized beds. Powder Technology, 370, 64-79.

Li, Y., et al. IMPACT OF FLUIDIZED BED HYDRODYNAMICS ON THE DISTRIBUTION OF LIQUID SPRAYED INTO THE BED. in CFB 13. 2021. Vancouver, Canada.